HAL
open science

On the physical properties of poly(ethylene 2,5-furandicarboxylate)

Jesper Gabriël van Berkel

To cite this version:

Jesper Gabriël van Berkel. On the physical properties of poly(ethylene 2,5-furandicarboxylate). Material chemistry. COMUE Université Côte d'Azur (2015 - 2019), 2018. English. NNT : 2018AZUR4075 . tel-01958692

HAL Id: tel-01958692

https://theses.hal.science/tel-01958692v1

Submitted on 18 Dec 2018

HAL is a multi-disciplinary open access archive for the deposit and dissemination of scientific research documents, whether they are published or not. The documents may come from teaching and research institutions in France or abroad, or from public or private research centers.

L'archive ouverte pluridisciplinaire **HAL**, est destinée au dépôt et à la diffusion de documents scientifiques de niveau recherche, publiés ou non, émanant des établissements d'enseignement et de recherche français ou étrangers, des laboratoires publics ou privés.

UNIVERSITÉ CÔTE D'AZUR

ÉCOLE DOCTORALE
SCIENCES FONDAMENTALES ET APPLIQUÉES

THÈSE DE DOCTORAT

Propriétés Physiques du Poly(éthylène 2,5-furandicarboxylate)

On the Physical Properties of Poly(ethylene 2,5-furandicarboxylate)

Jesper Gabriël VAN BERKEL

Institut de Chimie de Nice

Présentée en vue de l'obtention du grade de docteur en Matériaux **d'**Université Côte d'Azur
Dirigée par : Dr. Nicolas Sbirrazzuoli, Professeur, Université Côte D'Azur
Encadrée par : Dr. Nathanaël Guigo, Maître de Conférences, Université Côte D'Azur (Examinateur)
Soutenue le : 2 Juillet 2018

Devant le jury, composé de :
Dr. Dimitrios N. Bikiaris, Professeur, Université de Thessaloniki, Grece (Rapporteur)
Dr. Sanjay Rastogi, Professeur, Université de Maastricht, Pays-Bas et Université de Loughborough, Royaume-Uni (Rapporteur)
Dr. Noëlle Billon, Professeur, Centre de Mise en Forme des Matériaux, France (Examinateur)
Dr. Hendrikus A. Visser, Chef d'équipe, Synvina, Pays-Bas (Examinateur)

Funding organisations

avantium

SYNVINA
functional. sustainable. bioplastics.

European Commission

On the Physical Properties of Poly(ethylene 2,5-furandicarboxylate)

Jury :

Rapporteurs

Dr. Dimitrios N. Bikiaris, Professeur, Université de Thessaloniki, Grece

Dr. Sanjay Rastogi, Professeur, Université de Maastricht, Pays-Bas et Université de Loughborough, Royaume-Uni

Examinateurs

Dr. Noëlle Billon, Professeur, Centre de Mise en Forme des Matériaux, France

Dr. Nathanaël Guigo, Maître de Conférences, Université Côte D'Azur

Dr. Nicolas Sbirrazzuoli, Professeur, Université Côte D'Azur

Dr. Hendrikus A. Visser, Chef d'équipe, Synvina, Pays-Bas

ABSTRACT

Plastics have become an integral part of our lives, while the petrochemical feedstocks used to make them are not sustainable on the long term. In pursuit of production processes starting from renewable feedstocks, furanics were found to form quite readily from abundant plant-based carbohydrates and to bring new functionality as intermediates. Poly(ethylene 2,5-furandicarboxylate) or PEF is one of the plastics that can be made through 2,5-furandicaboxylic acid (FDCA) as an intermediate. It can be produced analogously to the ubiquitous material Poly(ethylene terephthalate) (PET) but has only recently been gaining more attention including the finding that it has greatly reduced gas permeability and a higher modulus and glass transition temperature, rendering it interesting as a packaging material. In the first part of this work we study the crystallization behavior of PEF, relevant for production and handling of pellets as well as transparency and thermal properties in end-use applications, as a function of molecular weight and the type of catalyst used. Mathematical models were found that describe both isothermal crystallization kinetics and non-isothermal kinetics for PEF, which is generally slower than PET. PEF crystallization from the glass found to be atypical and was modeled using unconventional models and the isoconversional approach. The origin of this behavior was found to be nucleation at low temperatures, which can be influenced to accelerate its crystallization. The second part of this work relates to the thermomechanical behavior of PEF, relevant for its processing and application in particular. The higher glass transition temperature was found to not increase as much by crystallinity as PET, and could be attributed to a reduced chain mobility compensated by increased free volume. The loose entanglement of PEF could be explained by reduced unperturbed chain dimensions following quite directly from the reduced bond length of FDCA. No significant conformational restictions were found, thus any mobility reduction should be intermolecular. A higher temperature and strain rate dependence of the melt viscosity was found for PEF across various molecular weights and catalyst types, which was described mathematically and can also be explained by a more loosely entangled network. The amorphous mechanical properties and higher strain rate dependence at room temperature also point to a low entanglement network although mobility reduction may also play a role. Biaxial orientation of PEF in the rubbery state, relevant for producing films and bottles, showed that higher draw ratios are needed than for PET until molecular orientation is maximized and strain hardening begins. However, it was found that upon using higher stretch ratios, oriented PEF can exhibit increased strength and T_g compared to oriented PET and further reduced gas permeability.

GLOSSARY

Apparatii, expressions & latin abbreviations

A	pre-exponential factor	s^{-1}
C_p	heat capacity	$J.g^{-1}.K^{-1}$
C_p^*	complex heat capacity	$J.g^{-1}.K^{-1}$
C_p'	in-phase component of C_p^*	$J.g^{-1}.K^{-1}$
C_p''	out-of-phase component of C_p^*	$J.g^{-1}.K^{-1}$
C_v	isochoric heat capacity	$J.g^{-1}.K^{-1}$
DMA	dynamic mechanical analysis	
DSC	differential scanning calorimetry	
E^*	complex tensile modulus	MPa
E'	tensile storage modulus (in-phase component of E^*)	MPa
E''	tensile loss modulus (out-of-phase component of E^*)	MPa
E_α	apparent/effective activation energy	$J.mol^{-1}$
f	correction factor in HL theory	-
$f(\alpha)$	mathematical function associated to the reaction mechanism	
G	crystalline growth rate	$cm.s^{-1}$
G^*	complex shear modulus	MPa
G'	shear storage modulus (in-phase component of G^*)	MPa
G''	shear loss modulus (out-of-phase component of G^*)	MPa
G_N^0	rubber plateau modulus	MPa
G_0	pre-exponential factor of crystalline growth rate	$cm.s^{-1}$
GPC	gel permeation chromatography	
k_B	Boltzman constant	$J.K^{-1}$
K_g	nucleation constant	K^2
$k(T)$	rate constant	S.I.

MAF	mobile amorphous fraction	
M	molecular weight of a monomeric unit	$g.mol^{-1}$
M_n	number-average molecular weight	$kg.mol^{-1}$
M_w	weight-average molecular weight	$kg.mol^{-1}$
M_e	molecular weight between entanglements	$kg.mol^{-1}$
N_A	Avogadro's number	mol^{-1}
N_α	number of monomeric units per V_{crr}	-
PDI	polydispersity index	-
Q	reaction heat released	$J.g^{-1}$
R	gas constant	$J.mol^{-1}.K^{-1}$
RAF	rigid amorphous fraction	
SSP	solid-state polymerization	
TGA	thermogravimetric analysis	
TMDSC	temperature modulated differential scanning calorimetry	
TOPEM	stochastic temperature modulated DSC	
T_c	crystallization temperature	°C
T_g	glass transition temperature	°C
T_m	melting temperature	°C
T_m^0	equilibrium melting temperature	°C
T_α	loss modulus α-relaxation peak temperature (dynamic T_g)	°C
T_β	loss modulus β-relaxation peak temperature	°C
T_∞	chain immobilization temperature	°C
$Tan\ \delta$	damping factor	none
U^*	activation energy of segmental jump	$J.mol^{-1}$
$V_{crr} = \xi^3_{T\alpha}$	volume of cooperative rearranging region	nm^3
WAXD	wide-angle X-ray diffraction	
X_c	degree of crystallinity	-

α	extent of converstion	-
α_i	extent of conversion at time i (t_i)	-
β	heating rate	°C.min^{-1}
γ	shear strain	-
δT	mean temperature fluctuation	°C
ΔC_p	heat capacity step at constant pressure	J.g^{-1}.K^{-1}
$\Delta C_p^{0\%}$	heat capacity step of 100% amorphous material	J.g^{-1}.K^{-1}
ΔH_m^0	melting enthalpy of a pure crystal	J.g^{-1}
ΔH_{tot}	total heat	J.g^{-1}
ΔH_c	crystal enthalpy	J.g^{-1}
ΔT	degree of undercooling	°C
ε	tensile strain	-
η^*	complex melt viscosity	Pa.s
$[\eta]$	intrinsic viscosity in solution	dL.g^{-1}
$\xi_{T\alpha}$	characteristic length of cooperative rearranging region (CRR)	nm
ρ	density	kg.m^{-3}
σ	tensile stress	MPa
σ_e	free energy of chains folding surface	J
τ	shear stress	kPa
ω	oscillation frequency	Hz

TABLE OF CONTENTS

GLOSSARY vii
TABLE OF CONTENTS x
CHAPTER 1 GENERAL INTRODUCTION 1
1 PLASTIC FEEDSTOCKS 2
2 SUGARS AS PLASTIC FEEDSTOCK 5
2.1 FDCA AS AN INTERMEDIATE 6
3 THIS WORK 9
4 REFERENCES 11
CHAPTER 2 BACKGROUND 13
1 PHYSICAL PROPERTIES OF POLYMERS 14
2 SYNTHESIS AND PROPERTIES OF PET 19
3 SYNTHESIS AND PROPERTIES OF PEF 21
4 DISCUSSION 23
5 REFERENCES 27
CHAPTER 3 ISOTHERMAL CRYSTALLIZATION KINETICS 29
1 INTRODUCTION 30
2 EXPERIMENTAL 32
2.1 MATERIALS 32
2.2 METHODS 34
DENSITY AND MELT ENTHALPY OF PURE PEF CRYSTAL 34
MELT CRYSTALLIZATION KINETICS 34
3 RESULTS & DISCUSSION 35
3.1 DENSITY AND MELT ENTHALPY OF PURE PEF CRYSTAL 35
3.2 MELT CRYSTALLIZATION KINETICS 37
3.3 EFFECT OF THE POLYMERIZATION RECIPE 44
4 CONCLUSIONS 46
5 REFERENCES 48
CHAPTER 4 NON-ISOTHERMAL CRYSTALLIZATION KINETICS 51
1 INTRODUCTION 52
2 EXPERIMENTAL 53
2.1 MATERIALS 53
2.2 METHODS 54
2.3 THEORY 54

3 EVALUATION OF KINETIC MODELS 59
3.1 MODELING ADDITIONAL CRYSTALLIZATION PROCESSES 68
3.2 COMPARISON TO THE OZAWA METHOD 70
3.3 THE ADVANCED MODEL-FREE ISOCONVERSIONAL METHOD 72
4 SIMULATION OF HEAT FLOW CURVES AND ACTIVATION ENERGIES 73
5 CONCLUSIONS 77
6 REFERENCES 78
CHAPTER 5 CRYSTAL NUCLEATION BEHAVIOR 79
1 INTRODUCTION 80
2 EXPERIMENTAL 82
2.1 MATERIALS 82
2.2 METHODS 82
3 RESULTS & DISCUSSION 85
3.1 ISOTHERMAL CRYSTALLIZATION 85
3.2 EFFECT OF COOLING RATES 88
3.3 EFFECT OF LOW TEMPERATURE ANNEALING 91
4 CONCLUSIONS 94
5 REFERENCES 95
CHAPTER 6 GLASS TRANSITION AND CHAIN COOPERATIVITY OF PEF *vs* PET 97
1 INTRODUCTION 98
2 EXPERIMENTAL 100
2.1 MATERIALS 100
2.2 METHODS 100
SAMPLE PREPARATION 101
STOCHASTIC TMDSC 103
CONVENTIONAL DSC FOR KINETIC COMPUTATIONS 103
2.3 COMPUTATIONAL METHODS 104
SIZE OF THE COOPERATIVE REARRANGING REGION (CRR, ξ^3_{Tg}) 104
GLASS TRANSITION KINETICS 105
3 RESULSTS & DISCUSSION 106
3.1 DSC INVESTIGATION 106
3.2 DMA ANALYSIS 111
3.3 ESTIMATION OF THE SIZE OF THE CRR FROM THERMAL DATA 115
3.4 GLASS TRANSITION KINETICS FOR PEF *vs* PET 120
4 CONCLUSIONS 124
5 REFERENCES 126

CHAPTER 7 MELT AND AMORPHOUS GLASS MECHANICS OF PEF *vs* PET 129
1 INTRODUCTION 130
2 EXPERIMENTAL 131
2.1 MATERIALS 131
2.2 METHODS 133
3 RESULTS & DISCUSSION 136
3.1 SOLUTION VISCOSITY 136
3.2 MELT VISCOSITY 138
3.2.1 ZERO SHEAR VISCOSITY 138
3.2.2 SHEAR RATE DEPENDENCE 141
3.3 MECHANICAL PROPERTIES 144
3.4 ENTANGLEMENT DENSITY 149
4 CONCLUSIONS 153
5 REFERENCES 154
CHAPTER 8 BIAXIAL ORIENTATION AND ORIENTED PROPERTIES OF PEF *vs* PET 155
1 INTRODUCTION 156
2 EXPERIMENTAL 157
2.1 MATERIALS 157
2.2 METHODS 159
BIAXIAL ORIENTATION 159
TESTING OF ORIENTED PROPERTIES 159
3 RESULTS & DISCUSSION 160
3.1 BIAXIAL ORIENTATION 160
3.2 PROPERTIES OF ORIENTED SAMPLES 162
CRYSTALLINITY AND SHRINKAGE 162
DYNAMIC THERMAL BEHAVIOR 166
3.3 MECHANICAL PROPERTIES 168
3.4 PERMEABILITY 171
4 CONCLUSIONS 171
5 REFERENCES 175
CHAPTER 9 GENERAL CONCLUSIONS AND OUTLOOK 177
1 CONCLUSIONS 178
2 OUTLOOK 180
LIST OF PUBLICATIONS AND PATENT APPLICATIONS 183
ACKNOWLEDGEMENTS 185

CHAPTER 1
GENERAL INTRODUCTION

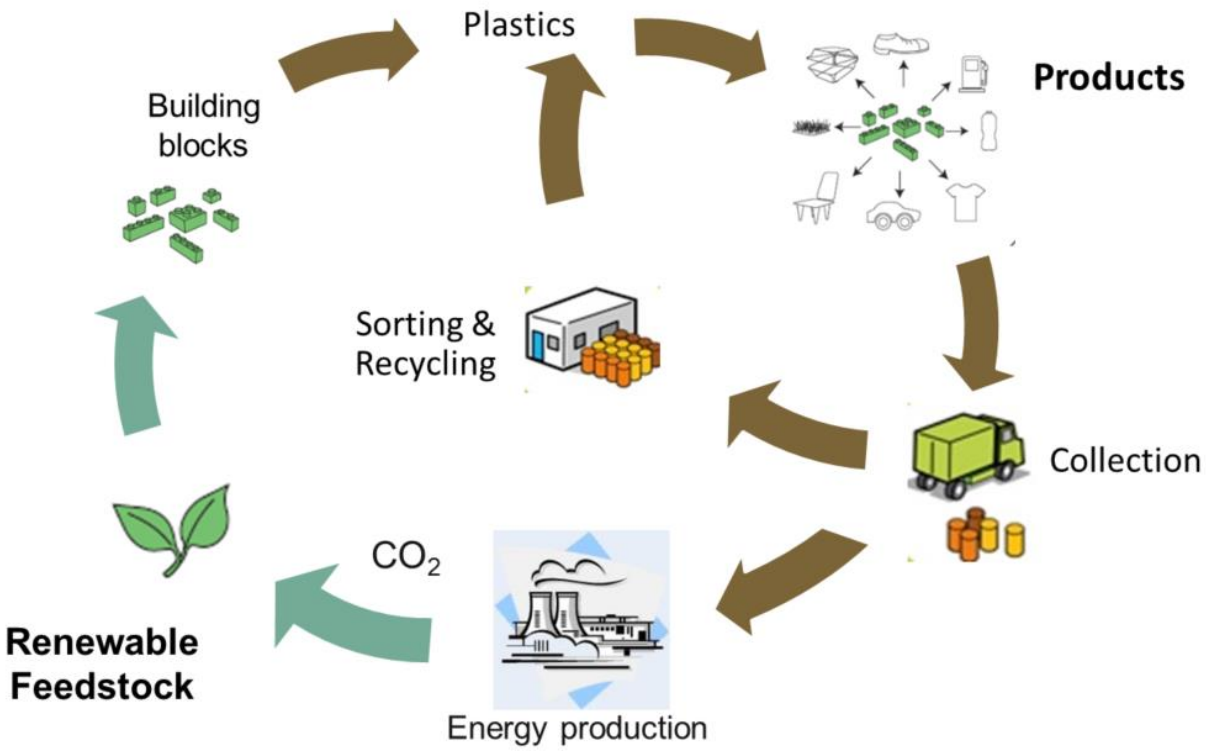

1 PLASTIC FEEDSTOCKS

Polymeric materials have been given the name 'plastics' due to their processability into a wide variety of shapes, ranging from fibers to films to complex physical parts. Since their conception at the beginning of the 20th century, synthetic polymers have become a distinct class of widely used materials characterized by a high strength and stiffness compared to a relatively light weight (low density). This is illustrated well by the Ashby plots[1] in Figure 1, which show how polymers have been filling an apparent gap between natural organic materials (wood, leather) and inorganic materials (glasses, ceramics and metals).

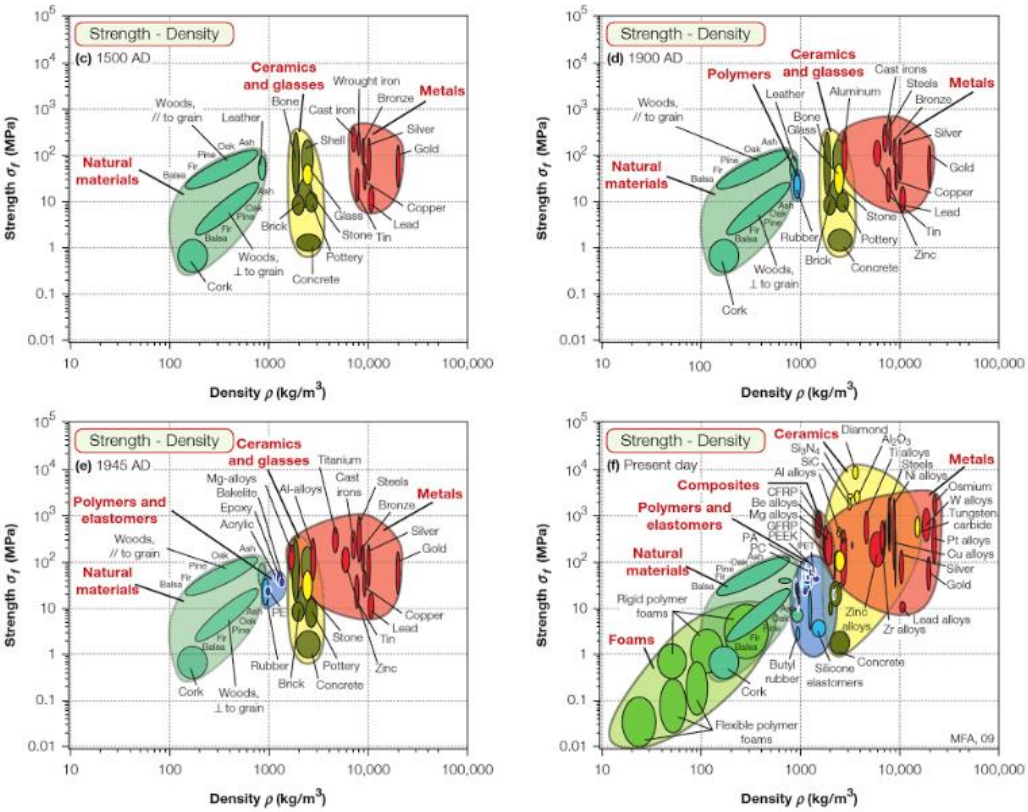

Figure 1 – Ashby material selection charts in time, adapted from M.F. Ashby 'Materials Selection in Mechanical Design'.[1]

Although many natural and some early experimental materials were polymeric, the advent of deliberite polymer synthesis towards materials with favorable properties was marked by Staudingers proposal in 1920 that these were chain-like molecules.[2] Amongst the first synthetic polymers were cellulose derivatives, styrene-butadiene rubber (SBR), polystyrene

(PS), poly(vinyl chloride) (PVC) and polyamides (PA).[3] The widespread use of polymers today followed the availability of petrochemical feedstock, i.e. by-products of the various processes devised for optimized fuel production from crude oil during the First and Second World War, the most notable being the olefins, e.g. ethylene, propylene and butadiene, and the aromatics, i.e. benzene, toluene and xylene.[4] After World War II, poly(ethylene terephthalate) (PET), polyurethanes (PUR) and even simpler direct olefin derivatives such as polyethylene (PE) and polypropylene (PP) became commercialized, which together with the aforementioned PS and PVC are the dominant polymers in the market today.[5]

At the same time, the inherent finity of petrochemical feedstock is becoming more and more apparent, with estimated global reserves set to deplete within 55 years if the present production rate is maintained, let alone increased to meet the growing demand.[6] The majority of these reserves is present in a limited and decreasing number of countries, many of which have political instabilities, and on top of that the CO_2 released upon burning of fuels and derivatives from crude oil and other fossil-based feedstock is a major cause of global climate change. At the present time, the risks versus the economic advantages of maintaining fossil feedstock supply is an active topic of political debate, particularly as the increasing availability of renewable energy sources such as solar and wind energy is forming an additional driving force to reduce the demand. Although petrochemical (by-)products constitute only 11 to 15 percent of the total petroleum supply and plastics constitute only about 30 percent of that[5], the aforementioned factors are likely to affect their price and availability in the near future. Furthermore, since this small fraction of crude oil actually represents the largest portion of the value[7], finding alternative sources for the downstream products may form an additional driver to move away from the use of fossil feedstock.

As opposed to energy however, plastics require physical matter to build up their composition. Since their feedstock needs to be organic and abundant at the same scale as crude oil, biomass

is the only real alternative. This is put into perspective in Table 1 which shows the production of various feedstocks in 2015 as gathered from their respective industry associations. Another advantage of biomass is that it is globally available in a variety of forms, as opposed to crude oil and mineral ores that form in local deposits.

Table 1 – Estimates of global production of raw materials in 2015 (including all derivatives) - densities are estimated despite their known large deviations

Raw Material	**x 10^6 m^3/yr**	**Density (t/m^3)**	**Mt/yr**
Crude oil	4350*	0.8-1.0	<4350
Wood	3700[8]	0.4-1.2	<3700
Cereals	>2560	0.4-1.2	2560[9]
Cement	1460**	3.2**	4600[10]
Plastics	~300	0.8-1.3	322[5]
Steel	~200	7.7-8.1	1600[11]
Glass	78	2.5***	195[12]
Aluminum	21	2.7	58[13]

*Volume calculated from 75 million barrels per day at 159 L/barrel[6]
**Specific density of Portland Cement, bulk density of cement and concrete are lower, yielding higher volumes
***Density of Soda Lime, the most common type of glass

The wood production in Table 1 is associated with many by-product streams and actually constitutes for almost 50% of wood fuel, which could potentially be replaced by other renewable energy sources. Cereals such as maize, rice, wheat and other grains, form the most abundant group of staple food and their production is associated with an equal or higher amount of inedible residue such as straw, chaff and stovers. Such residues or by-products are jointly called ‘lignocellulosic biomass’ by the major compounds they contain, namely lignin, cellulose and hemi-cellulose. Cellulose and hemi-cellulose are part of a larger class of macromolecules that form the most abundant class of compounds in all plant-based biomass, namely the carbohydrates or polysaccharides, of which the subunits are sugars. It is therefore not surprising that, despite their competition with the food chain and difficulties in obtaining them from inedible feedstock, sugars are regarded as the principal alternative feedstock for chemicals and materials.[14,15]

2 SUGARS AS PLASTIC FEEDSTOCK

The best known use of sugars as industrial feedstock is through fermentation, which besides the traditional preparation of ethanol for human consumption is nowadays used for the production of a variety of chemicals for non-food applications. An overview of common pathways to bioplastics from fermentation products is given in Figure 2.

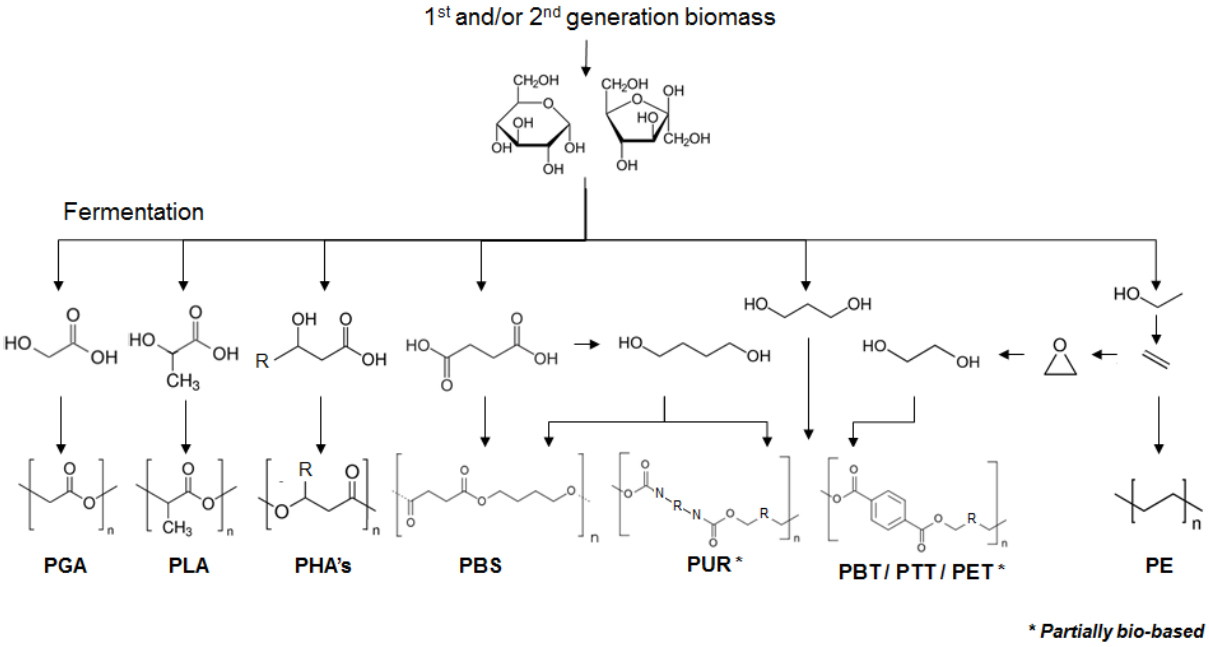

Figure 2 – Common bio-based polymers obtained from fermentation products.

Poly(glycolic acid) (PGA) and poly(lactic acid) (PLA) are notable examples of bio-based polymers that, although the suggested routes in Figure 2 can be followed, are typically produced through ring-opening polymerization of their corresponding dimers to achieve a high molecular weight. Originally combinations of these materials were used for *in vivo* applications due to their biodegradability, but for PLA this feature as well as its relatively good mechanical properties as a glassy polymer are now being utilized for agricultural and food packaging products. A disadvantage of PLA is however that aside from its biocompostability it does not bring any additional features over existing polymers, while it is more costly and manufacturing processes have to be adapted to a new material.

The examples of bio-based PE and partially bio-based PET in Figure 2 do not have this drawback; as indicated in the first paragraph there has been sufficient time for the industry to develop optimized manufacturing and nowadays even recycling technologies.[5] In their case however a disadvantage is that the respective monomers ethylene and particularly ethylene glycol are not directly available from fermentation, but multiple conversion steps are needed to obtain these monomers from ethanol. Furthermore, PET is in this case only partially bio-based. Fully bio-based PET, as well as many varieties of PUR and for example PS, would require a bio-based route to aromatics, i.e. benzene, toluene and xylene. These compounds require even more intermediate steps from known fermentation products and as such form an active topic of research and pre-commercial development, which also include non-fermentative routes from sugars as well as from lignin and unrefined biomass.[16]

2.1 FDCA AS AN INTERMEDIATE

Research into the direct chemical conversion of sugars has led for example to new routes to ethylene glycol, but also to new molecules. Notable therein are the furans, a class of aromatics that form quite readily from dehydration of sugars in their furanose form (containing a 5-membered ring). Furans can be used as intermediates for the production of commonly used aromatics through Diels-Alder reactions, but can also be used to form building blocks more directly. One of those building blocks is 2,5-furandicarboxylic acid (FDCA), which is gaining increased attention for its potential use in analogous ways to terephthalic acid (PTA). Routes to both monomers from direct conversion of sugars are presented in Figure 3, which examplifies how direct formation of FDCA avoids conversion steps when going through intermediates as 5-halomethylfurfural (XMF), 5-hydroxymethylfurfural (HMF) or 5-alkoxymethylfurfural (RMF). It also shows the need of ethylene (C_2H_4) for the Diels Alder reaction from 2,5-dimethylfuran (DMF) or 5-(hyrdoxymethyl)furoic acid (HMFA) to paraxylene (PX) or 4-(hydroxymethyl)benzoic acid (HMBA), highlighting the inherently

unfavorable mass balance towards a C_8 aromatic diacid compared to a C_6 aromatic diacid when starting from sugars. Figure 3 also shows more recently explored routes from C_5-sugar based Furoic acid, via reaction with either carbon dioxide to form FDCA directly or with carbon monoxide to 2,5-furandicarboxylic acid alkyl ester (FDCA-DRE).[17,18] The latter can also be used as a monomer and is more typically prepared by esterification of FDCA.

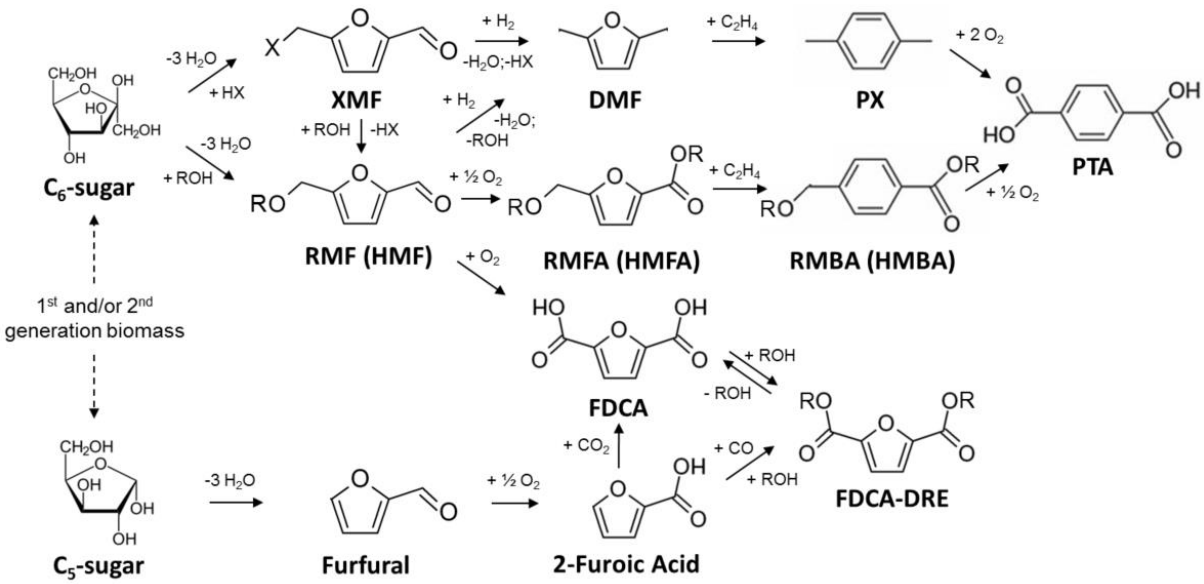

Figure 3 – Pathways from C_6 and C_5 sugars (fructose and xylose) to FDCA and PTA, in which R is an alkyl group, or hydrogen in the case of HMF, HMFA and HMBA**.**

Following work on these routes, an increasing number of applications for FDCA have been investigated in recent years, of which polyesters were amongst the first and still a very notable part.[19,20] Indeed, a review by Papageorgiou et al. considers reports of FDCA-based homo- and copolymers with over twenty diols, although the most frequently reported are poly(ethylene 2,5-furandicarboxylate) (PEF), poly(trimethylene 2,5-furandicarboxylate) (PTF, also called poly(propylene 2,5-furandicarboxylate) or PPF) and poly(butylene 2,5-furandicarboxylate) (PBF), whose PTA-based counterparts are industrially common. The reported work is however often features a single synthesis result and subsequent thermal characterization, with varying outcomes particularly in molecular weight and glass transition as shown in Table 2.

Table 2 – Thermal properties of FDCA-based polyesters cited by Papageorgiou et al.[20]

Polymer	**References**	**M_n (g/mol)**	**T_g (°C)**	**T_m (°C)**
PEF	6	8.000 - 105.300	81.5±6.9	213.0±2.0
PTF	5	10.100 - 60.200	50.4±6.6	173.4±2.4
PBF	6	5.800 - 24.400	36.3±5.2	171.6±2.9
PHF	3	13.400 - 32.100	18.6±13.5	146.6±1.9
POF	2	20.700 - 34.500	8.4±19.0	144.3±6.1

Mechanical properties are reported less frequently in the review of Papageorgiou et al., with two, one and four references respectively for PEF, PTF and PBF. Work on PEF showed relatively good agreement with break elongations of 2.81 ± 0.69 and 4.2 % and moduli of 2450 ± 220 and 2070 MPa, although the break stresses of 35 ± 8 and 66.7 MPa are notably different. For PBF, more disagreement was shown, e.g. a break elongation of 2.8, 55 ± 10, 256 ± 19 and 1108 ± 108 % and a modulus of 875 ± 18, 964 ± 37, 1110 and 1860 ± 160 MPa. Asides from methodological differences, one of the main explanations for the differences is the molecular weight obtained in each study. This is illustrated well by the work of Zhu et al., who synthesized PBF of various molecular weights and reported the glass transition, E-modulus and break elongation dependence thereon, as shown in Figure 4. This shows that the melting temperature does not vary significantly with molecular weight, while E-modulus and glass transition increase towards a plateau. The same is observed with break elongation, but at a higher molecular weight. The significance of the variation indicates the importance of molecular weight and possible other synthesis aspects on reported properties on FDCA-based polyesters or other newly introduced polymers, although these relations are often ignored in the literature. This work therefore aims to take a deeper look into the physical and mechanical properties of a new polymer in appreciation of their dependence on molecular weight and other aspects of its synthesis route. PEF was selected as its similar chemistry and thermal transitions render it a potential alternative to its ubiquitous PTA-based counterpart PET.

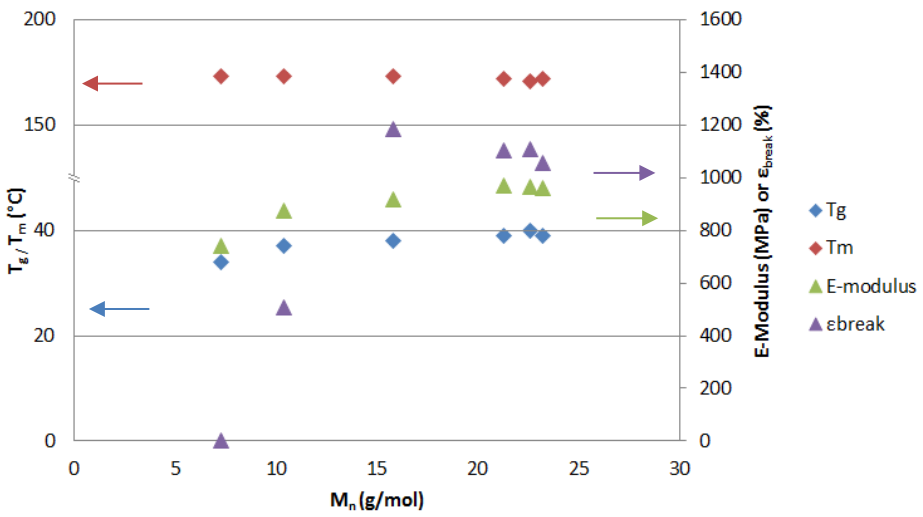

Figure 4 – PBF thermal and mechanical properties *versus* molecular weight.[21]

3 THIS WORK

Avantium Chemicals B.V. has played a catalyzing role in the industrialization of FDCA and FDCA-based polyesters, by developing an industrially viable production route through RMF as an alternative to HMF[22], and for the first time synthesizing FDCA-based polyesters on kilogram-scale.[23] These activities are now continued as Synvina C.V., a joint venture between Avantium and BASF. In 2011 I joined Avantium as a project leader in the FDCA application development team led by René Dam and overseen by Gert-Jan Gruter and Jeff Kolstad, where I have conducted many projects on the physical behavior of PEF and came to lead the 'physics' group. At this time I was also involved in the European project "Biopolymers and Biofuels from FURan" also called BIOFUR, initiated by Ed de Jong as part of the "Marie Curie Industry Academia Partnerships and Pathways" (IAPP) framework (FP7-PEOPLE-2012-IAPP). Within this project I worked with the group of Professor Nicolas Sbirrazzuoli at the Laboratory of Condensed Matter Physics (LPMC), now Institut de Chimie de Nice (ICN) on deeper thermophysical characterization of PEF. They have furthermore invited me and helped me in placing my work at Avantium in a scientific context. The collection of the work under BIOFUR and at Avantium is what constitutes this thesis.

Overall, the objective of this thesis is twofold;

1. To characterize and mathematically describe the thermal and mechanical properties of PEF, a novel bio-based polymer, as function of molecular weight where applicable.
2. To expand the understanding of polymer structure-property relations by comparing PEF and PET as a case example.

To this end, the thesis is structured as follows;

Chapter 2 will give background on physical properties and structure-property relations of polymers, as well as an excerpt of the existing knowledge on PET and of prior work on PEF.

Chapter 3, 4 and 5 describe the crystallization behavior of PEF. Chapter 3 shows the isothermal crystallization across molecular weights and synthesis routes and gives a first mathematical description of PEF crystallization following conventional theories. Chapter 4 focuses on mathematical modeling of non-isothermal crystallization behavior, showing discrepancies from conventional theories and alternative descriptions using the model-free isoconversional approach. Chapter 5 finally explores the melting behavior and how nucleation behavior of PEF influences crystallization by using Fast-Scanning Calorimetry.

Chapter 6, 7 and 8 venture into the physical and mechanical behavior of PEF compared to PET. Chapter 6 describes the dynamics of PEF and PET glass transition and the influence of crystallinity thereon. Chapter 7 describes the basic mechanics of PEF compared to PET in the amorphous glassy and molten state versus molecular weight and synthesis route, exploring some of the fundamental principles behind their differences in behavior. Chapter 8 then focuses on biaxial orientation in the rubbery state and properties of oriented PEF and PET, combining several of the aspects studied in earlier chapters.

Chapter 9 will conclude this work and provide an outlook for continued efforts in the field.

4 REFERENCES

[1] M.F. Ahsby, “Materials Selection in Mechanical Design”, 4th Edition, Elsevier, 2011
[2] N.G. McCrum, C.P. Buckley, C.B. Bucknall, “Principles of Polymer Engineering”, 2nd edition, Oxford University Press, 2011
[3] J.L. White, “Polymer Engineering Rheology”, John Wiley & Sons, 1990
[4] J.H. Gary, G.E. Handwerk, M.J. Kaiser, "Petroleum Refining, Technology and Economics", 5th Edition, CRC Press, 2007
[5] PlasticsEurope, Plastics – The Facts 2017, 2017
[6] Organization of the Petroleum Exporting Countries, “OPEC Annual Statistical Bulletin”, 2016
[7] National Research Council, “Opportunities and Obstacles in Large-Scale Biomass Utilization: The Role of the Chemical Sciences and Engineering Communities: A Workshop Summary.” The National Academies Press, Washington D.C., 2012
[8] Food and Agriculture Organization of the United Nations, “FAO yearbook of Forest products 2010-2014”, 2016
[9] Food and Agriculture Organization of the United Nations, “Food Outlook, Biannial Report on Global Food Markets”, October 2015
[10] The European Cement Association, Activity report 2015, 2016
[11] World Steel Association, Monthly Crude Steel Production 2015, 2016
[12] Glassglobal.com – Plants overview, visited September 2016
[13] World Aluminium Association, Results of the 2015 Anode Effect Survey, 2016
[14] M.E. Himmel, S.Y. Ding, D.K. Johnson, W.S. Adney, M.R. Nimlos, J.W. Brady, T.D. Foust, “Biomass Recalcitrance, Engineering Plants and Enzymes for Biofuels Production”, Science, 315 (2007)
[15] S.R.A. Collins, N. Wellner, I.M. Bordonado, A.L. Harper, C.N. Miller, I. Bancroft, K.W. Waldron, Biotech. For Biofuels, 7 (2014), 121
[16] P. Imhof, J.C. van der Waal, Catalytic Process Development for Renewable Materials, Wiley-CH, 2013
[17] G.R. Dick, A.D. Frankhouser, A. Banerjee, M.W. Kanan, Green Chem. 19 (2017), 2966.
[18] S. Zhang, J. Lan, Z. Chen, G. Yin, G. Li, ACS Sustainable Chem. Eng. 5 (2017), 9360.
[19] A.F. Sousa, C. Vilela, A.C. Fonseca, M. Matos, C.S.R. Freire, G.M. Gruter, J.F.J. Coelho, A.J.D. Silvestre, Polym. Chem. 6 (2015) 5961-5983
[20] G.Z. Papageorgiou, D.G. Papageorgiou, Z. Terzopoulou, D.N. Bikiaris, Eur. Pol. J. 83 (2016) 202.
[21] J. Zhu, J. Cai, W. Xie, P. Chen, M. Gazzano, M. Scandola, R. Gross, Macromolecules 46 (2013), 796.
[22] G.J.M. Gruter, WO2007104514
[23] L.Sipos, G.J.M. Gruter, J.J. Kolstad, M.A. Dam, WO2013062408

CHAPTER 2
BACKGROUND

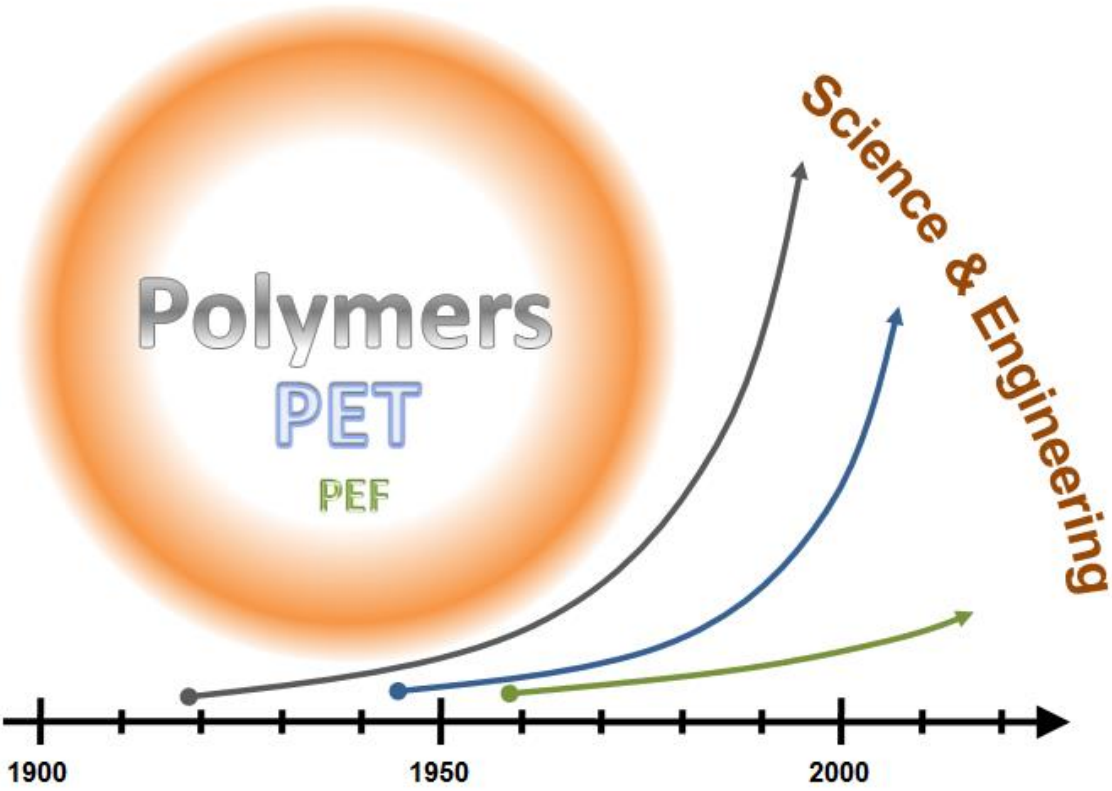

In this chapter, the theoretical framework and scientific context for the work in this thesis are posed by providing a summary of some of the current theories on the physical properties of polymers, relevant developments and studies of PET and relevant work on PEF done so far.

1 PHYSICAL PROPERTIES OF POLYMERS

Polymers, due to their chain-like structure, exhibit different states than the classical solid, liquid and gas; roughly speaking a glassy, rubbery and a molten state. These states are furthermore viscoelastic, exhibiting both solid and liquid characteristics and showing an equivalent mechanical response to temperature and the rate at which tensile strain (ε) or shear strain (γ) is applied. The elastic and viscous component of the tensile (E) or shear (G) modulus in each state can be obtained by oscillatory or 'dynamic' analysis of the force response, respectively known as storage and loss modulus, as shown in Figure 1. Figure 1 also highlights the transitions of the glassy state, namely the γ-relaxation associated with vibrational and stretching motion, the β-relaxation associated with rotational side-group motions and the α-relaxation (T_α) or glass transition temperature (T_g) where cooperative chain motion sets in.[1] The melting temperature (T_m) is not directly associated with chain

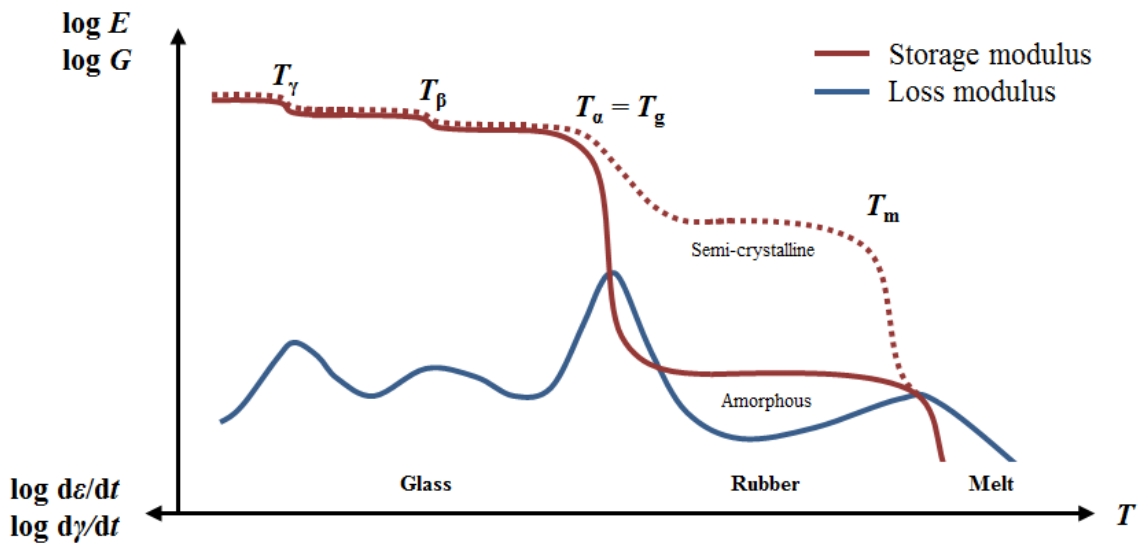

Figure 1 – Polymer states and transitions observed by dynamic mechanical analysis.

motion but rather with the semi-crystalline state, which can occur in polymers with a sufficiently regular chain-structure to form crystals. If the chain structure is irregular, for example in an atactic homopolymer or random copolymer, it will stay amorphous. A crystallizable polymer exhibits a melting temperature which, as with regular solids, occurs when the enthalpy gain is equal to the entropy loss from the liquid state. Following the theory of Hoffman and Lauritzen, only fully extended polymer chain crystals of high molecular weight exhibit the true theoretical melting temperature T_m^0, but in practice shorter crystals are formed by chain folding which exhibit a lower actual T_m. The rate of crystallization is determined by the rate of nucleation, which as with regular solids increases with the degree of undercooling, but also with the rate of chain folding which increases with increasing temperature. As such, the rate exhibits a maximum as shown in Figure 2.[2] Given that chain mobility is necessary for chain folding, a higher molecular weight (M) will reduce the rate of crystallization and vice versa, and crystallization virtually ceases in the glassy state. Primary crystallization typically occurs through formation of spherulites, which greatly increases the rubbery state elasticity and can furthermore broaden the T_g by confining a fraction of the amorphous chains as indicated in Figure 1.

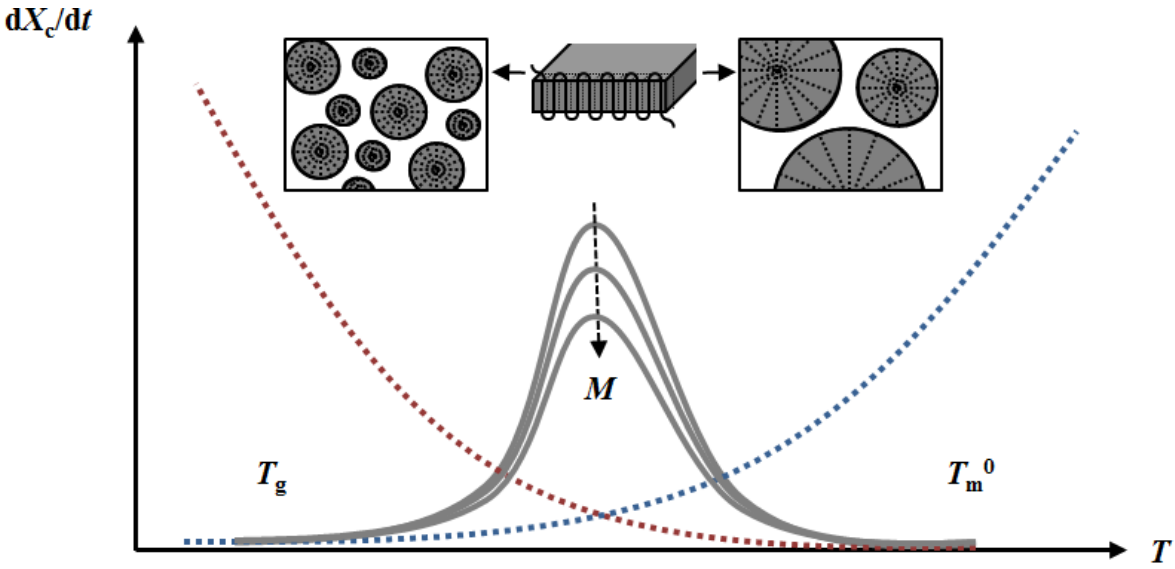

Figure 2 – Schematic representation of the kinetics of polymer crystallization, highlighting the contributions of the nucleation rate (red) and chain folding or growth (blue).

The melt point, lower temperature transitions and moduli are relatively fixed values for a given polymer, given that a certain chain length is reached. Fox and Flory first posed an explanation for the molecular weight dependence of the glass transition by the reduction of free volume, i.e. chain ends have a larger free volume while the free volume of mid-chain segments is limited, meaning more chains have to cooperate to undergo the glass transition.[3] Furthermore, De Gennes proposed that this confinement limits chain motion to a linear motion, *i.e.* reptation, causing the viscosity to increase much more significantly once a certain critical molecular weight M_c is reached.[4] The value of M_c is typically reached when the polymer chains form on average two to three entanglements, or two to three times the molecular weight between entanglements (M_e); a parameter that depends on the chemical structure of the polymer. The additional chain confinement furthermore prevents chain disentanglement, which at larger deformations leads to higher overall stress (σ) known as strain hardening. This in turn allows strain (ε) to delocalize and continue deformation until a larger strain at break (ε_b), resulting in a higher toughness.[5] The molecular weight dependence of the viscosity, intrinsic properties and toughness is depicted in Figure 3.

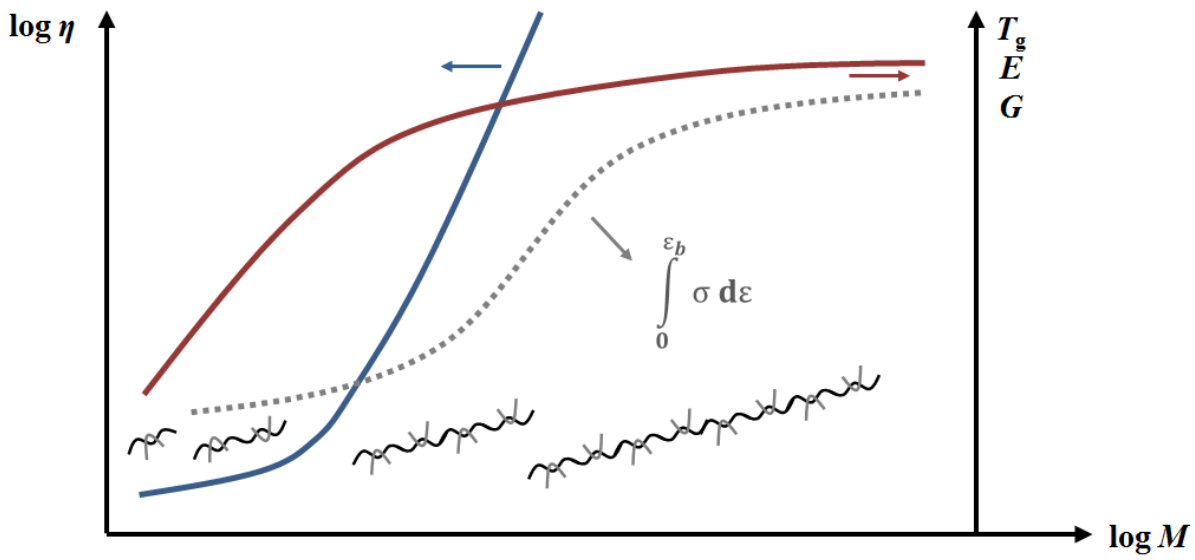

Figure 3 – Viscosity, intrinsic properties and toughness dependent on molecular weight, with schematic representation of the increase in entanglements.

The possibility of polymers to undergo large deformations without disentanglement yields molecular orientation, as is depicted schematically in Figure 4. When drawing in the glassy or rubbery state, polymers of sufficient molecular weight exert an increase in the resistance to drawing once polymer chains between entanglements reach maximum molecular orientation, which is called the natural draw ratio (NDR). At insufficient molecular weight or at too high temperatures, a NDR is absent due to disentanglement of the polymer chains. Drawing in the rubbery state can furthermore result in strain-induced crystallinity (SIC) in crystallizable polymers through promotion of nuclei formation by molecular orientation.

Both molecular orientation and SIC significantly improve the properties of a material in the drawing direction. Furthermore, strain-induced crystals exhibit the aforementioned effect of broadening the T_g and increasing rubbery state elasticity while remaining transparent, as opposed to spherulites which typically scatter light. This behavior is utilized in industrial manufacturing both uniaxially in the case of fiber spinning and biaxially in the case of film orientation or bottle blowing. In the latter cases, orientation and SIC also improve the barrier to gas permeation, by respectively reducing chain mobility and forming a tortuous path.

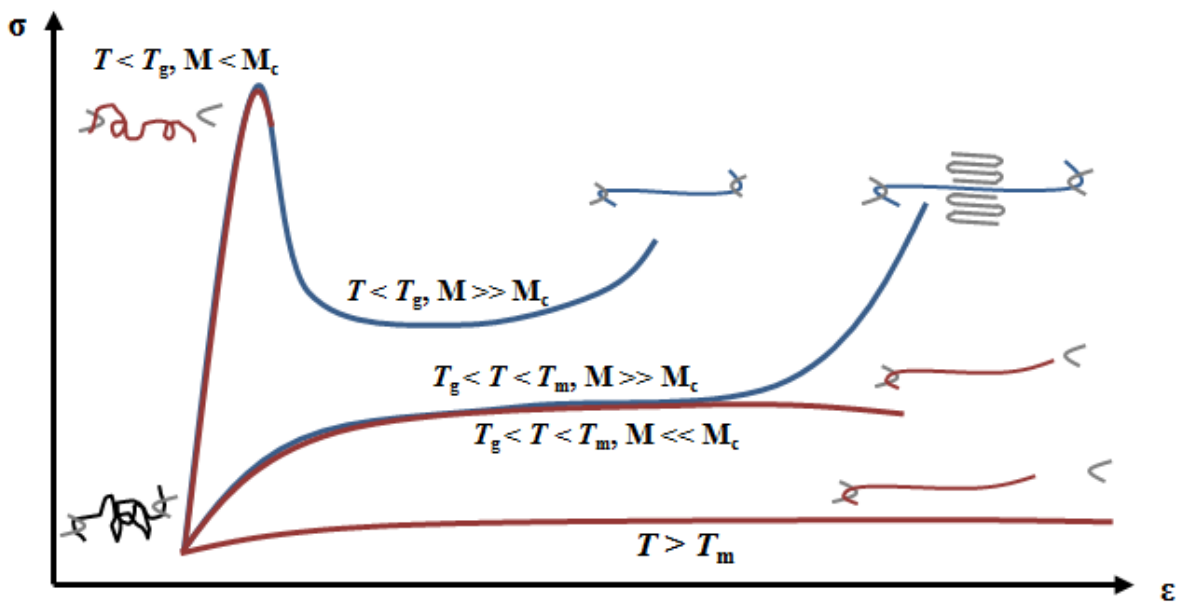

Figure 4 – Molecular orientation by large deformation at various temperatures.

Typically polymeric materials do not comprise chains of equal length but variety of lengths. These can be characterized by separation on basis of hydrodynamic volume in solution using size exclution chromatography (SEC) followed by refractive index detection to determine the concentration of each fraction. The molecular weight of each fraction can then be intrapolated from a calibration curve of elution time *vs* peak molecular weight M_p of known standards, or determined *in situ* by a combination of light scaterring and differential solution viscometry. Typical examples of the resulting distributions are shown in Figure 5, highlighting the number and weight average molecular weights M_n and M_w calculated over all fractions as well as the Intrinsic Viscosity $[\eta]$ obtained from differential solution viscometry. Radical and ring-opening polymerizations typically yield a narrow distribution, since each chain is effectively started by a single initiator, whereas step-growth polycondensates have a broader distribution due to continuous chain interchange during reaction. A broad distribution promotes molecular orientation during deformation; shorter chains induce partial disentanglement and plasticize the longer chains that maintain the entanglement network. This can however also more readily yield brittle behavior in the case of low average molecular weights.

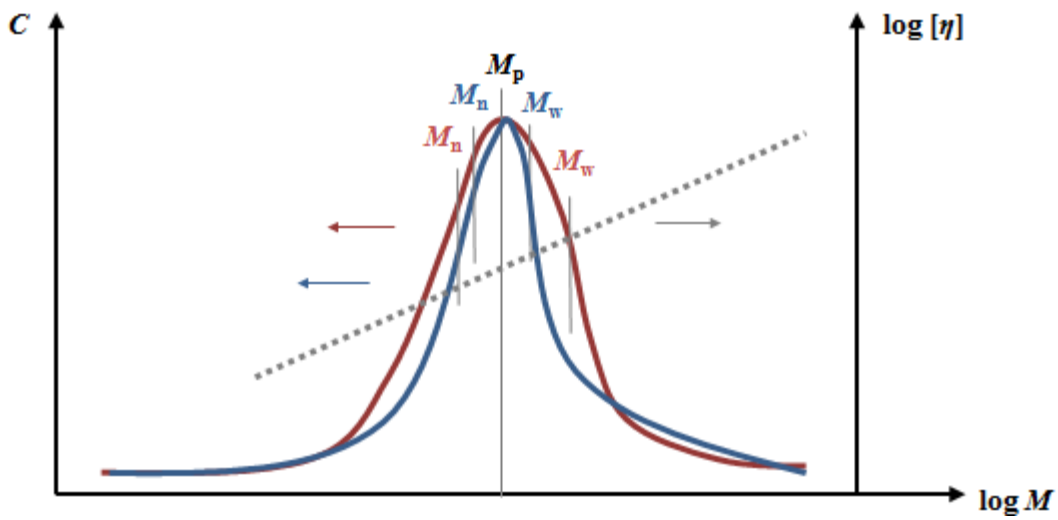

Figure 5 – Examples of a broad and narrow molecular weight distributon with equal M_p overlaid by a typical intrinsic viscosity response at those molecular weights.

2 SYNTHESIS AND PROPERTIES OF PET

Polyesters were amongst the first polymers to be deliberately synthesized, as part of the pioneering work of W.H. Carothers in 1930. Although fibers could be drawn from aliphatic polyester melts, their initially low temperature and hydrolytic stability resulted in moving his work to polyamides. However, in 1940 J.R. Whinfield conceived the use of terephthalic acid to overcome these initial 'weaknesses' of polyesters, which he confirmed within a year in his work at the Calico Printers Association.[6] After the grant of Whinfield's patent in 1946, ICI and DuPont started the commercialization of PET under license, for use in fibers and films.

Commercial PET polymerization was initially done using dimethyl terephthalate (DMT), since DMT allowed achieving the required monomer purity for low color high molecular weight PET via distillation. When polymerizing DMT, the monomer is first dissolved in an excess of ethylene glycol and trans-esterified to a mixture of bishydroxyethylene terephthalate (BHET) and short chain oligomers under distillation of methanol, typically aided by a trans-esterification catalyst such as an alkali metal, Zinc or Manganese. The oligomer mixture is then polymerized at high temperature in vaccum to further remove ethylene glycol in the presence of a polycondensation catalyst such as Antimony or Titanium. Figure 6 shows the main structures involved in this process, oligomers typically being combinations thereof.[7]

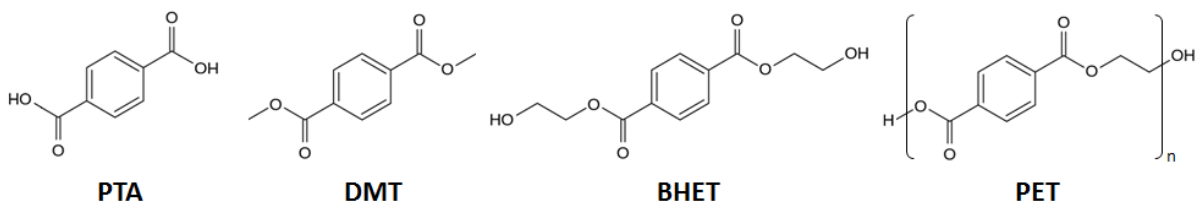

Figure 6 – Main structures involved in the PET polymerization process.

In the late 1960s, an effective direct production process for high purity PTA was commercialized, which later became the dominant route. As opposed to DMT, PTA is insoluble in ethylene glycol and is esterified as a slurry under distillation of water. After

sufficient esterification the reactants are however homogenized to a similar reaction mixture as the BHET and oligomer mixture after trans-esterification and the polycondensation can proceed similarly. In this case however, the mixture may contain carboxylic end-groups which allow a water-forming esterification reaction during polycondensation.

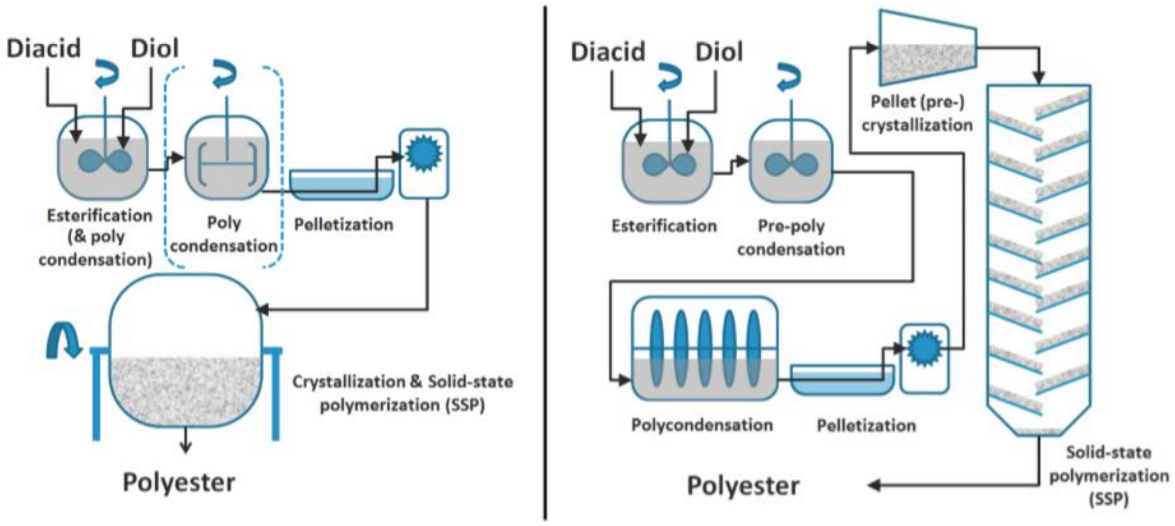

Figure 7 – Schematic of batch polymerization with optional separate polycondensation (left) and continuous polymerization with two-step polycondenstation (right).

PET can be polymerized in batch and continuous processes, as shown in Figure 7. The (trans-) esterification and polycondensation reactions are often separate steps, since the former requires stirring of a boiling liquid or slurry, whereas the latter requires stirring of a substance with increasing viscosity. The polycondensation step also requires high vacuum to remove sufficient ethylene glycol to obtain a reasonable degree of polymerization. Since the viscosity increases so drastically with molecular weight, melt polycondensation is sometimes conducted in two or three separate steps that are optimized to handle the viscosity at that stage. Furthermore, additional increases in molecular weight may be obtained by solid state polymerization (SSP) on crystallized pellets close to the melt point, using either vacuum or nitrogen to remove ethylene glycol over prolongued reaction times.

Many aspects of polymer behavior in the previous paragraph were generalized during the commercialization of PET. Thompson and Woods as well as Kawaguchi were among the first authors to highlight the significants effect of crystallinity as well as orientation on the glass transition and moduli of PET in 1956 and 1958.[8,9] Farrow et al. and Illers and Breurer in 1960 and 1963 related the β-transition of PET and other terephthalic polyesters to local motions of the glycol and carboxylic acid units, while attributing the glass transition to the activation of motion of the terephthalic moiety.[10,11] Although fiber orientation and properties were already reported earlier, properties of oriented films were reported in 1965 and isotropic crystallization into spherulites in 1967.[12,13] Stearne and Ward reported the molecular weight dependence of the brittle-ductile transition of PET in 1969 followed by a paper by Duckett et al. a year later on the strain rate dependence of the yield stress using theories developed at the time.[14,15] Following that, the rheology as function of molecular weight was reported by D.R. Gregory in 1972.[16]

Later reports highlight the influence of synthesis aspects other than molecular weight on PET properties. Certain catalysts were found to act as homogeneous or heterogeneous nucleating agents. [17,18] The catalysts and polymerization route also strongly influences the formation of diethylene glycol (DEG) during polymerization, which also affects the crystallization as well as the melting behavior.[19,20,21] Moisture also has effects on crystallization as well as drawing by acting as a plasticizer.[22,23]

3 SYNTHESIS AND PROPERTIES OF PEF

PEF synthesis was first reported in a patent application by J.G. Drewitt and J. Lincoln of Celanese submitted in 1946, only five years after the submission of the initial work on PET.[24] Although less industrially widespread, early academic work by L.G. Kazaryan and F.M. Medvedeva described a crystal structure for PEF in 1968 and other early synthesis work has been reported by Gandini in 1977 and Moore and Kelly in 1978.[25,26,27] Recent attention has

increased, particularly due to the additional pathways that have been found for FDCA as an alternative to petrochemical feedstock as mentioned in the introduction and by the finding by Sipos et al. that PEF exhibits significantly superior barrier properties to PET.[28,29,30] This higher gas barrier has been corroborated and studied more in-depth by Burgess et al., with published works on the permeability of oxygen, water and carbon dioxide.[31,32,33] Papageorgiou et al., Codou et al. and Stoclet et al. together with Burgess et al. were among the first to study the physical behavior of PEF, initially focusing on the crystallization kinetics and melting behavior.[34,35,36,37] Martino et al, Papageorgiou et al. and Codou et al. have furthermore looked into the preparation of PEF nanocomposites, which show limited effect on the glass transition temperature but increased thermal stability.[38,39,40] More recently, Kriegel and Bucknall have reported an alternative crystal structure for PEF to that of Kazaryan et al., although both propose two repeating units in the longitudinal direction and a nearly identical density.[41] Similar to Chapter 7 of this work, Stoclet et al. and Mao et al. have looked into strain hardening and strain-induced crystallization of PEF, where the former indicated a narrow drawing window where strain hardening could be obtained while the latter obtained strain hardening at higher temperatures.[42,43] The discrepancy can be attributed to a higher molecular weight used by the latter authors, although both report an ordered molecular structure that they attribute as the cause of strain hardening, and find strain induced crystallization once the onset of strain hardening is surpassed.

An overview of the basic properties of PEF and PET from various studies is presented in Table 1. Most of the values are from different studies, although Burgess et al. measured some of them in direct comparison in a study into the molecular origin of the differences between PEF and PET.[44] They propose that the chain mobility of PEF is reduced by the furan ring's dipole moment and the bond length and angle between the carboxylic end groups of the FDCA moiety, at 4.83 Å and 129.4° respectively compared to the 5.73 Å and 180°

respecitvely of PTA, and quantify this by the reduced magnetization decay of carbonyl carbon atoms in solid state ^{13}C NMR in comparison to poly(ethylene isophthalate) (PEI) and poly(ethylene naphthalate). The molecular motion of aromatic ring flipping was pinpointed as one of the causes, and was indeed not detected for PEF in centerband-only detection of exchange (CODEX) measurements under conditions where it was detected for PET.

Table 1 – Overview of Properties of PEF and PET.

Property	**Unit**	**PEF**	**PET**
ρ_a	kg/m^3	1430[44]	1335[44]
ρ_c	kg/m^3	1562[41], 1565[25]	1455[45]
ΔH_m^0	J/g	137[34], 140[35]	136[46], 140[47]
T_m^0	°C	225[36], 240[48],247[35], 265[34]	290[49]
T_g	°C	85[44],87[37]	70[11], 76[44],80[37]
T_β	°C	-50[44]	-65[11], -61[44]
σ_y	MPa	35 ± 8[48], 66.7, 100[50]	55[14]
M_e	g/mol	3500[36], 3550[29]	1170[51], 1450[52]

4 DISCUSSION

Considering the original invention of PET as a high-melting polymer for use in synthetic fibers, PEF at a first glance does not seem to bring very favorable characteristics. For the packaging applications where PET is used today, however, PEF's higher glass transition and barrier properties seem advantageous, and the main limitations appear to be the industrial scale availability of FDCA and knowledge of differences in polymerization and properties.

One of the most reported properties of PEF to date is its crystallization behavior, which is relevant for the optical clarity and thermal stability of end-products as well as the Solid State

Polymerization process used in PET to achieve sufficiently high molecular weights. Although there is disagreement in the theoretical melting temperature of fully extended crystals T_m^0 for PEF, a generally lower value than PET at comparable equilibrium melting enthalpy ΔH_m^0 is in line with the finding of a more ordered crystal structure, since this indicates a higher entropy gain associated with melting ΔS_m^0 and $\Delta G_m^0 = \Delta H_m^0 - T_m^0 \cdot \Delta S_m^0 = 0$. PEF is generally reported as slow crystallizing, which is likely caused by both the low melting temperature and the reduced chain mobility that Burgess et al. proposed. The contributions of both of these effects as well as influence of molecular weight and catalyst that are known to affect PET are however not reported, and as such are studied in this work following Hoffman-Lauritzen theory and model-free isoconversional analysis.

The reduced chain mobility also poses an explanation for PEF's higher glass (α) and β transitions by respectively restricting the activation of cooperative chain motion and local motions. The absence of the local motion of aromatic ring flipping proposed by Burgess et al. is plausible, but other local motions were not discussed in their work. One example is carboxyl group rotation, which is known to be activated in the β transition of PET.[11] Further considering the crystalline structures of PTA and FDCA, not only the length of FDCA is reduced but also the maximum width of the FDCA unit in the in-plane conformation is increased, as is highlighted in Figure 7.[53,54] If crystalline monomer dimensions were maintained in the polymer, the width of the benzene ring of PET would exceed the maximum width between oxygen atoms of 2.27 Å in the trans conformation. The width of the furan ring at 2.14 Å would however be drastically lower than that of the displayed cis confirmation or the nearly identical width of the in-plane trans conformation. It would however even be lower than the out-of-plane trans conformation, which would have a width of 2.44 Å if crystalline monomer dimensions were maintained.

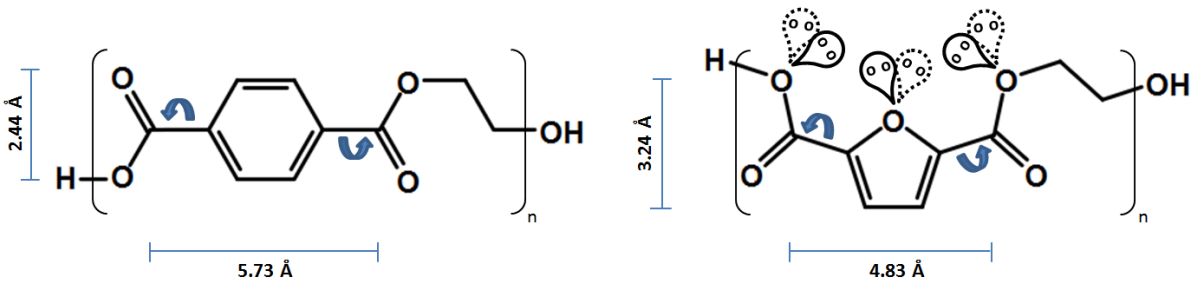

Figure 8 – Schematic representation the repeating units of PET and PEF with dimensions of crystalline PTA and FDCA in the in-plane confirmation, as well as a schematic depiction of carboxyl group rotation and the lone pairs of some of the PEF oxygen atoms.

The increased space requirement for carboxyl group rotation can be expected to impose an energy barrier for this local motion. Furthermore, the motion may be additionally restricted by a repulsive effect of the lone pairs of the oxygen atoms in the FDCA moiety, as also indicated in Figure 7. The out of plane bending of the carboxylic oxygen atoms in crystalline FDCA with an angle of 175.6° respective to each other can be seen as evidence of the existence of such an effect. This would provide an additional explanation to the 14.6 ms magnetization decay time for PEF over the 10.6 ms for PEI and the 2.8x higher oxygen barrier of PEF over PEI, which otherwise has comparable bond angles to PEF.[33,44]

Besides the reduced chain mobility the free volume also affects the bulk properties, and Burgess et al. estimate this to be somewhat higher for PEF based on group contribution theory. Since the density of PEF is higher than PET, a higher free volume seems somewhat counterintuitive. However, considering Figure 8 it could be imagined that spatial requirements in the transvere directions exceed the reduction in chain length in the longitudinal direction. One way to look at this is through the unperturbed end-to-end distance of a freely rotating chain analogously to the work of Kamide et al., who compared PET to poly(ethylene 1,2-Diphenoxyethane *p,p'*-Carboxylate) (PEPC), a polyester from ethylene glycol with a flexibilized aromatic diacid.[55] Following this approach, a freeling rotating chain can be assumed with a bond length $\langle l^2 \rangle$ according to Equation (1) using $l_{\text{C-O,carboxyl}}$ = 1.34 Å, $l_{\text{O-C,glycol}}$

= 1.44 Å and $l_{C\text{-}C,glycol}$ = 1.55 Å for both polymers and $l_{C1\text{-}C6,FDCA}$ = 4.83 Å and $l_{C1\text{-}C8,PTA}$ = 5.73, and a bond angle of θ = 109.5. Then, using Equation (2) one can calculate the unperturbed end-to-end distance of $(\langle r_{0f,PEF}^2\rangle/M)^{1/2}$ = 0.607 Å·mol$^{1/2}$·g$^{-1/2}$ and $(\langle r_{0f,PET}^2\rangle/M)^{1/2}$ = 0.669 Å·mol$^{1/2}$·g$^{-1/2}$. Since the theoretical end-to-end distance is 9.3% lower for PEF than PET while the density is only 6.7% higher, this implies a higher free volume for PEF.

$$\langle l^2\rangle = \sum_i l_i^2 \tag{1}$$

$$\left(\langle r_{0f}^2\rangle/M\right)^{1/2} = \left(\langle l^2\rangle/M\,\frac{1-cos\langle\theta\rangle}{1+cos\langle\theta\rangle}\right)^{1/2} \tag{2}$$

This outcome furthermore suggests a higher entanglement density, since $M_e \propto \rho^{-2}\left(\langle r_{0f}^2\rangle/M\right)^{-3}$.[51] Another perspective is that the linear chain density difference $M/\langle l^2\rangle^{1/2}$ between PEF and PET is the exact same as the ratio between the amorphous densities of both materials, implying that the free volume is identical and PEF simply has ‘heavier chains’. Although perliminary findings confirm a somewhat higher free volume and M_e for PEF, a more detailed study into this concept as well as the consequences for the properties has not yet been coducted and will be part of this work.

In most applications, the oriented properties of PEF are more relevant than the un-oriented properties. Considering above discussion one could imagine that the drawing behavior will also be affected by the entanglement density and rotational freedom of PEF. The recent studies into orientation and oriented properties however do not focus on mechanical and thermal aspects during drawing and the resulting properties on drawn PEF compared to PET, which will be highlighted in this work. Biaxial orientation is used in this case, due to its higher relevance for packaging applications than uniaxial orientation.

5 REFERENCES

[1] N.G. McCrum, B.E. Read, G. Williams, "Anelastic and Dielectric Effects in Polymeric Solids", John Wiley & Sons (1967)
[2] J. D. Hoffman, G. T. Davis, J. I. Lauritzen, "*Treatise on Solid State Chemistry"*, N. B. Hannay edition, Plenum (1976).
[3] T.G. Fox, P.J. Flory, J. Appl. Phys. 21 (1958), 581-591
[4] P.G. De Gennes, J. Chem. Phys. 55 (1971), 572-579
[5] H.G.H. Van Melick, L.E. Govaert, H.E.H. Meijer, Polymer 44 (2003), 2493-2502
[6] J.R. Whinfield, J.T. Dickson, GB578079 (1941)
[7] J. Scheirs, T. E. Long, "Modern Polyesters: Chemistry and Technology of Polyesters and Copolyesters", John Wiley & Sons (2003)
[8] A.B. Thompson, D.W. Woods, Trans. Faraday Soc. 52 (1956), 1383-1397
[9] T. Kawaguchi, J. Pol. Sci. 32 (1958), 417-424
[10] G. Farrow, J. McIntosh, I.M. Ward, Macromol. Chem. (1960), 147-158
[11] K.H. Illers, H. Breuer, J. Coll. Sci. 18 (1963), 1-31
[12] C.F. Heffelfinger, P.G. Schmidt, J. Appl. Pol. Sci. 9 (1965), 2661-2680
[13] G.S.Y. Yeh, P.H. Geil, J. Macromol. Sci. B. Phys. 1 (1967), 235-249
[14] J.M. Stearne, I.M. Ward, J. Mat. Sci. 4 (1969), 1088-1096
[15] R.A. Duckett, S. Rabinowitz, I.M. Ward, J. Mat. Sci. 5 (1970), 909-915
[16] D.R. Gregory, J. Appl. Pol. Sci. 16 (1972), 1479-1487
[17] S.A. Jabarin, J. Appl. Pol. Sci. 34 (1987), 85-96
[18] S.A. Jabarin, J. Appl. Pol. Sci. 34 (1987), 97-102
[19] J.-W. Chen, L.-W. Chen, J. Polym. Sci., Polym. Chem. Ed., 37 (1999), 1797–1803.
[20] L.-W. Chen, J.-W. Chen , J. Appl. Polym. Sci, 75 (2000), 1229–1234.
[21] M. Patkar, S.A. Jabarin, J. Appl. Polym. Sci., 47 (1993), 1748.
[22] S.A. Jabarin, J. Appl. Polym. Sci., 34 (1987), 103–108.
[23] E. Dargent, G. Denis, C. Caron, J.M. Saitier, J. Grenet, J. Appl. Polym. Sci. 77 (2000), 1056-1066
[24] J.G. Drewitt, J. Lincoln, GB621971 (1946)
[25] L. G. Kazaryan, F. M. Medvedeva, Vysokomol. Soedin., Ser. B. 10 (1968), 305
[26] A. Gandini, Adv. Polym. Sci. 10 (1977), 47-96
[27] J.A. Moore, J.E. Kelly, Macromolecules 11 (1978), 568-573
[28] L.Sipos, G.J.M. Gruter, J.J. Kolstad, M.A. Dam, WO2013062408
[29] R.M. Kriegel, R.D. Moffit, M.W. Schultheis, Y. Shi, X. You, WO2015031907.
[30] M. Bouffand, A. Colloud, P. Reutenauer, WO2014032730.
[31] S.K. Burgess, O. Karvan, J.R. Johnson, R.M. Kriegel, W. J. Koros, Polymer, 55 (2014) 4748-4756.
[32] S. K. Burgess, D.S. Mikkilineni, D.B. Yu, D.J. Kim, C.R. Mubarak, R.M. Kriegel, W.J. Koros, Polymer 55 (2014) 6870-6882.
[33] S.K. Burgess, R.M. Kriegel, W.J. Koros, Macromolecules 48 (2015) 2184-2193.
[34] G.Z. Papageorgiou, V. Tsanaktsis, D. Bikiaris, Phys. Chem. Chem. Phys. 16 (2014), 7946-7958
[35] A. Codou, N. Guigo, J. van Berkel, E. de Jong, N. Sbirrazzuoli Macromol. Chem. Phys. 215 (2014) 2065−2074
[36] G. Stoclet, G. Gobius du Sart, B. Yeniad, S. de Vos, J.M. Lefebvre, Polymer 72 (2015), 165-176
[37] V. Tasnaktsis, D.G. Papageorgiou, S. Exarhopoulos, D.N. Bikiaris, G.Z. Papageorgiou, Cryst. Growth Des. 15 (2015), 5505-5512

[38] L. Martino, V. Niknam, N. Guigo, J.G. Van Berkel, N. Sbirrazzuoli, RSC Adv. 6 (2016), 59800-59807
[39]N. Lotti, A. Munari, M. Gigli, M. Gazzano, V. Tsanaktsis, D.N. Bikiaris, G.Z. Papageorgiou, Polymer 103 (2016), 288-298
[40] A. Codou, N. Guigo, J.G. Van Berkel, E. de Jong, N. Sbirrazzuoli, Carbohydrate Polymers 174 (2017), 1026-1033
[41] Y. Mao, R. Kriegel, D. Bucknall, Polymer 102 (2016), 308-314
[42] G. Stoclet, J.M. Lefebvre, B. Yeniad, G. Gobius du Sart, S. de Vos, Polymer 134 (2018), 227-241
[43] Y. Mao, R. Kriegel, D. Bucknall, Polymer 139 (2018), 60-67
[44] S.K. Burgess, J.E. Leisen, B.E. Kraftschik, C.R. Mubarak, R.M. Kriegel, W.J. Koros, Macromolecules 47 (2014) 1383-1391.
[45] R. d. P. Daubeny, C. W. Bunn, C. J. Brown, Proc. R. Soc. London, Ser. A 226 (1954), 531.
[46] J. P. Jog, J. Macromol. Sci., Rev. Macromol. Chem. Phys. C35 (1995), 531.
[47] C. M. Roland, Polym. Eng. Sci. 31 (1991), 849.
[48] R. J. I. Knoop, W. Vogelzang, J. Haveren, D. S. Es, J. Polym. Sci., Part A: Polym. Chem. 51 (2013), 4191.
[49] G. Groeninckx, H. Reynaers, H. Berghmans, G. Smets, J. Polym. Sci. Pol. Phys. Ed. 18 (1980), 1311.
[50] R.P.L. Dolmans, "Bewertung kommerziell erhältlicher, biobasierter Polymere in der Textilen Filamentextrusion", Dissertation RWTH Aachen (2013).
[51] L.J. Fetters, D.J. Lohse, D. Richter, T.A. Witten, A. Zirkel, Macromolecules 27 (1994), 4639-4647
[52] S. Wu, J. Pol. Sci. B. Pol. Phys. 27 (1989), 723-741
[53] M. Bailey, C.J. Brown, Acta Cryst. 22 (1967), 387
[54] E. Martuscelli, C. Pedone, Acta Cryst. 24 (1968), 175
[55] K. Kamide, Y. Miyazaki, H. Kobayashi, Polym. J. 9 (1977), 317-327

CHAPTER 3
ISOTHERMAL CRYSTALLIZATION KINETICS

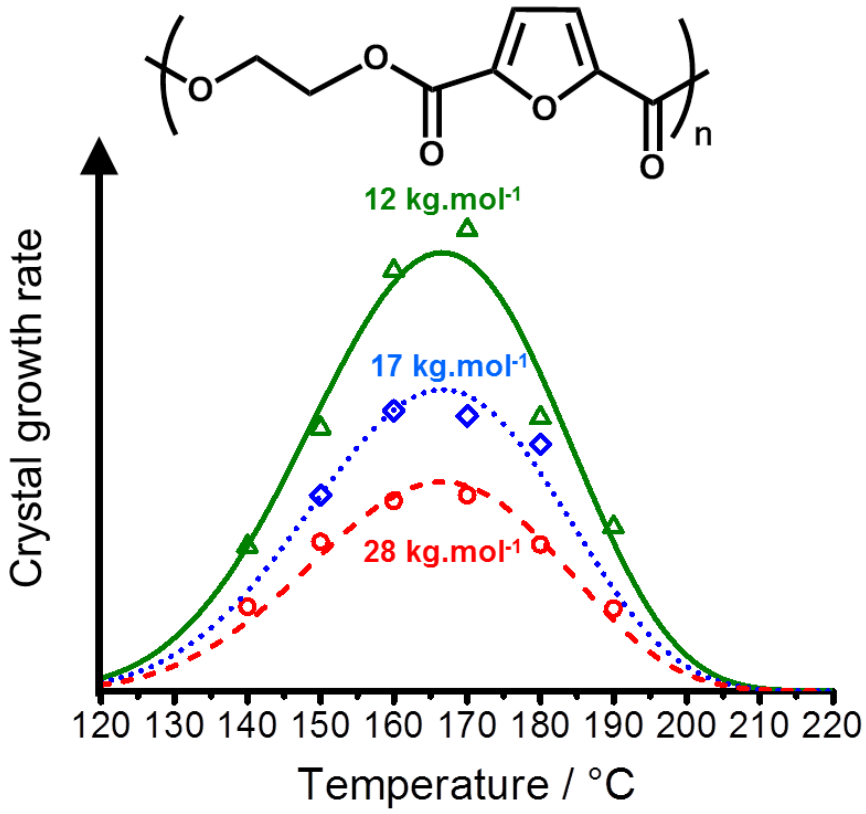

This chapter is also published as part of "Isothermal Crystallization Kinetics of Poly(ethylene 2,5-Furandicarboxylate" by J.G. Van Berkel, N. Guigo, J.J. Kolstad, L. Sipos, B. Wang, M.A. Dam, N. Sbirrazzuoli, Macromol. Mat. Eng. 300 (2015), 466.

This chapter presents the isothermal crystallization kinetics for PEF in relation to molecular weight and catalyst, the key parameters for its synthesis. The isothermal crystallization kinetics were studied using the Avrami and the Hoffman-Lauritzen theory, in which a single set of Hoffman-Lauritzen parameters could provide a linear relationship between the reference growth rate and the reciprocal molecular weight for catalyst-free PEF. Particularly a higher activation energy for the segmental jump (U^*) that is related to the diffusion process was found for PEF compared PET, which was attributed to more restricted conformational changes of PEF chains and limits the crystallization rate of PEF. The effect of the presence of various catalysts was highlighted near the optimum crystallization temperature.

1 INTRODUCTION

It can be stated that quiescent crystallization behavior is one of the key physical properties of PET, as it is relevant for the solid-state polymerization (SSP) step in its production, for the establishment of minimum processing temperatures, and, by its absence, for maintaining optical clarity in applications where this is needed.[1] For PET, the commonly cited crystal structure was determined by Daubeny et al.[2] using X-ray diffraction measurements on drawn PET fibers. This crystal structure is triclinic with dimensions a = 4.56 Å, b = 5.94 Å, c = 10.75 Å, α = 98.5°, β = 118° and γ = 112°, which comprises one repeating unit and yields a crystal density of 1.455 g/cm^3. The amorphous density of PET is reported as 1.335 g/cm^3 at ambient conditions and for the equilibrium melting enthalpy of PET, values have been reported of ΔH_m^0 = 117.5 J/g, 135.8 J/g and 140 J/g.[3,4] Groeninckx et al.[5] determined the melting point T_m^0 for fully extended PET chain crystals of 290°C by the Hoffman-Weeks method, and demonstrated by WAXS and SAXS that the melt point increase arose solely from lamellar thickening and that no alternate crystal phases were formed. The same paper shows a maximum degree of crystallinity of 60% for fully annealed PET. In a study on isothermal melt crystallization kinetics, the transition from primary to secondary crystallization kinetics

was found to occur at 35-40% crystallinity, with a maximum rate at 175°C.[6] However, many examples of PET literature reveal that crystal parameters and crystallization kinetics are influenced by catalyst residue and by the presence of co-monomers, which highlights the importance of the polymerization route on the observed behavior of the final polymer.[7,8,9]

For PEF, the crystal structure was estimated in an early study by Kazaryan and Medvedeva[10] using the same method as Daubeny and Bunn on PET.[2] This also yielded a triclinic unit cell, but with dimensions a = 5.75 Å, b = 5.35 Å, c = 20.10 Å, α = 133.3°, β = 90° and γ = 112°, comprising two repeating units and resulting in a crystal density of 1.565 g/cm^3. Recently, Papageorgiou et al.[11] published a first value on the equilibrium melting enthalpy of PEF of ΔH_m^0 = 137 J/g, while various values are reported for the theoretical melting point of fully extended PEF chain crystals of T_m^0 = 240, 247 and 265°C.[12,13] Knoop et al.[12] presented initial results on crystallization kinetics of PEF with a maximum rate at 150°C. The Hoffman-Lauritzen parameters found by Papageorgiou et al.[11] suggest 165°C, although lower temperatures than 165°C were not applied. In both cases the polymer was prepared using Titanium and the molecular weight was relatively low compared to PEF used for industrial applications.[14] On the other hand, Codou et al.[13] studied the non-isothermal crystallization kinetics of a higher molecular weight PEF material produced from FDCA with antimony catalyst, by combining both melt and glass crystallization for the evaluation of the Hoffman-Lauritzen parameters, resulting in a maximum rate at 150°C from the glassy state and a maximum of 165°C from the melt. It is however worth noting that non-isothermal kinetics behave differently from isothermal kinetics. This paper aims to gain new insights into PEF crystal development and structure as a fundamental complement to the initial abovementioned works on PEF crystallization. For this purpose, isothermal crystallization kinetics from the melt were studied using PEF that was prepared autocatalytically from FDCA i.e. without any added catalyst, to avoid any possible effects thereof on crystallization kinetics as has

previously been found for PET. Of this material, samples of three molecular weights were evaluated to give a first indication of the relation thereof to molecular weight. Subsequently, the effect of catalyst loading in pilot scale PEF polymerization on crystallization kinetics was explored for ex-reactor materials of comparable molecular weight near the optimum crystallization temperature.

2 EXPERIMENTAL

2.1 MATERIALS

An overview of the materials used in this study is shown in Table 1. All materials are poly(ethylene 2,5-furandicarboxylate) produced by Avantium, and synthesized from either 2,5-furandicarboxylic acid (FDCA) or dimethyl-2,5-furandicarboxylate (FDCA-DME). Catalysts that were added to the polymerization reactor for the trans-esterification (1) and/or polycondensation (2) steps are listed in Table 1.

Table 3 – Overview of poly(ethylene 2,5-furandicarboxylate) materials.

Name	Monomer	Catalyst 1		Catalyst 2		SSP	M_n (kg/mol)	M_w (kg/mol)	A_{400nm}[b]
		Type	ppm[a]	Type	ppm[a]				
PEF1	FDCA-DME	$Ti(OPr)_4$	400	Sb_2O_3	400	Yes	31	80	-
PEF2-M12	FDCA	-	-	-	-	No	12	29	0.007
PEF2-M17	FDCA	-	-	-	-	Yes	17	33	0.024
PEF2-M28	FDCA	-	-	-	-	Yes	28	58	0.030
PEF3	FDCA	-	-	Sb_2O_3	380	No	15	32	0.018
PEF4	FDCA-DME	$Ca(Ac)_2$	1700	Sb_2O_3	400	No	14	30	0.002
PEF5	FDCA-DME	$Ca(Ac)_2$	1700	Sb_2O_3	880	No	16	30	0.043
PEF6	FDCA-DME	$Ti(OPr)_4$	300	Sb_2O_3	400	No	16	34	0.040
PEF7	FDCA-DME	$Ti(OPr)_4$	400	Sb_2O_3	400	No	16	34	0.044
PEF8	FDCA-DME	$Ti(OPr)_4$	400	Sb_2O_3	400	No	17	40	0.062

[a]Mol/mol FDCA, [b]Absorbance of 30 mg/mL in HFIP/DCM 80/20 solution by UV/VIS spectrophometry at a wavelength of 400 nm

High molecular weight material PEF1 was chosen to determine the equilibrium melting enthalpy and density of the 100% crystalline material in order to reduce the influence of chain ends during lamellar thickening. PEF1 was polymerized in two 2.5 kg batches in a pilot-scale stainless steel PET esterification and polycondensation reactor, and extruded to form 3-4 mm granules, subsequently subjected to SSP at 195°C using 1.5 m^3/min nitrogen sweep in a 5 kg Premex reactor up to a final IV of 0.80 dL/g as determined in a mixture of 60% phenol and 40% tetrachloroethane (w/w). This process and final IV are comparable to one used for relatively high molecular weight industrial PET.[1]

PEF1-M12, i.e. PEF1 having M_n of 12 kg/mol, was prepared in glassware autocatalytically from FDCA and MEG to highlight the intrinsic isothermal crystallization behavior of PEF, while avoiding the influence of catalyst presence. The PEF1-M12 was subjected to SSP on 100 mg quantities of a 0.6-1.4 μm sieve fraction using glass tubes with N_2 flow (4 mL/min) at 210°C to explore the relation of the kinetics to molecular weight. After moderate SSP, the material reaches M_n ~ 17 kg/mol (designated PEF1-M17) while longer SSP leads to M_n ~ 28 kg/mol (designated PEF1-M28).

PEF 3 through 8 (Table 1) were again prepared in pilot scale stainless steel reactors, to a comparable final molecular weight to examine differences in crystallization behavior that may occur by using different production methods for PEF. For the PEF materials used the trans-esterification or esterification was carried out at 190°C for 3-4 hours under nitrogen at atmospheric pressure, and the polycondensation was done at 240°C for 3-4 hours under high vacuum (3 mbar). The molecular weight distributions presented in Table 1 were determined by classical calibration with PS standards, using a Merck-Hitachi LaChrom HPLC system equipped with two PLgel 5 μm MIXED-C (300x7.5 mm) columns. A mixture of 40% of 2-Cl-Phenol and 60% of Chloroform was used as the eluent (w/w).

2.2 METHODS

DENSITY AND MELT ENTHALPY OF PURE PEF CRYSTAL

Disks with d = 25 mm and h = 1.5 mm were injection molded from PEF1 using a Haake MiniJet with T_{melt} = 255°C, T_{mold} = 55°C and p_{inj} = 1000 bar. The disks were then annealed between a 'sandwich' of a face-up and face-down hot-plate set to the equal temperature, using various times and temperatures to achieve different degrees of crystallinity. Furthermore, two pellet SSP samples of PEF1 prior to plaque injection molding were added to verify the effect of longer isothermal treatment at higher temperatures on crystallinity.

WAXS analysis was carried out on these samples using a Phillips X'Pert X-ray diffraction system with a wavelength of 1.5406 Å (source: Cu-kα). The samples were scanned from 2Θ = 5° to 2Θ = 60°. Relative crystallinity was calculated based on the deconvoluted area of crystalline reflections compared to the area of the amorphous in the WAXS spectrum, similar to the approach by Fontaine et al.[15]. Density was measured on the same samples by buoyancy in a density gradient column of di- and tetrachloromethane with a working range from 1.420 to 1.480 g/cm^3. The net melt enthalpy of the samples was determined by heating at 10°C/min in DSC from 25°C to 250°C on ~ 4 mg samples in a Mettler Toledo DSC 1 equipped with the STAR^e software, calibrated using In and Zn standard. Care was taken to respect the ICTAC kinetics committee recommendations for DSC sample preparations prior to kinetic computations.[16]

MELT CRYSTALLIZATION KINETICS

Crystallization from the melt was studied using the same DSC set-up as described in the previous paragraph. The rate of primary crystallization was studied by applying multiple cycles of heating a sample with 10°C/min up to 250°C, well above the initially observed melt-point, and after quenching with 50°C/min holding the sample at an isothermal crystallization

temperature for various intervals of time. Rather than integration of the isothermal crystallization peak, the total melting enthalpy in the heating curve following each isothermal interval was determined and interpreted as the total crystallinity that developed during the preceding isothermal time interval, analogous to the work of J. Kolstad on PLA.[17] This method was chosen to avoid the misinterpretations that can arise by integration of crystallization from isothermal curves, for instance by misplacement of the baseline when crystallization starts prior to reaching the isothermal temperature or when the transition from primary to secondary crystallization is not clear.

The method was applied using 12 randomized isothermal steps between 2-72 minutes, using isothermal temperatures between 140°C and 190°C with 10°C increments for the autocatalyzed PEF1-(M12 to M28) samples. Subsequently, the crystallization temperature which showed the highest observed rate in catalyst free PEF was chosen for isothermal DSC experiments on PEF2-8, in order to provide an initial indication of the effect of the catalyst content.

3 RESULTS & DISCUSSION

3.1 DENSITY AND MELT ENTHALPY OF PURE PEF CRYSTAL

The WAXS patterns obtained from samples of PEF1 are shown in Figure 1. As can be seen, the location and amount of crystalline reflections does not shift significantly with varying crystallization time and temperature, indicating that a single crystal structure is present. The values of WAXS crystallinity ($X_{c,WAXS}$) were calculated by deconvolution of the WAXS patterns into six crystalline reflections and one broad amorphous band, and subsequently dividing the areas of the crystalline reflections by the total area of the WAXS pattern.

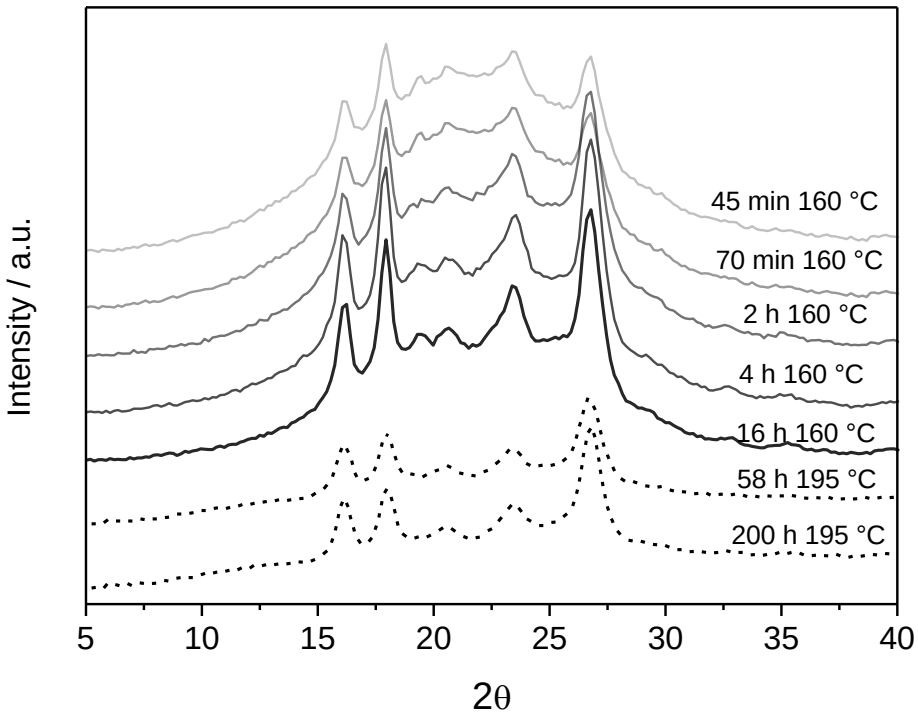

Figure 1 – WAXS patterns of PEF1 disks (top solid lines) and pellets (bottom dash lines) annealed at different conditions. The annealing conditions are indicated by each curve.

Figure 2a shows the linear regression of density vs $X_{c,WAXS}$, which gives by extrapolation to X_c = 1, a crystal density of ρ_c = 1.548 ± 008 g/cm^3 and by extrapolation to X_c = 0 an amorphous density of ρ_a = 1.434 ± 003 g/cm^3. The crystal density found here agrees well with the value of ρ_c = 1.565 g/cm^3 derived from the crystal structure of PEF proposed by Kazaryan et al.[10]. Fixing this latter value for the crystal density, an alternative extrapolation yields ρ_a = 1.426 ± 002 g/cm^3 respectively for the amorphous phase (Figure 2a). Figure 2b shows linear regressions of melting enthalpy vs. $X_{c,WAXS}$ or crystallinity fitted from crystal density proposed by Kazaryan et. al.[10], which give estimates for the 100% crystal phase of ΔH_m^0 = 187 ± 7 J/g and ΔH_m^0 = 185 ± 12 J/g respectively. The standard error is higher when using data from the density correlation but it highlights that the linear regression of the two datasets with melting enthalpy are comparable from a statistical point of view. The found value of ΔH_m^0 is higher than the highest reported value of ΔH_m^0 = 140 J/g for PET, even when

comparing the molar value of 34.0 kJ/mol to 26.9 kJ/mol. This is however in line with a lower value of 24.9 kJ/mol (ΔH_m^0 = 103 J/g) reported for PEN[18], which has higher melting point than PET vs the lower melting point of PEF.

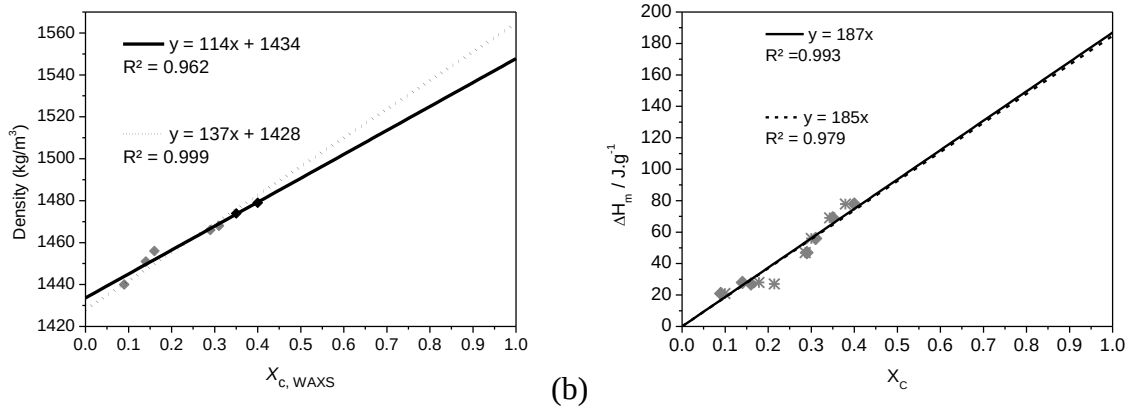

Figure 2 – (a) Density *vs.* crystallinity obtained by deconvolution of WAXS patterns from PEF1 disks (gray diamonds) and pellets (black diamonds). The linear fits were done without conditions (solid line) and fixing the crystal density to ρ_c = 1.565 g/cm^3 (dot line).

(b) Melting enthalpy *vs.* crystallinity obtained by deconvolution of WAXS patterns (grey diamonds fitted by solid line) or crystallinity fitted from crystal density proposed by Kazaryan et. al. (grey star fitted by dot line).

3.2 MELT CRYSTALLIZATION KINETICS

Figure 3 shows the melting behavior that was observed for PEF1-M12 during heating at 10°C/min after the longest isothermal interval (72 min) for each crystallization temperature used, and is typical of the behavior observed throughout this kinetics study.

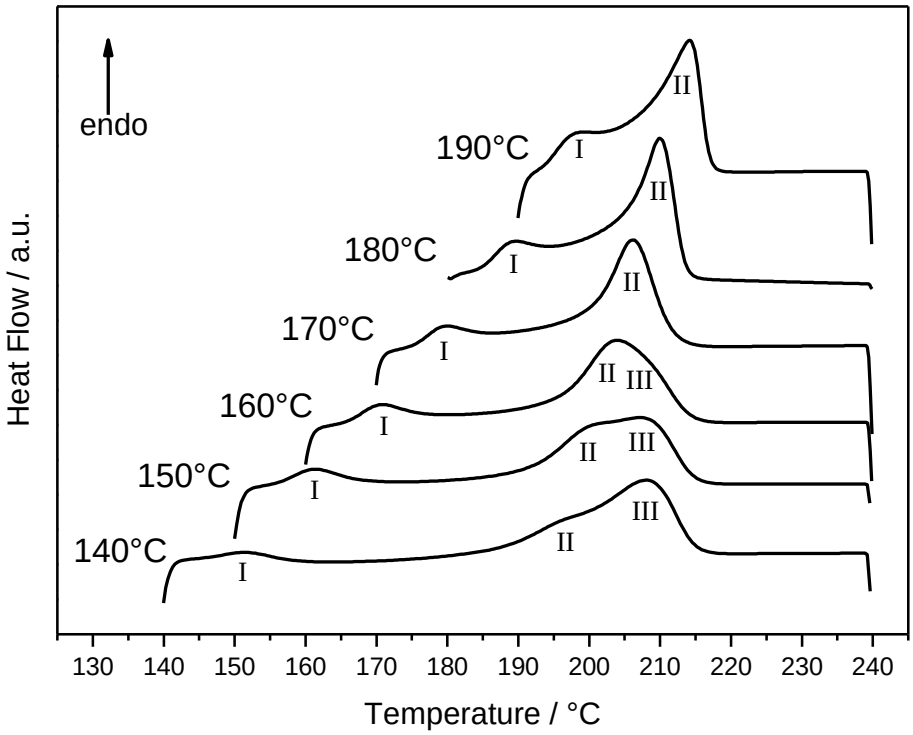

Figure 3 – DSC melting curves (heating rates 10 K/min) of PEF1-M12 after crystallization for 72 min at several isothermal temperatures, which are indicated at each curve.

In analogy with PET, three melting endotherms can be distinguished in Figure 3. Endotherms II and III were found for PET by Groeninckx et al.[5] and endotherm I was found by Kong et al.[19]. Endotherm I corresponds to earliest melting crystals and scales with the crystallization temperature, and was associated for PET with the melting of crystals that are formed at early stages of secondary crystallization, due to the appearance of additional lamella between the primary lamella. This is a different than the lamella thickening as crystals are perfected, which is also known as secondary crystallization. These crystals have thinner lamella due to physical hindrance during their formation and therefore melt early. However, this endotherm is absent in the study of Groeninckx et al.[5] as it merges with endotherm II after sufficient crystallization time. On the other hand, endotherm II is explained in both studies[5,20] as the melting of the crystals that are formed during primary crystallization, and is therefore attributed to the thermodynamically stable crystal form that appears at a certain crystallization temperature. Endotherm III does not scale with crystallization temperature and is therefore

associated with crystals of higher lamellar thickness that are formed by re-crystallization upon heating in DSC. It was also observed that all endotherms merge with endotherm II at higher crystallization temperatures, which was also observed by Groeninckx et al. [5] for PET. In this work, the total integral over all three peaks was defined as the enthalpy of the crystallization that occurred during the time in the preceding isothermal step, or $\Delta H_c(t)$. Dividing the crystallization enthalpy by the maximum enthalpy for primary crystallization before transition to secondary crystallization, $\Delta Hc_{,\infty}$, provides a relative crystallinity $X(t)$, which can be used to describe the kinetics according to the Avrami equation, i.e. Equation (1).[21,22]

$$X(t) = 1 - \exp\left(-Kt^n\right) \qquad (1)$$

Where K is the growth function and n is the Avrami exponent. The Equation (1) can be linearized as follows:

$$\log\left\{-\ln\left[1 - X(t)\right]\right\} = n \log t + \log K \qquad (2)$$

Linear fits of Equation (2) were constructed for each isothermal temperature and molecular weight to obtain the values for $\Delta H_{c,\infty}$, K and n which are gathered in Table 3 through 5. These K and n were further used to calculate the crystallization half-time $t_{1/2}$ using Equation (3),

$$t_{1/2} = \left(\frac{\ln 2}{K}\right)^{1/n} \qquad (3)$$

Values for $\Delta H_{c,\infty}$ were generally estimated by minimizing the error on the slope of the linearized Avrami curves. Only for PEF1-M28 (Table 5) the values were estimated based on those of the other materials. Comparing the $\Delta H_{c,\infty}$ values to the melting enthalpy of the pure crystal yields percent crystallinity values at complete primary crystallization between 19% and 27%, which is low compared to PET. This could indicate relatively early space filling, i.e. a high nucleation density. For PEF1-M12, the n value approaches the value of 4 at 190°C

which is typical for spherulitic growth with continued nucleation and then decrease and passes through a minimal value of about 2.5 at 170°C which, in agreement with the $t_{1/2}$ value, would also indicate that the rate of crystallization is maximal in this temperature range. At 140°C, *n* was found to be close to 3, corresponding to spherical growth from instantaneous nucleation. For PEF1-M17, the *n* values pass also through a minimum at 170°C (Table 4). This trend is less obvious for the *n* values of PEF-M28 (Table 5) that are above 4, which can be attributed to a poorer fit of relatively low degrees of crystallinity for the time intervals applied. In a recent paper we applied the Ozawa method on the non-isothermal crystallization of PEF exhibiting similar molecular weight (i.e. 19 kg/mol) as PEF1-M17, which yielded lower n values with a different minimum.[13] This difference is expected to originate from the nature of the non-isothermal experiments, since when coming from the melt, relatively low relative degrees of crystallinity (or ’conversion‘) are reached at higher temperatures and relatively high extents of crystallinity are found at lower temperatures (See Supporting Information of ref 19, Figure 5). In isothermal experiments using Avrami theory the used range starts close to 0 and approaches 1 at any given temperature. Only at 170°C a good comparison can be made, since the range of relative crystallinity is large for the non-isothermal experiments (between 0.1 to 0.8), and the *n* values of 2.09 (Table 4) and 2.3 (Figure 4 in ref. 19) are in good agreement.

Table 3 – Avrami parameters found for PEF1-M12 with M_n = 12 kg/mol.

T (°C)	140	150	160	170	180	190
$\Delta Hc_{,\infty}$ (J/g)	39.9	44.9	46.6	51.3	44.3	42.9
K (min^{-n})	$8.77\cdot10^{-6}$	$2.11\cdot10^{-4}$	$9.66\cdot10^{-4}$	$5.81\cdot10^{-4}$	$2.26\cdot10^{-5}$	$2.71\cdot10^{-7}$
n	2.84	2.40	2.26	2.52	3.19	3.84
$t_{1/2}$ (min)	53.0	29.1	18.2	16.6	28.0	46.7

Table 4 – Avrami parameters found for PEF1-M17 with M_n = 17 kg/mol.

T (°C)	140	150	160	170	180	190
$\Delta Hc_{,\infty}$ (J/g)	-	36.0	40.2	48.7	48.0	-
K (min^{-n})	-	$1.43\cdot10^{-5}$	$3.57\cdot10^{-4}$	$6.63\cdot10^{-4}$	$3.07\cdot10^{-4}$	-
n	-	2.94	2.29	2.09	2.25	-
$t_{1/2}$ (min)	-	39.1	27.3	27.8	31.0	-

Table 5 – Avrami parameters found for PEF1-M28 with M_n = 28 kg/mol.

T (°C)	140	150	160	170	180	190
$\Delta Hc_{,\infty}$ (J/g)	36.0	36.0	41.0	41.0	36.0	36.0
K (min^{-n})	$3.14\cdot10^{-8}$	$7.22\cdot10^{-8}$	$1.06\cdot10^{-6}$	$8.22\cdot10^{-7}$	$2.52\cdot10^{-9}$	$4.99\cdot10^{-11}$
n	3.75	4.13	3.62	3.72	4.91	5.15
$t_{1/2}$ (min)	90.8	51.3	40.3	39.1	52.2	93.0

Assuming that formation of heterogeneous nuclei is independent of temperature and that all sites are activated in the same time, it has been shown by Chan et al.[23] that the reciprocal crystallization half-time ($1/t_{1/2}$) is proportional to the linear growth rate, *G*. The temperature dependence of the linear growth rate (*G*) can be described by the Hoffman–Lauritzen rate equation.[24]

$$G = G_0 \exp\left(\frac{-U^*}{R(T - T_\infty)}\right)\exp\left(\frac{-K_g}{T\Delta Tf}\right) \qquad (4)$$

where G_0 is the preexponential factor and includes the molecular weight dependance, U^* is the activation energy of the segmental jump rate (associated with diffusion process), T_m^0 is the equilibrium melting temperature, $\Delta T=T_m^0-T$ is the undercooling, $f=2T/(T_m^0+T)$ is the correction factor, T_∞ is a hypothetical temperature where motion associated with viscous flow ceases which is taken as 30K below the glass transition temperature, T_g. The kinetic parameter K_g associated with the nucleation process has the form of Equation (5).

$$K_g = \frac{nb\sigma\sigma_e T_m^0}{\Delta h_f k_B} \qquad (5)$$

Where b is the surface nucleus thickness, σ is the lateral surface free energy, σ_e is the fold surface free energy, T_m^0 is the equilibrium melting temperature, Δh_f is the heat of fusion per unit volume of crystal, k_B is the Boltzmann constant, and n takes the value 4 for crystallization regime I and III, and 2 for regime II. Equation (4) can be re-written using the approach of Chan et al.[23] into Equation (6).

$$G \propto \left(\frac{1}{t_{1/2}}\right) = \left(\frac{1}{t_{1/2}}\right)_0 \exp\left(\frac{-U^*}{R(T-T_\infty)}\right)\exp\left(\frac{-K_g}{T\Delta Tf}\right) \qquad (6)$$

Non-linear fits of Equation (6) using the obtained $(1/t_{1/2})$ values for the different temperatures of the three autocatalyzed materials PEF1-M12/M18/M28 (Table 3, 4 and 5) and the actual values for the reciprocal crystallization half-times are presented in Figure 4. The onset temperature of cooperative motion was taken to be $T_\infty = T_g - 30$ K = 313.15 K and an equilibrium melting temperature determined from Hoffman-Weeks routine at T_m^0 = 520.15 K = 247°C. [13] The Origin 8.5 software was used for non-linear fitting. One single set of U^* and K_g parameter was used for the data of all three molecular weights, whereas $(1/t_{1/2})_0$ was only kept constant over the data points of a single molecular weight. The calculated $(1/t_{1/2})$ values from the Avrami parameters are shown versus the non-linear fits in Figure 4, which highlight a good relation of the temperature dependence of the growth rate. The fits give U^* = 10200

J/mol and K_g = 2.8 ·10^5 K^2 for the three dataset while the pre-exponential factor $(1/t_{1/2})_0$ displays a linear relation with $1/M_n$ as shown in insert figure of Figure 4. The correlation coefficient of the non-linear fits for the three dataset is R^2 ~ 0.954. The independence of U^* and K_g parameters over molecular weight variation and the dependence of the pre-exponential factor vs $1/M_n$ has previously been observed for PET.[25] Moreover, it should be stressed that the temperature of maximal crystallization rate ($T_{c,\max}$) is independent of molecular weight which was also the case for PET.[25] As shown in Figure 4, $T_{c,\max}$ ~ 167°C which agrees with the value of 165°C found in our non-isothermal melt crystallization kinetic study of PEF.[13]

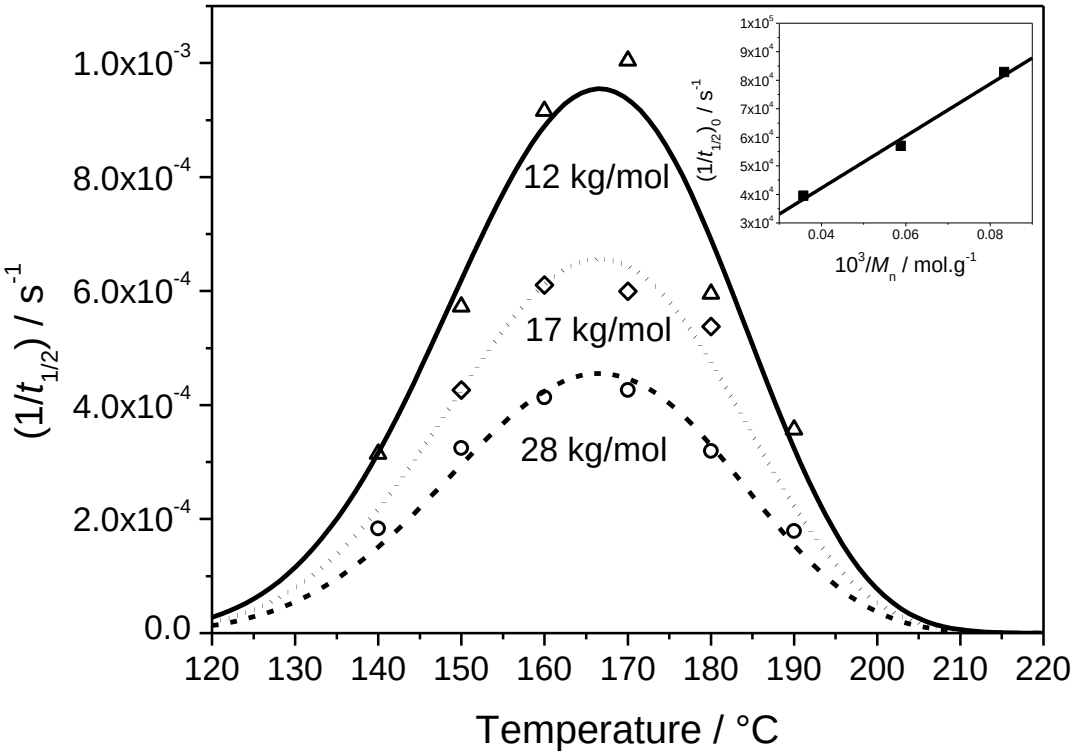

Figure 4 – Reciprocal crystallization half-time obtained at different isothermal temperatures for PEF1 of 12, 17 and 28 kg/mol; the lines represents the non-linear fitting of the Hoffman-Lauritzen equation obtained from each dataset. Insert graph: $(1/t_{1/2})_0$ vs reciprocal molecular weight.

Previous studies on isothermal crystallization of PET show maximum values obtained for $(1/t_{1/2})$ of about 3.3·10^{-3} s^{-1} (M_n = 16 kg/mol)[26], 2.5·10^{-3} s^{-1},[23] and 2.2·10^{-3} s^{-1}(M_n = 22 kg/mol).[27] As shown in Figure 4, the $(1/t_{1/2})$ maximal values for PEF are ranging between 4·10^{-4} s^{-1} and 1.1·10^{-3} s^{-1} which is between three to five times slower than PET whereas the

$(1/t_{1/2})_0$ values of PEF (insert of Figure 4) are of same order (between $4\cdot10^4$ and $8\cdot10^4$ s^{-1}) as the $(1/t_{1/2})_0$ reported for PET ($3.58\cdot10^4$ s^{-1}).[23] The rate differences can be explained by the resulting U^* and K_g values found for PEF. An overview of Hoffman-Lauritzen parameters from various literature studies on PET shows that mainly the universal value for U^* of 6300 J/mol is employed,[23,26] whereas values for K_g are typically reported between $1.9\cdot10^5$ and $3.7\cdot10^5$ K^2.[28] The K_g value is in line with PET and in perfect agreement with the K_g values of $2.8\cdot10^5$ K^2 found recently from the kinetic analysis of the non-isothermal PEF crystallization.[13] On the other hand, the value of U^* found for PEF is higher compared to the U^* employed for PET, which indicates a higher activation energy for the segmental jump that is related to the diffusion process. This would be correlated with the more restricted conformational changes of PEF chains proposed by Burgess et al.,[29] who also speculated that this chain rigidity is the cause of the lower crystallization rate of PEF. The growth rate differences between PEF and PET is largely attributed to the combination of this feature with the lower T_m^0 at similar K_g, and therewith a relatively lower degree of undercooling over the temperature range of crystallization.

3.3 EFFECT OF THE POLYMERIZATION RECIPE

The melt crystallization was studied for various pilot-scale PEF materials (Table 1) by applying similar isothermal DSC programs. This was done at 170°C, around the fastest temperature found for the autocatalyzed material. The results are shown in Figure 5, in comparison to a simulation at 175°C for PET of similar molecular weight based on the model found by Lin et al.[6]. It illustrates that PEF crystallizes more slowly than PET, but also that the applied catalyst loading can have a significant effect on the crystallization rate.

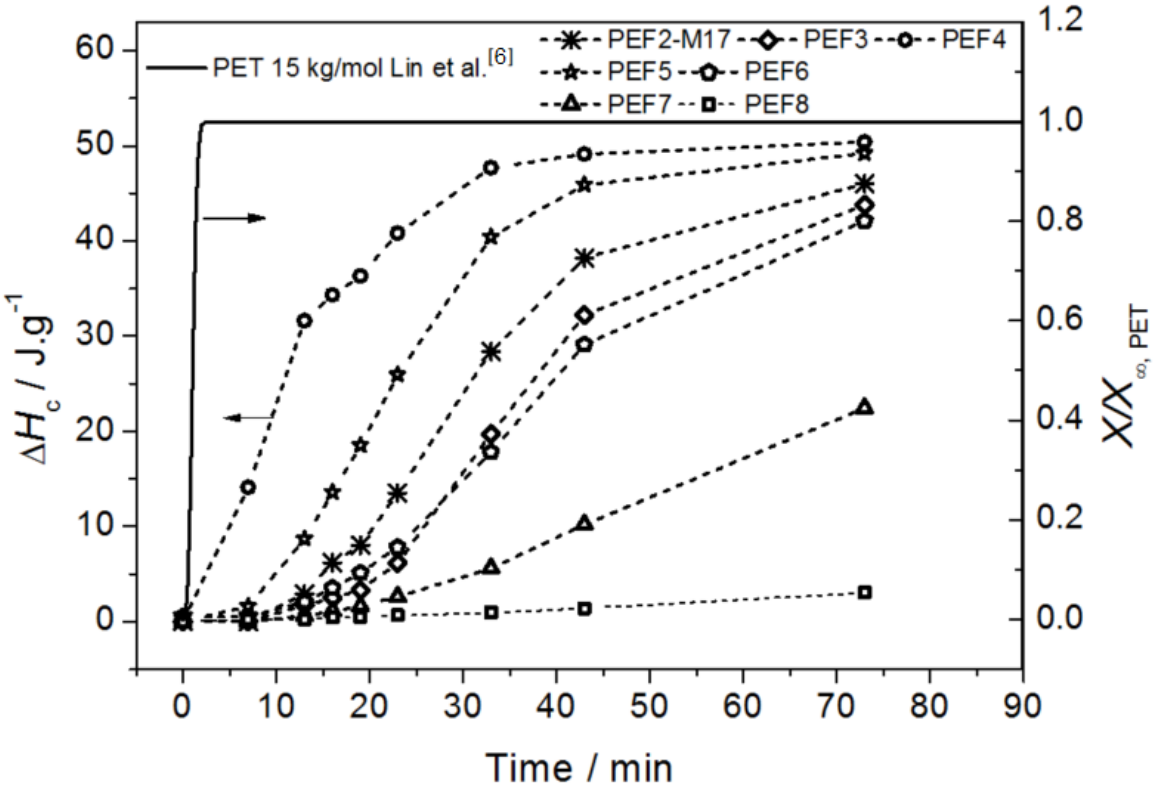

Figure 5 – Crystallization enthalpy vs crystallization time at 170°C after quenching from the melt. PEF samples presented are of comparable molecular weight with various catalyst contents; PEF1-M17 – No catalyst, PEF2 – Sb only, PEF3-5 – Ca+Sb, PEF5-8 – Ti+Sb.

Figure 5 shows that the use of Antimony as a catalyst of the PEF synthesis leads to a polymer with a slightly lower crystallization rate (PEF2) as compared to autocatalyzed PEF (PEF1-M17) for the initial stage of the crystallization, although this affect is limited and may be caused by the difference of reactor type. The use of Titanium in combination with Antimony (PEF5-8) lead to a higher decrease of the crystallization rate. For PET it is known that Titanium causes yellowness and accelerates the thermal degradation reaction that forms vinyl end-groups and acetaldehyde by in-chain ethylene glycol scission.[1,30] Yellowing in PET is not completely understood, but some proposed mechanisms involve decarboxylation and recombination into new dimeric species in the polymer chain.[1,31,32] It is hypothesized that Titanium can cause similar reactions in PEF, from which the resulting impurities may lead to crystal imperfections and a reduced crystallization rate if the level becomes too high. This is sustained by the lower crystallization rate with increased yellowness from PEF 6 to PEF 8

(Figure 5), which is shown by the increased absorbance at 400 nm in Table 1.[30] More interestingly, the use of Calcium in combination with Antimony leads to a polymer with a higher crystallization rate than autocatalyzed PEF in the case of PEF4 and to a much higher crystallization rate in the case of PEF3. Because the use of antimony alone shows a moderately decreased crystallization rate (PEF2), the increased crystallization rate of these samples is attributed to a nucleating effect of Calcium, as is known for PET.[33] The mechanism is believed to be analogous to that of alkali metals in PET, which form nucleating species for the polyester by coordinating with acid end-groups via chain-scission.[34,35] The higher rate in PEF3 compared to PEF4 (Figure 5) can be attributed to both a lower molecular weight and a higher purity as described before, which is indicated by the extremely low absorption at 400 nm (Table 1) for this material.

4 CONCLUSIONS

A correlation between degree of crystallinity obtained by WAXS measurements and density was found that is in agreement with the value derived from the PEF crystal structure proposed by Kazaryan et al.,[10] which correlates to an equilibrium melting enthalpy of 187 ± 7 J/g. The crystallization kinetics from the melt were described by the Avrami equation for autocatalyzed PEF with three molecular weights at different isothermal temperatures. Using the reciprocal half time, the temperature dependence of the crystal growth rate could be well described by Hoffman-Lauritzen theory. Non-linear fitting could be done over three molecular weights using a single set of U^* and K_g while the reference growth rates $(1/_{t1/2})_0$ were found to be linear to the reciprocal molecular weight. Especially the resulting value for the growth rate parameter U^* obtained for PEF was high compared to the typical values reported for PET, although overall $(1/_{t1/2})$ and $(1/_{t1/2})_0$ values were lower. The maximum growth rate computed with the Hoffman-Lauritzen parameters obtained was $T_{c,max}$ = 167°C. At T_c = 170°C, near the optimum temperature, it was found that the rate of quiescent melt

crystallization of PEF can vary significantly with the catalyst content and polymerization conditions, although exact relations have not been established in this work. Amongst the catalysts used, it was found that Titanium can decrease the crystallization rate whereas Calcium can increase the rate. Although the crystallization rate can be influenced by the catalysts used, the isothermal melt crystallization rate of PEF is generally lower than PET, which is an advantage for applications where optical clarity is desired and/or high degrees of orientation are applied in the rubbery state above the glass transition to achieve strain induced crystallization, e.g. in bottles, films and thermoformed articles.

5 REFERENCES

[1] J. Scheirs, T. E. Long, "*Modern Polyesters: Chemistry and Technology of Polyesters and Copolyesters"*, John Wiley & Sons, 2003.
[2] R. d. P. Daubeny, C. W. Bunn, C. J. Brown, *Proc. R. Soc. London, Ser. A* 226 (1954), 531
[3] J. P. Jog, *J. Macromol. Sci., Rev. Macromol. Chem. Phys.* C35 (1995), p531
[4] C. M. Roland, *Polym. Eng. Sci.* 31 (1991), p849
[5] G. Groeninckx, H. Reynaers, H. Berghmans, G. Smets, *Journal of Polymer Science: Polymer Physics Edition* 18 (1980), 1311.
[6] C. C. Lin, *Polym. Eng. Sci.* 23 (1983), 113.
[7] E. L. Lawton, *Polym. Eng. Sci.* 25 (1985), 348.
[8] B. Lee, J. W. Lee, S. W. Lee, J. Yoon, M. Ree, *Polym. Eng. Sci.* 44 (2004), 1682.
[9] Y. S. Hu, A. Hiltner, E. Baer, *J. Appl. Polym. Sci.* 98 (2005), 1629.
[10] L. G. Kazaryan, F. M. Medvedeva, *Vysokomol. Soedin., Ser. B.*10 (1968), 305.
[11] G. Z. Papageorgiou, V. Tsanaktsis, D. N. Bikiaris, *Phys. Chem. Chem. Phys.* 16 (2014), 7946.
[12] R. J. I. Knoop, W. Vogelzang, J. Haveren, D. S. Es, *J. Polym. Sci., Part A: Polym. Chem.* 51 (2013), 4191.
[13] A. Codou, N. Guigo, J. van Berkel, E. de Jong, N. Sbirrazzuoli, *Macromol. Chem. Phys.* 215 (2014), 2065.
[14] L. Sipos, G. J. M. Gruter, J. Kolstad, M. A. Dam, WO2013062408 (2013)
[15] F. Fontaine, J. Ledent, G. Groeninckx, H. Reynaers, *Polymer* 23 (1982**)**, 185.
[16] S. Vyazovkin, K. Chrissafis, M. L. Di Lorenzo, N. Koga, M. Pijolat, B. Roduit, N. Sbirrazzuoli, J. J. Suñol, *Thermochim. Acta* 590 (2014), 1.
[17] J. J. Kolstad, *J. Appl. Polym. Sci.* 62 (1996), 1079.
[18] B. Wunderlich, "The ATHAS database on heat capacities of polymers", in *Pure and Applied Chemistry*, 1995, 67/1019
[19] Y. Kong, J. N. Hay, *Polymer* 44 (2003), 623.
[20] Y. Kong, J. N. Hay, *Polymer* 44 (2003), 623.
[21] M. Avrami, *J. Chem. Phys.* 7 (1939), 1103.
[22] M. Avrami, *J. Chem. Phys.* 8 (1940), 212.
[23] T. W. Chan, A. I. Isayev, *Polym. Eng. Sci.* 34 (1994), 461.
[24] J. D. Hoffman, G. T. Davis, J. I. Lauritzen, "*Treatise on Solid State Chemistry"*, N. B. Hannay edition, Plenum, NY, 1976.
[25] F. Van Antwerpen, D. W. Van Krevelen, *J. Polym. Sci., Polym. Phys. Ed.* 10 (1972), 2423.
[26] X. F. Lu, J. N. Hay, *Polymer* 42 (2001), 9423.
[27] L. Sorrentino, S. Iannace, E. Di Maio, D. Acierno, *J. Polym. Sci., Part B: Polym. Phys.* 43 (2005), 1966.
[28] S. Vyazovkin, N. Sbirrazzuoli, *Macromol. Rapid Commun.* 25 (2004), 733.
[29] S. K. Burgess, J. E. Leisen, B. E. Kraftschik, C. R. Mubarak, R. M. Kriegel, W. J. Koros, *Macromolecules* 47 (2014), 1383.
[30] J. Yang, Z. Xia, F. Kong, X. Ma, *Polym. Degrad. Stab.* 95 (2010), 53.
[31] M. Edge, N. S. Allen, R. Wiles, W. McDonald, S. V. Mortlock, *Polymer* 36 (1995), 227.
[32] M. Edge, R. Wiles, N. S. Allen, W. A. McDonald, S. V. Mortlock, *Polym. Degrad. Stab.* 53 (1996), 141.

[33] B. Gümther, H. G. Zachmann, *Polymer* 24 (1983), 1008.
[34] R. Legras, C. Bailly, M. Daumerie, J. M. Dekoninck, J. P. Mercier, M. V. Zichy, E. Nield, *Polymer* 25 (1984), 835.
[35] R. Legras, J. M. Dekoninck, A. Vanzieleghem, J. P. Mercier, E. Nield, *Polymer* 27 (1986), 109

CHAPTER 4
NON-ISOTHERMAL CRYSTALLIZATION KINETICS

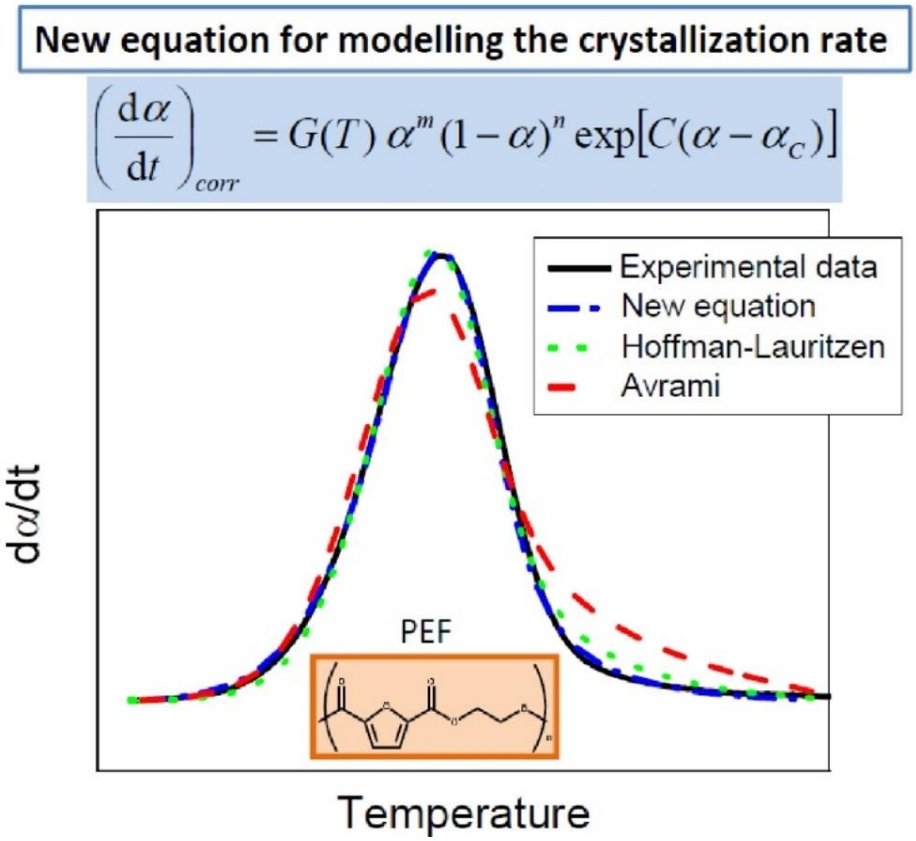

This chapter is also published as part of "Modelling the non-isothermal crystallization of polymers: Application to poly(ethylene 2,5-furandicarboxylate)" by N. Guigo, J.G. Van Berkel, E. de Jong, N. Sbirrazzuoli, Thermochimica Acta 650 (2017), 66

This chapter presents several interpretations of the non-isothermal crystallization behavior of PEF upon cooling from the melt and heating from the glass obtained by Codou et al.[1]. Several polymer crystallization theories have been applied in which the rate is assumed to be dependent on two separate functions, one depending only on temperature and the second depending only on extent of crystallization. The temperature dependence was described with the Hoffman–Lauritzen (HL) equation with the parameters of Chapter 3 and earlier work based on the temperature dependence of the activation energy (E_α) through an advanced isoconversional method (AIC). The dependence on the extent of crystallization was then described by the Avrami and Sestak-Berggren models, in comparison to simulations using Ozawa and model-free AIC methods. It was shown that the model-free approach is able to take into account additional phenomena occurring at the end of crystallization from the glass that are not considered in the classical HL, Avrami and Ozawa theories.

1 INTRODUCTION

Polymer crystallization kinetics have been widely described using single-steps models, such as Avrami equation[2,3,4] or Ozawa method.[5] To this end, the theories proposed by Fisher and Turnbull[6] or Hoffman–Lauritzen (HL)[7] offer an interesting alternative because two different limiting steps are considered in their equations; one step accounts for nucleation control which is rate determining at the early stages of melt crystallization, while the second step accounts for diffusion control which becomes rate determining at the end of the crystallization process. The processing of polyesters often occurs under nonisothermal heating/cooling conditions which then implies the use of non-isothermal crystallization kinetic models. Therefore, various modifications of the Avrami equations were proposed in order to take into consideration the non-isothermal temperature variation. The Ozawa equation is one of the most used but this model assumes constant heating/cooling rates. Based on the isokinetic assumption, several methods such as the Nakamura et al.[8] or the Kamal et al.[9] equations were

proposed for predicting non-isothermal crystallization kinetics from isothermal data but the predictions are not totally satisfactory.[10] Moreover, polyester crystallization is complex since the primary crystallization (i.e. formation of the more perfect crystalline lamellae) has to be distinguished from the secondary crystallization which corresponds to the formation of smaller and less perfect crystals between spherulites and interlamellar spaces. For primary crystallization, the extent of isothermal crystallization increases linearly with time while for secondary crystallization it rather increases linearly with the square root of time.[11] Therefore, secondary crystallization or crystal thickening could explain the deviations sometimes observed between experimental data and the HL model. Thus, the aim of this study is to try to understand the limit of applicability of the HL model and to propose new equations to simulate complex processes which occur along and beyond the nonisothermal primary crystallization. Non-isothermal crystallization is more complex because both time and temperature are changing simultaneously. Therefore, the experimental crystallization data obtained on PEF by Codou et al. were employed in the present paper to validate the applicability of additional equations to the HL model.[1]

2 EXPERIMENTAL

2.1 MATERIALS

Poly(Ethylene 2,5-Furandicarboxylate), PEF, was obtained from the direct esterification and polycondensation of FDCA from Avantium and bio-based ethylene glycol (from India Glycols), using antimony as the catalyst analogously to PET. Both polymerization steps were carried out in a 4.5 kg stainless steel melt polymerization reactor up to a final intrinsic viscosity (IV) of 0.61. The final IV was calculated using the Billmeyer equation[12] from a measured inherent viscosity of 0.59 dL g^{-1} at a concentration of 0.4 g dL^{-1} in a mixture of 60% phenol and 40% tetrachloroethane (w/w). The absolute M_n was determined to be 19.3 kg

mol^{-1} as derived from the total number of end groups by ^1H NMR, also corresponding to a typical industrial M_n after polycondensation of PET.

2.2 METHODS

DSC runs were carried out on a Mettler-Toledo DSC-1 equipped with a FRS5 sensor and STAR© software for data analysis. Temperature, enthalpy and tau lag calibrations were steadily done by using indium and zinc standards. Samples of about 4-5 mg were placed in 40 μL aluminium crucibles and sealed hermetically. To minimize problems due to potential thermal degradation of PEF at high temperature, fresh samples produced from the same batch were prepared for the different analysis. The nonisothermal experiments were performed under a N_2 atmosphere (80 $mL.min^{-1}$) at 0.5, 0.75, 1, 1.5, 5, 10 and 15 $K.min^{-1}$. Computation of kinetic parameters of crystallization was performed with the same temperature programs of 0.5, 0.75, 1 and 1.5 $K.min^{-1}$ on heating and on cooling. Before performing cooling experiments all samples were heated to 250°C and held at this temperature for 3 min in order to secure complete melting. Before performing experiments on heating and in order to obtain fully amorphous samples, the samples were quickly cooled from the melt in the DSC using a cooling rate of 50 $K.min^{-1}$.

2.3 THEORY

As in Chapter 3, isothermal crystallization kinetics are usually described in terms of the Avrami equation or Johnson – Mehl – Avrami – Erofeev – Kolmogorov (JMAEK), here represented as Equation (1), where $\alpha(t)$ is the relative extent of crystallinity at time t ranging from 0 to 1 and $k(T)$ is the overall (macroscopic) crystallization rate coefficient, n is the Avrami exponent which is dependent on the growth geometry of the crystals and on the type of nucleation and T the temperature.

$$\alpha(t) = 1 - \exp\left[-k(T)t^n\right] \qquad (1)$$

For kinetic studies, the general form of the basic rate equation is usually written as Equation (2), in which α represents conversion or in this case relative extent of crystallinity, $f(\alpha)$ is the function that represents a reaction model and $k(T)$ the rate constant which is dependent on temperature.[13,14]

$$\frac{\mathrm{d}\alpha}{\mathrm{d}t} = k(T)\, f(\alpha) \qquad (2)$$

This temperature-dependence is often described by an Arrhenius law in Equation (3), with E the activation energy, A the pre-exponential factor and R the universal gas constant.

$$k(T) = Ae^{-E\ /\mathrm{R}T} \qquad (3)$$

Equation (3) relies on the assumption that the dependence of the process rate on temperature is represented by the rate constant, $k(T)$, and the dependence on the relative extent of crystallization by the reaction model, $f(\alpha)$. The majority of kinetic methods used in the area of thermal analysis consider the rate to be a function of only these two variables.[14] Applying this to crystallization in DSC following Toda et al.[15], one can consider the heat flow of crystallization Φ proportional to the growth rate, G following Equation (4), in which Δh is the volumetric heat of crystallization and S is the total area of the growth surface.

$$\Phi = \Delta h\ S\ G \qquad (4)$$

In DSC, the overall crystallization rate is determined as the ratio of the heat flow to the total heat of crystallization, Q, as per Equation (5), which can thus be expressed as Equation (6).

$$\frac{\mathrm{d}\alpha}{\mathrm{d}t} = \frac{\Phi}{Q} \qquad (5)$$

$$\frac{\mathrm{d}\alpha}{\mathrm{d}t} = \frac{\Delta h\ S\ G}{Q} \qquad (6)$$

When assuming that the total area of the growth surface S is only a function of the extent of crystallization $S(\alpha)$ and that the growth rate G is only a function of temperature $G(T)$, we can now consider Equation (7) which shares a similar mathematical form to Equation (2) in which $G(T)$ is used instead of $k(T)$ while $S(\alpha)$ replaces $f(\alpha)$, and K is introduced as a constant ($K = \Delta h/Q$) since the volumetric heat of crystallization and the total heat of crystallization are constant for a given temperature program.

$$\frac{\mathrm{d}\alpha}{\mathrm{d}t} = K.G(T)\, S(\alpha) \qquad (7)$$

This relation indicates the link between the overall crystallization rate and the growth rate measured microscopically. The overall crystallization rate can be determined by DSC because crystallization is accompanied by a significant heat release which is assumed to be proportional to the macroscopic crystallization rate. The growth rate $G(T)$ can be described by the Hoffman–Lauritzen theory in Equation (8).[7]

$$G(T) = G_0 \exp\left(\frac{-U^*}{R(T - T_\infty)}\right)\exp\left(\frac{-K_g}{T\Delta T f}\right) \qquad (8)$$

Where U^* is the activation energy of the segmental jump, which is associated with diffusion process and characterizes molecular diffusion across the interfacial boundary between melt and crystal, K_g is a parameter associated with the nucleation process, G_0 is a pre-exponential factor, ΔT the degree of undercooling ($T^\circ_{\mathrm{m}} - T$) and $f = 2T/(T_m^\circ + T)$, T_m° is the equilibrium melting temperature, T_∞ is a hypothetical temperature where motion associated with viscous flow ceases that is taken 30 K below the glass transition temperature T_g. Several authors[16,17,18] have previously proposed to describe the temperature dependence of the rate constant $k(T)$ in crystallization kinetics studies on the basis of the Hoffman–Lauritzen theory. This relies on the assumption of proportionality between the rate coefficient $k(T)$ and the radial growth rate

G. The temperature dependence of the growth rate *G*(*T*) given by the Hoffman–Lauritzen theory describes crystallization as measured microscopically, while thermoanalytical methods measure the overall crystallization rate. Therefore, this transformation assumes that the overall crystallization rate find its origin in microscopic transformations of matter, i.e. there is a direct proportionality between microscopic transformations and overall heat flow released as measured by DSC. Another argument for the physical soundness of using the expression of *G*(*T*) is that it includes a term linked with diffusion and a term in relation with nucleation, which is not the case with the Arrhenius law. The Arrhenius law does not contain a diffusion term and is thus unappropriated to describe anti-arrhenian behaviors, such as crystallization from the melt. Therefore, Equation (7) can be written as Equation (8), where G_0' is the pre-exponential term ($G_0' = K \cdot G_0$).

$$\frac{\mathrm{d}\alpha}{\mathrm{d}t} = G_0^{'} \exp\left(\frac{-U^*}{R(T-T_\infty)}\right) \exp\left(\frac{-K_g}{T\Delta T f}\right) f(\alpha) \qquad (9)$$

The function *f*(*α*) can take various mathematical forms. Differentiating the JMAEK equation (1) to time and substituting the rate constant $k(T)^{1/n}$ by $K \cdot G(T)$ yields a form of Equation (9) in which *f*(*α*) is described as Equaton (10). This approach is mathematically similar to Chapter 3, where the growth rate *G* is assumed to be proportional to the reciprocal half time in the Avrami equation, i.e. $G \propto (K/\ln 2)^{1/n}$.

$$f(\alpha) = n\,(1-\alpha)\ \left[-\ln(1-\alpha)\right]^{(1-1/n)} \qquad (10)$$

An alternative to the derived Avrami equation is the general Sestak-Berggren model SB(*m*,*n*,*p*)[19] described in Equation (11), which is mathematically similar to Equation (10) but has additional kinetic exponents *m*, *n* and *p* that can be used as fitting parameters.

$$f(\alpha) = \alpha^m\,(1-\alpha)^n\,\left[-\ln(1-\alpha)\right]^p \qquad (11)$$

In addition, the reduced Sestak-Berggren model SB(m,n) displayed in Equation (12) is a simpler version with fewer parameters, i.e. only kinetic exponents m and n.

$$f(\alpha) = \alpha^m \, (1-\alpha)^n \tag{12}$$

Because crystallization is a highly exothermic process the relative extent of crystallization or relative degree of crystallinity at time t, α_t, can be estimated by DSC as per Equation (13).

$$\alpha_t = \frac{\int_0^t (\mathrm{d}H/\mathrm{d}t)\ \mathrm{d}t}{\int_0^\infty (\mathrm{d}H/\mathrm{d}t)\ \mathrm{d}t} = \frac{\alpha_{c(t)}}{\alpha_{c(\infty)}} \tag{13}$$

where $\alpha_{c(t)}$ and $\alpha_{c(\infty)}$ are the relative extent of crystallization at time t and at the end of crystallization (time $t \rightarrow \infty$), respectively. Compared to these data, simulations were conducted to describe the crystallization rate $(\mathrm{d}\alpha/\mathrm{d}t)_{\mathrm{calc}}$ using Equation (9) with Equations (10), (11) and (12). The mean square difference between the calculated crystallization rate $(\mathrm{d}\alpha/\mathrm{d}t)_{\mathrm{calc},i}$ and the measured crystallization rate $(\mathrm{d}\alpha/\mathrm{d}t)_{\mathrm{measured},i}$ is minimized for each temperature T_{i} and relative extent of crystallization α_{i}. This minimization procedure allows for the evaluation of the kinetic exponents m, n and p of Equations (10), (11) or (12) and of the pre-exponential factor $G_0^{'}$ of Equation (9). The values of the mean square errors $[(\mathrm{d}\alpha/\mathrm{d}t)_{\mathrm{measured},i} - (\mathrm{d}\alpha/\mathrm{d}t)_{\mathrm{measured},i}]^2$ were called *MSE* (which is the mean *MSE* over the various rates when several rates were used) and were minimized using Excel© software 2010. The Fisher test was conducted to show the statistical difference between the fits. The Fisher statistic parameter between two models was calculated as $F_{\mathrm{calc}} = MSE_{(1)}/MSE_{(2)}$ with the highest *MSE* in the denominator in order to get $F_{\mathrm{calc}} > 1$. The degree of freedom is equal to the number of data points minus the number of parameters. For each model, the degree of freedom is > 1000. It gives a critical F value (F_{crit}) of 1.05 for a confidence interval of 99 %. If $F_{\mathrm{calc}} > F_{\mathrm{crit}}$ then the two models are statistically different and vice versa.

In a second step, a numerical integration of the measured and calculated crystallization rates was performed using a software already described where additional procedures were specifically added for this work.[20,21] Thus, measured and calculated relative extent of crystallization were plotted to evaluate the accuracy of the fits more qualitatively. An additional approach was applied that was proposed by Vyazovkin and Sbirrazzuoli for evaluating the Hoffman–Lauritzen parameters from non-isothermal DSC data.[22,23,24] This approach is based on the isoconversional principle in Equation (14) applied to Equation (8), which leads to Equation (15).

$$\left[\frac{\partial \ln\left(\frac{\partial \alpha}{\partial t}\right)}{\partial T^{-1}}\right]_{\alpha} = -\frac{E_{\alpha}}{R} \tag{14}$$

$$E_{\alpha}(T) = U^{*}\frac{T^{2}}{(T-T_{\infty})^{2}} + K_{g}R\frac{\left(T_{m}^{0}\right)^{2} - T^{2} - T_{m}^{0}T}{(T_{m}^{0}-T)^{2}T} \tag{15}$$

Equation (15) expresses the temperature dependence of the effective activation energy of the crystal growth rate, $E_{\alpha}(T)$, which can be obtained by an advanced isoconversional (AIC) method.[25,26] In this work, the $E_{\alpha}(T)$ dependence has been derived from the E_{α} vs α dependence obtained by an AIC method by replacing α with the average temperature corresponding to the relative extent of crystallization at different temperature programs.

3 EVALUATION OF KINETIC MODELS

The reference growth rate $G_0^{'}$ of Equation (9) and kinetic parameter n of the JMAEK derivative Equation (10) were fit to the DSC data using the parameters U^* and K_g reported in Chapter 3 as well as those previously obtained by Codou et al.[1], i.e. U^* = 10200 J.mol^{-1} and 6017 J.mol^{-1} respectively and K_g = 2.8·10^5 K² for both cases. The fits were realized for each

cooling rate for melt crystallization and for each heating rate for glass crystallization. Thus, a set of kinetic parameters was obtained for each rate, as shown in Tables 1 and 2.

Table 1 – Kinetic parameters of melt and glass crystallization using Eq. (9) with U^* = 10200 J mol $^{-1}$ and K_g = 2.8 10^5 K^2 as reported in Chapter 3 and Eq. (10).

β [a] / K min^{-1}	$G_0^{'}$ / s^{-1}	n	MSE [b]	F_{calc} [c]
- 0.5	9.86 10^4	1.963	2.206 10^{-09}	1.62
- 1.0	1.22 10^5	2.287	9.185 10^{-10}	3.34
- 1.5	1.23 10^5	2.931	3.381 10^{-10}	4.92
0.5	1.26 10^6	1.423	5.641 10^{-09}	-
1.0	8.02 10^5	1.454	1.846 10^{-08}	-
1.5	5.05 10^5	1.445	2.072 10^{-08}	-

[a] Heating/cooling rate, [b] $\Sigma[(d\alpha/dt)_{measured,i} - (d\alpha/dt)_{computed,i}]^2/n$, [c] *vs* Table 2.

Table 2 – Kinetic parameters of melt crystallization using Eq. (9) with U^* = 6017 J mol $^{-1}$ and K_g = 2.8 10^5 K^2 as reported by Codou et al. [1] and Eq. (10).

β [a] / K min^{-1}	$G_0^{'}$ / s^{-1}	n	MSE [b]	F_{calc} [c]
- 0.5	2.52 10^3	1.713	3.571 10^{-09}	-
- 1.0	2.78 10^3	1.814	3.067 10^{-09}	-
- 1.5	2.67 10^3	1.986	1.662 10^{-09}	-
0.5	3.12 10^3	2.063	3.458 10^{-09}	1.63
1.0	3.28 10^3	2.118	1.159 10^{-08}	1.59
1.5	2.77 10^3	2.276	1.237 10^{-08}	1.68

[a] Heating/cooling rate, [b] $\Sigma[(d\alpha/dt)_{measured,i} - (d\alpha/dt)_{computed,i}]^2/n$, [c] *vs* Table 1.

In Table 1, the values for $G_0^{'}$ when cooling from the melt are close to the range of 4 10^4 $^{s-1}$ to 8 10^4 s^{-1} reported in Chapter 3, n is within the range of 2-4 typical for the JMAEK equation and the *MSE* is fairly low. For crystallization from the glass however, the reference growth rate obtained is 5 to 10 times higher, the value of n is low and the *MSE* is increased. Table 2 gives overall more similar values for $G_0^{'}$ and n for both the glass and melt, but the *MSE* values are higher than Table 1 when coming from the melt and lower from the glass. The Fisher test

values for F_{calc} indicate that using U^* of 10200 J mol^{-1} gives a significantly better fit when cooling while U^* = 6017 J mol^{-1} gives better fit when heating. The better quality of the fit of Table 1 upon fast cooling from the melt can be explained by those conditions being the most similar to the isothermal conditions in Chapter 3, while slower cooling from the melt increases the crystallization time at higher temperatures where Chapter 3 indicates that kinetics change since *n* values are becoming substantially higher. The Hoffman-Lauritzen parameters by Codou et al. were however derived as a single fit for melt and glass crystallization, therefore they can be expected to yield similar rate dependence parameters for both heating and cooling and provide a better fit for glass crystallization. Both descriptions however show a poorer fit when heating from the glass than from the melt, which is visualized in Figure 1.

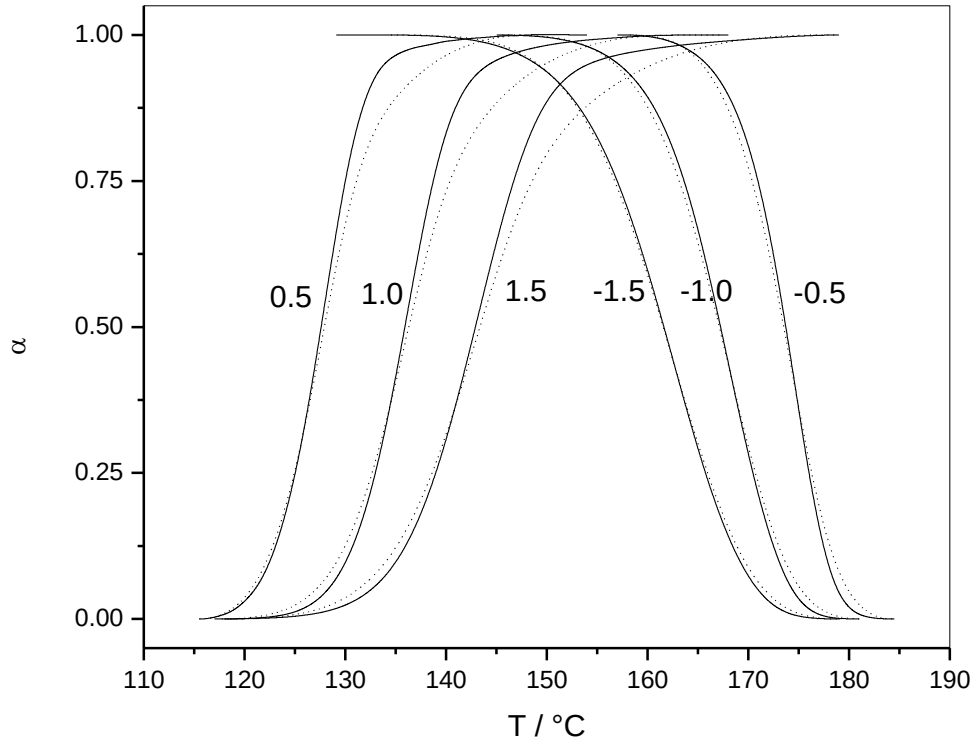

Figure 1 – Relative extent of crystallinity (α) vs. temperature (T) for melt and glass crystallization of PEF at 0.5, 1.0 and 1.5 K.min^{-1}. Measured data (solid lines) *vs* simulated data using kinetic parameters of Tables 1 (dotted lines).

Figure 1 indicates that even with U^* = 6017 J mol^{-1} a satisfactory fit from the melt can be obtained while in particular at the end of the glass crystallization (for α > 0.75) a high

deviation between experimental and calculated data can be observed. This deviation can be explained in term of a deviation from the classical Hoffman–Lauritzen theory at the end of the glass crystallization and is in good agreement with the deviation between theoretical model and experimental data expected for $0.60 < \alpha < 0.85$ ($137 < T < 141$ °C), as reflected on the activation energy dependence with temperature[1]. Note that a peak in this temperature range (around 140°C) has been observed in Chapter 3 as well as by Stoclet et al. and Papageorgiou et al.[27,28] which was attributed to the melting of secondary crystals that consist in fact in small and imperfects crystals formed during isothermal crystallization. Other mechanisms that may play a role are recrystallization processes or lamellar thickening. This result confirms the conclusions of Codou et al.[1] that have highlighted a faster crystallization rate at the end of the glass crystallization. This phenomenon has been explained by a more pronounced role of other mechanisms not considered in HL theory.

One approach to approve the fit is taken by using the Sestak-Berggren models. Initially the reduced model in Equation (12) was considered since it only adds a single kinetic parameter, while Equation (13) adds two additional parameters. An overview is presented in Table 3 and 4, again with U* of 10200 J mol^{-1} and 6017 J mol^{-1} respectively.

Table 3 – Kinetic parameters of melt and glass crystallization using Eq. (9) with U^* = 10200 J mol $^{-1}$ and K_g = 2.8 10^5 K^2 as reported in Chapter 3 and Eq. (12).

β [a] / K min^{-1}	G_0' / s^{-1}	m	n	MSE [b]	F_{calc} [c]	F_{calc} [d]
- 0.5	2.870 10^5	0.668	1.061	2.383 10^{-10}	9.26	1.08
- 1.0	3.409 10^5	0.655	0.891	1.285 10^{-10}	7.15	1.43
- 1.5	3.761 10^5	0.671	0.738	1.355 10^{-10}	2.50	1.40
0.5	3.377 10^6	0.652	1.223	8.664 10^{-10}	6.51	-
1.0	2.635 10^6	0.759	1.322	1.584 10^{-9}	11.65	-
1.5	1.543 10^6	0.721	1.292	2.328 10^{-9}	8.90	-

[a] Heating/cooling rate, [b] $\Sigma[(d\alpha/dt)_{measured,i} - (d\alpha/dt)_{computed,i}]^2/n$, [c] *vs* Table 1, [d]vs Table 4.

Table 4 – Kinetic parameters of melt crystallization using Eq. (9) with U^* = 6017 J mol $^{-1}$ and K_g = 2.8 10^5 K^2 as reported by Codou et al. [1] and Eq. (12).

β [a] / K min^{-1}	G_0' / s^{-1}	m	n	MSE [b]	F_{calc} [c]	F_{calc} [d]
- 0.5	7.073 10^3	0.637	1.160	2.580 10^{-10}	13.84	-
- 1.0	7.208 10^3	0.615	1.046	1.836 10^{-10}	16.70	-
- 1.5	6.618 10^3	0.598	0.935	1.892 10^{-10}	8.78	-
0.5	1.102 10^4	0.812	1.086	7.911 10^{-10}	4.37	1.10
1.0	1.390 10^4	0.904	1.175	1.336 10^{-09}	8.68	1.19
1.5	1.193 10^4	0.909	1.134	1.957 10^{-09}	6.32	1.19

[a] Heating/cooling rate, [b] $\Sigma[(d\alpha/dt)_{measured,i} - (d\alpha/dt)_{computed,i}]^2/n$, [c] *vs* Table 2, [d]vs Table 3.

Tables 3 shows reference growth rates G_0' of an order of magnitude higher when coming from the glass, while G_0' for the glass in Table 4 is less than a factor 2 higher than in the melt. The m values of Table 3 have an average value of 0.69 ± 0.04 and show less variance than Table 4 with 1.09 ± 0.24. Table 4 shows an opposite trend, with more varying m values at 0.75 ± 0.15 and more similar n values at 1.09 ± 0.09. It is worth noting that in both cases n values have a similar average and trend increasing trend with decreasing cooling rate. F_{calc} shows that the fits have greatly improved for both cases, and that use of different values of U^* now has less influence of the quality of the fit. Overall however, the higher U^* = 10200 J mol^{-1} still fits better when cooling from the melt while the lower U^* = 6017 J mol^{-1} fits better when heating from the glass and consequently has a lower average *MSE*, as the *MSE* from the glass is in both cases higher than from the melt. The improvement in the fit from the glass can however be observed in Figure 2, which shows the fit using the values of Table 4.

To simplify the relation to describe both glass and melt crystallization, the computations were also done using Equation (12) for all the cooling rates of the melt crystallization and all the heating rates of glass crystallization simultaneously. Thus, a single set of kinetic exponents m and n was obtained for melt crystallization, and a single set of kinetic exponents was obtained for glass crystallization, which are presented in Table 5.

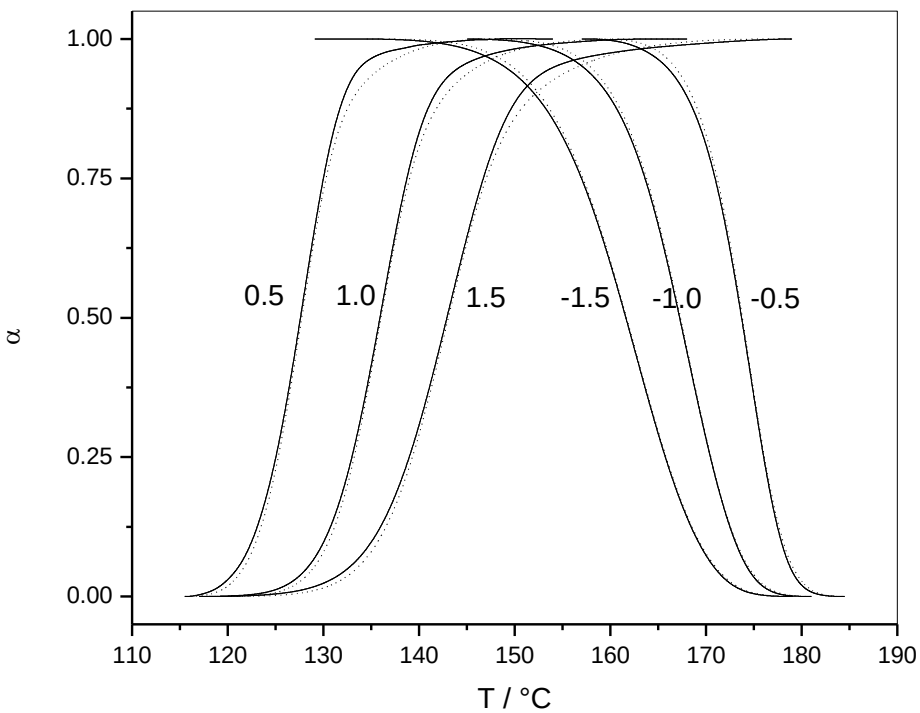

Figure 2 – Relative extent of crystallinity (α) vs. temperature (T) for melt and glass crystallization of PEF at 0.5, 1.0 and 1.5 K.min-1. Measured data (solid lines) *vs* simulated data using kinetic parameters of Table 4 (dotted lines).

The *MSE* of 1.8 10^{-9} and 1.9 10^{-9} are comparable, and higher than the average value of Table 3 and 4 but still lower than using the JMAEK equation as per Table 1 and 2. G_0' is still higher from the glass than from the melt, close to 11000 s^{-1} and 8200 s^{-1} respectively.

Table 5 – Kinetic parameters of melt crystallization using Eq. (9) with U^* = 6017 J mol $^{-1}$ and K_g = 2.8 10^5 K^2 and Eq. (12) with a single value for *m* and *n* for cooling and for heating.

β [a] / K min^{-1}	G_0' / s^{-1}	*m*	*n*	*MSE* [b]
- 0.5	7448	0.715	1.137	1.806 10^{-09}
- 1.0	8509			
- 1.5	8679			
0.5	10729	0.808	1.069	1.929 10^{-09}
1.0	11629			
1.5	10279			

[a] Heating/cooling rate, [b] $\Sigma[(d\alpha/dt)_{measured,i} - (d\alpha/dt)_{computed,i}]^2/n$.

In Table 6, the same kinetic model was used but melt and glass crystallization data were fit with a single set of kinetic exponents. This yielded similar G_0' values to Table 5 for melt and glass crystallization respectively. The *MSE* around 2.73 10^{-9} indicates that the fit is again slightly poorer than Table 5 as can be expected when using less free parameters, but is still improved over the JMAEK approach. The fit in Table 6 is shown in Figure 3.

Table 6 – Kinetic parameters of melt crystallization using Eq. (9) with U^* = 6017 J mol $^{-1}$ and K_g = 2.8 10^5 K^2 and Eq. (12) with a single value for *m* and *n*.

β [a] / K min^{-1}	G_0' / s^{-1}	*m*	*n*	*MSE* [b]
- 0.5	7448	0.765	1.094	2.734 10^{-09}
- 1.0	8509			
- 1.5	8679			
0.5	10657			
1.0	11535			
1.5	10164			

[a] Heating/cooling rate, [b] $\Sigma[(d\alpha/dt)_{measured,i} - (d\alpha/dt)_{computed,i}]^2/n$.

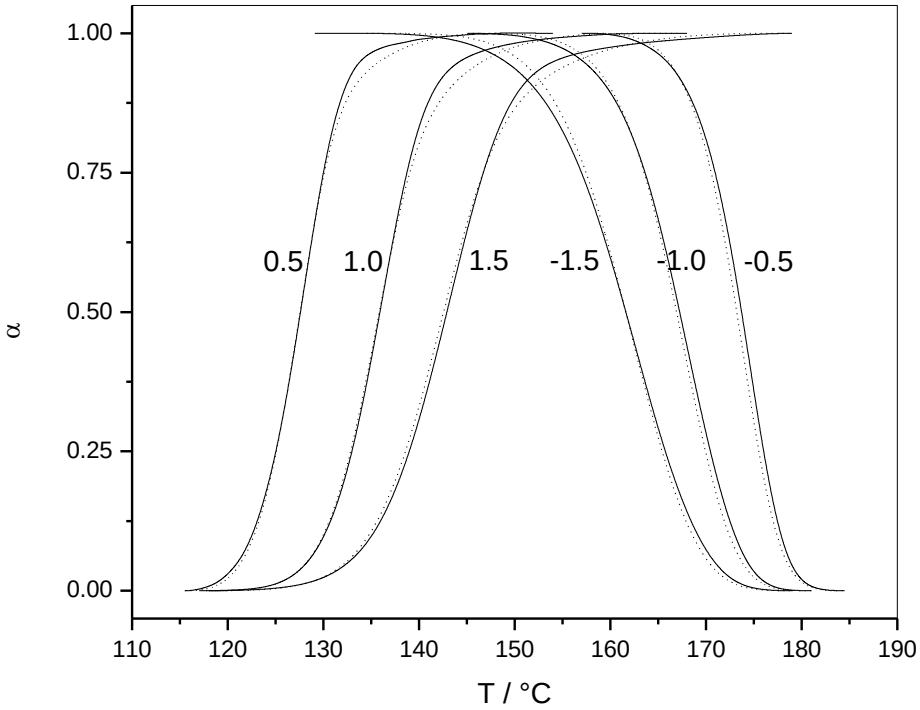

Figure 3 – Relative extent of crystallinity (α) vs. temperature (T) for melt and glass crystallization of PEF at 0.5, 1.0 and 1.5 K.min-1. Measured data (solid lines) *vs* simulated data using kinetic parameters of Table 6 (dotted lines).

As is shown in Figure 3, the fits obtained using a single set of parameters (U^* and K_g) for both melt and glass crystallization data and a same set of kinetic exponents (m and n) still lead to a good fit of the data. Comparison of Figures 1 and 2 shows that the quality of the fit is close when a single set of kinetic exponent is used for both melt and glass crystallization data, while it was shown that crystallization from the melt and from the glassy state show different dynamics.[1] Thus, obtaining an accurate fit is not the proof of the physical meaning of the model used. Nevertheless, the use of parameters of Table 6 is of interest for modelling purposes. The main difference at the end of the glass crystallization (for $\alpha > 0.75$) persists, where the crystallization rate is underestimated by the theoretical model.

In Table 7, the same computations were done using an extended kinetic SB(m,n,p) model (Equation 11) and melt and glass crystallization data were fitted with a single set of parameters. The values for G_0' are comparable to the SB(m,n) model. Nevertheless, the accuracy of the fit is not significantly increased ($F_{calc} = 1.02 < F_{crit}$ compared to Table 6) when an additional kinetic exponent is added. Furthermore, addition of this new parameter does not correct the deviation observed between experimental and calculated data at the end of the glass crystallization (for α >0.75).

Table 7 – Kinetic parameters of melt crystallization using Eq. (9) with $U^* = 6017$ J mol $^{-1}$ and $K_g = 2.8\ 10^5$ K^2 and Eq. (11) with a single value for m, n and p.

β [a] / K min^{-1}	G_0' / s^{-1}	m	n	p	MSE [b]
- 0.5	7373	0.379	1.255	0.389	2.679 10^{-09}
- 1.0	8422				
- 1.5	8590				
0.5	10566				
1.0	11444				
1.5	10080				

[a] Heating/cooling rate, [b] $\Sigma[(d\alpha/dt)_{measured,i} - (d\alpha/dt)_{computed,i}]^2/n$.

With the exception of Table 2, in all fits $G_0^{'}$ still shows considerable variation while Equation (15) was obtained by stating that G_0 values does not vary with temperature and thus, with heating or cooling rates. Indeed, $G_0^{'}$ is equal to the product $K.G_0$ in which G_0 is the true pre-exponential factor and K is a parameter that takes accounts for the magnitude of the crystallization peak and is related to the final value of crystallization enthalpy ($\Delta h/Q$). If variations in the final crystallization enthalpies are taken into account, it is seen that the variation of G_0 within the three heating or the three cooling rates is not significant. However, the higher G_0 values for glass crystallization remain, which can be explained by the experimental observation (supporting data of[1]) that the nucleation density is higher when the material is crystallized in the glassy state.

As Table 2 is the only exception, for comparison, fits were performed simultaneously with a single value of n for the JMAEK equation with $U^* = 6017$ J mol^{-1}. When all the cooling and heating experiments were fitted simultaneously, the accuracy of the fit went down as expected and we obtained a *MSE* around 1.33 10^{-8} which is statistically much higher than the value reported in Table 6 (2.734 10^{-9}) according to the Fisher test ($F_{calc} = 4.86 > F_{crit}$).

The discrepancy between experimental data and the Avrami model cannot be explained by the sole decrease of the flexibility of the model, because results of Table 7, compared to Table 6, show that increasing the model flexibility does not systematically solve the problem of the difference between measurements and theoretical data that appears at the end of the glass crystallization. One reason the JMAEK equation leads to a lower accuracy between experimental and simulated data, especially for high extent of conversion, is that it was derived for primary crystallization. Indeed, Avrami plots of ln[-ln(1-α)] vs. ln t derived from Eq.(1) for each heating/cooling rate are not linear (results not presented here) and contain at least 3 or 4 different regions.

3.1 MODELING ADDITIONAL CRYSTALLIZATION PROCESSES

To account for additional crystallization processes occurring at high relative extent of crystallinity values (i.e. $\alpha > 0.75$ for data of Figure 1), Equation (16) can be used to obtain a corrected crystallization rate $(\mathrm{d}\alpha/\mathrm{d}t)_{\mathrm{corr}}$, where $(\mathrm{d}\alpha/\mathrm{d}t)_{\mathrm{calc}}$ is the crystallization rate calculated according to Equation (9) and $h(\alpha)$ is a correction function that takes into account additional crystallization processes not included by the various forms of $f(\alpha)$.

$$\left(\frac{\mathrm{d}\alpha}{\mathrm{d}t}\right)_{corr} = \left(\frac{\mathrm{d}\alpha}{\mathrm{d}t}\right)_{calc} h(\alpha) \qquad (16)$$

Thus, $h(\alpha)$ is a function that should consider lamellar thickening, secondary crystallization or any additional crystallization processes occurring at α values higher than α_{C} and that were not considered in the derivation of the various forms of Equation (9). We propose here that $h(\alpha)$ takes the form $h(\alpha) = \exp[C(\alpha - \alpha_{\mathrm{C}})]$, where C is a constant and α_{C} is the relative extent of crystallinity where additional crystallization processes starts to become significant. Then, Equation (16) based on Equation (9) and the reduced SB model in Equation (11) can be rewritten as Equation (17).

$$\left(\frac{\mathrm{d}\alpha}{\mathrm{d}t}\right)_{corr} = G(T)\,\alpha^{m}(1-\alpha)^{n}\exp\left[C(\alpha-\alpha_{C})\right] \qquad (17)$$

When this correction factor is applied to glass crystallization data of PEF at 1.0 K.min^{-1} (data of Table 2), the resulting parameters were obtained: $G_0^{'}$ = 16471 s^{-1}, m = 0.63, n = 1.48, α_{C} = 0.61, C = 1.44, MSE = 4.03 10^{-10}. The value estimated for α_{C} of about 61% corresponds to the extent of crystallization where additional crystallization processes cannot be neglected. This value is in good agreement with the deviation between theoretical model and experimental data expected for $0.60 < \alpha < 0.85$.[1] Thus, introducing this correction factor increases the accuracy of the fit because additional crystallization processes are taken into account in the

new equation proposed, which can be seen in the decrease of *MSE* from 1.3 10^{-09} (without correction) to 4.0 10^{-10} (with correction). This result is confirmed by the analysis of Figure 6 that represents the comparison between experimental and simulated crystallization rates vs. temperature (*T*) for glass crystallization of PEF at 1.0 K.min^{-1}. It is clearly seen that the deviation between experimental and computed crystallization rates is highly reduced. It is especially the case at the end of the glass crystallization where the simulated curves are quasi superimposed with the experimental curves when the corrected Hoffman-Lauritzen SB(*m*,*n*) model of Equation (17) is used. This confirms our hypothesis that Equation (17) is suitable to take into account for additional crystallization processes occurring at higher relative extent of crystallinity. In contrast, application of this correction to an overall fit of the Avrami equation (12) does not allow to accurately describe the end of the glass crystallization, as also shown in Figure 4. The values obtained in this case are $G_0^{'}$ = 2529 s^{-1}, n = 4.62, α_C = 0.13, C = -1.04, *MSE* = 9.13 10^{-9}.

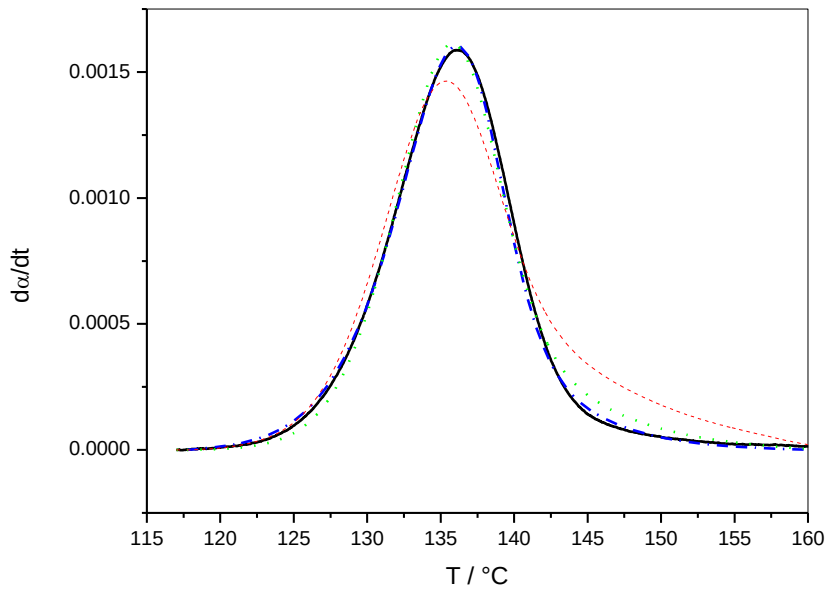

Figure 4 – Experimental and simulated crystallization rates vs. temperature (*T*) for glass crystallization of PEF at 1.0 K.min^{-1}. Measured data (solid line), simulated data using data of Table 2 (Eqs. (9) and (11), Hoffman-Lauritzen SB(*m*,*n*), dotted line), simulated data using Eq. (17) (corrected Hoffman-Lauritzen SB(*m*,*n*), dash-dotted line), simulated data using a corrected version of Eq. (12) (dashed line).

3.2 COMPARISON TO THE OZAWA METHOD

Fits using the Ozawa method for the determination of the Avrami exponent were realized according to Equations (18), (19) and (20), where β is the linear heating or cooling rate.[29]

$$\ln\{-\ln[1-\alpha(T)]\} = \ln[\gamma(T)] - n\ln\beta \qquad (18)$$

$$\gamma(T) = nA\int_{To}^{T}\left[\exp(-E/RT)(T-To)^{n-1}\right]dT \qquad (19)$$

$$\alpha = 1-\exp\left[-\frac{\gamma(T)}{\beta^n}\right] \qquad (20)$$

The Avrami exponent n and ln $\gamma(T)$ values used were those of Codou et al.[1]. These values were fitted with temperature (in Kelvin) using a third order polynomial function as $n(T)$ and ln $\gamma(T)$ presented in Table 8. Two sets of $n(T)$ and ln $\gamma(T)$ were used to fit separately glass and melt data. The resulting fits using these parameters obtained from Ozawa's method are presented in Figure 4.

Table 8 – Fit of Ozawa's parameters vs. temperature (in Kelvin) for glass and melt crystallization

Ozawa's parameters	a	b	c	d	r^2
$n(T)$ glass[a]	3.60 10^{-4}	-0.444	182	-24910	0.999
$\gamma(T)$ glass[b]	-1.37 10^{-3}	1.685	- 689	93716	0.999
$n(T)$ melt[a]	1.68 10^{-4}	-0.213	90	-12669	1.000
$\gamma(T)$ melt[b]	-1.38 10^{-3}	1.766	- 756	107943	1.000

[a] $n(T) = aT^3 + bT^2 + cT + d$, [b] $\gamma(T) = aT^3 + bT^2 + cT + d$

Codou et al. have shown that the non-isothermal crystallization of PEF is a complex process that involves several steps.[1] Because the Avrami equation applies for a single-step process, it is expected that the use of Ozawa method will lead to a large discrepancy between simulated

and experimental data. Figure 5 shows that this method is less accurate than the method derived from Hoffman–Lauritzen equation, except for the lowest rate and at low conversions. Despite its lower accuracy the method does not completely fail in simulating the experimental data. The single-step approximation used is compensated by the use of a temperature dependent Avrami exponent, $n(T)$, although this can be considered more as a fitting parameter than to a real kinetic exponent with a physical meaning. The discrepancies observed at high rates and high conversions are explained by the fact that the method requires the relative degree of crystallinity $\alpha(T)$ to be evaluated for a same temperature T at i heating/cooling rates β. For example, for the melt crystallization at T =173°C α = 1.8% when β = 1.5 K min^{-1} and at T =160°C α = 99.8% when β = 0.5 K min^{-1}. Thus, very low and high values of α are used in the computations and it is known that these values, corresponding to the beginning and to the end of the thermal process, are associated to large experimental errors.

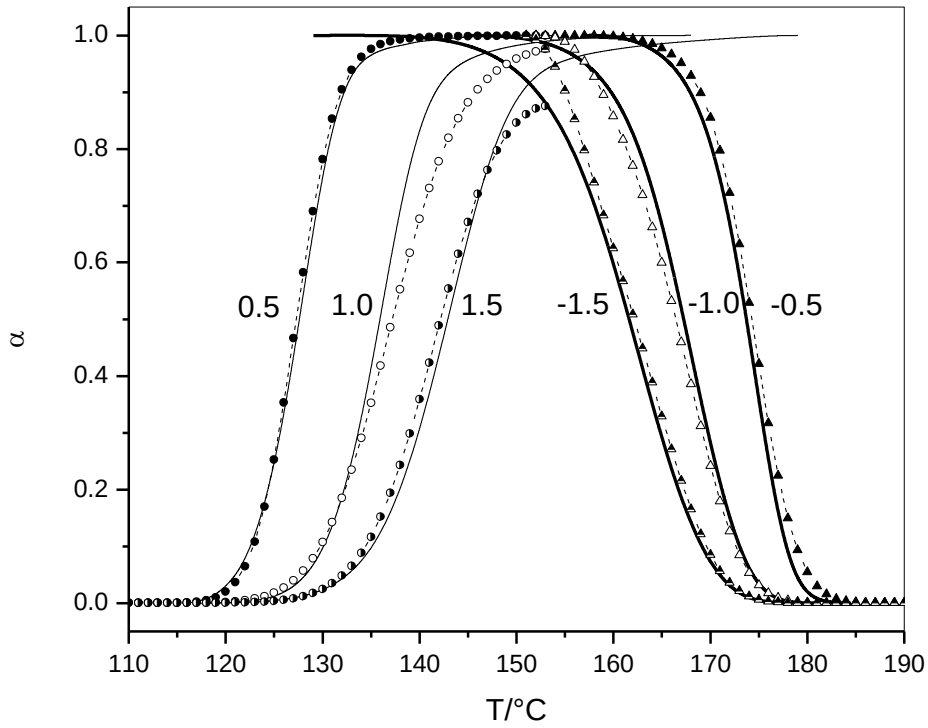

Figure 5 – Relative extent of crystallinity (α) vs. temperature (T) for melt (bold lines) and glass (thin lines) crystallization of PEF at 0.5, 1.0 and 1.5 K.min^{-1}. The heating/cooling rates are indicated by the lines. Measured data (line), simulated data using Ozawa method (Eqs. 18-20), circles: glass crystallization, triangles : melt crystallization.

3.3 THE ADVANCED MODEL-FREE ISOCONVERSIONAL METHOD

The use of a model-free method could be an interesting alternative because it is free of approximations on the crystallization model.[14,24,26,20,21] Following integration of Equation (6), one can write Equation (21) for a given extent of crystallinity α and for a set of k experiments performed under different temperature programs $i = 1 .. k$.

$$g_i(\alpha) \equiv \int_0^{\alpha} \frac{\mathrm{d}\alpha}{f(\alpha)} = A \int_0^{t_\alpha} \exp\left[-\frac{E}{RT_i(t_\alpha)}\right] \mathrm{d}t = A\, J\left[E\ , T_i(t_\alpha)\right] \qquad (21)$$

If J is evaluated over small intervals to take into account for the variation of E this gives Equation (22).

$$g_i(\alpha) = A_\alpha \int_{t_{\alpha-\Delta\alpha}}^{t_\alpha} \exp\left[\frac{-E_\alpha}{RT_i(t)}\right] dt \qquad (22)$$

On the basis of the isoconversional assumption, the crystallization mechanism is the same for a same value of the extent of crystallinity α, yielding Equation (24) through Equation (23).

$$g_1(\alpha) = g_2(\alpha) = \ldots = g_k(\alpha) \qquad (23)$$

$$\int_{t_{\alpha-\Delta\alpha}}^{t_\alpha} \exp\left[\frac{-E_\alpha}{RT_1(t)}\right] dt = \int_{t_{\alpha-\Delta\alpha}}^{t_\alpha} \exp\left[\frac{-E_\alpha}{RT_2(t)}\right] dt = \ldots = \int_{t_{\alpha-\Delta\alpha}}^{t_\alpha} \exp\left[\frac{-E_\alpha}{RT_n(t)}\right] dt \qquad (24)$$

Thus, Equation (24) allows for the evaluation of t_α and T_α for each α, by using the sole E_α-dependence, i.e. without any assumption on the mathematical function that describes the crystallization mechanism. The parameters for computations were dt = 0.01s and the step on α for E_α-dependence was 0.01 with α varying from 0.01 to 0.99.

The resulting data are presented in Figure 6. As seen in this Figure, the quality of the fit is very good and is higher than the one obtained with any other methods, i.e. SB(m,n), SB(m,n,p) or JMAEK. This confirms the hypothesis that the model-free method based on the

dependence of the activation energy at agiven extent of conversion gives a more general description of the crystallization process, including nucleation, growth but also other phenomena that are not taken into account in model-fitting methods such as Avrami and Hoffman–Lauritzen theories. These additional phenomena can be related to secondary crystallization or lamellar thickening processes in the case of glass crystallization of PEF.

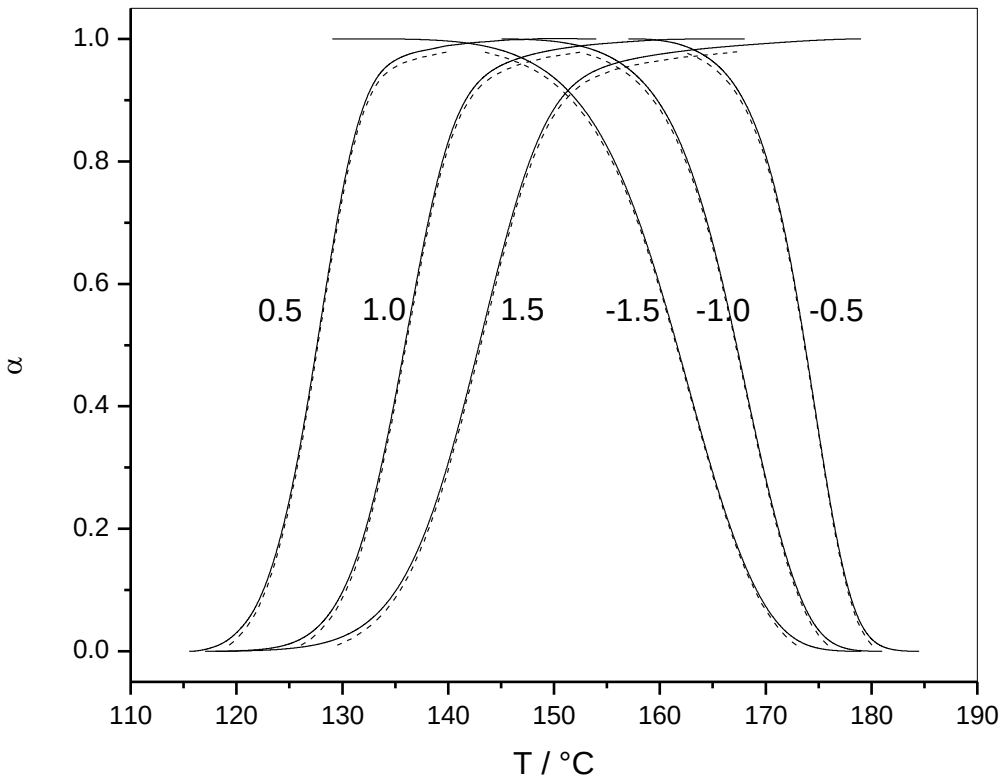

Figure 6 – Relative extent of crystallinity (α) vs. temperature (T) for melt and glass crystallization of PEF at 0.5, 1.0 and 1.5 K.min^{-1}. The heating/cooling rates are indicated by the lines. Measured data (line), simulated data using advanced model-free non-linear method (Eq. 24) (dot).

4 SIMULATION OF HEAT FLOW CURVES AND ACTIVATION ENERGIES

Heat flow rate DSC curves can be plotted according to the equations and to the parameters previously evaluated. Experimental and simulated crystallization heat flow curves vs. temperature (T) for melt and glass crystallization are presented in Figure 7. Simulated data were calculated from (i) the Hoffman–Lauritzen equation (Equations 9 and 11) with parameters of Table 1, 2 and 5 and (ii) from the advanced non-linear model-free

isoconversional method. Note that in the case of HL equation with data of Tables 1-2, the number of parameters is very high and the accuracy is not greatly increased. The simulations of the six (d*H*/d*t*)-*T* heating and cooling curves require 20 parameters, i.e. one set of (G_0, *m*, *n*) for each rate plus the two values of U^* and K_g. In the case of the advanced non-linear model-free isoconversional method, derivative data of Figure 5 were used (and crystallization enthalpy values). Both data lead to an accurate fit of the experimental curves, while it can be noticed that the data of model-free isoconversional method are quite perfectly superimposed to them. In order to distinguish these values from experimental ones we have suppressed many points and used crosses in the graph. Note that crystallization rate curves can be obtained by the simple transformation $d\alpha/dt = (dH/dt)(1/Q)$.

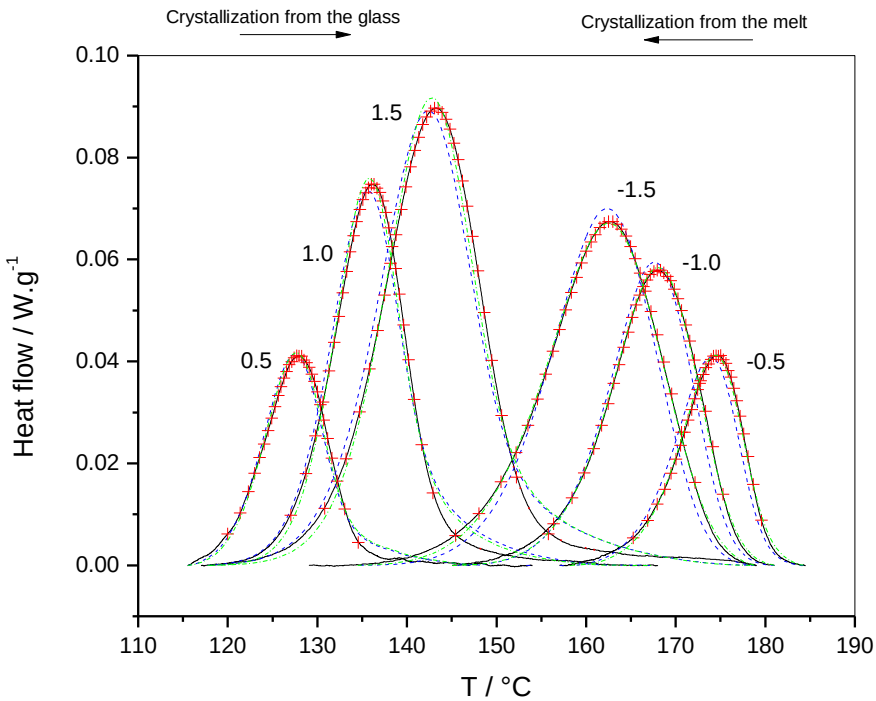

Figure 7 – Experimental (black line) and simulated crystallization heat flow curves vs. temperature (*T*) for glass and melt crystallization of PEF using the Hoffman–Lauritzen and SB(*m*,*n*) model in Eq. (9) and (11) with parameters of Table 5 (blue dashed line) and Tables 1-2 (green dashed-dotted line) and using the advanced non-linear model-free isoconversional method (red crosses, selected data points shown). The heating/cooling rates (in $K.min^{-1}$) are indicated by the curves.

These data have then been used to compute the effective activation energy dependence with temperature and conversion, as presented in Figure 8. The insert of Figure 8, confirms the

experimental finding[1,22,23,24,30,31] that application of an isoconversional method to crystallization data following a HL mechanism, should lead to positive decreasing values for crystallization from the glass and to negative increasing values for crystallization from the melt. Then, E_α-dependence vs temperature curves confirm that Hoffman–Lauritzen equation does not describe completely the end of the glass crystallization mechanism of PEF because a deviation is observed at around 141°C (414 K). On the other hand, the E_α-dependence obtained with the model-free isoconversional method are very close to experimental data. These discrepancies are attributable to additional mechanisms that are not taken into account in the HL theory and confirm that obtaining an accurate fit is not necessarily a proof of the validity of the proposed mechanism and that complementary analysis of the E_α-dependence could be very informative for mechanistic interpretations.

The data of Figure 4 (α-T data) have then been used to compute the E_α-dependence from data simulated with Ozawa method and the results are presented in Figure 8. Despite some discrepancies with experimental dependence, it is interesting to notice that positive decreasing values are obtained for the glass crystallization and negative increasing values are obtained for melt crystallization until 440 K, in agreement with the HL theory. This result is in contradiction with the Avrami equation. Indeed, application of the isoconversional principle to Equation (12), leads to Equation (25) and (26).

$$\frac{\partial \ln(\mathrm{d}\alpha/\mathrm{d}t)}{\partial T^{-1}} = \frac{\partial \ln\left[k^{1/n}\ f(\alpha)\right]}{\partial T^{-1}} = -\frac{E_\alpha}{R} \tag{25}$$

$$E_\alpha = E/n \tag{26}$$

From Equation (26) it is clear that E_α should be constant and positive, and therefore cannot be in agreement with the HL theory. In fact, the observed E_α variations are only possible because n has been replaced by a fitting parameter function of temperature, $n(T)$.

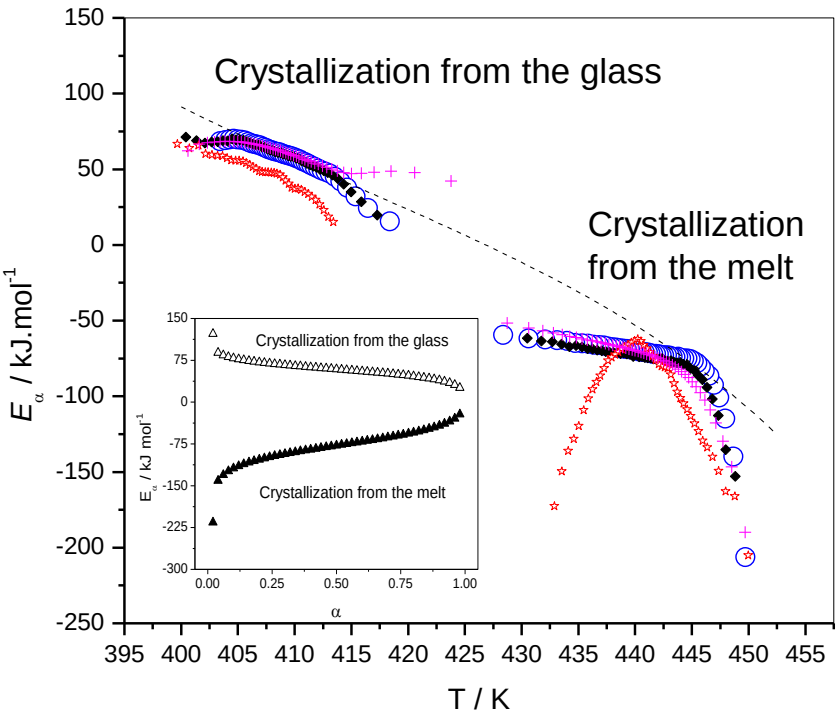

Figure 5 – Effective activation energy (E_α) dependence on temperature (T) computed for original DSC data (open circles) and fit of glass and melt crystallization data using Eq. (15) with U^* = 6017 J.mol^{-1} and K_g = 2.8·10^5 K^2)[1], as well as simulated crystallization heat flow curves of Figure 7 based on the Hoffman-Lauritzen and SB (m,n) model with parameters in Table 1 and 2 (crosses) and the model-free isoconversional method (solid diamonds), and simulated data using the Ozawa method (open stars). Insert: Effective activation energy (E_α) with extent of conversion (α) obtained from crystallization heat flow curves simulated with Eqs (9) and (11).

Some authors have proposed to describe the nonisothermal crystallization kinetic using a two-stage kinetic equation with two Avrami models[32], to increase the accuracy of the fits. Equation (27) shows such a two stage model, with rate constants k_1 and k_2, Avrami exponents n_1 and n_2, activation energies E_1 and E_2, pre-exponential factors A_1 and A_2. Application of the isoconversional principle yields Equation (28).

$$\frac{d\alpha}{dt} = k_1^{1/n_1} \; f_1(\alpha_1) + k_2^{1/n_2} \; f_2(\alpha_2) \tag{27}$$

$$E_\alpha = \frac{\left(\frac{E_1}{n_1}\right) k_1^{1/n_1} \; f_1(\alpha_1) + \left(\frac{E_2}{n_2}\right) k_2^{1/n_2} \; f_2(\alpha_2)}{k_1^{1/n_1} \; f_1(\alpha_1) + k_2^{1/n_2} \; f_2(\alpha_2)} \tag{28}$$

It can be observed that Equation (28) can yield multiple solutions for the same E_α dependence and as such can not be fit. In contrast, Equation (15) is only a function of T and not of α, thus the mechanism $f(\alpha)$ does not appear and U^* and K_g are evaluated separately in a first fitting procedure of the E_α-dependence, while the kinetic exponents related to the crystallization mechanism are evaluated in a second step by fitting the $(d\alpha/dt)$–T curves.

5 CONCLUSIONS

The Hoffman–Lauritzen (HL) equation is suitable to describe the temperature dependence of the crystallization rate under non-isothermal conditions. Together with the Avrami equation it could be used to simulate PEF crystallization during cooling from the melt with a particularly good fit with U^* = 10200 J mol^{-1}, although the the crystallization from the melt and glass combined was better described by a reduced Sestak-Berggren model with U^* = 6017 J mol^{-1}. The study shows that accurate modelling of the data can be obtained using parameters without a real physical meaning. The advanced model-free isoconversional method has led to very accurate simulations of the non-isothermal crystallization of PEF without requiring an explicit form for the mathematical function describing the crystallization mechanism, using a single E_α-dependence as basis to describe the process over the full range of temperatures and heating rates. Additional crystallization phenomena occurring at the end of the crystallization from the glass on heating explain the decrease of the crystallization rate observed. A new equation has been proposed to correctly describe the whole crystallization process that cannot entirely be described by the HL theory. Simulations confirm differences in mechanisms between melt and glass crystallization and the experimental finding that crystallization from the melt should results in increasing negative values of the overall rate coefficient (E_α) and that crystallization from the glass should result in decreasing positive values when computed using an advanced isoconversional method, in agreement with the HL theory.

6 REFERENCES

[1] A. Codou, N. Guigo, J. van Berkel, E. de Jong, N. Sbirrazzuoli, *Macromol. Chem. Phys.* 215 (2014), 2065.
[2] M. Avrami, *J. Chem. Phys.* 7 (1939), 1103.
[3] M. Avrami, *J. Chem. Phys.* 8 (1940), 212.
[4] M. Avrami, *J. Chem. Phys.* 9 (1941), 177.
[5] T. Ozawa, *Polymer* 12 (1971), 150.
[6] D. Turnbull, J. C. Fisher, *J. Chem. Phys.* 17 (1949), 71.
[7] J. D. Hoffman, G. T. Davis, J. I. Lauritzen, Jr., in: ‘‘Treatise on Solid State Chemistry’’, N. B. Hannay, Ed., Plenum, New York 1976, Vol. 3, p.497.
[8] K. Nakamura. K. Katayama, T. Amano, *J. Appl. Polym Sci.* 17 (1973), 1031.
[9] M. R. Kamal, E. Chu, *Polym Eng. Sci.* 23 (1989), 27.
[10] R. M. Pate1, J. E. Spruiell, *Polym Eng. Sci*. 31 (1991), 73.
[11] Z. Chen, J. N. Hay, M. J. Jenkins, *Europ Polym. J.* 81 (2016), 216.
[12] F. W. Billmeyer, Methods for Estimating Intrinsic Viscosity. *J. Polym. Sci.* IV (1949), 83.
[13] S. Vyazovkin, in: The Handbook of Thermal Analysis & Calorimetry, Vol.5: Recent Advances, Techniques and Applications, Eds. M. E. Brown, P. K. Gallagher, Elsevier, 2008, p. 503.
[14] S. Vyazovkin, A. K. Burnham, J. M. Criado, L. A. Pérez-Maqueda, C. Popescu, N. Sbirrazzuoli, *Thermochim. Acta* 520 (2011), 1.
[15] A. Toda, T. Oda, M. Hikosaka, Y. Saruyama, *Polymer* 38 (1997), 233.
[16] J. M. Kenny, A. Maffezzoli, L. Nicolais, *Thermochim. Acta* 227 (1993), 83.
[17] E. Urbanovici, H. A. Schneider, H. J. Cantow, *Journal of Polymer Science: Part B: Polymer Physics* 35 (1997), 359.
[18] Y. Márquez, L. Franco, P. Turon, J. Puiggali, *Thermochim. Acta* 585 (2014), 71.
[19] J. Sestak, G. Berggren, *Thermochim. Acta* 3 (1971), 1.
[20] N. Sbirrazzuoli, *Macromol. Chem. Phys*. 208 (2007), 1592.
[21] N. Sbirrazzuoli, *Thermochim. Acta* 564 (2013) 59.
[22] S. Vyazovkin, N. Sbirrazzuoli, *Macromol. Rapid Commun*. 25 (2004), 733.
[23] S. Vyazovkin, J. Stone, N. Sbirrazzuoli, *J. Therm. Anal. Calorim*. 80 (2005), 177.
[24] S. Vyazovkin, N. Sbirrazzuoli, *Macromol. Rapid Commun*. 27 (2006), 1515.
[25] N. Sbirrazzuoli, L. Vincent, S. Vyazovkin, *Chemom. Intell. Lab. Syst.* 54 (2000), 53-60.
[26] S. Vyazovkin, *J. Comput. Chem*. 22 (2001), 178.
[27] G.Z. Papageorgiou, V. Tsanaktsis, D. Bikiaris, Phys. Chem. Chem. Phys. 16 (2014), 7946.
[28] G. Stoclet, G. Gobius du Sart, B. Yeniad, S. de Vos, J.M. Lefebvre, Polymer 72 (2015), 165.
[29] T. Ozawa, *Polymer* 12 (1971), 150.
[30] N. Bosq, N. Guigo, E. Zhuravlev, N. Sbirrazzuoli, *J. Phys. Chem.* B 117 (2013), 3407.
[31] N. Bosq, N. Guigo, J. Persello, N. Sbirrazzuoli, *Phys. Chem. Chem. Phys.* 16 (2014), 7830.
[32] Y. Xu, S. Shang, J. Huang, *J. Matter Sci*. 46 (2011), 4085.

CHAPTER 5
CRYSTAL NUCLEATION BEHAVIOR

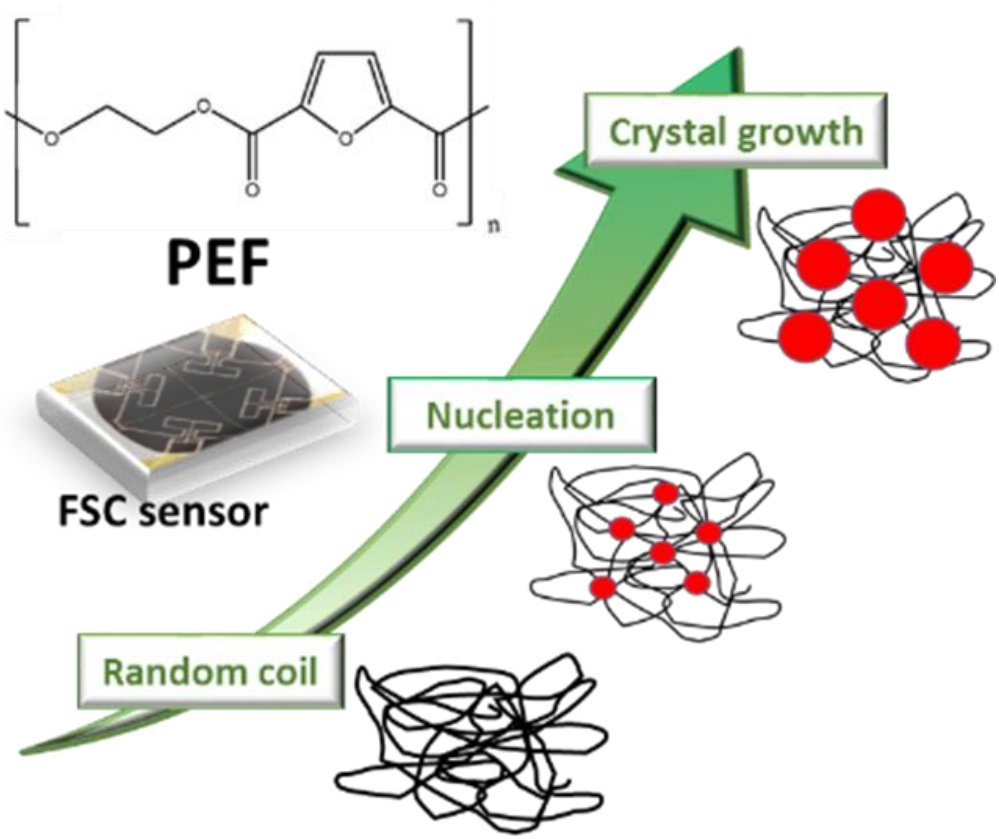

This chapter is also published as part of "Nucleation and Self-Nucleation of Bio-Based Poly(ethylene 2,5-Furandicarboxylate) Probed by Fast Scanning Calorimetry" by L. Martino, N. Guigo, J.G. Van Berkel, J.J. Kolstad, N. Sbirrazzuoli, Macromol. Mat. Eng. 301 (2016), 586.

This chapter focuses on the influence of nucleation processes on the crystallization of bio-based Poly(ethylene 2,5-furandicarboxylate) (PEF). Nuclei formation has been studied by means of Fast Scanning Calorimetry (FSC) both when cooling from the melt (non-isothermal conditions) and when annealing at low temperatures (isothermal conditions). FSC results showed that nucleation on cooling can be avoided by using fast rates, allowing to keep the polymer in its amorphous state, whereas cooling at moderate rates resulted in sample nucleation with a subsequent increase of the crystallization rate. Isothermal pre-treatment just above the PEF glass transition temperature (T_g) resulted in nuclei formation whose rate decreases when the nucleation temperature approaches PEF T_g.

1 INTRODUCTION

The rate of crystallization of polyesters is influenced by nucleation, which occurs during cooling from the melt, e.g. in pelletizing or injection molding, as well as during heating from the glassy state to higher temperatures, e.g. in pellet crystallization or stretch-blow-molding. Therefore, understanding nucleation kinetics as well as the factors governing the nuclei formation in polymers (e.g., addition of nucleating agents, thermal treatments) is of great significance for the successful industrial implementation of new bio-plastics such as PEF. The previous conclusion that crystallization of PEF is limited by the chain diffusion process, indicating that nucleation plays a big role in the overall observed crystallization rate. Very recently, Tsanaktsis et al.[1] investigated the PEF crystallization behavior under different conditions such as solvent induced crystallization, melt and cold crystallization reporting the observation of different crystalline structures for this polyester. The present work aims to go beyond the earlier reports by investigating for the first time the relation between nucleation and crystal growth of PEF. In order to separate the nucleation and the crystal growth contribution from crystallization, in this work nuclei were created in the polymer under different thermal conditions prior crystallization. This enables to study exclusively the

influence of the nucleation on the subsequent crystal growth. To this end, the recently developed Fast Scanning Calorimetry (FSC) instrument offers new and unique investigation opportunities for polymer crystallization because very high heating and cooling rates can be employed, allowing study into a temperature dependent process as nucleation in a highly controlled manner. Several studies have been carried out using FSC to study polymer nucleation kinetics.[2,3,4,5,6,7,8,] The comprehension of polymer primary crystallization is facilitated since fast heating rates by means of FSC allows avoiding recrystallization and reorganization of unstable crystals which otherwise occur during rather slow heating. Furthermore, fast scanning rates allow reaching higher degrees of supercooling prior to initiating the process of crystallization, promoting homogeneous primary nucleation at its highest rate, around the glass transition temperature.[3,6,9] Homogeneous nucleation on cooling can also be prevented by employing fast cooling rates and thus the sample can be quenched to any temperature in order to study nucleation and crystal growth from an amorphous state.

In this work the effect of nucleation under both non-isothermal (formation of nuclei during cooling from the melt) and isothermal conditions (annealing at either low- or high-temperatures) on PEF crystallization were investigated by means of FSC. Specific focus on both nucleation during cooling and under isothermal conditions at temperatures just above the glass transition temperature (annealing at low temperatures) allowed investigation of PEF homogenous nucleation. When an increase of nucleation density occurs due to either isothermal or non-isothermal treatments, an increase of the rate of quiescent crystallization can be observed during the subsequent heating. Following this principle, information about nucleation was derived in this work from analyzing the polymer melting behavior of a sample nucleated under different thermal treatments and crystallized under fixed isothermal conditions. The influence of both nucleation temperature and time on the PEF crystal growth mechanisms were investigated.

2 EXPERIMENTAL

2.1 MATERIALS

Poly(Ethylene 2,5-Furandicarboxylate), PEF, was obtained from the direct esterification and polycondensation of FDCA from Avantium and bio-based ethylene glycol (from India Glycols), using antimony as the catalyst analogously to PET. Both polymerization steps were carried out in a 4.5 kg stainless steel melt polymerization reactor up to a final intrinsic viscosity (IV) of 0.61. The final IV was calculated using the well-known Billmeyer equation from a measured inherent viscosity of 0.59 dL g^{-1} at a concentration of 0.4 g dL^{-1} in a mixture of 60% phenol and 40% tetrachloroethane (w/w). The absolute M_n was determined to be 19.3 kg mol^{-1} as derived from the total number of end groups by ^{1}H NMR, also corresponding to a typical industrial M_n after polycondensation of PET.

2.2 METHODS

Fast scanning calorimetry (FSC) measurements were performed using a Mettler-Toledo Flash DSC1. The sensors employed were first conditioned and temperature-corrected according to the instrument specification. Further details about the instrument and sensor specifications are reported elsewhere.[9] Specimens were prepared by cutting thin sections from PEF pellets using a microtome. The samples obtained were placed on the center of the FSC sensor using a microscope attached to the FSC apparatus. To provide a good thermal contact between the sample and the sensor, several heating and cooling scans were performed before the actual calorimetric experiments. The sample mass of $6.2 \cdot 10^{-8}$ g was estimated by comparing the measured melting enthalpy (J) obtained from FSC measurements after isothermal crystallization at 170°C for different times with that obtained by conventional DSC measurements (J g^{-1}). The slope of the linear fit of the experimental isothermal crystallization data was used to estimate the sample mass.

In order to erase the previous sample thermal history, FSC measurements were performed by initially heating the sample up to 250°C, which is the above the equilibrium melting temperature, T_m^0, estimated to be 247°C.[10] The sample was held at 250°C for 10 s and cooled down to 25°C at $2 \cdot 10^3$ K s^{-1}. All FSC experiments were then carried out as described below. PEF crystallization under isothermal conditions was investigated by heating the sample at $2 \cdot 10^3$ K s^{-1} to the crystallization temperature, T_c = 170 °C. After isothermal crystallization for different times t_n varying from 0 to 12 hours, the sample was cooled down to 25°C ($2 \cdot 10^3$ K s^{-1}). The melting enthalpy was determined during the subsequent heating run from 25 up to 250°C at 10^3 K s^{-1}.

In order to investigate PEF nucleation during cooling from the melt, FSC measurements were performed by applying different cooling rates (ranging from $2 \cdot 10^3$ K s^{-1} down to $1 \cdot 10^{-1}$ K s^{-1}) from 250°C down to 25°C, before isothermal crystallization at T_c = 170 °C for a given period of time. Then the sample was cooled to 25°C at $2 \cdot 10^3$ K $s^{-1}$and reheated up to 250 °C at 10^3 K s^{-1}. Figure 1a schematically shows the thermal procedure used.

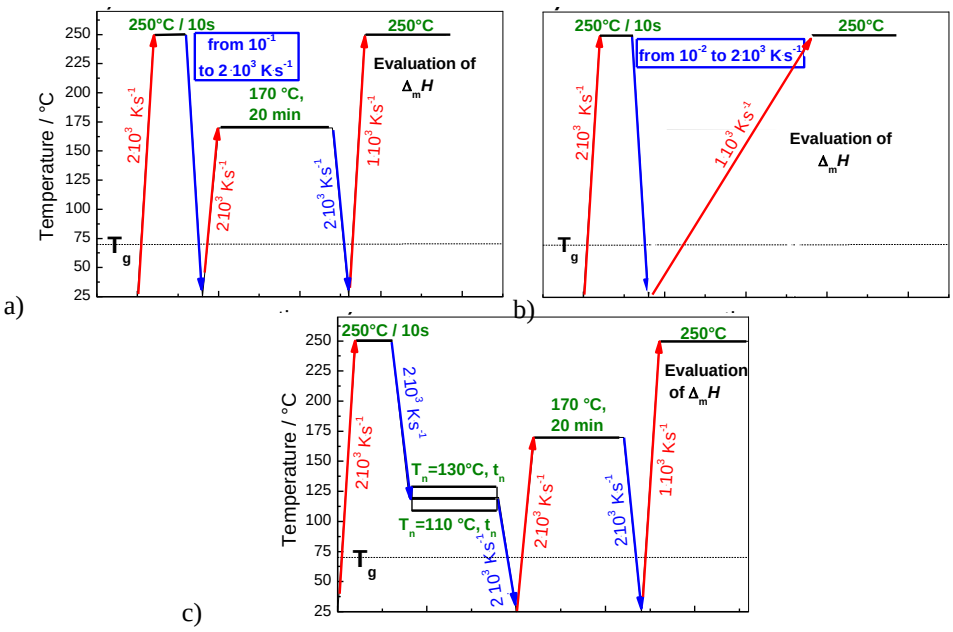

Figure 1 – Schematic representation of the thermal procedures used to investigate: PEF nucleation at different cooling rates (from $2 \cdot 10^3$ K s^{-1} up to $1 \cdot 10^{-1}$ K s^{-1}) with (a) or without (b) isothermal crystallization at 170°C; c) PEF nucleation at different temperatures (T_n) just above PEF glass transition for different times (t_n).

In order to check whether the sample crystallizes upon cooling or not, parallel FSC heating scans after PEF cooling (at rates ranging from $2 \cdot 10^3$ K s^{-1} up to 10^{-2} K s^{-1}), but without intermediate isothermal crystallization, were also performed (Figure 1b). The influence on PEF crystallization by the presence of nuclei created during isothermal treatment at temperatures close to the polymer glass transition was also investigated in this work. Figure 1 shows the thermal procedure implemented to study the influence of nuclei formed close to the glass transition. The sample was first cooled down to an annealing temperature (T_n) in the range 100°C-130°C. After certain period of time at T_n, the sample was heated to 170°C and isothermally crystallized at this temperature for a certain time. Finally, the sample was subjected to heating at 10^3 K s^{-1} (Figure 1c). Several parallel FSC heating scans of the nucleated sample without isothermal crystallization were also collected, in order to check whether the sample crystallizes or not during the annealing at T_n. The standard error associated to the melting endotherm integration in FSC curves to calculate enthalpy melting values was estimated to be in the range of ± 1.5 J g^{-1}. In order to evaluate the contribution of the thermal lag caused by the temperature gradient in the sample due to the fast scanning rate[11,12] a temperature correction was estimated for each scanning rate. For this purpose, a small amount of indium was placed on the top of the PEF sample on the FSC sensor. The onset temperature of the Indium melting peak determined at the heating rate of 10^3 $K \cdot s^{-1}$ was 3.4 °C higher than the reference onset temperature of the Indium standard. This correction factor was used to estimate the real sample temperatures measured by FSC.

Regular Differential Scanning Calorimetry (DSC) measurements were carried out using a Mettler-Toledo DSC-1 apparatus. The sample (about 4 mg) was placed in 40 µL aluminum pan and sealed hermetically. DSC cooling and heating measurements were run at 50 °C min^{-1} in a nitrogen atmosphere. The sample was first heated to 250 °C and kept 3 min at this temperature to cancel previous thermal history. Then the sample was cooled to 25 °C, heated

to 170 °C and subsequently isothermally crystallized at this temperature for 1 hour. Lastly, the sample was cooled to 25°C and reheated to 250°C. In both FSC and DSC analysis, glass transition temperatures (T_g) were taken at the mid-point of the specific heat capacity change and the melting temperatures (T_m) were taken at the peak maximum of the melting endotherm. The degree of crystallinity, X_c, was calculated using Equation (1).

$$X_c = 100\% \cdot \frac{\Delta H_m}{\Delta H_m^0} \qquad (1)$$

Where ΔH_m is the experimental melting enthalpy obtained from the FSC scan and ΔH_m^0 is the melting enthalpy of 100% crystalline PEF which was taken at 140 $J \cdot g^{-1}$.[13,14]

3 RESULTS & DISCUSSION

3.1 ISOTHERMAL CRYSTALLIZATION

FSC measurements were performed by following the thermal procedure reported in Figure 1a but applying 1h isothermal crystallization at 170°C instead of 20 minutes. Isothermal crystallization for 1h was also performed by using DSC as described in the Experimental Section. Figure 2 shows subsequent heating curves by both DSC (at rates of 10^{-1} K s^{-1} and 1 K s^{-1}) and FSC measurements (at the rate of 10^3 K s^{-1}).

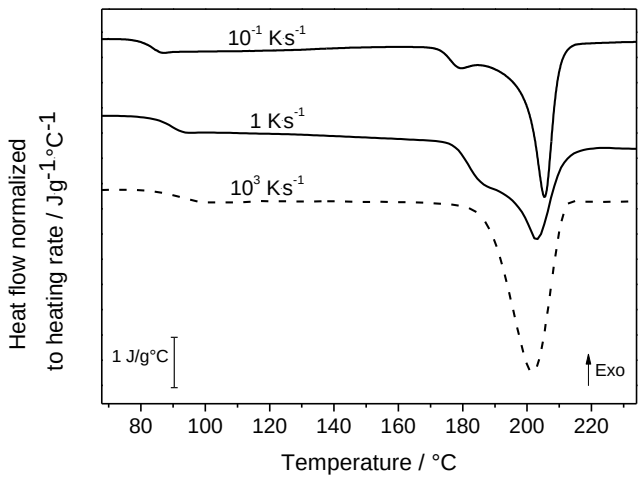

Figure 2 – PEF heating curves, after isothermal crystallization at 170°C for 1 hour, by DSC (continuous curves) and FSC (dashed curve) measurements. Scanning rates used are indicated on curves.

DSC curves (Figure 2, continuous lines) at heating rates of 10^{-1} K s^{-1} and 1 K s^{-1} show an endothermal base-line shift associated with the glass transition, T_g, at temperatures of 83°C and 89°C, respectively. In both curves, this thermal event is followed by a multiple melting endotherm displaying the highest temperature peak around 204°C, similar to the findings in Chapter 3. The FSC curve (Figure 2, dashed line) shows T_g at 93 °C which is at higher temperatures with respect to DSC analysis as expected due to the faster heating rate employed (10^3 K s^{-1} for FSC *vs* either 10^{-1} or 1 K s^{-1} for DSC). The melting endotherm of PEF under fast heating presents a single thermal event centered at T_m = 202 °C, in contrast to the melting behavior observed in the conventional DSC result. This trend implies that as opposed to the explanation in Chapter 3 peak II is formed by re-crystallization, which has sufficient time to take place at slower heating rates but not when faster heating rates are employed.[15,16] Such observations are consistent with peak I, the initially observed melting endotherm of PEF, being associated with the formation of a single distribution of lamellae thickness during PEF isothermal crystallization at 170°C. The increase of heating rate causes the onset of this melting endotherm to shift to higher temperatures, despite the temperature corrections applied (see the Experimental Section). In contrast, the heating rates employed in DSC are not high enough to prevent re-crystallization on heating that lead to the formation of different lamellae thickness distributions.

A fast heating rate (10^3 K s^{-1}) was used in the following FSC experiments in order to study the PEF primary crystallization free of any recrystallization effects. Isothermal crystallization was conducted at 170°C for different times ranging from 0 to 12 hours by FSC analysis. The melting enthalpy values obtained during the subsequent heating scan are reported as function of the crystallization time in Figure 3.

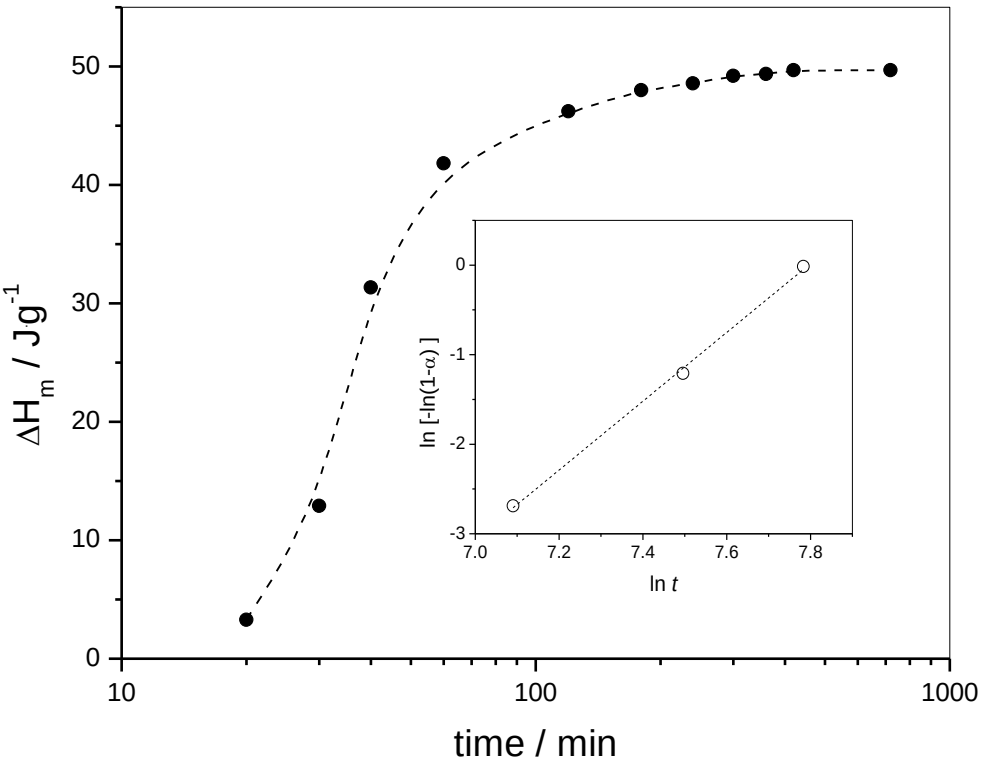

Figure 3 – Melting enthalpy as function of the crystallization time at 170 °C (on a logarithmic scale). Inset: Avrami plots using datasets taken between 20 < *t* < 40 min (left-hand plot). The dashed line is a guide for the eyes.

It is shown that with increasing crystallization time, the melting enthalpy increases and reaches a maximum value of about 50 J g^{-1} after crystallization at 170°C for 300 min. This melting enthalpy value corresponds to a degree of crystallinity (X_c), calculated according to Equation 1, of about 36%. According with previous works,[1,14] PEF exhibits an ordered crystalline form, called α, at temperature of crystallization ≥ 170°C; whereas a more defective α' crystalline structure evolves below this temperature. An additional β crystalline form by solvent induced crystallization was also observed in PEF.[13] Since the presence of α and α' forms only depends on the temperature of crystallization and no phase transition was observed by varying the crystallization time,[14] it can be supposed that the PEF sample crystallized in this work exhibits an α crystalline structure. In Figure 3, the melting enthalpy values obtained are equal to the enthalpies of isothermal crystallization, since neither concomitant

reorganization and recrystallization processes nor cold-crystallization occur during heating by FSC. Interestingly, the values of the melting enthalpies found here for the small PEF sample deposited on the FSC chip sensor compare well with those obtained for the bulk PEF in Chapter 3.

The Avrami equation[17] was applied to the data of Figure 3 taking the initial part of the curve i.e., the primary crystallization stage. Excellent linear fit was obtained (r^2 = 0.9987) leading to the Avrami parameters $k_1(T)$ = 9.82 10^{-14} $s^{-3.84}$ and n_1 = 3.84 (inset of Figure 3). The n_1 value found presently for the early stage of isothermal crystallization approaches 4 which is typical for spherulitic growth combined with homogeneous nucleation.

In the following sections, the objective is to highlight changes in polymer crystallization behavior due to the initial thermal treatment. For this, a crystallization time of 20 min has been selected because it leads to incomplete crystallization (ΔH_m = 3.3 J g^{-1}) (Figure 3) when no initial thermal treatment is applied.

3.2 EFFECT OF COOLING RATES

With the aim to investigate the potential formation of nuclei on cooling from the melt, FSC measurements were performed by applying cooling at different rates ranging from 10^{-1} K s^{-1} up to $2 \cdot 10^3$ K s^{-1}. Then the sample was heated to 170°C and crystallized for 20 min at this temperature, according to the temperature program of Figure 1a. Figure 4a shows PEF heating curves obtained after cooling at different rates. The melting enthalpy values measured are also reported in Figure 4b as function of the logarithmic value of the cooling rate.

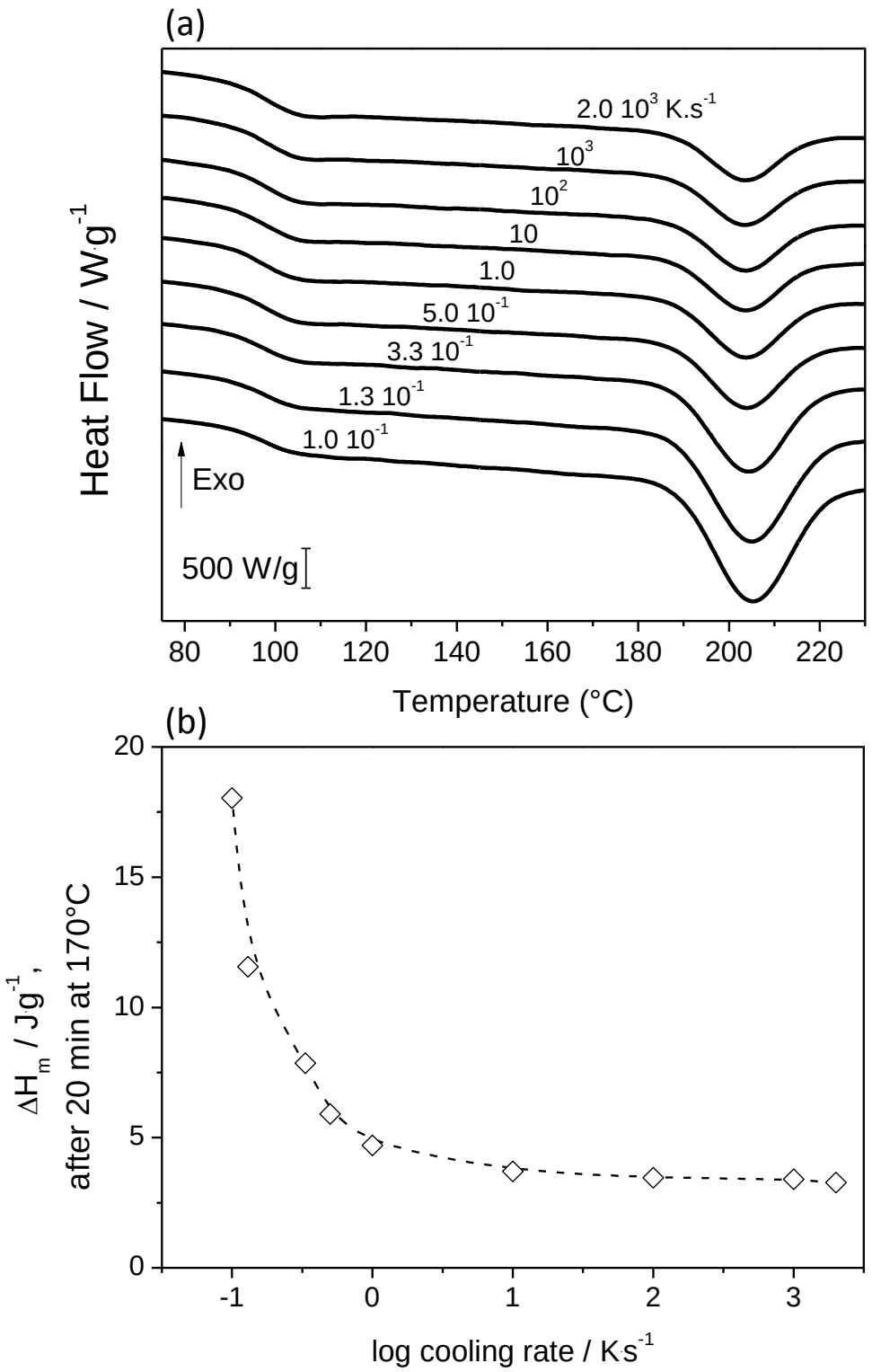

Figure 4 – (a) FSC heating curves at 10^3 K s^{-1} obtained after cooling from the melt at various cooling rates (ranging from 10^{-1} to 2 10^{-3} K s^{-1}) followed by isothermal crystallization at 170°C during 20 min. (b) Melting enthalpy after 20 min. at 170°C as function of the logarithm of the cooling rate. The dashed line is to guide the eyes.

PEF FSC heating curves show melting behavior which is dependent on the cooling rate. Melting enthalpy values decrease until reaching a constant value (within the error of measurement) as the cooling rate increases from 10^{-1} to $2 \cdot 10^{3}$ K s^{-1} (Figure 5b). The melting enthalpy decreases from an initial value of 18.0 J g^{-1} (X_c = 13%) when the slowest cooling rate of 10^{-1} K s^{-1} is employed to a value of 3.3 J g^{-1} (which corresponds to a crystallinity degree of about X_c = 2%) at the fastest cooling rate of $2 \cdot 10^{3}$ K s^{-1}. In the same way, the heat capacity change attributed to PEF glass transition decreases with decreasing cooling rate, due to the sample crystallinity increase.

It is worth noting that FSC heating curves (not shown) after cooling at such rates without performing the isothermal crystallization step at 170°C (Figure 1b) did not show any endothermal events. Only when the cooling rate becomes slower than $1 \cdot 10^{-1}$ K s^{-1} (6 K min^{-1}), a melting endotherm due to the sample crystallization during cooling was observed (not shown in graph). Therefore, the change of the melting enthalpy by varying the cooling rate shown in Figure 4 is due to development of nuclei during cooling from the melt: at slow cooling rates a higher number of nuclei develops that increase the number of growing crystals during the successive rather short isothermal step at 170°C. On the other hand, the absence of significant variation of the melting enthalpy at rates faster than $5 \cdot 10^{-1}$ K s^{-1} (30 K min^{-1}) suggests that no nuclei are formed under such cooling conditions. Thus, the critical cooling rate to keep the PEF sample amorphous is comparable with that of slow crystallizing polymers such as polylactic acid, PLA, (around $8.3 \cdot 10^{-1}$ K s^{-1}),[18] and much lower than other polymers like polycaprolactone ($2 \cdot 10^{3}$ K s^{-1}).7

3.3 EFFECT OF LOW TEMPERATURE ANNEALING

As it was shown in section 3.2., employing sufficiently fast rates by means of FSC analysis, nuclei development on cooling can be prevented, allowing study of isothermal nuclei formation and successive crystal growth from an amorphous state. In the FSC experiments illustrated in Figure 1c, fast cooling rates such as $2 \cdot 10^3$ K s^{-1} were used to reach different nucleation temperatures (T_n), namely 130°C, 120°C, 110°C and 100°C. The PEF glass transition temperature during cooling at $2 \cdot 10^3$ K s^{-1} is observed at 87°C. Therefore, the selected temperatures are located at 43, 33, 23 and 13°C above the PEF glass transition temperature, respectively. After annealing at T_n for different times, the sample was crystallized at 170°C for 20 min (see Figure 1c). The effect of the nucleation was estimated from the melting enthalpy change observed during the final heating scan (10^3 K s^{-1}). Indeed, the use of a standardized thermal procedure (e.g., fixed heating rates, cooling rates and isothermal crystallization conditions) for all measurements allows direct correlation of the sample melting behavior, and thus of polymer crystallization, to the prior isothermal nucleation treatment. Figure 5 reports the measured PEF melting enthalpy values obtained during heating as function of the nucleation time, after isothermal nucleation at different temperatures (indicated on Figure 5) and subsequent sample crystallization at 170°C after 20 minutes. In order to ensure that only nucleation occurred, and not significant crystal growth, during the isothermal step at T_n, FSC heating scans were also performed immediately after annealing for different times. If any melting during such scans was detected, then it was concluded that large crystals, and not only nuclei and small crystals, have developed during that period. This was observed when exceeding annealing times of $1.5 \cdot 10^3$ s, $3 \cdot 10^3$ s, $1.4 \cdot 10^4$ s and $6 \cdot 10^4$ s for annealing at 130°C, 120°C, 110°C and 100°C, respectively. Therefore, such measurements allowed estimation of a ‘limiting time’ for each annealing temperature T_n below which only nuclei formation occurs, as indicated in Figure 5.

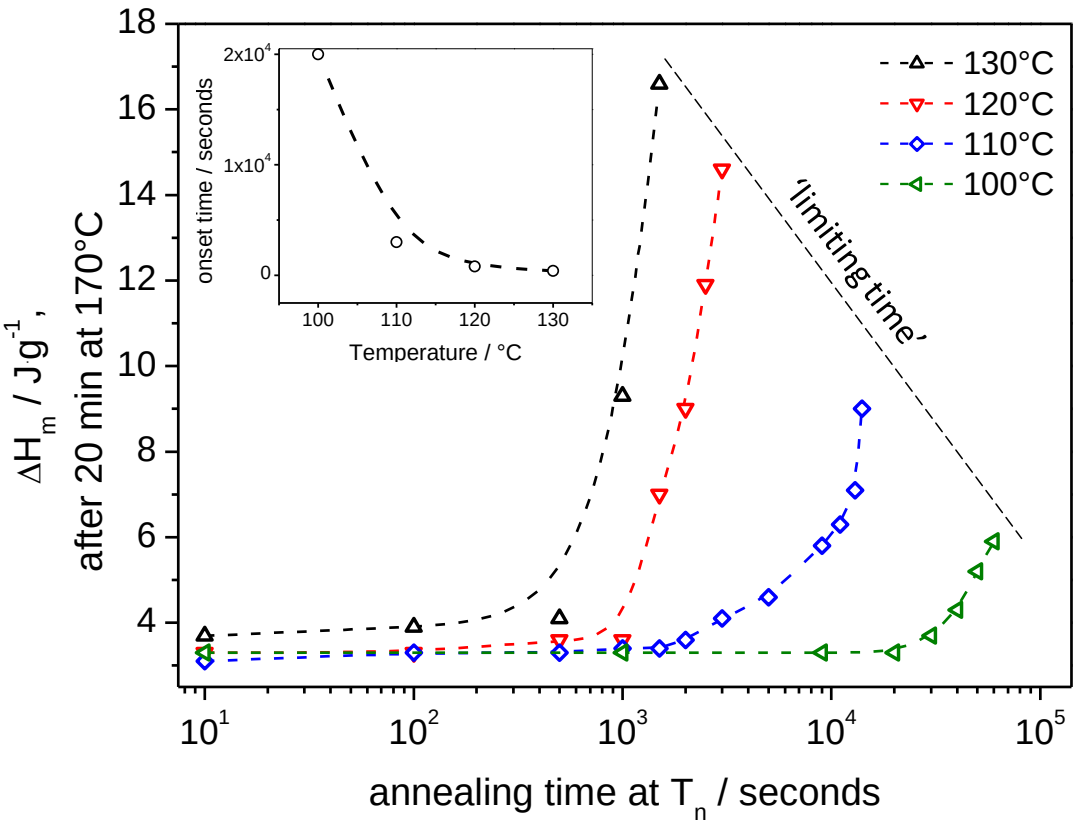

Figure 5 – Melting enthalpy of melting of PEF after 20 minutes at 170°C as function of annealing time at different temperatures (T_n) indicated in the legend (on a logarithmic scale). Inset: onset time of nucleation as a function of annealing temperatures (130°C, 120°C, 110°C and 100°C). The lines are guide for the eyes.

Figure 5 shows that the value of ΔH_m varies with both the annealing time and the temperature of annealing. The melting enthalpy increase reflects a higher number of growing crystals formed during the subsequent isothermal crystallization at 170°C, because on average each crystal will have grown to the same size during 20 minutes at 170 C (i.e. constant radial growth rate of the crystals). The highest amount of crystallinity is obtained when the sample is nucleated at the highest temperature, i.e. 130°C where the ΔH_m value shifts from about 3.3 J g^{-1} up to about 16.6 J g^{-1} after 1500 s of nucleation at this temperature. Because the sample does not crystallize during the annealing treatment at T_n, as previously mentioned, the observed increase of crystallinity is attributed to nuclei formation during isothermal treatment at low temperatures above T_g. A higher number of nuclei is originated after a longer residence time. During the fixed duration of 20 min at 170 °C, the presence of pre-existing nuclei allows

the system to develop the crystal growth of the higher quantity of crystallites. Upon decreasing temperature of annealing T_n, the melting enthalpy increases to a lesser extent as function of the residence time, as the result of the different nucleation rate at the various annealing temperatures. For instance, after 1500 s of annealing, ΔH_m reaches a value of 7.0 J g^{-1} at 120 °C while no melting change is observed at 110 and 100 °C for the same duration of annealing. Therefore, upon decreasing T_n from 130°C to 100 °C, a longer annealing time is needed until an effect on the melting enthalpy value is observed, i.e., a longer onset time of nuclei formation is necessary. This effect is attributed to the reduced cooperative mobility of polymer chain segments at temperatures approaching the glass transition temperature.[9,19] As previously proposed,[2] the onset time of nucleation can be used to obtain information about the kinetics of nucleation. Inset of Figure 5 reports the onset time of nucleation as function of temperature of isothermal nucleation. Such a time was obtained from data of Figure 5 by extrapolation of the time corresponding to a first deviation from the melting enthalpy value measured for the non-nucleated sample at T_n. It can be seen that the onset time significantly increases as the temperature of annealing decreases within the temperature range investigated. The onset time value shifts from $4 \cdot 10^2$ s up to $2 \cdot 10^4$ s when the temperature of annealing decreases from 130°C to 100°C, showing a nucleation kinetic slowdown of about two orders of magnitude as temperatures approach close to the PEF glass transition temperature (87°C). Upon cooling from the melt the nucleation rate is anti-Arrhenian, i.e. the rate increases when the temperature decreases and it passes through a maximum. The above-mentioned results would indicate that the chosen temperatures of isothermal nucleation (100-130°C) are located below the temperature of the maximal nucleation rate since, in this range, the nucleation slows down when the temperature decreases showing an Arrhenian behavior (Figure 5). Such a slowdown close to the glass transition temperature was already observed for polymers such as PLA.[2]

4 CONCLUSIONS

In this work homogeneous nucleation behavior of bio-based PEF for the first time has been investigated by FSC analysis. Initially, it has been shown that the multiple melting process previously reported for PEF ascribed to the different lamella thickness distributions during crystallization, is due to polymer re-crystallization since it disappears when fast heating rates are used. Homogeneous nucleation has been investigated both during cooling from the melt and under isothermal conditions at temperatures just above the PEF glass transition. It has been shown that cooling at high rates allows the polymer amorphous state to be retained and preventing sample nucleation; whereas cooling at lower rates resulted in nuclei formation which increases the rate of the subsequent crystal growth. The critical rate to prevent homogeneous nucleation on cooling has been determined to be around $5 \cdot 10^{-1}$ K s^{-1}. Higher cooling rate such as $2 \cdot 10^{-1}$ K s^{-1} were used to quench the sample to annealing temperatures (T_n) close to PEF glass transition in order to study nucleation mechanism from an amorphous state. The results showed that the crystallization rate increases when nuclei formation occurs during the isothermal treatment at T_n. Both nucleation temperature and time influence the mechanism of nuclei formation and thus the crystal growth, as well as the melting of the crystals. Longer annealing times are necessary as the annealing temperature approaches the glass transition temperature in order to observe nuclei formation, due to the reduced cooperative mobility of the polymer chains.

5 REFERENCES

[1] V. Tsanaktsis, D. G. Papageorgiou, S. Exarhopoulos, D. N. Bikiaris and G. Z. Papageorgiou, *Cryst. Growth Des.* 15 (2015), 5505.
[2] R. Androsch , M. L. Di Lorenzo. *Macromolecules* 46 (2013), 6048.
[3] R. Androsch , M. L. Di Lorenzo. *Polymer* 54 (2013), 6882.
[4] A. Mollova, R. Androsch, D. Mileva, C. Schick , A. Benhamida. *Macromolecules* 46 (2013), 828.
[5] A. M. Rhoades, J. L. Williams , R. Androsch. *Thermochim. Acta* 603 (2015), 103.
[6] I. Stolte, R. Androsch, M. L. Di Lorenzo , C. Schick. *J. Phys. Chem. B* 117 (2013), 15196.
[7] A. Wurm, E. Zhuravlev, K. Eckstein, D. Jehnichen, D. Pospiech, R. Androsch, B. Wunderlich , C. Schick. *Macromolecules* 45 (2012), 3816.
[8] E. Zhuravlev, J. W. P. Schmelzer, B. Wunderlich , C. Schick. *Polymer* 52 (2011), 1983.
[9] E. Schulz. *Kristall und Technik* 12 (1977), K11-K12.
[10] A. Codou, N. Guigo, J. van Berkel, E. de Jong, N. Sbirrazzuoli, *Macromol. Chem. Phys.* 215 (2014), 2065.
[11] G. Poel, D. Istrate, A. Magon and V. Mathot, *J. Therm. Anal. Calorim.* 110 (2012), 1533.
[12] E. Zhuravlev and C. Schick, *Thermochim. Acta*, 505 (2010), 14.
[13] G.Z. Papageorgiou, V. Tsanaktsis, D. Bikiaris, Phys. Chem. Chem. Phys. 16 (2014), 7946.
[14] G. Stoclet, G. Gobius du Sart, B. Yeniad, S. de Vos, J.M. Lefebvre, Polymer 72 (2015), 165.
[15] A. A. Minakov, D. A. Mordvintsev , C. Schick. *Faraday Discuss.* 128 (2005), 261.
[16] Z. G. Wang, B. S. Hsiao, B. B. Sauer , W. G. Kampert. *Polymer* 40 (1999), 4615.
[17] M. Avrami. *J. Chem. Phys.* 7 (1939), 1103.
[18] S. M. Sánchez, V. B. F. Mathot, G. Vanden Poel , J. L. Gómez Ribelles. *Macromolecules* 40 (2007), 7989.
[19] J. Hoffman, G. T. Davis , J. Lauritzen, Jr. In Treatise on Solid State Chemistry; Hannay, N. B., Ed.; Springer US, 1976, p497-614.

CHAPTER 6
GLASS TRANSITION AND CHAIN COOPERATIVITY OF PEF *vs* PET

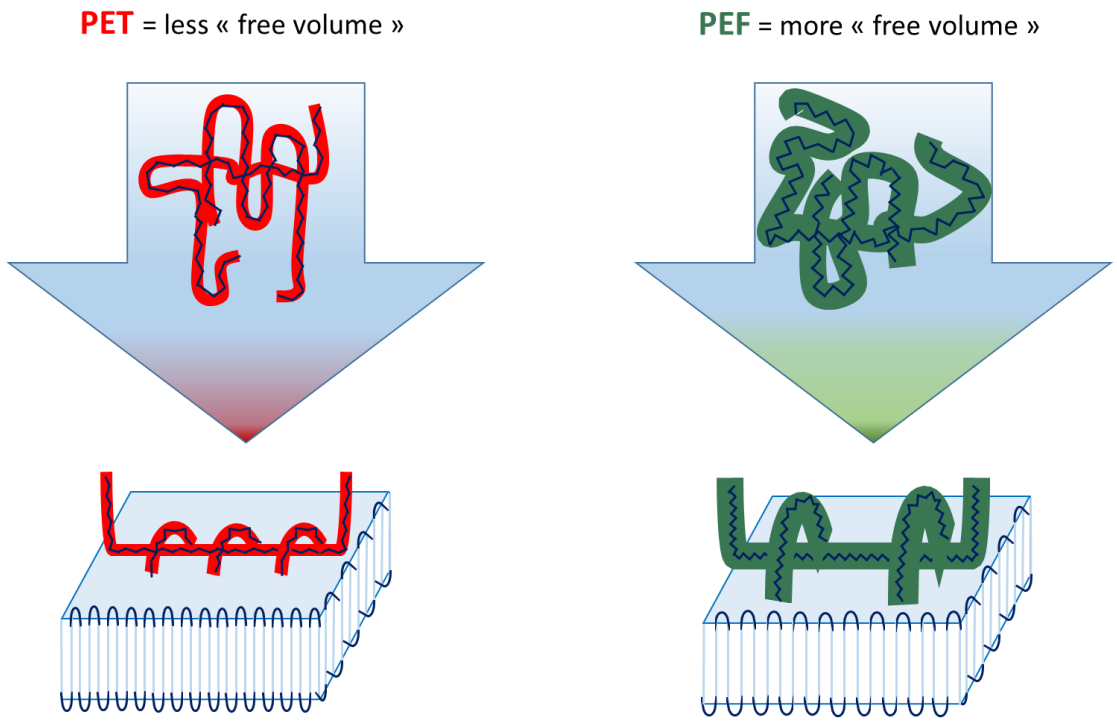

This chapter is also published as part of "Glass transition dynamics and cooperativity length of poly(ethylene 2,5-furandicarboxylate) compared to poly(ethylene terephthalate)" by A. Codou, M. Moncel, J.G. Van Berkel, N. Guigo, N. Sbirrazzuoli, Phys. Chem. Chem. Phys. 18 (2016), 16647.

This chapter investigates the glass transition of PEF in comparison to *poly*(ethylene terephthalate) (PET). The investigations were conducted at different crystallinities by means of stochastic modulated differential scanning calorimetry (stochastic TMDSC) and dynamic mechanical analysis (DMA). The length of cooperative rearranging regions (CRR) was similar for both materials. Additionally, the variations of the effective activation energy *E* of PEF and PET at glass transitions were determined by isoconversionnal kinetic analysis. The rate of decrease in *E* was similar for the two amorphous polyesters. Upon crystallization, the glass transition of PEF is broadened but its temperature range is not increased as with PET. The creation of Rigid Amorphous Fraction (RAF) with crystallinity is lower in PEF than in PET. The difference in free volume also explains the lower coupling between the crystalline and the amorphous phase in PEF.

1 INTRODUCTION

The development of crystalline structures in PEF can induce progressive reduction of amorphous phase whose motional processes are considerably modified. The three-phase model has been proposed to explain the incomplete decoupling between the crystalline and the amorphous phases. This model assumes that the crystalline phase coexists with the Mobile Amorphous Fraction (MAF) and the Rigid Amorphous Fraction (RAF).[1] The RAF is located in the neighbourhood of crystals and its close interaction with the crystalline lamella induces restriction in the molecular mobility. In the case of Strain Induced Crystallization (SIC) the RAF and MAF composition may be further influenced by the degree of orientation applied. Accordingly, the relaxation of RAF occurs at higher temperature and can be decoupled to the relaxation of MAF.[1,2,3] The interplay between those three phases and the impact on the conformational mobility in such confined nano-structures has been largely described for various polyesters such as PET and polylactide (PLA).[2,3,4]

In addition to the three phase model, the concept of cooperative rearranging regions (CRR) was introduced by Adam and Gibbs[5] and was defined as a subsystem presenting a rearrangement of its configuration under a thermal fluctuation, independently of its environment. Donth[6] proposed a thermodynamic fluctuation formula to obtain the length of the CRR that gives information on the spatial aspect of the system dynamic heterogeneity.

This paper aims to acquire additional knowledge on the molecular-scale motions of PEF with a special emphasis on the cooperative alpha relaxation process occurring in amorphous and semi-crystalline PEF samples. It should be noted that the morphological aspects of crystallinity are not included in this study. In order to highlight the peculiarities of the PEF relaxation process, experimental comparisons were made with PET. For this purpose, stochastically temperature modulated differential scanning calorimetry (i.e. stochastic TMDSC) has been employed to obtain the heat capacity (C_p) variation during the PEF and PET glass transition, permitting the determination of the coupling between the crystalline and the amorphous phase for various crystallinities. The stochastic TMDSC allows to obtain a "quasi static" heat capacity in one single experiment without performing blank curve subtractions. It is a clear-cut advantage compared to regular TMDSC whose C_p variations are dependent on the modulation frequency. In addition to the calorimetric determination of heat capacity step during the glass transition, DMA were conducted on PEF and PET samples to provide the mechanical response of the α-relaxation process. While not employed in the present study, it should be stressed that the dielectric spectroscopy can be very useful for the determination of the relaxation map on very large frequency domains.[7,8] The average sizes of the CRR were calculated for amorphous and semi-crystalline PEF and PET samples after estimation of the mean temperature fluctuation from the loss peaks obtained both with calorimetric, i.e. stochastic TMDSC (C_p") and mechanical, i.e. DMA (E") data. Finally, the glass transition kinetics of PEF and PET were investigated for the first time using a model-

free approach. An effective activation energy throughout the glass transition was determined with an advanced isoconversional analysis for PEF and PET. The intrinsic values and the dependence of the effective activation energy were commented and correlated with the earlier findings on CRR and dynamic fragility.

2 EXPERIMENTAL

2.1 MATERIALS

Samples of p*oly*(ethylene 2,5-furandicarboxylate) (PEF) and *poly*(ethylene terephthalate) (PET) used in this work were provided by Avantium in The Netherlands. PEF is obtained from the direct esterification and polycondensation of bio-based 2,5-furandicarboxylic acid (FDCA) from Avantium and bio-based ethylene glycol from India Glycols, using antimony as the catalyst analogously to PET. To mimic industrial PET resin production, both polymerization steps were carried out in a 4.5 kg stainless steel melt polymerization reactor up to a target intrinsic viscosity (IV) of around 0.60, typical for commercial PET after polycondensation. The final IV was calculated using the well-known Billmeyer equation from a measured inherent viscosity of 0.59 $dL.g^{-1}$ at a concentration of 0.4 $g.dL^{-1}$ in a mixture of 60% Phenol and 40% Tetrachloroethane (w/w). The number average molecular weights are M_n = 19.3 kg/mol and M_n = 27.8 kg/mol for PEF and PET respectively, as derived from the total number of end-groups by ^{1}H NMR. This also corresponds to a typical industrial M_n after polycondensation of PET. The density of wholly amorphous samples is 1.435 $g.cm^{-3}$ and 1.335 $g.cm^{-3}$ respectively for PEF and PET.

2.2 METHODS

Standard DSC and stochastic TMDSC (TOPEM® by Mettler-Toledo) runs were carried out on a Mettler-Toledo DSC 1 equipped with a FRS5 sensor and STAR© software for data analysis. Temperature, enthalpy and tau lag calibrations were steadily done by using indium and zinc

standards. The samples for DSC and TOPEM® were analyzed in 40 μL sealed aluminum pans of about 8 mg. The experiments were performed under a N_2 atmosphere (50 mL/min). The specific heat capacities for amorphous and semi-crystalline PEF and PET samples were measured using the sapphire as reference.

Dynamic mechanical analyses were conducted on a Mettler-Toledo DMA 1 in tensile mode. The experiments were performed under a N_2 atmosphere at a frequency of 1 Hz from -100 to 250 °C and heated at 2 °C/min. The plates of amorphous samples were obtained by compression molding and delivered by Avantium, and then cut using a Charly4U milling machine to obtain rectangular bars (15 × 2 × 1.5 mm^3).

SAMPLE PREPARATION

PEF and PET amorphous and semi-crystalline samples were prepared by the following in situ procedures directly in the DSC device.

For PEF, the samples were first heated at 250 °C (i.e. 30 °C above the observed melting temperature) for 5 min and quenched (≈ -50 °C/min) to 25°C to obtain a fully amorphous sample (called PEF-am). During cooling it was observed that the cooling rate is controlled and fast enough to avoid crystallization of PEF. Then the samples were cold crystallized following different temperature programs (Table) to obtain specific degree of crystallinity. The sample was heated to 120 °C for 30 min to allow nucleation to take place, and rapidly heated up to 170 °C during 30 min (PEF-C0) or 90 min (PEF-C1). This temperature was chosen because it is close to the temperature of maximal crystal growth rate found previously.[5, 6] To reach a higher degree of crystallinity, the primary crystallized sample was slowly heated at 3.5 °C/min to 205 °C and kept at this temperature during 60 min to allow secondary crystallization by lamellar thickening (PEF-C2). After obtaining the desired crystallinities, the samples were quenched to 25 °C.

For PET, the sample were first heated at 280 °C (i.e. +30 °C above the observed melting temperature) for 4 min and quenched directly in liquid nitrogen bath from the melt to obtain fully amorphous PET (PET-am). Then the sample was cold crystallized at 130°C during 30 min (PET-C1; Table 1) in order to obtain comparable crystallinity as PEF-C1. As the PET crystallization rate is faster than the one of PEF, no pre-crystallization step was necessary.

Table 1 – Temperature programs used to crystallize the samples

Step	Pre-crystallization		Crystallization		Annealing		Crystallinity (%)
	T (°C)	*t* (min)	*T* (°C)	*t* (min)	*T* (°C)	*t* (min)	
PEF-am	-	-	-	-	-	-	0
PEF-C0	120	30	170	30	-	-	20
PEF-C1	120	30	170	90	-	-	31
PEF-C2	120	30	170	90	205	60	43
PET-am	-	-	-	-	-	-	0
PET-C1	-	-	130	30	-	-	34

DSC runs were carried out to control the crystallinity of each sample. By integration of the total area of the exothermic and endothermic peaks, crystallization and melting enthalpies were determined. The sample crystallinity was calculated considering the equilibrium melting enthalpy of fully crystalline PEF ΔH^0_m ~ 140.0 J/g taken from two recent papers.[7, 8] Another value of ΔH^0_m ~ 185.0 J/g was also reported elsewhere[6] which show that this topic merits further work. However, the value of ΔH^0_m = 140.0 J/g was retained in this work for PEF since it is similar to that usually reported for PET ($\Delta H^0_{m\ (PET)}$ = 140.0 J/g)[9]. Prior to further DSC or stochastic TMDSC experiments (see 2.3 b and c) the samples were heated at 50 °C/min from 25 °C up to a temperature above the glass transition range in order to erase the thermal history of the glassy state, while maintaining crystallinity. Immediately, the samples were cooled rapidly to 25°C at 50 °C/min thus allowing minimal aging.

For the DMA measurements, the PEF and PET samples were first cut into rectangular stripes and crystallized in an oven controlled at ± 2°C following the above mentioned temperature program (Table 1). Thereby four PEF samples (PEF-am, C0, C1, C2) and two PET samples (PET-am, PET-C1) were prepared for PEF and PET. The crystallinities of these DMA specimens were controlled by DSC and were corresponding at ± 2% to those mentioned in Table 1.

STOCHASTIC TMDSC

After sample preparation and thermal history removal described in the previous section, stochastic TMDSC measurements were conducted using the TOPEM® technique from Mettler Toledo at an average heating rate of 2 K/min with a scanning temperature ranging from 25 to 125°C. The pulse amplitude was fixed at ± 0.25 K for all the experiments and the stochastically distributed periods were ranging from 15 to 30 s. The calculation window width was fixed to 120 s and the smoothing window to 90 s. The evaluations were made on the measured heat flow. These calculation parameters were chosen in line with the sensor time constant and the sample masse, giving the best signal according to the apparatus and these samples. For the calculation of the CRR size, the complex heat capacity, C_p*, was considered at a frequency of 16 mHz. From the $C_p*_{(16\ mHz)}$ signal, the in-phase component noted $C_p'_{(16\ mHz)}$ and the out of phase component noted $C_p''_{(16\ mHz)}$ were obtained.

CONVENTIONAL DSC FOR KINETIC COMPUTATIONS

Immediately after the thermal program presented in 2.3a and erasing the thermal history, the PEF and PET samples were subjected to heating throughout the glass transition via regular DSC. The measurements were conducted at heating rates of 10, 20 and 40 °C/min from 25 °C to 140 °C. The DSC curves were utilized to obtain normalized heat capacity curves thus allowing kinetic computations. From the DSC temperature programs afore mentioned the samples of different crystallinities were prepared. Computation of the activation energy (E_α)

of the glass transition was performed using standard DSC at heating rates of 10, 20 and 40 °C/min. ICTAC kinetics committee recommendations for collecting thermal analysis data for kinetic computations and for performing kinetic computations on thermal analysis data were followed.[10,11]

2.3 COMPUTATIONAL METHODS

SIZE OF THE COOPERATIVE REARRANGING REGION (CRR, ξ^3_{Tg})

The CRR is defined as a "subsystem" in metastable equilibrium which can rearrange its configuration into another, independently of its environment. Each CRR has its own glass transition temperature and its own free volume, both linked to its own relaxation time value. The size of the CRR derived from the molecular-kinetic theory of Adam and Gibbs gives a spatial aspect of dynamic heterogeneity because an average value of the relaxation time is obtained. This average volume of CRR at T_α is determined from the thermodynamic fluctuation formula of Donth in Equation (1).[6,12,13,14]

$$\xi^3{}_{T_g} = \frac{k_B T_g^2 \Delta\left(C_v^{-1}\right)}{\rho(\delta T)^2} \qquad (1)$$

Where k_B is the Boltzman constant, T_g is the glass transition measured at the maximum of the loss heat capacity (C_p'') peak from stochastic TMDSC or the maximum of the loss modulus E'' for DMA and ρ the density. C_v represents the isochoric heat capacity. It is assumed that difference between the heat capacity step at constant pressure and at constant volume is negligible, so we can estimate as per Equation (2).

$$\Delta(1/C_v) \approx \Delta(1/C_p) = (1/C_p)_{glass} - (1/C_p)_{liquid} \qquad (2)$$

$(\delta T)^2$ is the mean square temperature fluctuation related to the dynamic glass transition of one CRR, which can be derived from a Gaussian fit of the imaginary part of the C_p'' obtained with stochastic TMDSC experiments. Such a fit can be constructed using Eq. (3) and (4).[15,16]

$$C_p^{''} = y_o + \frac{A}{w\sqrt{\pi/2}} \exp\left(-2\left(\frac{T - T_\alpha}{w}\right)^2\right) \tag{3}$$

$$w = \frac{2\delta T}{\sqrt{\ln(4)}} \tag{4}$$

Where w is the standard deviation, δT is the dispersion of the Gauss transformation, T the temperature at a given point within the distribution, T_g the maximum peak temperature of the $C_p^{''}$ curve, y_o and A constants. Following the same idea, the $E^{''}$ curves can be fitted by Eq. (3) and it allows to obtain δT necessary for Eq. (1). Moreover, a CRR contains a number of monomeric units (N_α) determined following Equation (5).

$$N_\alpha = \frac{\xi^3 T_\alpha \rho N_A}{M_0} \tag{5}$$

With ρ as the density, N_A as Avogadro's number and M_0 as the molecular weight of the monomeric unit.

GLASS TRANSITION KINETICS

The extent of conversion during the glass transition α, can be evaluated from DSC data with the normalized heat capacity[17] as per Equation (6).

$$C_p^N = \frac{(C_p - C_{pg})\big|_T}{(C_{pe} - C_{pg})\big|_T} \tag{6}$$

where C_P is the observed heat capacity, and C_{pg} and C_{pe} are respectively the glassy and equilibrium (liquid) heat capacity. Because the values of C_{pg} and C_{pe} are temperature dependent, they must be extrapolated into the glass transition region. According to Hodge[17] the C_p^N value provides a precise approximation to the temperature derivative of the fictive temperature. This procedure was applied to the glass transition measured on heating after rapid quenching with nitrogen.

3 RESULSTS & DISCUSSION

3.1 DSC INVESTIGATION

Figure shows the quasi-static heat capacity C_P^0 variation of the PEF and PET samples obtained from stochastic TMDSC measurements on heating. The glass transition on heating corresponds to the transition from the non-equilibrium glassy state to a metastable rubbery state and is marked by a well-known heat capacity sigmoidal increase. Although it is known to be difficult to determine absolute C_P values, an average value of three to six stochastic TMDSC experiments for PEF and PET is presented for the glassy state and rubbery state of both materials in Table 2.

Table 2 – Absolute heat capacity values obtained by stochastic TMDSC on amorphous PEF and PET samples.

Material	C_p [J.g^{-1}.°C^{-1}]			C_p [J.mol^{-1}.°C^{-1}]		
	Glass (50°C)	Rubber (95°C)	($C_{p,95°C}$ - $C_{p50°C}$)	Glass (50°C)	Rubber (95°C)	($C_{p,95°C}$ - $C_{p,50°C}$)
PEF-am	1.18 ± 0.10	1.76 ± 0.10	0.58 ± 0.02	215 ± 17	321 ± 20	105 ± 5
PET-am	1.20 ± 0.11	1.67 ± 0.14	0.47 ± 0.03	230 ± 22	321 ± 27	90 ± 5

It can be seen that no significant differences were found between the absolute C_P values of PEF and PET both on a weight and on a molar basis, however it was found that the relative difference between the glassy and the rubbery state is significantly higher for PEF than for PET. The thermodynamic parameters of this transition such as T_g and ΔC_P are gathered in Table 3. The PEF-am exhibits slightly higher T_g (+5 °C) compared to PET-am. In agreement with previous reports,[18,19] this indicates that chain motions are more constrained in PEF thus leading to higher T_g. Focusing on the actual heat capacity step-increase of a fully amorphous sample at the inflection temperature, $\Delta C_P^{0\%}$ values could be found at ~0.34 J.g^{-1}.K^{-1} (~ 65.3 J.mol^{-1}.K^{-1}) for PET and at ~ 0.47 J.g^{-1}.K^{-1} (~ 85.5 J.mol^{-1}.K^{-1}) for PEF. The value for PET is

in good agreement with previous literature,[20] but the higher $\Delta C_P^{0\%}$ of PEF lies more in the range reported for PLA (~ 0.48 $J.g^{-1}.K^{-1}$).[3,21]

During the α-relaxation process that occurs between these states, the increase in heat capacity denotes changes from vibrational motions in the solid glass to large amplitude motions such as rotations in the liquid state. To strictly compare the ΔC_P values between different polymeric structures, Wunderlich proposed to adopt a calculation of $\Delta C_P^{0\%}$ per mol of beads. The beads are the smallest molecular units whose movements may change the "hole equilibrium".[20] For instance the PET contains five beads which are respectively the two CH_2, the two carboxylate (-O-C=O) and the benzene ring. Following this approach, PET exhibits a $\Delta C_P^{0\%}$ value of ~13.1 $J.K^{-1}$ per mol of beads and PEF a $\Delta C_P^{0\%}$ of ~17.1 $J.K^{-1}$ per mole of beads. Such a normalized heat capacity increment is particularly high in PEF in comparison with glass forming liquids or polymeric glasses for which ΔC_P per mole of beads was found to be approximatively constant at 11 ± 3 $J.K^{-1}.mol^{-1}$.[20] These results might indicate that the assumption of five beads per unit would not stand for PEF as in PET. Instead of reasoning per beads size which can be somehow arbitrary, other authors have shown that ΔC_P x T_g = constant.[22,23] Then, in agreement with the Hirai-Eyring theory,[24] ΔC_P should decrease when T_g increases. Thus, the PEF presents an exception because both ΔC_P and T_g are increasing. As ΔC_P is directly linked to the free volume, it indicates that the spaces between neighbouring molecular chains, facilitating their cooperative motions, are higher in PEF than in PET. This result is in good agreement with Burgess et al.[25] who have shown that PEF exhibits higher fractional free volume in comparison to PET. As those authors have also indicated, the higher free volume in PEF might be explained by the geometry of the furan ring in contrast with the benzene ring. As demonstrated by Wu et al.[26], the angle between the two carboxylic groups in FDCA is ~130° which is considerably less linear than in the terephthalic acid where the angle is about 180°, which might prevent efficient packing of the chains. In addition, the free

electron-doublet of the furan oxygen hetero-atom could induce additional electrostatic repulsion compared to a phenyl ring. Both of these molecular aspects could explain the higher free volume in PEF, and by extension the higher C_P increment at glass transition, compared to the highly linear PET. Opposing these volumetric considerations, it has previously been proposed that the inherent chain mobility is slower in PEF due to hindered furan-ring flipping attributed to this absence of linearity.[25] Additionally, however, the furan ring can also be considered as a dienophile with a dipolar moment.[27] Then, it is likely that dipole-dipole interactions can also occur between the PEF chains. Both the decreased mobility and the potential dipole-dipole interactions can contribute to a higher T_g in comparison with PET in addition to a higher free volume.

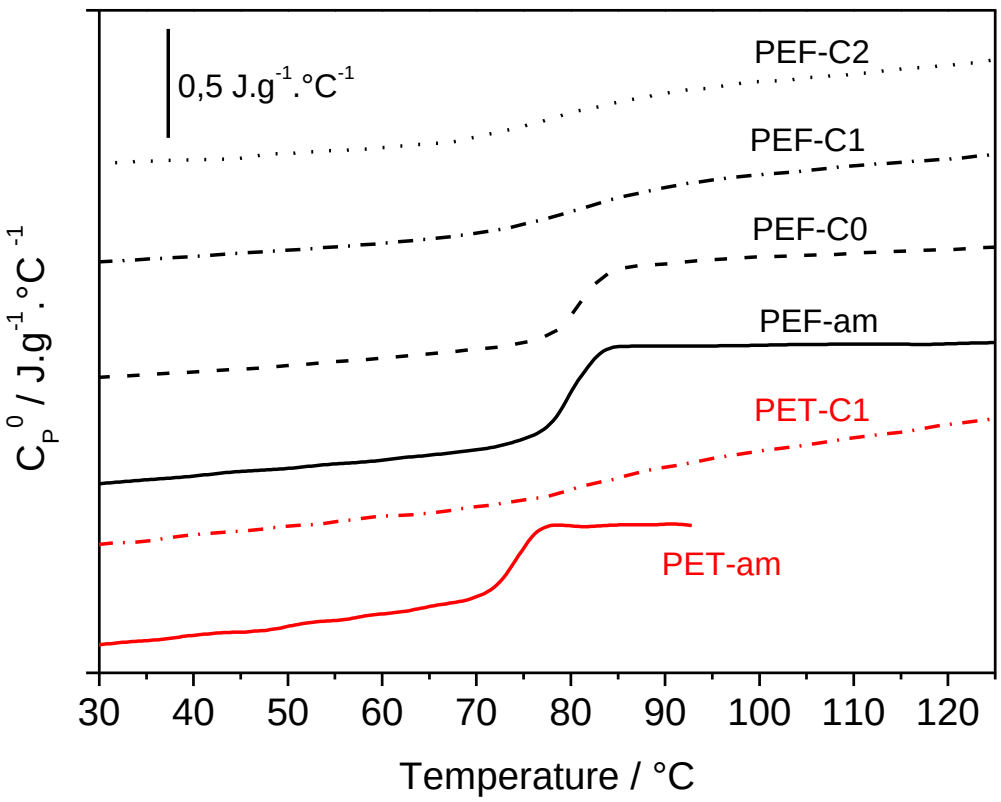

Figure 1 – Temperature dependence of the heat capacities C_P^0 of PEF-am (black solid line), PEF-C0 (black dashed line), PEF-C1 (black dashed dotted line) and PEF-C2 (black dotted line); temperature dependence of the heat capacities C_P^0 of PET-am (red solid lines) and PET-C1 (red dotted line).

Figure 1 and Table 3 show the effect of crystallinity on the relaxation behaviour of PEF and PET compared to the fully amorphous materials, which displays a different response. For both polyesters, the heat capacity increment at the glass transition decreases in presence of crystallites. Equation (7) allows to calculate the mobile amorphous fraction, in which ΔC_P is the heat capacity step at T_g for a crystallized sample, and $\Delta C_P^{0\%}$ for a completely amorphous sample corresponding to a perfect mobile amorphous sample. As mentioned before, the $\Delta C_P^{0\%}$ values of PEF and PET were respectively taken at 0.47 $J.g^{-1}.K^{-1}$ and 0.34 $J.g^{-1}.K^{-1}$. In certain cases, $X_{MAF} + X_c$ are lower than 1 which means incomplete decoupling between the crystalline and the amorphous phase. Consequently, the rigid amorphous fraction (RAF) should be also considered as a third phase and is calculated using Equation (8).

$$X_{MAF} = \frac{\Delta Cp}{\Delta C_p^{0\%}} \quad (7)$$

$$X_{RAF} = 1 - X_c - X_{MAF} \quad (8)$$

With X_c being the crystallinity of the sample. For more accuracy, three replicates were performed for each sample. Therefore, the MAF and the RAF values in Table 3 correspond to the mean value of the three replicates with the standard deviation.

In agreement with previous reports,[2,3] PET can be described by the three-phase model. Indeed, PET-C1 contains ~25 % of RAF (Table 3) and the remaining mobile amorphous phase becomes even more rigid and constrained as suggested by the shift of T_g to higher temperature (around 8 °C). The crystallites present in PET are strongly influencing the amorphous phase. For PEF, the influence of crystals is slightly less pronounced. First, the PEF-C0 which already contains about 20% of crystals can be described by a two-phase model (i.e. no RAF) with practically no influence of the crystals on the relaxation of MAF (Table 3) as shown by a nearly constant value of T_g. After completion of the primary crystallization, PEF-C1 exhibits

~ 7 % of RAF which is significantly lower than in PET-C1 (~ 25 %). While being broader, the absence of T_g increase versus PEF-am (Table 3) indicates that MAF is not subjected to major influences of crystallites. Moreover, the uncertainties tend to increase with the degree of crystallinity because the C_P variation broadens and becomes progressively lower.

Table 3 – Experimental parameters obtained by stochastic TMDSC on amorphous and crystallized PEF and PET samples.

Samples	X_c[a] (%)	T_g[b] (°C)	ΔC_p[c] ($J.g^{-1}.K^{-1}$)	X_{MAF}[d] (%)	X_{RAF}[e] (%)
PEF-am	0	81 ± 1	0.47	100	0
PEF-C0	20	82 ± 1	0.38	80 ± 3	0
PEF-C1	31	82 ± 1	0.26	55 ± 4	7 ± 4
PEF-C2	43	79 ± 2[f]	0.24	51 ± 7	6 ± 7
PET-am	0	76 ± 1	0.34	100	0
PET-C1	34	84 ± 1	0.14	41 ± 3	25 ± 3

[a] Degree of crystallinity calculated with ΔH^0_m = 140 $J.g^{-1}$, [b]glass transition temperature taken on the C_p'' curve, [c]heat capacity step at the glass transition. The standard deviation is ± 0.05 $J.g^{-1}$, [d]Mobile amorphous fraction, [e]rigid amorphous fraction, [f]higher error value explained by a broader T_g peak

The increased decoupling between the crystalline and the amorphous phases in PEF compared to PET could be explained by the higher free volume in PEF discussed previously, i.e. the larger degree of freedom caused by the less linear arrangement of PEF chains makes the confinement by the crystalline lamellae less efficient. Additionally, the morphology of the crystals may affect the way in which the crystals interact with the amorphous phase. Generally, the progressive presence of crystals induces a broadening of the glass transition in PEF (Figure 1), but seems unable to create a large amount of RAF and increase the T_g, as in PET.[13]

3.2 DMA ANALYSIS

To get additional information on the influence of crystalline phase on the relaxation behaviour, the samples were subjected to mechanical strain by means of DMA. Figure 2 displays the elastic modulus (*E*') measured vs. temperature on heating for the different PEF and PET samples under study. It should be noted that the elastic moduli in the glassy state are slightly higher for the PEF samples. In agreement with the work of Burgess et al.[25] it confirms that the PEF chains are more rigid than those of PET.

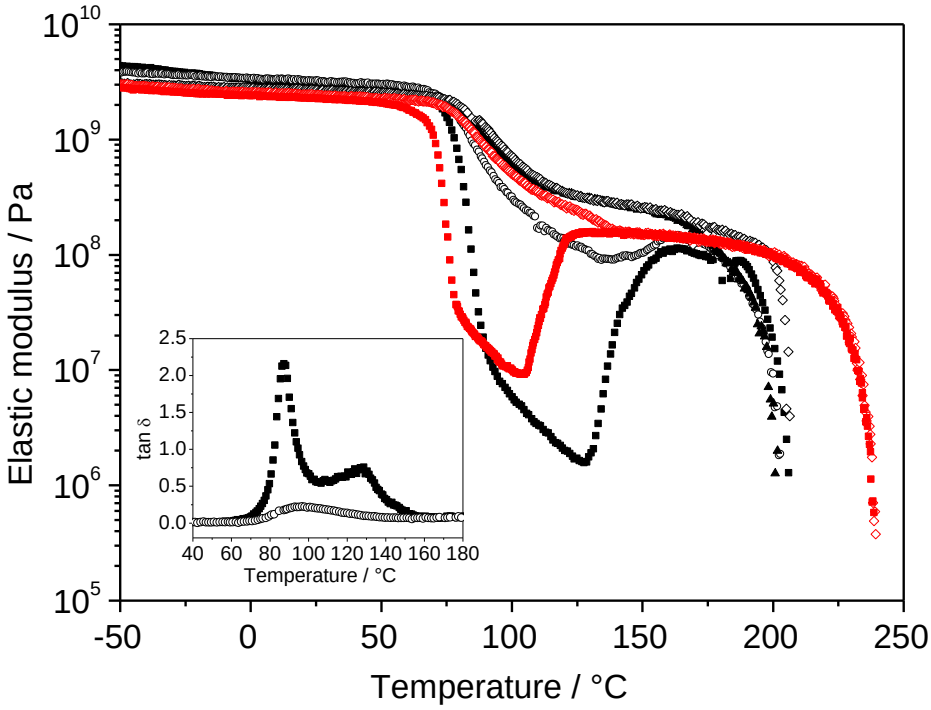

Figure 2 – DMA curves of elastic modulus (*E'*) and tan δ (inset) versus temperature for PEF-am (black solid squares), PEF-C0 (black open circles), PEF-C1 (black solid triangles) and PEF-C2 (black open diamonds) and for PET-am (red solid squares) and PET-C1 (red open diamonds). Inset: tan δ vs temperature for PEF-am (solid squares) and PEF-C2 (open circles).

The DMA curves of the amorphous samples show three major mechanical events (Figure 2). First a significant decrease of *E*' is noticed for PEF and PET in the temperature range between 70-125 °C and 60-105 °C respectively which is attributed to the α-relaxation process. This drop is higher for PEF than PET, which is consistent with previous observations[19,25] and is likely caused by the lower chain entanglement density in PEF. Although a clear rubber

plateau is not reached, the trend indicates a lower plateau value for PEF than PET and therefore a higher molecular weight between entanglements, matching well with earlier findings.[19] The second event highlighted on the amorphous curves in Figure 2 is an increase of the modulus that can be attributed to cold crystallization on heating. The temperature range corresponding to the crystallization process is much larger for PEF, which is consistent with its slower crystallization kinetics compared with PET described in the previous chapters. Finally, the last drop of modulus is associated with the melting of crystals.

For the semi-crystalline samples the *E*' in the glassy state are significantly higher compared to the fully amorphous materials (Figure 2). PEF-C0 presents a small increase of the modulus in the rubbery state which is consistent with completion of the cold crystallization, analogous to PEF-am. PEF-C1 demonstrates an overall higher modulus in the rubbery state compared to PET-C1. In agreement with DSC data in previous chapters and other work[18,19] the PEF crystals melt at lower temperature, although the crystals in PEF-C2 melt at higher temperature and thus seem to be more stable than those of PEF-C1 (Figure 2), which could be a result of lamellar thickening occurring during annealing at 205°C.

To emphasize more on the relaxation process, the evaluation of the loss modulus (*E*") peak and the tan δ peak gives complementary information on the different modes of molecular motions.[28] The maximum of the *E*" peak is generally associated with local segmental motions (LSM) of polymer chains. On the other hand, the maximum of the tan δ peak is rather ascribed to the Rouse modes (RM) which are larger molecular motions of subsystems containing several repeat units of the main chain.[29] The RM, which are entropic in nature, occur at higher temperatures in comparison with the LSM and are not detected by DSC.[30] Figure 3 shows the evolution of the *E*" curves obtained for the amorphous and semi-crystalline samples. The inset in Figure 2 shows the tan δ curves obtained for PEF-am and

PEF-C2. In addition to the curves, the Table 4 gathers the T_g values obtained respectively at the maximum of the *E*" peak ($T_{g(E")}$) and the tan δ peak ($T_{g(tan\delta)}$). Compared to PET-am, PEF-am has both a higher $T_{g(E")}$ and $T_{g(tan\delta)}$ which means that the both short (i.e. LSM) and large motions (i.e. RM) are more hindered in PEF. Moreover, the relaxation spectrum (i.e. the temperature range on which the different motional processes occur) is broader in amorphous PEF compared to PET. Indeed the difference between $T_{g(E")}$ and $T_{g(tan\delta)}$ is about 9 °C for PEF while it is only 5 °C for PET. This can be easily connected to the distribution of the free volume holes. In LSM, the segments need smaller free volume holes to move while in RM larger free volume holes are necessary. As mentioned earlier, the PEF chain is less linear than PET and thus possesses less anisotropic axial motions. This could explain the broader distribution of free volume holes found in PEF. These results also correlate the higher ΔC_p found for PEF at the glass transition.

Table 4 – T_g values ($T_{g,max\ E"}$, $T_{g,max\ tan\delta}$) obtained from DMA curves on amorphous and crystallized PEF and PET.

Samples	X_c [a] (%)	$T_{g(max\ E")}$ [a] (°C)	$T_{g,(max\ tan\delta)}$ [a] (°C)
PEF-am	0	78.4	87.2
PEF-C0	20	80.2	89.8
PEF-C1	31	83.8	92.8
PEF-C2	43	87.8	96.6
PET-am	0	72.1	77.2
PET-C1	34	83.8	92.7

[a]Degree of crystallinity calculated with $\Delta H^0_m = 140$ J.g^{-1}, [b]glass transition temperature taken at the maximum of *E''* curve and [c]temperature range at T_g, both with standard deviation ± 1°C

As shown in Figure 3 and Table 4, the semi-crystalline PEF and PET samples exhibit different relaxation behaviour compared to the amorphous samples. The semi-crystalline PEF samples show a progressive increase of both the $T_{g(E")}$ and $T_{g(tan\delta)}$ values with the crystallinity.

In comparison with PEF-am, this shift of $T_{g(E")}$ is about 1.8, 5.4 and 9.4 °C respectively for PEF-C0, PEF-C1 and PEF-C2. The relaxation *E"* peak also tends to broaden with the crystallinity.

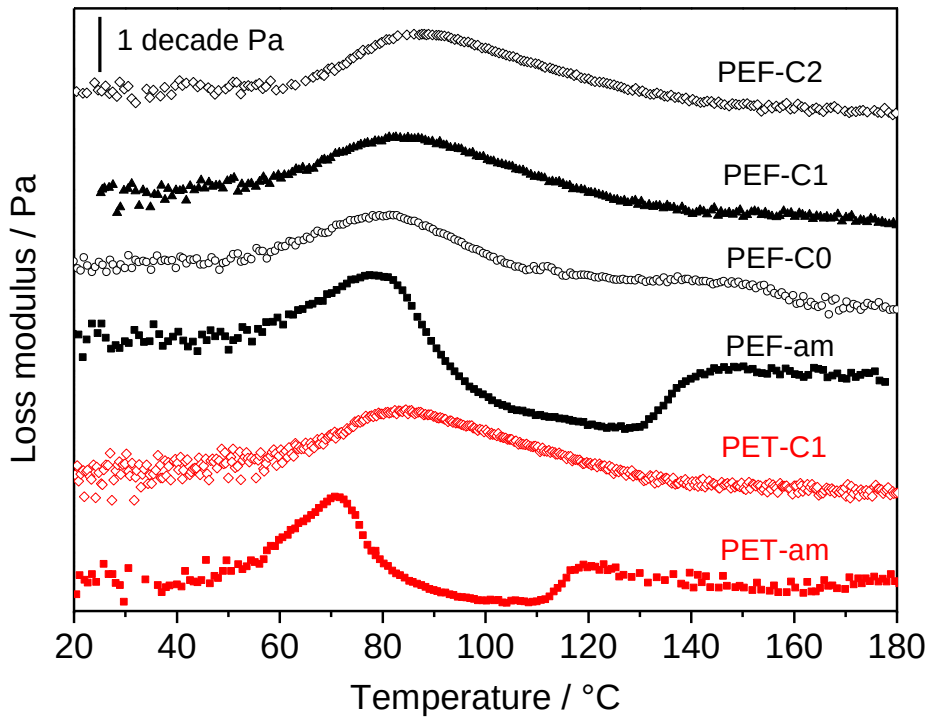

Figure 3 – Figure 3: Loss modulus curves (*E*") versus temperature of PEF-am (black solid square), PEF-C0 (black open circles), PEF-C1 (black solid diamonds) and PEF-C2 (black open triangles) and PET-am (red solid squares) and PET-C1 (red open diamonds).

These features indicate that the PEF crystals restrict the molecular mobility especially after lamellar thickening. It is worth noting that the difference between $T_{g(E")}$ and $T_{g(tan\delta)}$ remains of about 9 °C for all the PEF semi-crystalline samples as it was already the case for PEF-am (Table 4). It suggests that the restriction of mobility due to the presence of PEF crystals is the same for the different modes of molecular motions (i.e. both LSM and RM). On the other hand, the PET is much more affected by the presence of crystals compared to PEF. Interestingly the PET-C1 exhibits similar T_g values compared to PEF-C1. However, the $T_{g(E")}$ increment of PET-C1 is about 11.7 °C compared to PET-am, while it is only 5.4°C for PEF-C1. Moreover, the difference between $T_{g(E")}$ and $T_{g(tan\delta)}$ is about 9 °C for PEF-am while it was

only 5 °C in PET-am. Such results demonstrate that the PET crystals will restrict more the amorphous molecular motions compared to the PEF crystals and that this restriction is more pronounced for the entropic RM which implies larger motions. In comparison with PET, the less-marked influence of PEF crystals on the alpha relaxation process obtained from DMA confirms the above-mentioned conclusions from the DSC data. The sketch in Figure 4 depicts the coupling between the amorphous and the crystalline phase. The higher free volume found for PEF explain the lower coupling between the amorphous and crystalline phase and the lower restriction of amorphous mobility in comparison with PET.

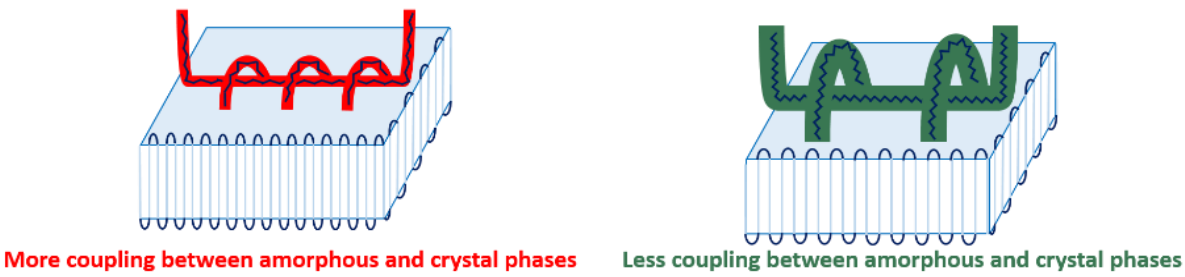

Figure 4 – Sketch representing the coupling between the amorphous phase and the crystalline phase for PET (red, left) and PEF (green, right).

3.3 ESTIMATION OF THE SIZE OF THE CRR FROM THERMAL DATA

The evaluation of the CRR size for amorphous and semi-crystalline samples give further insights on the effect of confinement due to the development of crystalline fractions. It should be noted that the CRR size is related only to the mobile amorphous regions and cannot be associated to the RAF. For this purpose, both DMA and stochastic DSC (TMDSC) data were employed. This last technique superimposes series of small stochastic temperature pulses on an underlying heating rate. The phase lag between the heating rate and the measured heat flow leads to frequency-dependent complex heat capacity, C_p* without need for other calibration procedures and that can be determined over a wide frequency range.[31] This complex heat capacity can be separated in two components namely the real part (C_p') and the imaginary part

(C_p”). In the glass transition region, C_p’ appears as a sigmoidal increase of the heat capacity while C_p” shows a peak whose maximum can be used to identify the glass transition temperature.

Figure 5 shows the C_p’ and C_p” curves obtained for the PEF-C0. The C_p’’ peak was fitted with a Gaussian function (Eq. 3) in order to obtain the values of T_g and δT required to calculate the ξ^3_{Tg} from Eq. 1. More detailed explanations on the determination of these parameters from temperature modulated DSC curves can be found elsewhere.[16] The $\Delta(C_v^{-1})$ values were calculated with Eq. 2 after estimation of the $(C_p^{-1})_{glass}$ and $(C_p^{-1})_{liquid}$ from the C_p’ curves normalized to the MAF content.

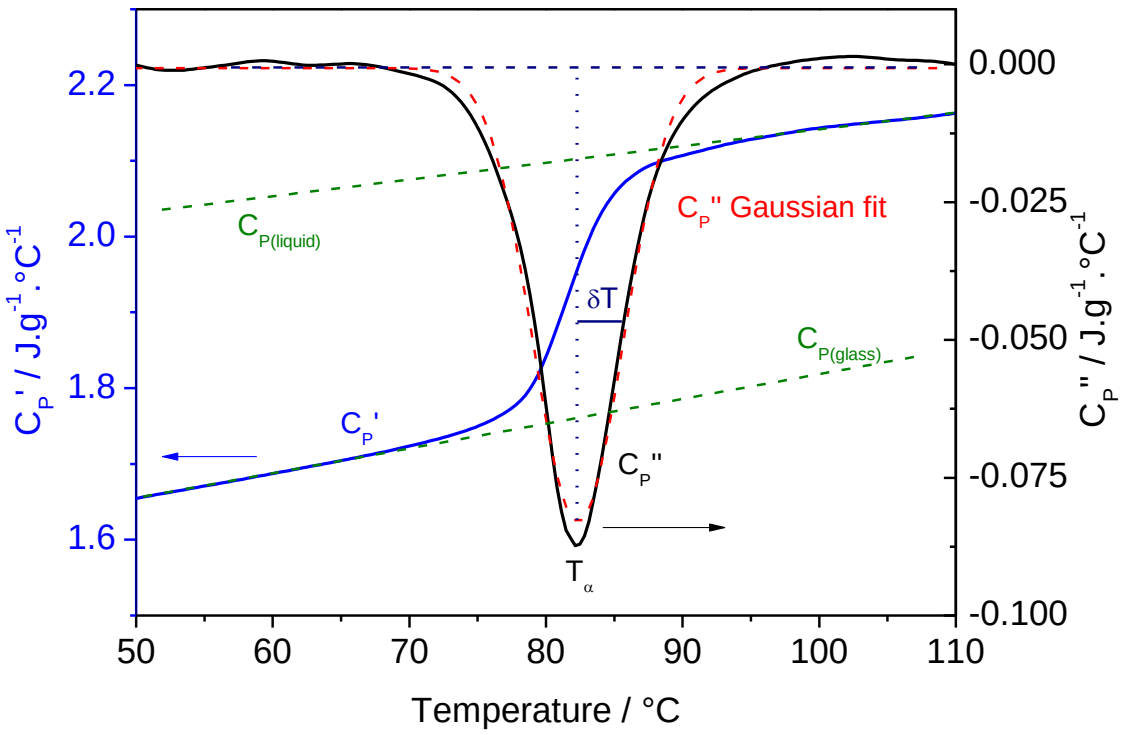

Figure 5 – Real (C_P’) and imaginary (C_P’’) parts of the complex heat capacity evaluated from stochastic TMDSC measurements. The figure shows how to estimate T_g, and δT for PEF-C0 sample at 16 mHz frequency. Red dash line corresponds to the Gaussian fit of C_P’’

Table 5 gathers the parameters obtained from the evaluation of the C_p’ and C_p” curves for amorphous and semi-crystalline samples. The temperature fluctuation (δT) of amorphous PEF is similar to the amorphous PET. Despite having a higher T_g, the length of CRR (ξ_{Tg}) is

comparable between amorphous PEF (2.8 nm) and amorphous PET (2.6 nm). The ξ_{Tg} is linked to the constraints in the mobile amorphous regions. The larger is the size of the fluctuating subsystem (ξ_{Tg}) and the less mobile are the relaxing entities. In addition to the T_g value itself, Equation (1) shows that the calculation of the CRR size also takes into account the dispersion zone of this transition (δT) and the so-called calorimetric relaxation strength (ΔC_p). The consideration of all these key thermodynamic parameters in the CRR size allows thus to describe more precisely the relaxation process. Then, the difference between the relaxation processes of two different polymers becomes more accurate when comparing (ξ_{Tg}) than just simply comparing the T_g values. Consequently, it appears that PEF-am and PET-am have comparable CRR size and, in other words, comparable length scale of the mobility pattern while the simple consideration of T_g simply indicate lower mobility for PEF. Indeed the higher ΔC_p found for PEF-am (and by analogy the higher ($\Delta(1/C_p)$) in comparison with PET-am directly compensates the higher T_g value. Comparable CRR size results in larger number of monomeric units per CRR for the PEF-am (~ 98 units), instead of 77 for PET-am, since the molecular weight per monomeric unit is lower in the furanic polyester ($M_{0\ (PEF)}$ = 182 g.mol^{-1} ; $M_{0\ (PET)}$ = 192 g.mol^{-1}).

The temperature fluctuation δT was also determined from the Gaussian fit of the loss modulus (E") obtained by DMA. Indeed, the calculation of CRR (eq. 1) is derived from the fluctuation-dissipation theorem and according to Donth[14] the term dissipation can come from the loss peak of susceptibilities. The susceptibilities can be compliance (entropy compliance, shear compliance) or modulus (e.g. shear modulus, elastic modulus, dielectric modulus, compression modulus, etc.). Then δT can be estimated from the Gaussian fit of the loss peaks of susceptibilities. Lixon et al.[32] and Delpouve et al.[33] have used the Gaussian fit of the loss modulus for the estimation of δT and have observed some deviations with the values obtained from TMDSC. The Figure 6 shows an example of the Gaussian fit used for the estimation of

δT from the loss modulus. For the calculation of the CRR length, the T_g values were taken at the maximum of the E" peak (Figure 6). Table 5 gathers the parameters obtained from the evaluation of the E" curves in DMA. Overall, the δT values obtained from the DMA evaluation are larger than those obtained from the calorimetric C_p" curves thus resulting in lower values of the CRR lengths. The temperature fluctuation of the amorphous phase in the semi-crystalline sample tends to increase with the amount of crystallite, excepted for samples subjected to annealing (PEF-C2) were secondary crystals have developed.

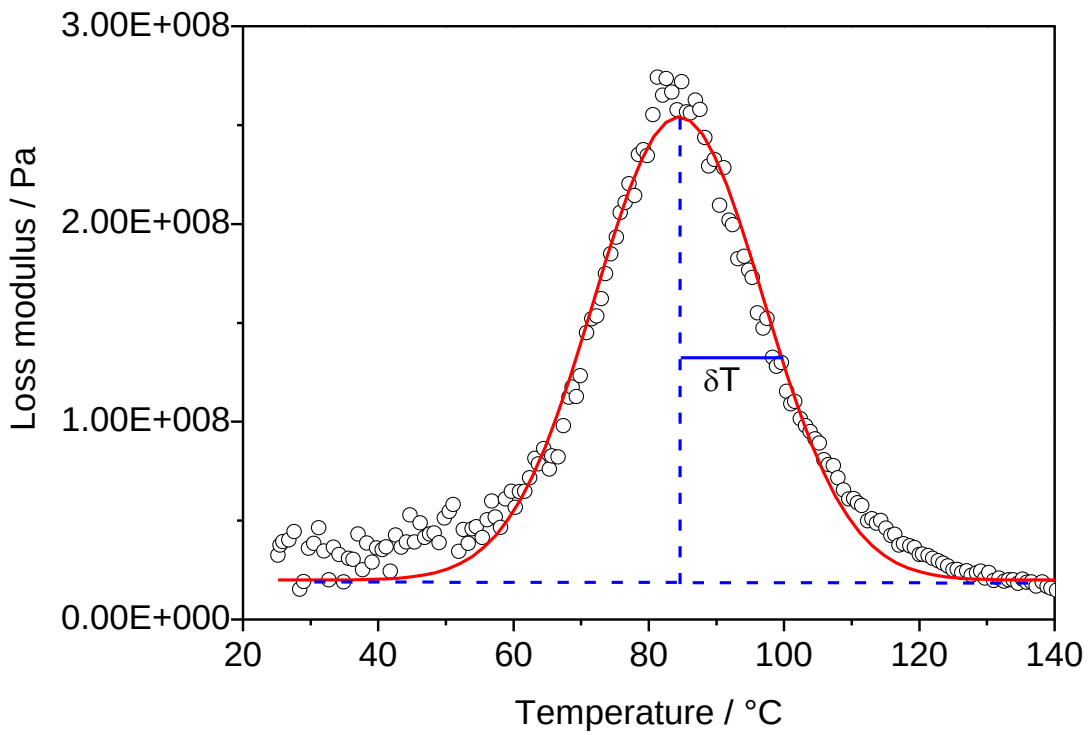

Figure 6 – Peak of loss modulus obtained by DMA for PEF-C1 sample. The red line corresponds to the Gaussian fit used to calculate the ξ_{Tg} size.

As shown in Table 5 and most explicitly in Figure 7, the CRR length of PEF decreases with increasing crystallinity.

Table 5 – Experimental parameters obtained from DMA and stochastic TMDSC on amorphous and crystallized PEF and PET

Samples	X_c[a] (%)	X_{RAF}[b] (%)	DSC			DMA		
			δT[c] (°C)	ξ_{Tg}[d] (nm)	N_α[e]	δT (°C)	$\xi_{T\alpha}$ (nm)	N_α
PEF-am	0	0	3.2	2.8	98	7.0	1.6	19
PEF-C0	20	0	3.9	2.3	59	11.2	1.4	7
PEF-C1	31	7±4	9.7	1.1	7	13.0	0.9	4
PEF-C2	43	6±7	8.9	1.1	7	11.8	0.9	4
PET-am	0	0	3.0	2.6	77	4.0	2.0	33
PET-C1	34	25±3	10.7	1.0	5	12.7	0.8	2

[a]Degree of crystallinity calculated with ΔH^0_m = 140 J.g^{-1}, [b]rigid amorphous fraction, [c]mean temperature fluctuation, [d]characteristic length of the CRR, [e]repeating units per CRR

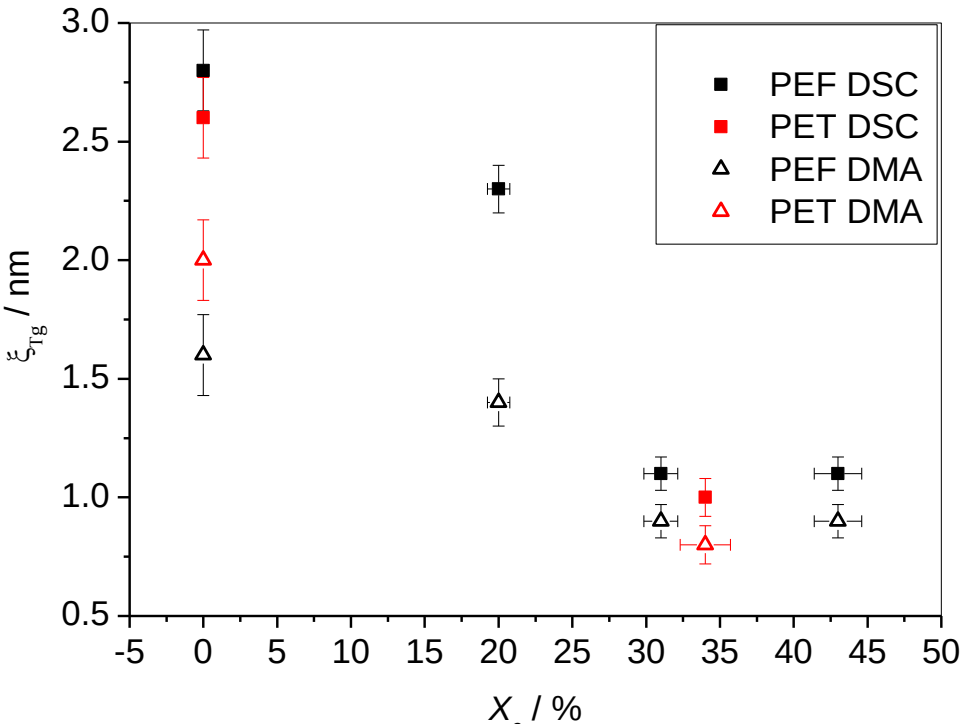

Figure 7 – Variation ξ_{Tg} as function to X_c for PEF (black points) and PET (red points) determined by DSC (filled) and DMA (open)

For PEF-C1, it thus leads to a CRR size of about 1.1 nm or 0.9 nm when calculation is done respectively from DSC or DMA data. The thermal annealing does not impact the size as the PEF-C2 and PEF-C1 both have similar CRR size. Several studies[34,35,36] have demonstrated that the CRR length, ξ_{Tg}, is proportional to the thickness of the amorphous mobile layer and

thus it progressively decreases when the crystalline fraction increases in agreement with the results of Table 5 and Figure 7. However, no correlation was found between the T_g values and the amorphous layer.[36] As shown in Figure 7, the PEF, in the same line as PET, also demonstrates a reduction of the CRR size under the confinement of the crystalline lamellae. In crystalline PEF (i.e. PEF-C1 and PEF-C2) the number of monomeric unit involved in one CRR drops to only few units (between 4 and 7).

3.4 GLASS TRANSITION KINETICS FOR PEF *vs* PET

Temperature dependence of the normalized heat capacity at various heating rates was obtained for PET and PEF by transforming regular DSC data according to Eq. (6). The results are presented in Figure 8. The C_P increment from the glassy state to the rubbery state follows a sigmoidal curvature. For the amorphous samples (i.e. PEF-am and PET-am), the peak going beyond the limit of the extent of conversion maximum ($C_P^N = 1$) corresponds to the signature of the amorphous relaxation on heating after physical aging. On the other hand, the partially crystalline samples do not exhibit such relaxation since the physical aging is reduced in that case. As observed in Figure 8 the glass transition on heating occurs in range between 60 and 110 °C and shift to higher temperature with increasing heating rate. In agreement with the stochastic DSC data or the DMA data, the C_P^N curves in Figure 8 shows that the relaxation of the PEF-C1 is much less influenced by the presence of crystals since the relaxation is less shifted to higher temperature in comparison with PET-C1.

The C_P^N data were treated with an advanced isoconversional method.[37,38,39] This method provide a way of obtaining kinetic parameters without any assumption on the mechanism of the transformation that can be a chemical reaction (polymerization, curing, thermal degradation) or a physical transition (crystallization, gelation, glass transition, melting).[10] These methods only assume that the mechanism is the same for a same value of the relative extent of conversion α and not for the whole temperature range where the transition occurs.

The extent of conversion reflects the relative degree of evolution of the transition with temperature. In the present study the E_α values were determined using a non-linear procedure described elsewhere. The software developed by N. Sbirrazzuoli was used to compute a value of E_α for each value of α lying in between 0.02 to 0.98 with a step of 0.02.[39,40,41]

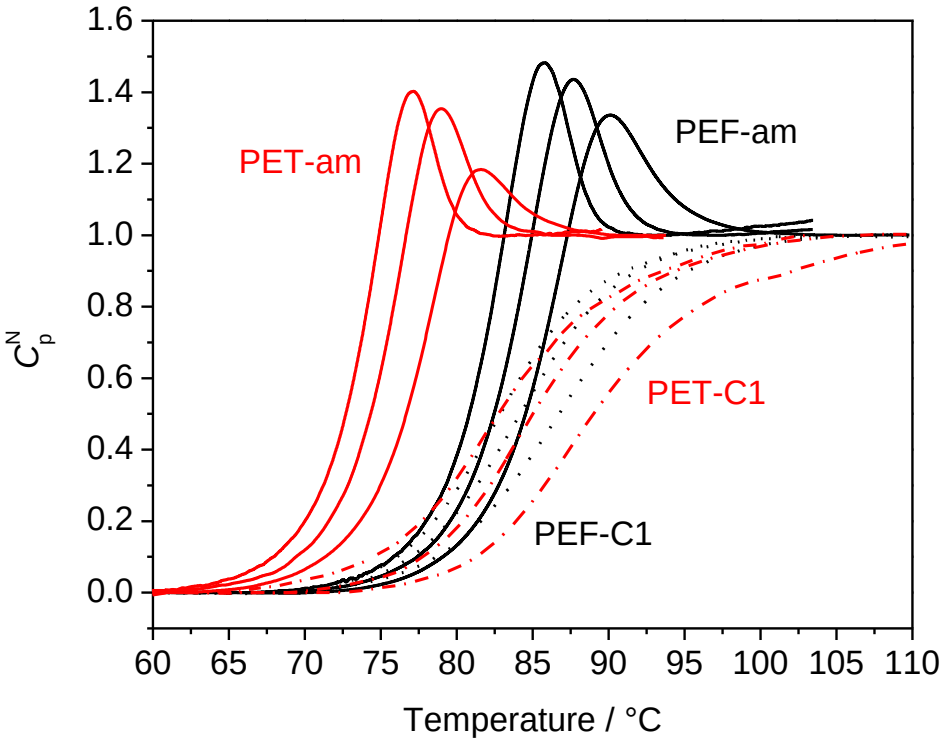

Figure 8 – Temperature dependence of the normalized heat capacity C_P^N determined for PEF-am (black lines), PET-am (red lines), PEF-C1 (black dotted lines) and PET-C1 (red dotted lines) at 10, 20 and 40 K.min^{-1}.

Figure 9a represents the variation of the effective activation energy (E_α) for both PET and PEF amorphous and semi-crystalline samples as a function of the extent of conversion. A decrease of the effective activation energy E_α with the extent of conversion is observed for all samples. A similar tendency was already obtained in previous works.[40,42,43] First, it is worth mentioning that this decrease cannot be attributed to the error generated by the overshoot of the amorphous relaxation because it is also observed for the semi-crystalline samples which do not undergo such relaxation (Figure 9). Additionally, fully amorphous epoxy resins which do not present any relaxation phenomena have also decreasing values of E_α with the extent of

the glass transition.[44] This significant decrease of E_α values can be interpreted in terms of cooperative motion of the chain segments. The glassy state is characterized by a very low molecular mobility that only allows for local motions of the chain segments. As the temperature rises, the molecular motion intensifies and translational motion of the segments and eventually of the whole chain becomes possible. This process requires a great degree of cooperativity between the chain segments, which is associated with a large energy barrier as reflected in the high value of the effective activation energy at the early stages of the transition, i.e., at low α values. However, as the temperature increases, the mobility becomes higher, which allows the chain segments to relax more independently, i.e., with a lower degree of cooperativity. This results in decreasing energetic constrains which is reflected in a decrease of the effective activation energy.

For PEF-am, E_α decreases from 450 to 300 kJ.mol^{-1}. This range is consistent with the sole reported value of 475 kJ.mol^{-1} found for the activation energy of the PEF glass transition by Burgess et al.[25]. As previously proposed,[42] a variability parameter, Δ_E, can be introduced to characterize the rate of change of E_α with temperature:

$$\Delta_E = \frac{E_{0.25} - E_{0.75}}{T_{0.25} - T_{0.75}} \qquad (9)$$

where $E_{0.25}$ and $E_{0.75}$ are the values of E_α at α = 0.25 and 0.75 respectively and $T_{0.25}$ and $T_{0.75}$ are the values of T_α for the respective α values.

It has been demonstrated that the variability of E_α at the glass transition (-Δ_E) increases with the index of the dynamic fragility, *m* in approximately exponential fashion.[42] This qualitative correlation was shown for various polymers and glass-formers. According to Angell[45,46],the fragility concept characterizes the departure from the Arrhenius temperature dependence of the relaxation time within and above the glass transition range. The “strong” glass-forming

liquids, which present low *m* values, exhibit an Arrhenian temperature dependence while the "fragile" glass-forming liquids (generally polymers) with high *m* values deviate from the Arrhenian behaviour. The temperature dependence of the fragile specimens is fitted with a Vogel-Tamman-Fulcher (VTF) model.[47,48,49]

Considering the data from Figure 9, the resulting Δ_E from Equation (9) were respectively -21.1 and -18.2 kJ.mol^{-1}.K^{-1} for PEF-am and PET-am. The rate of E_α decrease is thus of the same magnitude between the two polyesters in their amorphous state as it can be qualitatively observed from the E_α *vs* $f(T)$ dependences (Figure 9b). Following the idea of a correlation between Δ_E and the fragility, it would indicate similar index of fragility between PEF-am and PET-am. From the above Δ_E values and from the correlation already established for a series of glass formers,[42] we can estimate the index of fragility of PEF-am and PET-am at around $m \sim 125$ which is in good agreement with the *m* values found elsewhere for PET.[3] On the other hand, the variability parameters, Δ_E, differs between the two semi-crystalline samples. The resulting Δ_E value is reduced to ~ -10.3 kJ.mol^{-1}.K^{-1} for PEF-C1 and significantly reduced to ~ -0.1 kJ.mol^{-1}.K^{-1} for PET-C1 which indicates smaller and broader decrease in *E* compared to PET-am (Figure 9b). This can be associated with a severe decrease in the fragility index when the PET becomes semi-crystalline. Indeed, previous reports[3,50] have demonstrated that the semi-crystalline PET tends to go toward a "strong character" because the percentage of mobile amorphous phase becomes weaker. This is in perfect agreement with results of Table 3, where X_{MAF} drop to 41% for PET-C1 instead of 55% for PEF-C1. However, as shown in Figures 9a and 9b, the E_α decrease of PEF-C1 for $\alpha < 0.7$ compares well with the PEF-am dependence. The very slight E_α increase observed for $\alpha > 0.7$ is not consistent with general decreasing trends reported for different polymers[42] and might arise from experimental and computational uncertainties due to the very weak increase of α at the end of the curve. Focusing between $\alpha = 0.25$ and 0.75, the application of equation 9 to the data of PEF-C1 lead

to Δ_E ~ -10.3 kJ.mol^{-1}.K^{-1} which is lower compared to the PEF-am. Nevertheless, the decrease in Δ_E when the PEF becomes semi-crystalline is much less pronounced in comparison with the PET. It suggests that the appearance of the crystalline phase in PEF would have lower influence on the decrease of the fragility character and that the material remains mainly fragile. It follows the above-mentioned conclusions drawn from stochastic TMDSC and DMA data and in which the PEF crystals induce lower variation of the glass transition compared to PET due to the weaker coupling between the RAF and the MAF. Interestingly, the PLLA which demonstrates a weak coupling between crystal and amorphous phases exhibits comparable fragility index for the amorphous and the semi-crystalline materials.[3]

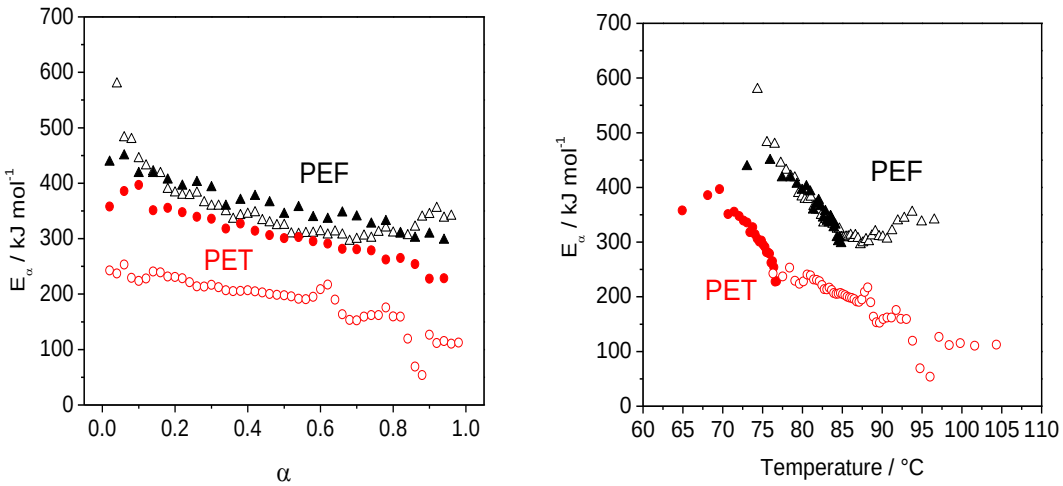

Figure 9 – Dependence of the effective activation energy E_α with (a) the extent of conversion and (b) with temperature for PEF-am (black solid triangles), PEF-C1 (black open triangles), PET-am (red solid circle) and PET-C1 (red open circles).

4 CONCLUSIONS

The glass transition of PEF and PET was investigated by means of stochastic TMSDSC and DMA. Amorphous PEF presents a higher relaxation extent (ΔC_P) and broader relaxation spectrum compared to PET. A reduced efficiency of chain packing in the glassy state generates higher free volume and larger distribution of free-volume holes. The higher T_g of PEF is thus purely related to segmental mobility and specific interactions in PEF. The higher

relaxation extent of amorphous PEF is compensating the more constrained mobility, resulting in comparable cooperativity length (ξ_{Tg}) for amorphous PEF and PET. The variability of E_α at the glass transition is also similar between the two amorphous polyesters, which indicates that PEF and PET exhibit a comparable fragility index.

The influence of crystallites on the amorphous relaxation of PEF was also investigated. Better decoupling between the crystalline and the amorphous phase is observed for PEF as suggested by the lower amount of RAF in comparison with PET. Compared to PET, the PEF crystals are less influencing the relaxation of the remaining amorphous phases. The effect of crystallinity on the reduction of E_α at the glass transition was less observed for PEF than for PET.

5 REFERENCES

[1] B. Wunderlich, *Prog. Polym. Sci.* 28 (2003), 383.
[2] R. Androsch and B. Wunderlich, *Polymer* 46 (2005), 12556.
[3] M. Arnoult, E. Dargent and J. F. Mano, *Polymer* 48 (2007), 1012.
[4] N. Delpouve, L. Delbreilh, G. Stoclet, A. Saiter and E. Dargent, *Macromolecules* 47 (2014), 5186.
[5] G. Adam and J. H. Gibbs, *J. Chem. Phys.* 43 (1965), 139.
[6] E. Donth, *J. Polym. Sci., Part B: Polym. Phys.* 34 (1996), 2881.
[7] M. Encinar, M. G. Prolongo, R. G. Rubio, F. Ortega, A. Ahmadi and J. J. Freire, *Eur. Phys. J. E: Soft Matter Biol. Phys.* 34 (2011), 114 pp.
[8] M. Encinar, E. Guzmán, M. G. Prolongo, R. G. Rubio, C. Sandoval, F. González-Nilo, L. Gargallo and D. Radić, *Polymer* 49 (2008), 5650.
[9] B. Wunderlich, *Macromolecular Physics, Vol. 3: Crystal Melting*, Academic Press, 1980.
[10] S. Vyazovkin, A. K. Burnham, J. M. Criado, L. A. Pérez-Maqueda, C. Popescu and N. Sbirrazzuoli, *Thermochim. Acta* 520 (2011), 1.
[11] S. Vyazovkin, K. Chrissafis, M. L. Di Lorenzo, N. Koga, M. Pijolat, B. Roduit, N. Sbirrazzuoli and J. J. Suñol, *Thermochim. Acta* 590 (2014), 1.
[12] E. Hempel, G. Hempel, A. Hensel, C. Schick and E. Donth, *J. Phys. Chem. B* 104 (2000), 2460.
[13] E. Donth, *Journal of Non-Crystalline Solids* 53 (1982), 325.
[14] E. Donth, *The Glass Transition: Relaxation Dynamics in Liquids and Disordered Materials*, Springer-Verlag, 2001.
[15] S. Weyer, A. Hensel, J. Korus, E. Donth and C. Schick, *Thermochim. Acta* 304 (1997), 251.
[16] C. Schick, *Eur. Phys. J. Spec. Top.* 189 (2010), 3.
[17] I. M. Hodge, *Journal of Non-Crystalline Solids* 169 (1994), 211-266.
[18] G. Z. Papageorgiou, V. Tsanaktsis and D. N. Bikiaris, *Phys. Chem. Chem. Phys.* 16 (2014), 7946.
[19] G. Stoclet, G. Gobius du Sart, B. Yeniad, S. de Vos and J. M. Lefebvre, *Polymer* 72 (2015), 165.
[20] B. Wunderlich, *The Journal of Physical Chemistry* 64 (1960), 1052.
[21] N. Delpouve, A. Saiter, J. F. Mano and E. Dargent, *Polymer* 49 (2008), 3130.
[22] R. F. Boyer, *Journal of Macromolecular Science, Part B* 7 (1973), 487.
[23] T. Hatakeyama and H. Hatakeyama, *Thermochim. Acta* 267 (1995), 249.
[24] N. Hirai and H. Eyring, *J. Polym. Sci.*, 37 (1959), 51.
[25] S.K. Burgess, J.E. Leisen, B.E. Kraftschik, C.R. Mubarak, R.M. Kriegel, W.J. Koros, Macromolecules 47 (2014) 1383.
[26] J. Wu, P. Eduard, S. Thiyagarajan, J. van Haveren, D. S. van Es, C. E. Koning, M. Lutz and C. Fonseca Guerra, *ChemSusChem* 4 (2011), 599.
[27] A. Gandini and M. N. Belgacem, *Prog. Polym. Sci.* 22 (1997), 1203.
[28] E. Donth, M. Beiner, S. Reissig, J. Korus, F. Garwe, S. Vieweg, S. Kahle, E. Hempel and K. Schröter, *Macromolecules* 29 (1996), 6589.
[29] J. D. Ferry, *Viscoelastic Properties of Polymers*, John Wiley & Sons, New York, 3rd edn., 1980.
[30] Z. Lei, W. Xing, J. Wu, G. Huang, X. Wang and L. Zhao, *J. Therm. Anal. Calorim.*116 (2014), 447.
[31] J. E. K. Schawe, T. Hütter, C. Heitz, I. Alig and D. Lellinger, *Thermochim. Acta* 446 (2006), 147.

[32] C. Lixon, N. Delpouve, A. Saiter, E. Dargent and Y. Grohens, *Eur. Polym. J.* 44 (2008), 3377.
[33] N. Delpouve, C. Lixon, A. Saiter, E. Dargent and J. Grenet, *J. Therm. Anal. Calorim.* 97 (2009), 541.
[34 C. Schick and E. Donth, *Phys. Scr.* 43 (1991), 423.
[35] C. Schick and J. Nedbal, *Prog. Colloid Polym. Sci.* 78 (1988), 9.
[36] E. Donth, E. Hempel and C. Schick, *Journal of Physics: Condensed Matter* 12 (2000), L281.
[37] N. Sbirrazzuoli, L. Vincent and S. Vyazovkin, *Chemom. Intell. Lab. Syst.* 54 (2000), 53.
[38] S. Vyazovkin and N. Sbirrazzuoli, *Macromol. Rapid Commun.* 27 (2006), 1515.
[39] N. Sbirrazzuoli, *Thermochim. Acta* 564 (2013), 59.
[40] N. Bosq, N. Guigo, E. Zhuravlev and N. Sbirrazzuoli, *J. Phys. Chem. B* 117 (2013), 3407.
[41] N. Sbirrazzuoli, A. Mititelu-Mija, L. Vincent and C. Alzina, *Thermochim. Acta* 447 (2006), 167.
[42] S. Vyazovkin, N. Sbirrazzuoli and I. Dranca, *Macromol. Chem. Phys.* 207 (2006), 1126.
[43] S. Vyazovkin, N. Sbirrazzuoli and I. Dranca, *Macromol. Rapid Commun.* 25 (2004), 1708.
[44] C. Alzina, PhD thesis, University Nice Sophia Antipolis, 2009.
[45] C. A. Angell, *Journal of Non-Crystalline Solids* 131 (1991), 13.
[46] C. A. Angell, *Science* 267 (1995), 1924.
[47] H. Vogel, *Phys. Z.* 22 (1921), 645.
[48] G. Tamman and W. Hesse, *Z. Anorg. Allg. Chem.* 156 (1926), 245.
[49] G. S. Fulcher, *Journal of the American Ceramic Society*, 8 (1925), 339.
[50] E. Dargent, E. Bureau, L. Delbreilh, A. Zumailan and J. M. Saiter, *Polymer* 46 (2005), 3090.

CHAPTER 7
MELT AND AMORPHOUS GLASS MECHANICS OF PEF *vs* PET

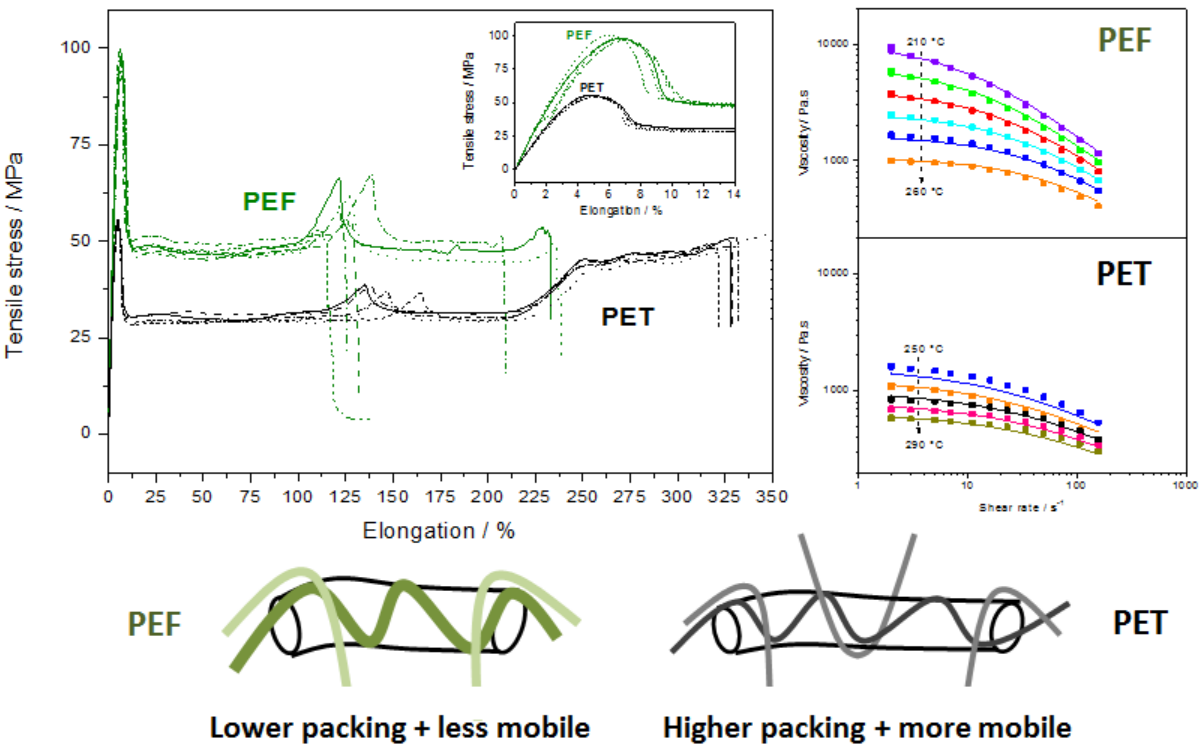

This chapter investigates the mechanics of molten and amorphous poly(ethylene 2,5-furandicarboxylate) as a function of its molecular weight in comparison to poly(ethylene terephthalate). Molecular weight and solution viscosity were both analyzed for the selected materials. Subsequently, the dependence of the melt viscosity on molecular weight, temperature and shear rate was evaluated for PEF using plate-plate rheometry and described mathematically using known methods in comparison to PET literature data in reference samples. The dynamic tensile behavior was also investigated for both materials. The observed differences in the mechanics of both materials could be explained by the difference in glass transition temperature and entanglement density.

1 INTRODUCTION

The mechanics of polymers in the molten and glassy state are intrinsic behavior determined by their chemical structure, and set many of the boundary conditions for their applicability. Polymer behavior in the molten state determines the melt processability through common practices, such as injection molding or extrusion into sheets, tubes or filaments through various shapes of dies. The glassy state behavior, on the other hand, affects the structural integrity of melt processed articles such as bottle preforms and cast film as well as direct end-use of molded parts. Both of these aspects of polymer behavior are dependent on temperature and deformation rate and have a strong relation to molecular weight. Indeed, for end-use applications the molecular weight is typically chosen as a compromise between melt processability and glassy state properties; a higher molecular weight improves glassy properties, such as ductility, while the resulting higher viscosity reduces melt processability. It is also generally accepted that a critical molecular weight exists above which the polymer chains form entanglements. These entanglements give rise to typical polymeric viscoelastic behavior such as defined tensile, shear and bulk moduli and transitions such as the β- and α-relaxations or glass-transition.[1,2]

PET is often used to exemplify the relationships existing between molecular weight, solution viscosity, viscoelastic behavior and mechanical properties for polymers in general since for it, those relationships have been reported from the 1960's through the 1980's.[3,4,5,6,7] Furthermore, Farrow et al.[8] in the same period showed the progression of the transition temperatures for PTA-based polyesters with longer diols, something which has recently been reviewed by Papageorgiou et al. for FDCA-based polyesters.[9] Later work in this period also compares the influence of isophthalic acid (IPA) on the critical molecular weight to form entanglements compared to PET.[10] Furthermore Kamide et al. similarly looked into the dynamics of PET and a polyester of a more flexible aromatic diacid, 1,2-diphenoxyethane-p,p'-dicarboxylic acid.[11]

The present work establishes basic relations for the solution viscosity, melt viscosity and mechanical properties of PEF to molecular weight, including a direct comparison to PET to rationalize similarities and differences based on the difference in molecular structure.

2 EXPERIMENTAL

2.1 MATERIALS

An overview of the materials used in this study is given Table 1. PEF samples were prepared either from dimethyl 2,5-furandicarboxylic acid (DMFDCA) or 2,5-furandicarboxylic acid (FDCA). In the case of DMFDCA, two 50 L stainless steel reactors were used in which the first reactor was equipped with a long distillation column for controlled distillation of methanol to conduct trans-esterification, whereas the second reactor was employed with a wall-scraping anchor stirrer for high vacuum polycondensation into PEF. The trans-esterification reaction was aided by calcium acetate or titanium isopropoxide as catalysts, and antimony trioxide was added as a polycondensation catalyst. In the case of FDCA, a single 50 L stainless steel reactor was used for the slurry esterification with ethylene glycol under

distillation of water and the subsequent polycondensation into PEF, in which Antimony Trioxide is used as the catalyst. The PEF materials were subsequently pelletized via strand-cutting and either used as is, or after solid state polycondensation in a vacuum tumbledryer. PET 1 was obtained from terephthalic acid via the same equipment as PEF from FDCA, whereas PET 2, 3 were commercial PET samples from Indorama Polymers, namely RamaPET W170 and Auriga 1101E.

Table 1 – Overview of materials used in this study.

Material	Monomer	SSP	$[\eta]$ (dL/g)	$M_{n,\,PS}$ (kg/mol)	$M_{w,\,PS}$ (kg/mol)	$M_{n,\,3SEC}$ (kg/mol)	$M_{w,\,3SEC}$ (kg/mol)	PDI_{3SEC} (-)
PEF-Ti/Sb 1	DMFDCA	No	0.35	14.0	30.0	9.7	19.6	2.0
PEF-Ti/Sb 2	DMFDCA	Yes	0.81	31.0	80.0	24.5[a]	55.1[a]	2.2
PEF-Ti/Sb 3	DMFDCA	Yes	0.83	31.3	87.3	24.2	61.2	2.5
PEF-Ca/Sb 1	DMFDCA	No	0.41	14.1	34.0	10.0[a]	23.0[a]	2.3
PEF-Ca/Sb 2	DMFDCA	Yes	0.60	24.2	54.4	19.7	42.2	2.1
PEF-Ca/Sb 3	DMFDCA	Yes	0.73	28.5	68.2	28.0	55.0	2.0
PEF-Sb 1	FDCA	No	0.54	23.2	52.8	15.7	31.8	2.0
PEF-Sb 2	FDCA	Yes	0.79	34.9	79.5	26.5	51.1	1.9
PEF-Sb 3	FDCA	Yes	0.88	38.7	89.4	29.7	56.8	1.9
PET-Sb 1	TPA	No	0.61	25.5	56.3	19.7[a]	38.5[a]	2.0
PET-Sb 2	TPA	Yes	0.74	33.5	71.9	28.5[a]	49.4[a]	1.7
PET-Sb 3	TPA	Yes	0.82	40.1	85.3	32.8[a]	58.8[a]	1.8

[a]Interpolation using $M_{n,\,3SEC}=0.1958\cdot M_{n,\,PS}^{1.1351}$ and $M_{w,\,3SEC}=0.5418\cdot M_{w,\,PS}^{1.0212}$

The intrinsic viscosity $[\eta]$ of all samples was measured according to ASTM D4603 using a mixture of 40% Phenol and 60% Tetrachloroethane by weight at 30°C. The number and weight average molecular weights were determined via two Gel Permeation Chromatography methods. The first method has previously been reported by Sipos et al.[12], employing classical callibration to polystyrene standards in a mixture of 40% 2-Chlorophenol and 60% Chloroform by weight, from which the results are reported as $M_{n,PS}$ and $M_{w,PS}$ in Table 1. The second method used 1,1,1,3,3,3-hexafluoro-2-propanol (HFIP), a more common solvent used for polyesters due to the high solubility and high refractive index response d*n*/d*c*, in combination with triple detection to estimate the absolute molecular weight moments, reported as $M_{n,\,3SEC}$ and $M_{w,\,3SEC}$ in Table 1. For PEF Ti/Sb 2 and PEF Ca/Sb 1 the molecular

weight distribution was not measured in HFIP but interpolated from the other results using the power law relations described below the table. This relation was derived from the actual values, and was also used to calculate the absolute molecular weight numbers for the PET samples.

2.2 METHODS

A Thermo Scientific Haake MiniJet was used for the preparation of all test specimens. All materials were dried for 16 to 17 hours at 140 °C in vacuum and then kept under inert atmosphere until the time of sample preparation. Prior to drying, amorphous pellets, i.e. materials that had not undergone SSP, were first annealed for 0.5 hour at 120 °C and then crystallized 1 hour at 170 °C. The dried resins were loaded to the melt chamber with a temperature of 260 °C and the material was allowed to melt for three to four minutes. Subsequently, the molten material was driven into a mold using a piston with a pressure of 800 bar over a 5 second time period including hold time, after which the sample was extracted and the process repeated two more times to produce three specimens from one loading. The mold temperature was controlled at 40 °C. The method was used to prepare at least three Rheology disk specimens with a radius of 25 mm and a thickness of 1 mm. For samples that underwent SSP at least five dogbone specimens of shape ISO 527-5A with a thickness of 2 mm were also produced. All specimens were transparent and free of haze, indicating that crystallinity in those materials was absent or present in a very low degree. After production, the specimens were stored at room temperature in a low humidity environment (in a glove box < 5 ppm H_2O). For selected specimens, the sprue was used to determine the molecular weight as shown in Table 2.

Table 2 – Weight average molecular weights of injection molded specimens. The sample numbers in the first column correspond to material numbers in Table 1. Polydispersity indices were found to range between 2.02 and 2.05.

↓ Specimens	$M_{w,PS}$ [kg/mol]	$M_{w,PS}$ [kg/mol]	$M_{w,PS}$ [kg/mol]	$M_{w,PS}$ [kg/mol]
Materials →	PEF-Ti/Sb 1	PEF-Ca/Sb 1	PEF-Sb 1	PET-Sb 1
Disk A	27.2	27.0	37.3	56.3
Disk B	27.6	27.4	37.3	55.9
Materials →	PEF-Ti/Sb 2	PEF-Ca/Sb 2	PEF-Sb 2	PET-Sb 2
Disk A	58.9	39.0	64.4	58.5
Disk B	64.9	40.7	68.3	65.4
Dogbone	56.9	45.0	63.0	68.0
Materials →	PEF-Ti/Sb 3	PEF-Ca/Sb 3	PEF-Sb 3	PET-Sb 3
Disk A	70.1	61.0	70.6	69.4
Disk B	77.0	63.2	79.5	75.9
Dogbone	68.7	58.8	79.7	80.5

Rheometry was conducted using an Anton Paar MCR 101 rheometer equipped with a d = 25 mm plate-plate geometry with a fixed electronically heated bottom plate and a rotating top plate. Both plates were contained under an electronically heated cap under nitrogen atmosphere. The injection molded disks were loaded at the selected starting temperature directly after being removed from the glove box. The specimens were heated for two minutes, after which the gap width was reduced from 1.25 mm to 1.1 mm. Then, the edges were trimmed and the gap further reduced to 1 mm at which the measurement was carried out. Oscillatory frequency sweeps from 100 Hz to 1 Hz were conducted at various temperatures following one out of the four temperature programs in Table 3, with a residence time of under two minutes per cycle. A strain of 2% was used, which was determined to be in the linear visco-elastic region using an amplitude sweep.

Table 3 - Rheometry temperature programs

Cycle	1	2	3	4	5	6	7	8	9	10
Program 1 (°C)	220	230	240	250	220 (repeat)	210	200	195	260	270
Program 2 (°C)	250	240	230	220	210	200	190			
Program 3 (°C)	240	230	220	210	200	190				
Program 4 (°C)	230	220	210	200	190					

Program 1 was applied to at least one specimen for each material, with sweep cycles 1 through 8 to characterize the main molten regime while adding 9 and 10 to check high temperature viscosity at the end, to avoid excessive degradation before the other temperatures were measured. In some cases, Program 2, 3 or 4 was applied on the second disk to verify consistency. The programs were selected to highlight the temperature dependence of the melt viscosity while ruling out effects of degradation, crystallinity or specimen equilibration.

Tensile testing was conducted using an Instron 5565 universal testing machine equipped with a calibrated 1 kN load cell and manually operated tensile clamps with a maximum capacity of 5 kN. Samples were conditioned two days at ambient temperature and humidity and then loaded at a gap distance of 30 mm and tensile testing was run using the Bluehill Software at deformation rates of 15, 75 and 150 mm/min equating to nominal strain rates of 0.01, 0.05 and 0.1 s^{-1} relative to the 25 mm gauge length. The strain (rate) was determined from the crosshead displacement sensor and thus the compliance of the setup and local differences in deformation in the specimens were not taken into account. The reported moduli are therefore only of qualitative value. Six replicates were tested for each material sample.

Estimations of the entanglement density of PEF were made via rheometry using the earlier described set-up using additional frequency sweeps at lower temperatures for materials that were slow crystallizing.

3 RESULTS & DISCUSSION

3.1 SOLUTION VISCOSITY

A simple regression of the intrinsic viscosity and absolute molecular weight measurements in Table 1 allows the construction of a Mark Houwink relation of $[\eta] = 1.72 \cdot 10^{-4} \cdot M_w{}^{0.77}$ for PEF in Phenol/CCl_4 40/60 w/w at 30 °C with R^2 = 0.980. For PET we obtained $[\eta] = 4.80 \cdot 10^{-4} \cdot M_w{}^{0.68}$ with R^2 = 0.985, close to $[\eta] = 4.68 \cdot 10^{-4} \cdot M_w{}^{0.68}$ described by Gregory using the same solvent and indicating validity of the calculated molecular weights for PET.[3,5] The data and the regression are shown in Figure 1, indicating that despite the different relations, PEF and PET have relatively similar intrinsic viscosities at the same molecular weight.

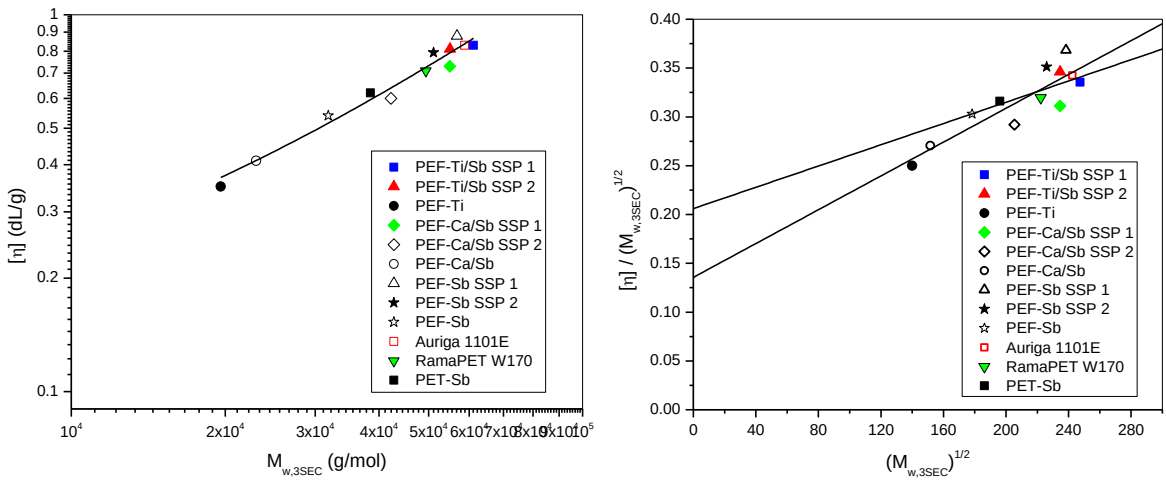

Figure 1 – Mark-Houwink plots (left) and Stockmayer-Fixman plots (right) of various samples of PEF-Ti/Sb, PEF-Ca/Sb, PEF-Sb and PET, including linear regression curves for all PEF samples combined and all PET samples combined.

Figure 1 also shows Stockmayer-Fixman plots, which present a different view. The Stockmayer-Fixman relation in Equation (1) defines the solvent interaction parameter *B* as the slope and the intercept K_Θ as the Mark Houwink constant under theta conditions, where it relates to the unperturbed root-mean-square end-to-end distance $(\langle r_0^2 \rangle / M)^{1/2}$ as per Equation (2), in which Φ is the Flory parameter.

$$[\eta]/M_w^{1/2} = K_\Theta + BM_w^{1/2} \quad (1)$$

$$K_\Theta = \Phi(\langle r_0^2\rangle/M)^{3/2} \quad (2)$$

Values for the intercept were determined at K_Θ = 0.136 ± 0.037 dL.mol$^{1/2}$.g$^{3/2}$ over all PEF samples and at K_Θ = 0.206 ± 0.062 dL.mol$^{1/2}$.g$^{3/2}$ for PET. The average value found for PET agrees with K_Θ = 0.202 dL.mol$^{1/2}$.g$^{3/2}$ by Kamide et al.[11] but is lower than K_Θ = 0.242 dL.mol$^{1/2}$.g$^{3/2}$ by Wallach[3] and K_Θ = 0.270 dL.mol$^{1/2}$.g$^{3/2}$ by Aharoni[10], although those values are still within the error of our determination. The ~35% lower value for PEF than PET is similar to the ~26% lower value of *poly*(ethylene isophthalate) (PEI) found by Aharoni compared to PET as well as the ~35% lower value found by Kamide et al. for PET compared to *poly*(ethylene 1,2-diphenoxyethane *p,p*'-carboxylate), a polyester of a longer aromatic diacid.

The ratios between the unperturbed chain dimensions and theoretical chain dimensions are often calculated as a measure of chain rigidity. Analagous to Wallach et al.[3] the unperturbed root-mean-square end-to-end distance $(\langle r_0\rangle/M)^{1/2}$ was calculated using Equation (2) from the average values of K_Θ and a Flory parameter of $\Phi = 2.68\cdot10^{21}$, giving 0.797 and 0.916 Å·mol$^{1/2}$·g$^{-1/2}$ for PEF and PET. Following the approach of Kamide et al.[11], the root-mean-square end-to-end distance of a freely rotating chain $(\langle r_{0f}^2\rangle/M)^{1/2}$ was calculated using l_{FDCA} = 4.83 Å and l_{TPA} = 5.73 Å for the calculation of $\langle l\rangle^2$ and a bond angle of 109.5°, giving 0.607 and 0.669 Å·mol$^{1/2}$·g$^{-1/2}$ respectively for PEF and PET. The steric parameter σ indicates chain stiffnes of the real chain compared to a freely rotating chain as per Equation (3), and was calculated at 1.31 and 1.37 for PEF and PET respectively. The characteristic ratio C_∞, indicating stiffness versus a freely jointed chain as per Equation (4), was determined at 3.46 and 3.75 respectively for PEF and PET.

$$\sigma = (\langle r_0^2\rangle/M)^{1/2}/\left(\langle r_{0f}^2\rangle/M\right)^{1/2} \quad (3)$$

$$C_\infty = (K_\Theta/\phi)^{2/3} M/\langle l \rangle^2 = \langle r_0^2 \rangle/\langle l \rangle^2 \qquad (4)$$

The comparability of these findings indicates the absence of conformational restrictions for PEF compared to PET in theta conditions, and that the shorter bond length of FDCA compared to PTA quite directly influences the unperturbed chain dimensions. This is similar to Aharoni's finding for PET and PEI[10], and may have various consequences as will be discussed later. One of the consequences that was reported for PEI but not observed for PEF is the lower intrinsic viscosity at comparable molecular weights in the Phenol/Tetrachloroethane 60/40 *w*/*w* solvent at 30 °C. This can be explained by PEF being further removed from theta conditions than PET in this solvent system, as highlighted by Equation (5), which relates the intrinsic viscosity in an arbitrary solvent $[\eta]$ to the intrinsic viscosity under theta conditions $[\eta]_\Theta$ through the hydrodynamic expansion parameter α_h and the Stockmayer-Fixman parameters.

$$[\eta]/[\eta]_\Theta = \alpha_h^3 = 1 + BM_w^{1/2}/K_\Theta \qquad (5)$$

Since PEF has lower value of K_Θ than PET but a higher slope in Figure 1, i.e. a higher value of B in Phenol/Tetrachloroethane 60/40 *w*/*w* at 30 °C, the hydrodynamic expansion factor of PEF is larger and the hydrodynamic volume increased in this solvent system. Another indication is the Mark Houwink α of 0.77 for PEF compared to the value of 0.68 for PET, again highlighting further removal of PEF from the ideal value of 0.50 under theta conditions.

3.2 MELT VISCOSITY

3.2.1 ZERO SHEAR VISCOSITY

The complex viscosity was measured via frequency sweeps at various temperatures for each specimen presented in the materials section. For many specimens a relatively long Newtonian plateau was observed, therefore the complex viscosity determined at the lowest frequency, i.e.

1 Hz, was taken as a (quasi-)zero shear viscosity $\eta^{*,0}$. These values of $\eta^{*,0}$ were related to the absolute temperature through the Arrhenius equation (6), in which E is the activation energy in kJ mol^{-1} and R is the gas constant of 8.3145 kJ mol^{-1} K^{-1}. Figure 2 shows Arrhenius plots of the values of $\eta^{*,0}$ versus reciprocal temperature for all PEF and PET disks.

$$\eta^{*,0} = A \cdot e^{E/RT} \tag{6}$$

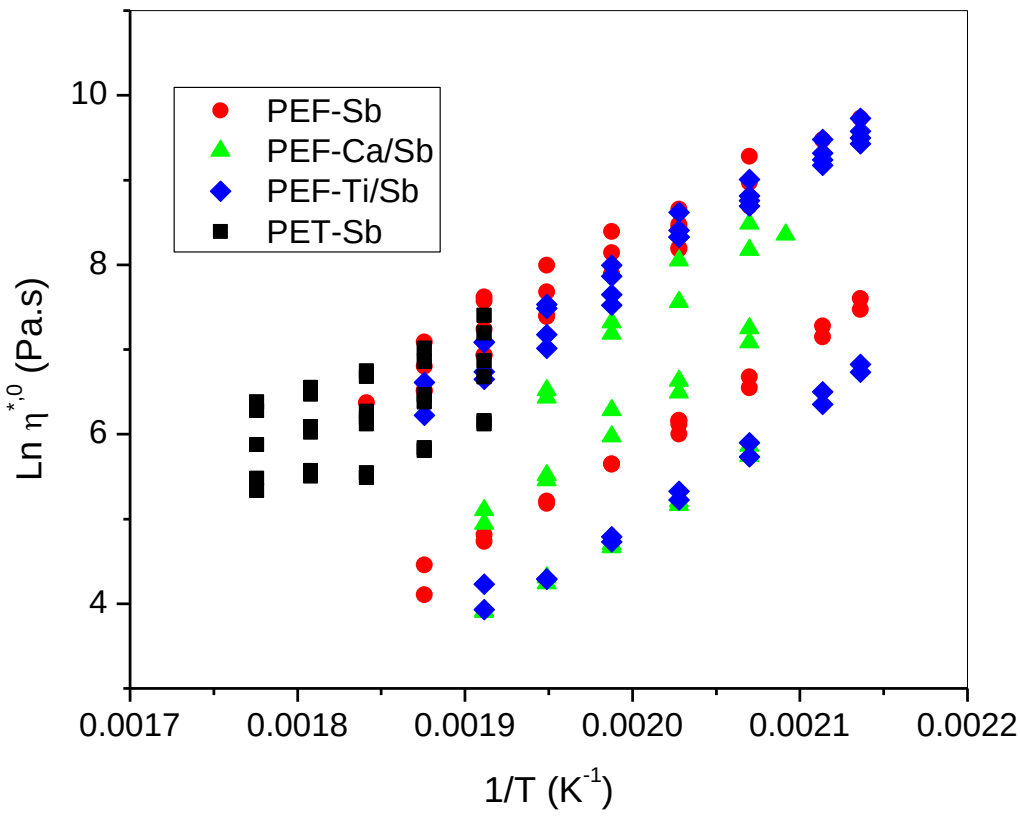

Figure 2 – Arrhenius plot of the (quasi-)zero shear complex viscosity at 1Hz, $\eta^{*,0}$, for PEF-Ti/Sb (blue), PEF-Ca/Sb (green), PEF-Sb (red) and PET-Sb (gray), at various temperatures for material 1 disks A/B (bright/dark triangles), material 2 disks A/ B (bright/dark circles) and material 3 disks A/B (bright/dark squares) having increasing molecular weight.

The activation energy was calculated for each of the various PEF specimens, and analyzed to determine whether or not the catalyst or the monomer (diester or diacid) had an influence on the temperature response of the zero shear viscosity, giving activation energies of 101.4 ± 4.8, 106.0 ± 9.5 and 96.4 ± 4.4, for PEF-Ti/Sb, PEF-Ca/Sb and PEF-Sb respectively. Specimens of PEF-Ca/Sb had a slightly higher activation energy which could be attributed to nuclei

formation at temperatures below 200 °C due to the nucleating effect of calcium acetate.[13] However, generally the activation energies of PEF are in good agreement and combining all values yields an activation energy of 101.0 ± 7.2 kJ mol^{-1} for PEF compared to 51.6 ± 9.0 kJ mol^{-1} for PET. The value found for PET is in good agreement with the value of 56.5 kJ mol^{-1} reported by Gregory.[5]

When using the resin IV as input parameter, the (quasi-)zero shear viscosities obtained from the model of Gregory match well with the measurements in this work, as will be shown in the next paragraph. In this work however, the melt was injected into a disk-shape before the actual measurement and an intermediate molecular weight could be measured. The disk M_w of both PEF and PET decreased compared to the resin M_w while M_n is virtually unchanged, which was attributed to trans-esterification during sample preparation starting from a high polydispersity index after SSP to the statistical polydispersity index of 2.0 for polycondensates. This also explains a higher drop for PEF. The specimens can be seen as having reached equilibrium, since the results of Figure 2 show a consistent temperature dependence while the temperature program is varied over the samples both in heating and cooling. Thus, the disk M_w of PEF was correlated to the pre-exponential factor A obtained from that disk using the previously obtained E = 101.0 kJ mol^{-1} as depicted in Figure 3, with coefficient of determination of R^2 = 0.9792. Subsequently, substituting A in equation (6), the complex (quasi-)zero shear viscosity of PEF can be expressed as equation (7) or (8) analogous to Gregory, in which E is the activation energy for PEF with a value of 101.0 kJ mol^{-1}, R the gas constant and T the temperature in Kelvin.[5]

$$\eta_{\mathrm{PEF}}^{*,0} = 4.99 \cdot 10^{-24} \cdot e^{E/RT} \cdot M_{w,PS}^{3.36} \qquad (7)$$

$$\eta_{\mathrm{PEF}}^{*,0} = 3.73 \cdot 10^{-23} \cdot e^{E/RT} \cdot M_{w,3\mathrm{SEC}}^{3.29} \qquad (8)$$

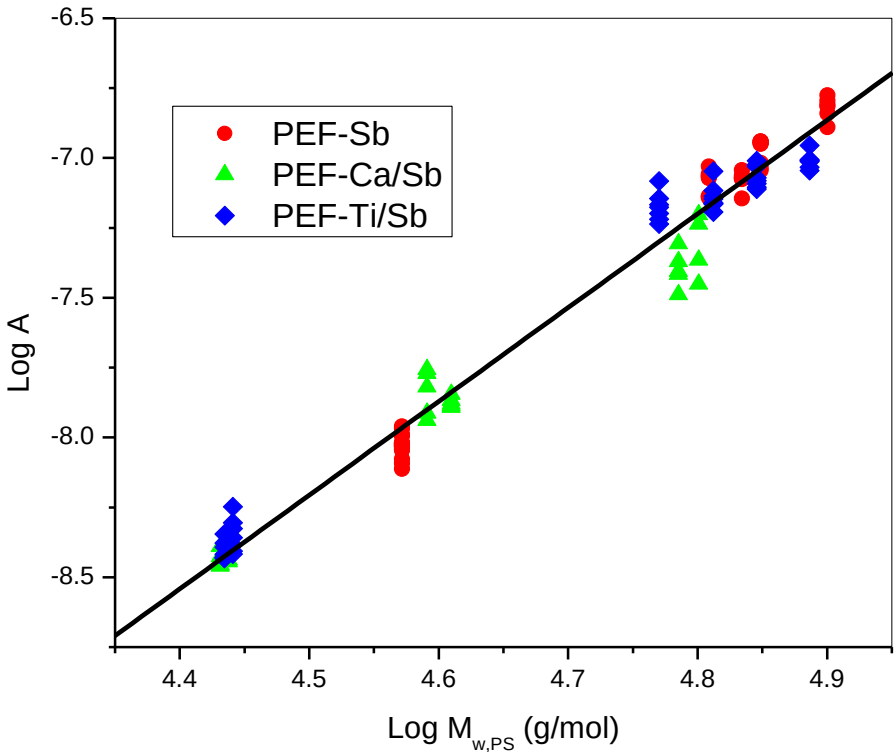

Figure 3 – Determination of the molecular weight shift factor of PEF based on values of A from equation (6) for PEF-Ti/Sb (blue), PEF-Ca/Sb (green right), PEF-Sb (red)

$M_{w,\mathrm{PS}}$ represents the weight average molecular weight vs. polystyrene, as measured on the actual disks after melt homogeneization (Table 2), while Equation (8) was established using the correlation of $M_{w,\mathrm{PS}}$ to $M_{w,\mathrm{3SEC}}$ in Table 1. For both equations however, the exponents for the dependence of melt viscosity on M_{w} agree well with the typical range of 3.3-3.5 for polymers that are sufficiently above the critical entanglement molecular weight. Although Figure 3 shows the general correlation is good, some of the data points are still deviating from the trend within the same sample, which can be explained by the variability in both the method of molecular weight determination and the zero shear measurement.

3.2.2 SHEAR RATE DEPENDENCE

To compare the shear rate dependence of PEF and PET, samples B from materials 2 and 3 of PEF-Sb and PET-Sb were selected due to their comparable molecular weight and production route. To aid the comparison, the empirical Cross-model was applied which is shown here as

Equation (9), in which η is the shear viscosity, $\dot{\gamma}$ the shear rate in s^{-1} and τ^* and n are fitting parameters corresponding roughly to the respective onset and slope of shear thinning.[14]

$$\eta(\dot{\gamma}) = \frac{\eta^0}{1+(\dot{\gamma}\cdot\eta^0/\tau^*)^{1-n}} = \eta^*(\omega) = \frac{\eta^{*0}}{1+(\omega\cdot\eta^{*0}/\tau^*)^{1-n}} \qquad (9)$$

In order to fit the data, the complex viscosity η^* was used instead of the shear viscosity η and the shear rate $\dot{\gamma}$ was replaced by the angular frequency ω by applying the Cox-Merz rule. Table 4 shows the values obtained when fitting the data for the four samples of PEF and PET using Equation (9) and Figure 4 shows both the data as well as the fit. Both Figure 4 as well as the low sum of squares error in Table 4 show a good fit of the model with the data.

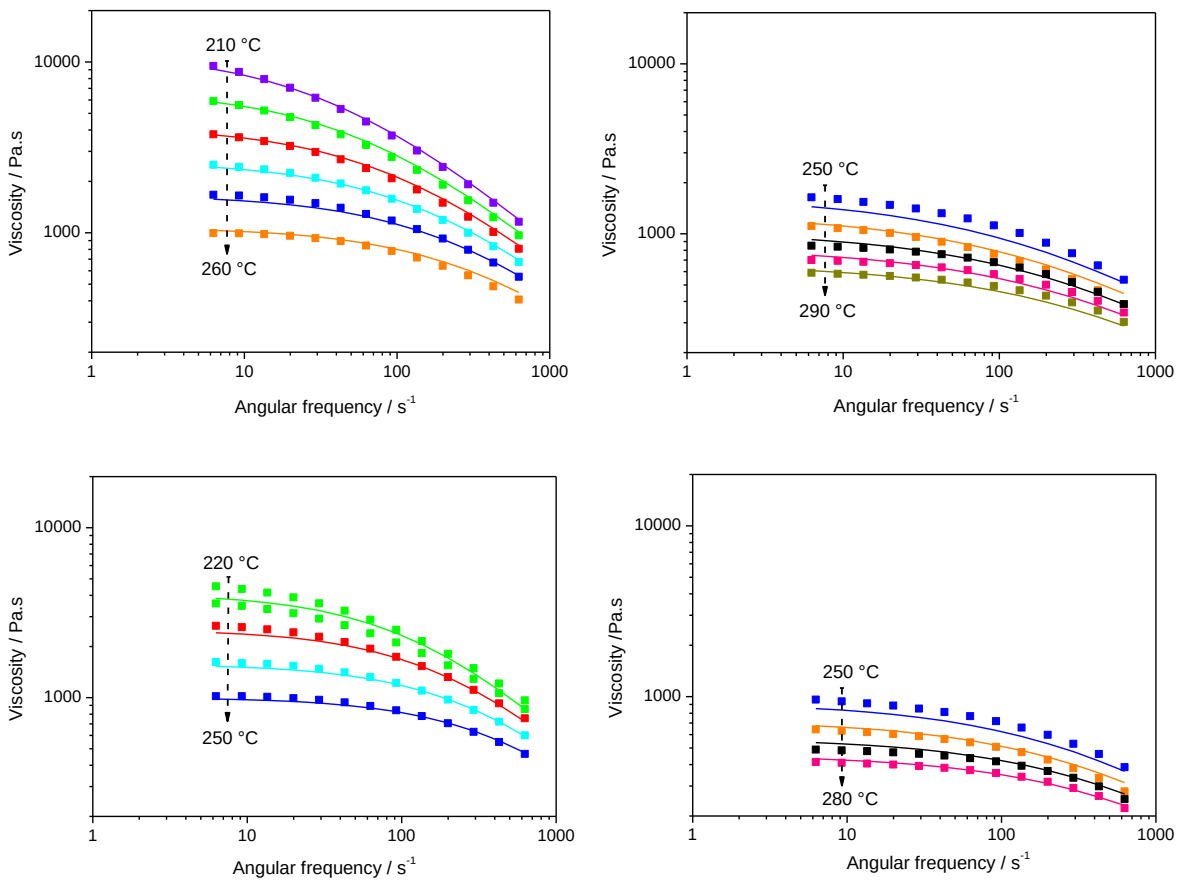

Figure 4 – Shear rate dependence of PEF-Sb disk 3B from 220 °C to 260 °C (top left) and for PET-Sb disk 3B from 250 °C to 290 °C (top right), as well as PEF-Sb disk 2B (bottom left) and PET-Sb disk 2B (bottom right), overlaid with a Cross-model for all curves.

Table 4 – Fitting parameters and sum of square error compared to actual data for the Cross model, equation (9), as displayed in Figure 4. The zero shear viscosity used as an input was calculated from the Disk $M_{w,PS}$ using equation (7) for PEF and from the resin IV as per the equation of Gregory.[10] Its value at 250 °C, $\eta^{*,0}_{250\,°C}$, is shown for relative comparison.

Sample	$M_{w,PS}$ [kg/mol]	$\eta^{*,0}_{250\,°C}$ [Pa.s]	τ^* [kPa]	n	SSE^a [Pa.s]
PEF-Sb 3B	79.5	1666	432	0.237	0.364
PET-Sb 3B	75.9	1640	265	0.417	0.150
PEF-Sb 2B	68.3	1001	557	0.131	0.315
PET-Sb 2B	65.4	961	299	0.369	0.239

[a]Sum of Squared Errors $\Sigma[(\eta^*)_{measured,i} - (\eta^*)_{computed,i}]^2$.

From Table 4 it becomes clear that the PEF samples exhibit a comparable zero shear viscosity to PET at 250 °C, as can also be seen in Figure 4. It however indicates higher values of τ^* and lower values of $\eta^{*,0}_{250\,°C}/\tau^*$ for PEF at this temperature. The value of η^{*0}/τ^* can be seen as a measure of the reptation time of the polymer chain and is related to the onset of shear thinning, when the experiment time is shorter than this reptation time and starts to induce molecular orientation. For both PEF and PET this value increases with molecular weight, since the presence of more entanglements imposes additional constraint for a chain to leave its hypothetical 'tube'. The higher reptation time for PEF can be explained by the stiffer main chain resulting in a larger reptation tube diameter for PEF, which is proportional to the square root of the molecular weight between entanglements and the root-mean-square end-to-end distance.[2] This explanation is very similar to that of the larger free volume of PEF compared to PET found previously in the glassy state while PEF segmental mobility was more constrained.[15] The lower value of n for PEF indicates a steeper slope of shear thinning, which can also be observed in Figure 4 and explained by a higher possible degree of molecular orientation for a less entangled network. It can furthermore explain a higher temperature dependence of the zero shear viscosity. Naturally at lower temperatures the value of η^{*0}/τ^* increases, and shear thinning occurs at lower shear rates as is clear from Figure 4. The higher

activation energy of the zero shear viscosity can thus be seen as a higher temperature dependence of reptation for PEF, which is in line with a generally higher tube diameter, i.e. a less entangled network of chains.

3.3 MECHANICAL PROPERTIES

The stress-strain curves obtained at the lowest strain rate for the dogbones of the largest molecular weight, i.e. PEF-Sb 3 and PET-Sb 3, are shown in Figure 5.

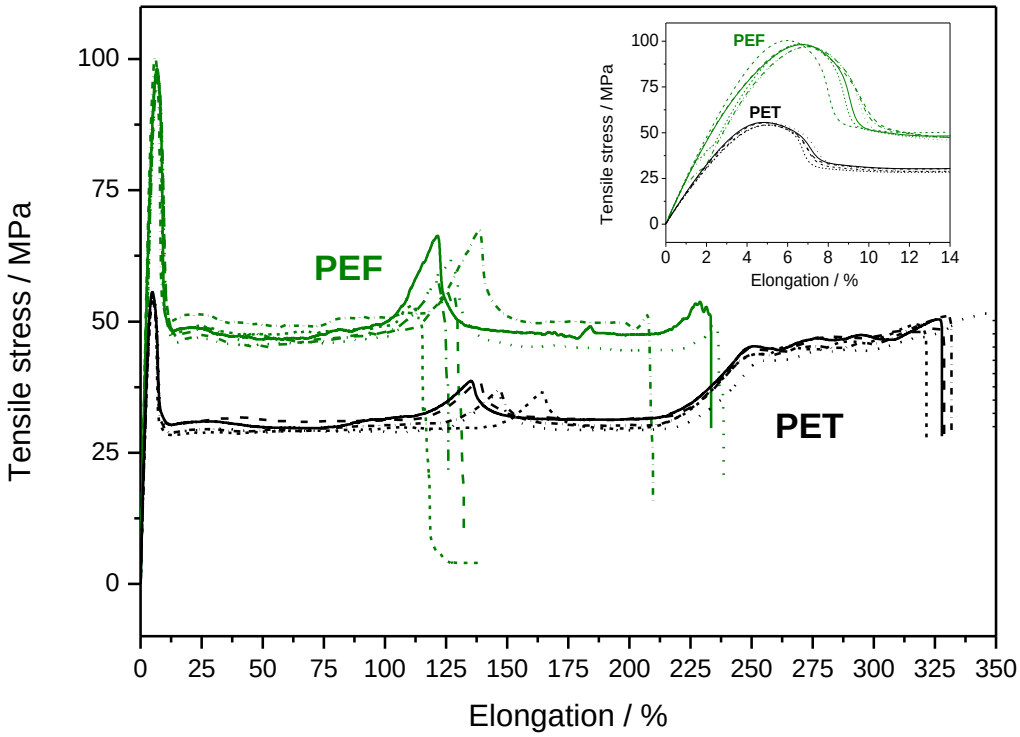

Figure 5 – Stress-strain curves obtained by tensile testing of ISO 527-5A Dogbone samples of PEF-Sb 3 (green) and PET-Sb 3 (black) at 0.25 mm/s, i.e. 0.01 s^{-1} *vs* the parallel-sided portion length of 25 mm. Inset graph: same stress-strain curves focused at low deformation.

PEF and PET were found to exhibit tensile moduli of 2.04 ± 0.04 GPa and 1.34 ± 0.04 GPa respectively, as the inset of Figure 5 qualitatively shows with a difference in slope. Furthermore, the yield stress of PEF is higher than PET, with values of 98.2 ± 1.2 MPa and 55.0 ± 0.8 MPa respectively. Following that is a continued deformation for both materials with energy dissipation at an average stress of around 47.1 ± 1.6 MPa for PEF and 29.9 ± 1.1 MPa for PET. The deformation subsequently shows spikes between 100% and 175%

elongation, occurring at the time when the neck reaches the widened portion at either side of the specimen. This led to fracture in some of the PEF specimens. When the deformation continued, both materials showed an increase between 200 and 225% when the neck also reached the other end of the specimen. This led to fracture in all specimens of PEF, whereas PET specimens could be drawn further while continuing to deform the wider portions.

Considering different materials and strain rates, A slight increase in modulus with increasing test rate and decreasing molecular weight could be discerned for PEF, but although this in line with the expectation it was within the margin of error and thus considered insignificant. Since no extensometer was used, only the relative difference of about 60% between the modulus of PEF and PET should be considered.

The most notable effects of molecular weight and strain rate are found in the elongation at break of PEF shown in Figure 6 in comparison to PET. This indicates ductile behavior for both PET samples at room temperature and generally more brittle behavior for PEF, although PEF shows increased ductility at lower strain rates such as shown in Figure 5 above $M_{w,PS}$ of 55.000 g/mol, corresponding to an $M_{n,3SEC}$ of 18.700 g/mol and an IV of 0.58 dL/g. Both the yield stress and increased elongation at break are comparable to PET at -50 ºC in the work of Stearne and Ward[6], which exhibits brittle behavior at M_n below 16.500 g/mol or IV 0.54 dL/g. It should however be noted that for PET in this work the stability of the neck is also somewhat reduced at the highest strain rate.

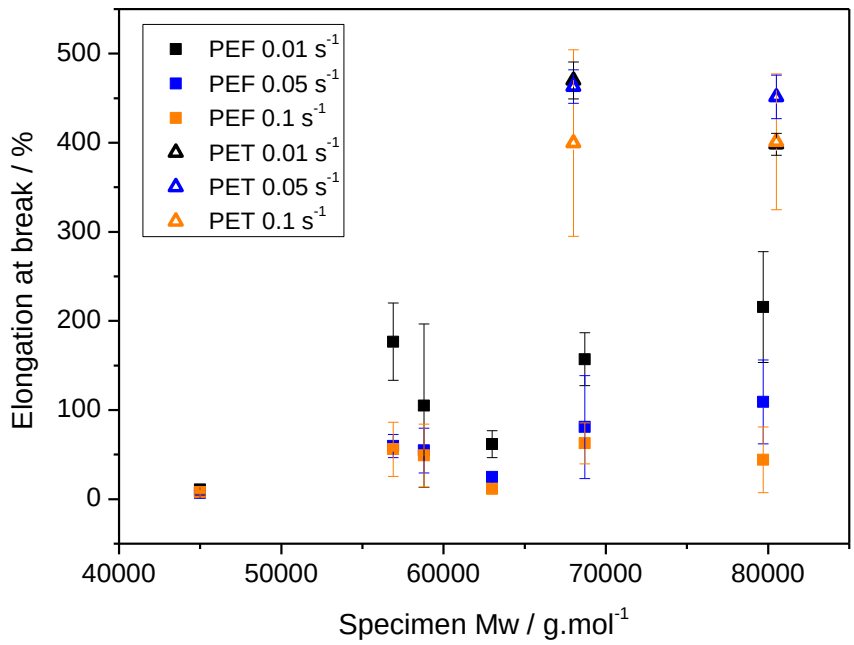

Figure 6 – Elongation at break for samples of PEF (green squares) and PET (blue spheres) versus molecular weight at strain rates of 0.01, 0.05 and 0.1 s^{-1} (bright to dark).

For both PEF as well as PET at -50°C the higher tendency towards brittleness can be explained by a higher yield stress, which induces a higher degree of strain softening, i.e. a higher degree of localized deformation that is more prone to failure than delocalized deformation. The higher yield stress in PEF is comparable to what has previously been shown by Dolmans[16] but disagrees with Knoop et al., who find a lower yield stress and a much more brittle response.[17] In view of absence of any notice by Knoop et al. of specimen molecular weight or optimization of the drying and processing conditions to retain it, the brittle behavior reported by those authors could be explained by molecular weight loss during sample preparation. The yield stresses of the various PEF and PET samples are shown in Figure 7, which show an 'upper' yield stress, i.e. the actual yield stress found during the experiment and a 'lower' yield stress, i.e. the stress exerted when a stable neck is formed. Figure 7 shows that for both materials the upper yield stress increases with strain rate while the lower yield stress remains constant or slightly decreases. The decrease could be explained by specimen heating by energy dissipation during deformation; at higher strain rates the amount of thermal

energy released due to dissipation is higher due to the higher yield stress over a shorter test period. For PEF this effect is stronger than for PET as the stresses at which plastic deformation occurs are higher. The (upper) yield stress for PEF on average increases with 11.5 ± 0.9 MPa per decade of strain rate, compared to 4.6 ± 0.3 MPa for PET. The yield stress of samples of PEF-Sb 2 and PEF-Ca/Sb 2 was not considered in this average due to absence of subsequent deformation, i.e. failure may have occurred at a lower maximum stress than the actual yield stress.

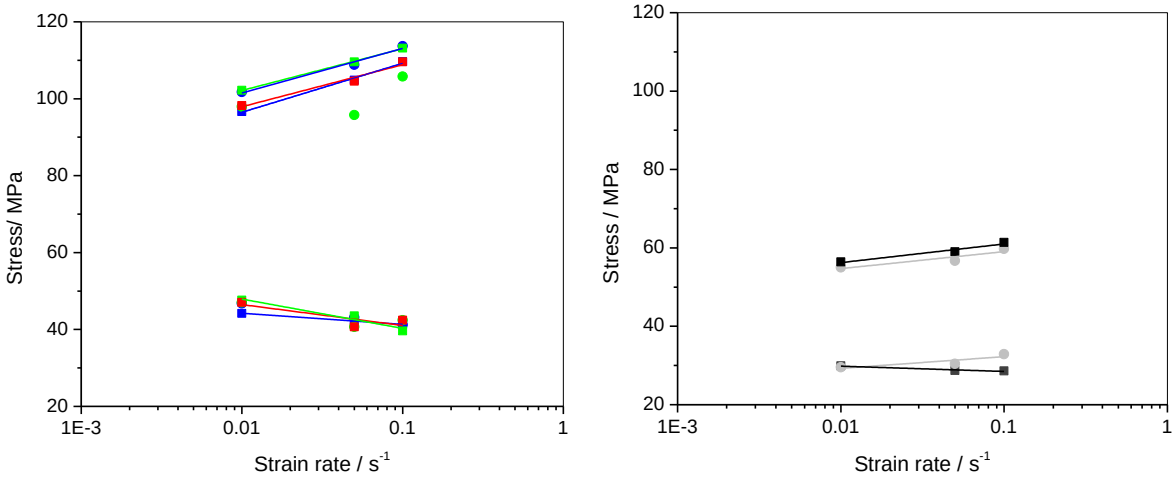

Figure 7 – Upper and lower yield stress at various strain rates for left: PEF-Ti/Sb (blue), PEF-Ca/Sb (green right), PEF-Sb (red), and right: PET-Sb (gray) in which material 2 samples are bright circles and material 3 samples dark squares. Superimposed are trendlines generated by linear regression.

The viscoelastic nature of the yield stress is often expressed by the Eyring theory and sometimes by the Robertson theory.[18,19] The Eyring flow expression in Equation (10) re-written as Equation (11) highlights the relationship of the yield stress σ_y with the strain rate $\dot{\varepsilon}$, in which $\dot{\varepsilon}_0$ is the reference strain rate, ΔU the activation energy of the flow process, k is Boltzmann's constant and v the activation volume.

$$\dot{\varepsilon} = \dot{\varepsilon}_0 \cdot e^{-\frac{\Delta U}{kT}} \sinh\left(\frac{\sigma_y v}{kT}\right) \approx \frac{\dot{\varepsilon}_0}{2} \cdot e^{\frac{-\Delta U + \sigma_y v}{kT}} \tag{10}$$

$$\sigma_y = \frac{1}{v}\left(\Delta U - kT \cdot \ln\frac{\dot{\varepsilon}_0}{2}\right) + \frac{kT}{v} \cdot \ln \dot{\varepsilon} \tag{11}$$

This shows that the derivative of the yield stress to the logarithm of the strain rate, or the slope of Figure 6, is inversely related to the activation volume v. The activation energy of the flow process ΔU and the reference strain rate $\dot{\varepsilon}_0$ determine the offset at $\dot{\varepsilon} = 1$. These parameters were calculated and shown in Table 5 for PEF and PET compared to previously obtained values by Stearne and Ward[6] for PET at various temperatures.

Table 5 – Yield stress and its strain rate dependence obtained from [a]this work and [b]the work of Stearne and Ward[6] at various temperatures.

Material	T (°C)	$\sigma_{y,\log\dot{\varepsilon}=0}$(MPa)	$\delta\sigma_y/\delta\log\dot{\varepsilon}$ (MPa.s)	v (nm^3)
PEF[a]	23	122.6 ± 2.2	11.5 ± 0.9	0.82
PET[a]	23	64.6 ± 4.6	4.6 ± 0.3	2.04
PET[b]	23	66.4	6.5	1.44
PET[b]	-40	111.4	11.2	0.66
PET[b]	-50	124.2	13.3	0.53

Table 5 shows that the yield stresses and slope found for PET agree relatively well with the work of Stearne and Ward, although the slightly higher slope in their work results in a significantly lower activation volume; the value of 2.04 nm^3 would suggest that either of ΔU and $\dot{\varepsilon}_0$ or both are higher for PET than PEF, whereas the value of 1.44 nm^3 would suggest that they are comparable. Furthermore, the yield stresses and slopes found for PEF are comparable to PET between -40 °C and -50 °C. The activation volume of PET is also lower in this case, which disagrees with the Eyring theory and originates from the β-transition of PET starting below -40 °C. This could indicate that certain chain motions that cease when cooling PET through the β-transition are already restricted for PEF at room temperature. One possibility is carboxyl group rotation[8], which offers an alternative view to the ring flipping motion proposed to be absent in PEF by Burgess et al.[20] On the other hand, the similar steric

parameter and characteristic ratio for PEF and PET in Paragraph 3.1 imply that such motional restrictions are the result of intermolecular interactions, such as dipole-dipole interactions or hydrogen bonding between ring hydrogen atoms and a neighboring ring oxygen atom. In order to confirm effects of such restrictions on the yield stress in particular, values for ΔU and $\dot{\varepsilon}_0$ should be obtained by conducting experiments at various temperatures, preferably in compression mode where the yield stress is an intrinsic phenomenon. An accurate value for v should also be determined under such conditions, although a 40-60% lower activation volume for PEF compared to PET is evident. This relative difference may be related to the entanglement density through the empirical relation by Ho et al.[18], yielding in a 60-80% lower entanglement density for PEF than PET. The next paragraph shows that entanglement density differences can explain this behavior to a large extent.

3.4 ENTANGLEMENT DENSITY

The entanglement density ρ_e, or inversely the molecular weight between entanglements M_e, is known as an important factor relating chain structure to macroscopic polymer behavior and can be calculated from the shear modulus in the rubber plateau using equation (12).[21]

$$G_N^0 = \frac{4}{5}\rho_e kT = \frac{4}{5}\frac{\rho RT}{M_e} \qquad (12)$$

Frequency sweeps were applied at low temperatures following melt rheometry of disks B of PEF-Ti/Sb 3 and PEF-Sb 3, shown in Figure 8. The normal force did not decrease during the measurements and the disks were found to be transparent after the measurement, indicating absence of crystallization during the test. From these curves, an average plateau modulus of G_N^0 = 1.49 ± 0.07 MPa could be determined, corresponding to a molecular weight between entanglements of PEF of M_e = 2640 ± 120 g/mol following Equation (12) with an amorphous density of 1.430 g/cm^3, or 3300 ± 150 g/mol when omitting the factor 4/5. The latter value

agrees well with the values of 3550 and 3500 ± 1000 g/mol reported by Kriegel et al. and Stoclet et al. respectively.[22,23]

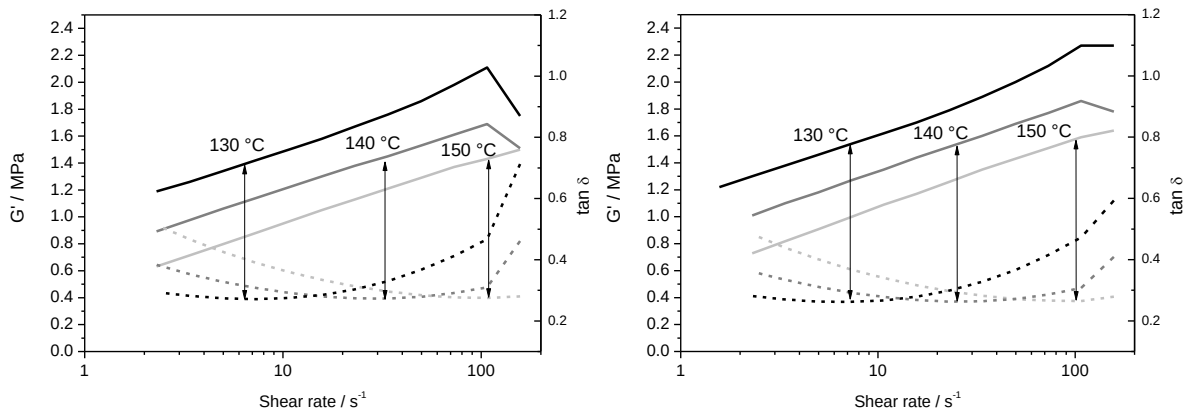

Figure 8. Storage shear modulus (solid lines) and tan δ (dashed lines) measured with rheometry for PEF-Ti/Sb 3(left) and PEF-Sb 3 (right) at indicated temperatures. The arrows highlight how the G_N^0 values were taken at the minimum of the corresponding tan δ curve.

As previously noted, these values are also higher than those reported for PET by Fetters et al. and Wu, at 1170 g/mol and 1450 g/mol respectively with or without the factor 4/5.[1,2] However, both Fetters et al.[2] and Wu[1] used a density of 0.989 g/cm^3 at 275 ºC in reference to Zoller and Bolli, [24] while those authors actually report a specific volume of 0.989 cm^3/g at 340 ºC and 0.852 cm^3/g at 275 ºC thus a density of 1.18 g/cm^3. This would yield a molecular weight between entanglements of 1390 g/mol following Equation (12) or 1740 g/mol without the factor 4/5. Furthermore the plateau modulus G_N^0 = 3.1 MPa reported by Wu was determined in the molten state to avoid discrepancies by crystallization in the actual rubber plateau, using the cross-over point $G' = G'' = G_c$, and a ratio G_N^0/G_c calculated from the polydispersity with values between 2.4 to 9.0 for polydispersities between 1 and 3. For the same reasons, also in this work an attempt was made to estimate G_c for PEF and PET in direct comparison as shown in Figure 9.

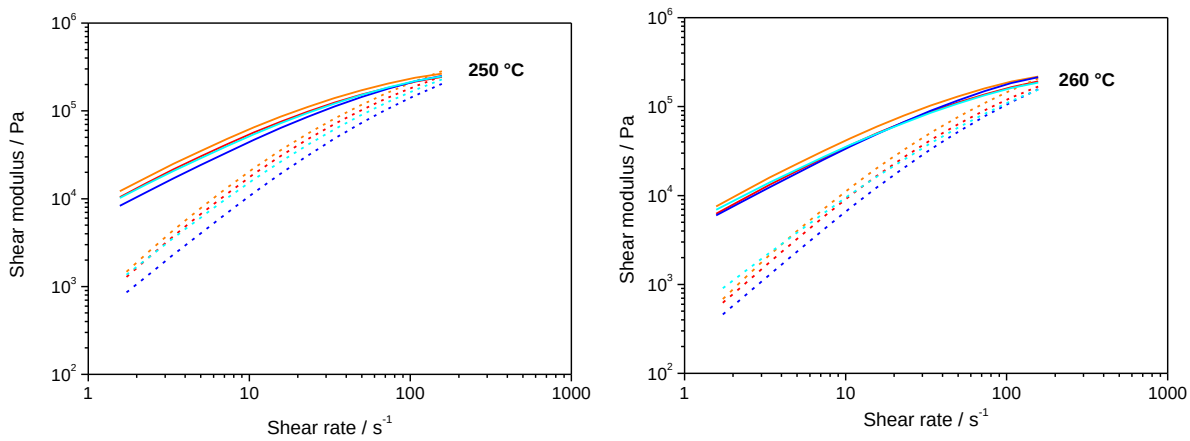

Figure 9 – *G*' (dashed lines) and *G*'' (solid lines) for PEF-Sb 3A and 3B (light and dark orange) and PET-Sb 3A and 3B (light and dark blue), at 250ºC (left) and 260ºC (right).

It can be observed that only PEF at 250 ºC displays a cross-over point at 0.25 MPa, and that under all conditions the moduli for PEF and PET seem to converge to a similar value. Using a G_N^0/G_c ratio of 7 from a polydispersity of 2.05 following Wu[7], this would yield G_N^0 = 1.7 MPa and an entanglement density of 0.24 nm^{-3} for both materials, and a molecular weight between entanglements M_e of 2420 g/mol for PET using a density of 1.19 g/cm^3 at 250 ºC estimated by Zoller and Bolli. If the density difference in the melt is similar to the 1.340 and 1.430 g/cm^3 for amorphous PET and PEF respectively, the same G_N^0 would yield a higher M_e value for PEF.

Fetters et al.[2] have proposed a general relation between the rubber plateau modulus to the inverse of a chain packing length p calculated from the unperturbed end-to-end distance $(\langle r_0^2\rangle/M)^{1/2}$ as per Equation (13), which combined with the molecular weight between entanglements M_e can also be used to calculate the reptation tube diameter d_t using Equation (14).

$$p = (\langle R^2\rangle_0/M)^{-1} \cdot \rho \cdot N_A \qquad (13)$$

$$d_t = (\langle R^2\rangle_0/M)^{1/2} \cdot (M_e)^{1/2} \qquad (14)$$

Table 6 – Calculated chain structure parameters using $G_N^0 = 10.52\ p^{-3}$ and Eq. (13) and (14).[2]

Polymer	T (K)	G_N^0 (MPa)	$(\langle r^2\rangle_0/M)^{1/2}$ (Å·mol$^{-1/2}$·g$^{-1/2}$)	ρ (g/cm^3)	p (Å)	$M_e \cdot 10^3$ (g/mol)	d_t (Å)
PET	548	1.8-2.6[a]	0.919-0.974[a]	0.989[a]	1.77-1.99[a]	1.7-2.4[a]	38.2-42.8[a]
	523	1.75[b]	0.876	1.19[c]	1.82	2.4	55.5
	523	2.3	0.916[b]	1.19[c]	1.66	1.9	47.5
	423	2.7	0.916[b]	1.26[c]	1.66	1.3	47.5
PEF	523	1.75[b]	0.846	1.28[c]	1.82	2.6	59.7
	523	1.23	0.797[b]	1.28[c]	2.04	3.8	77.2
	423	1.42-1.59[b]	0.792-0.808	1.36[c]	1.88-1.90	2.4-2.7	60.6-65.4
	423	1.46	0.797[b]	1.36[c]	1.93	2.6	64.1

Input values [a]as reported by Fetters et al.[6], [b]determined in this work, [c]determined from the amorphous PET density relation to temperature by Zoller and Bolli[24], applying a fixed ratio of 1.33:1.43 for the density of PEF.

Table 6 shows that the value of G_N^0 and associated value of M_e for this work are in agreement with the low and high bounds respectively reported by Fetters et al., but using the accurate density at this temperature leads to lower unperturbed end-to-end distance than their range. The average unperturbed end-to-end distance of 0.916 Å·mol$^{-1/2}$·g$^{-1/2}$ found in this work however does agree with the range of Fetters et al., pointing to a higher G_N^0 and lower M_e for PET than what was measured. The discrepancy may be explained by the inaccuracy of obtaining G_N^0 from G_c. Using the temperature of 150°C, where $G_N^0$was measured for PEF in this work, a value of M_e = 1300 g/mol could be calculated for PET in line with earlier reports.[25]**Error! Bookmark not defined.** For PEF the opposite is the case, i.e. the values found for PEF are in better agreement with the relation by Fetters et al. at 150°C while at higher temperatures the unperturbed dimensions predict a lower G_N^0 than what was observed.

Although exact values would require an accurate determination of the density versus temperature for PEF, the results generally point to a range of M_e = 2400-2700 g/mol for PEF compared to M_e = 1300-2400 g/mol for PET, or an entanglement density of ρ_e = 0.53-0.60 nm^{-3} and ρ_e = 0.56-0.97 nm^{-3} respectively for the two materials. PEI, for comparison, was reported to have a value of 2500 g/mol, i.e. ρ_e = 0.54 nm^{-3}.**Error! Bookmark not defined.** A reduction

in entanglement density for PEF of down to half that of PET explains the observed differences in melt rheology and to a large extent the higher strain rate dependence of PEF. The higher tube diameters furthermore explain a lower reptation time.

4 CONCLUSIONS

PEF exerts a lower unperturbed end-to-end distance than PET due to the reduced bond length of FDCA, while the conformational freedom under theta conditions is comparable for both materials. Reduced mobility in PEF as reported previously must therefore be significantly influenced by intermolecular interactions. Despite the lower unperturbed dimensions for PEF, a higher solvent interaction with Phenol/CCl_4 40/60 at ambient temperature results in similar intrinsic viscosity for PEF and PET of equal molecular weight under those conditions. The melt viscosity of PEF was described as a function of molecular weight. The temperature dependence of the melt viscosity shows a higher activation energy for PEF, and the shear rate dependence indicates a lower reptation time. In the glassy state, PEF of sufficient molecular weight shows ductility but overall a higher tendency to brittleness than PET, as a result of a significantly higher yield stress combined with a higher strain rate dependence. Various determinations of the plateau moduli in the rubbery and molten state confirm a significantly lower entanglement density for PEF to have a significant contribution to the rheology and mechanical properties of PEF, although in the glassy state the effects of reduced chain mobility cannot be excluded.

5 REFERENCES

[1] S. Wu, J. Pol. Sci. B. Pol. Phys. 27 (1989), 723-741
[2] L.J. Fetters, D.J. Lohse, D. Richter, T.A. Witten, A. Zirkel, Macromolecules 27 (1994), 4639-4647
[3] M.L. Wallach, Makromol. Chem. 103 (1967), 19-26
[4] A.B. Thompson, D.W. Woods, Trans. Faraday Soc. 52 (1956), 1384-1397
[5] D.R. Gregory, J. Appl. Pol. Sci. 16 (1972), 1479-1487
[6] J.M. Stearne, I.M. Ward, J. Mat. Sci. 12 (1969), 1088-1096
[7] C. Bonnebat, G. Roullet and A.J. de Vries, Polym. Eng. Sci. 21 (1981) 189-195.
[8] G. Farrow, J. McIntosh, I.M. Ward, Makromol. Chem. 96 (1960), 147-158
[9] G. Z. Papageorgiou, D. G. Papageorgiou, Z. Terzopoulou, D. N. Bikiaris, Eur. Polym. J. *83* (2016) 202.
[10] S.M. Aharoni, Makromol. Chem. 179 (1978), 1867-1871
[11] K. Kamide, Y. Miyazaki, H. Kobayashi, Pol. J. 9 (1977), 317-327
[12] G.J. Gruter, L. Sipos, M.A. Dam, Comb. Chem. High. Throughput Screen. 15 (2012), 180-188
[13] J.G. Van Berkel, N. Guigo, J.J. Kolstad, L. Sipos, B. Wang, M.A. Dam, N. Sbirrazzuoli, Macromol. Mat. Eng. 300 (2015), 466-474
[14] M.M. Cross, 'Rheology of non-Newtonian fluids : A new flow equation for pseudoplastic systems, J. Col. Sci. 20 (1965), 417-437
[15] A. Codou, M. Moncel, J.G. Van Berkel, N. Guigo, N. Sbirrazzuoli, Phys. Chem. Chem. Phys. 25 (2016), 16649-16658
[16] R.P.L. Dolmans, PhD thesis, RWTH Aachen 2014
[17] R.J.I. Knoop, W. Vogelzang, J. van Haveren, D.S.van Es, J. Pol. Sci. A. Pol. Chem. 51 (2013), 4191-4199
[18] J. Ho, L. Govaert, M. Utz, Macromolecules 36 (2003), 7398-7404
[19] I.M. Ward, J. Mat. Sci. 6 (1971), 1397-1417
[20] S.K. Burgess, J.E. Leisen, B.E. Kraftschik, C.R. Mubarak, R.M. Kriegel, W.J. Koros, Macromolecules 47 (2014) 1383-1391.
[21] W.W. Greasley, S. Edwards, Polymer 22 (1981), 1329
[22] R.M. Kriegel, R.D. Moffit, M.W. Schultheis, Y. Shi, X. You, WO2015031907, (2015)
[23] G. Stoclet, G. Gobius du Sart, B. Yeniad, J.M. Lefebvre, Polymer 72 (2015) 165-176
[24] P. Zoller, P. Bolli, J. Macromol. Sci. B 18 (1980), 555-568
[25] R.Y.F. Liu, Y.S. Hu, M.R. Hibbs, D.M. Collard, D.A. Shiraldi, A. Hiltner, E. Baer, J. Appl. Pol. Sci. 98 (2005), 1615-1628.

CHAPTER 8
BIAXIAL ORIENTATION AND ORIENTED PROPERTIES OF PEF *vs* PET

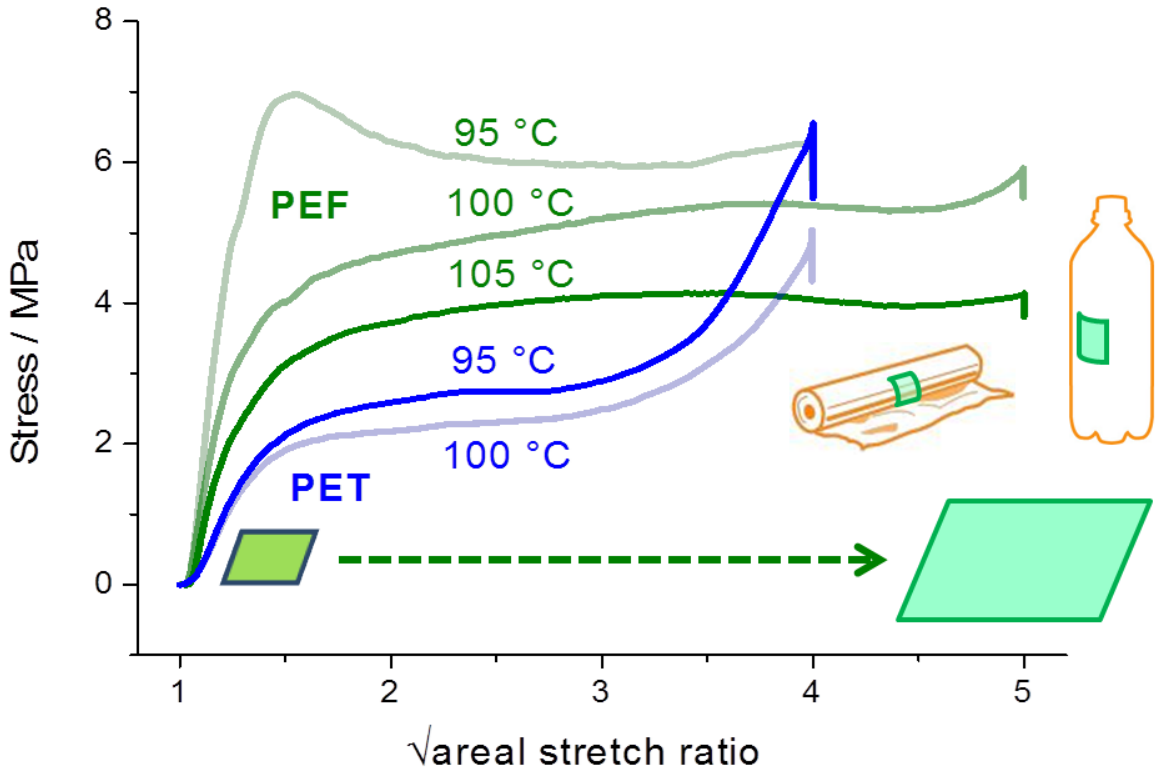

This chapter is also published as part of "Biaxial Orientation of Poly(ethylene 2,5-furandicarboxylate): An Explorative Study" by J.G. Van Berkel, N. Guigo, J.J. Kolstad, N. Sbirrazzuoli, Macromol. Mat. Eng. 303 (2018).

1 INTRODUCTION

The orientation behavior and oriented properties of polymers are relevant for many applications. More specifically, in packaging applications for which a high barrier material such as PEF is of interest, biaxial orientation can be found back. Examples are the stretch-blow molding process used in the production of bottles[1,2] and the stretching and blowing processes used for films[3]. The main reason that orientation is widely applied in polymers is that it generates more favorable properties, particularly increasing the tensile modulus and strength in the orientation directions at the expense of elongation at break.[4] One aspect thereof is the molecular alignment of the amorphous polymer chains in the direction of orientation, while simultaneously semi-crystalline polymers such as PET exhibit strain-induced crystallization (SIC). For uniaxial stretching, crystallites with typical rod-like or fibril-like microstructures can be formed upon sufficient level of orientation.[5,6] In the case of symmetrical biaxial stretching, the crystals are equally and highly oriented along the two draw directions (i.e. the machine or the transverse direction).[7] The crystal size is thus much larger in these directions than along the thickness direction thus leading to sheet-like microstructures.3 Furthermore, the amorphous oriented phase immediately surrounding the crystals exhibits constrained molecular motions due to their strong fixation to the crystal lamella and is called the rigid amorphous fraction (RAF), a concept that also applies for thermally (i.e. quiescent) crystallized polymer to explain the incomplete decoupling of the crystal and mobile amorphous phase.[8] In drawn PET for instance, the RAF appears simultaneously with the development of strain induced crystals after a certain level of orientation.[9] At low levels of orientation, both a non-oriented and an oriented mobile amorphous phase (also known as anisotropic non-crystalline phase) coexist, while at higher degrees of orientation there are oriented mobile and rigid amorphous phases. Both the presence of the rigid amorphous phase and the orientation of the mobile amorphous phase

affect the value and behavior of the glass transition.[10,11] It can be more generally stated that all three variables, that is the degree of (molecular) orientation, amount of SIC and the extent of amorphous chain confinement, contribute to the thermo-mechanical and barrier properties of the oriented material, a concept is generally referred to as the three-phase model.[12]

This study aims to provide a broad initial exploration of the biaxial orientation of PEF. First, the biaxial orientation behavior is investigated for PEF as function of orientation temperature with comparison to PET at selected reference conditions. Subsequently, samples stretched at those conditions to different degrees of orientation are tested for the strain-induced crystallization and amorphous mobility by DSC and DMA respectively, the high temperature shrinkage and the mechanical and barrier properties. Each of these properties is profoundly affected by both the conditions and the extent of the orientation. Finally the observed phenomena are discussed in relation to each other and the nature of the samples versus PEF and PET as polymers.

2 EXPERIMENTAL

2.1 MATERIALS

Poly(ethylene 2,5-furandicarboxylate) was prepared using 2,5-furandicarboxylic acid (FDCA) produced by Avantium and mono-ethylene glycol in an 100 L stainless steel batch autoclave reactor with antimony as the catalyst. Solid state polymerization was done in a tumble dryer using vacuum down to 3 mbar until reaching an Intrinsic Viscosity of 0.85 dL/g as determined in a mixture of 60% phenol and 40% tetrachloroethane (w/w). A commercial carbonated soft drink grade of poly(ethylene terephthalate) with brand name RamaPET N180 was supplied by Indorama Rotterdam, specified by the supplier as having an Intrinsic Viscosity of 0.80 ± 0.02 dL/g and containing a minor quantity of isophthalic acid (IPA) as co-monomer.

Both PEF and PET were dried for 16 hours in vacuum at 140°C and molded into plaques using a Carver hot press. Compression molding was done using a sandwich construction of a top and bottom stainless steel plate, Kapton® polyimide top and bottom films, and a stainless steel mold with four cavities of 90 x 90 x 1.5 mm. This entire sandwich construction was brought under vacuum in a Kapton® polyimide bag sealed hermetically with butyl rubber tape, to ensure absence of (micro)voids and avoid incidental moisture pick-up. Compression molding was done at 260 °C for PEF and 285 °C for PET, after which the samples were quenched to room temperature using a circulating cool water press to avoid crystallization and accelerated ageing upon cooling. All steps of the molding process were carried out with fixed time intervals to ensure reproducible sample quality. The number and weight average molecular weight before and after compression molding are presented in Table 1. These were determined by classical calibration with PS standards, using a Merck-Hitachi LaChrom HPLC system equipped with two PLgel 5 μm MIXED-C (300 x 7.5 mm) columns. A mixture of 40% of 2-Cl-Phenol and 60% of Chloroform was used as the eluent (w/w).

Table 1 – GPC results of PEF and PET before and after compression molding

Material	Before compression molding			After compression molding		
	M_w (kg/mol)	M_n (kg/mol)	PDI	M_w (kg/mol)	M_n (kg/mol)	PDI
PEF	89.4	38.7	2.31	72.8±2.7	34.0±1.1	2.14
PET	79.3	37.3	2.13	65.7±0.4	32.6±0.5	2.02

2.2 METHODS

BIAXIAL ORIENTATION

Compression molded PEF and PET plaques were biaxially oriented using a Brückner Karo IV laboratory stretcher following 120 s heating time and 150 %/s stretch rate. Various temperatures were used at these conditions and the force on both axes was recorded during the stretching process. Stretching was done simultaneously and equibiaxially up to areal stretch ratios between 9 and 25, i.e. between 3 x 3 and 5 x 5. The final biaxially oriented film samples were allowed to cool convectively to ambient temperature under tension prior to removal and storage under atmospheric conditions.

TESTING OF ORIENTED PROPERTIES

The net crystallinity of the biaxially oriented films was determined using a Mettler Toledo DSC 1 equipped with the STAR^{e} software, calibrated using In and Zn standard. For this, circles with a 5 mm radius were cut and placed in the bottom of a DSC pan, after which they were heated at 10 °C/min from 25 °C to 265 °C.

Linear shrinkage was determined by measuring 5 x 5cm squares that were cut from the biaxially oriented films before and after heating for 20 s in glycerol at 90 °C, 120 °C or 150 °C, following ASTM D2732-8 apart from the sample size.

Dynamic mechanical analyses were conducted on a Mettler-Toledo DMA 1 in tensile mode. The experiments were performed at a frequency of 1 Hz from -100 to 250 °C and heating at 2 °C/min. The displacement amplitude was fixed to 0.1 %. Rectangular strips with 3 mm width were placed between the clamps. The length between the clamps was fixed to 5 mm.

Tensile tests were carried out following ISO 527-3, but using three samples rather than five and calculation of the modulus by grip-to-grip extension rather than using an extensometer.

10 x 150 mm strips were cut from the biaxially oriented films and tested with an Instron 5565 tensile tester, equipped with smooth surfaced pneumatic clamps to ensure good grip while avoiding clamp breakage of the films. The testing speed was chosen at 50 mm/min.

The Oxygen and Carbon Dioxide transmission rate were measured on disks with an area of 5 cm^2 cut from the oriented film samples, using a Mocon OXTRAN and Mocon PERMATRAN C respectively at 25 °C and 0% relative humidity. At least one week of stabilization was allowed prior to the determination of the transmission rate under steady-state flow conditions without dynamic sorption effects. Permeability was calculated from the transmission rate results based on triplicate thickness measurements on the disks with a micrometer.

3 RESULTS & DISCUSSION

3.1 BIAXIAL ORIENTATION

The biaxial stress strain curves of PEF and PET are shown in Figure 1. For PET, the curves are very similar to previous investigations.[1,13,14] For the temperatures used the PET samples display a rubbery-type behavior, in which three main regions can be identified. First, the stress increases almost linearly with increasing areal stretch ratio (ASR) which corresponds to the elastic region (ASR < 1.5x1.5). Subsequently, the behavior shifts to a region of viscous flow where disentanglement starts to occur. This reaches a plateau between ASR of 2x2 and 3x3 where disentanglement is in balance with the increase in molecular orientation in the deformation directions. After a certain level of elongation (ASR > 3x3), the PET undergoes strain hardening as a result of a combination of increased molecular orientation over disentanglement and the formation of strain induced crystals. The onset of strain hardening is also called the natural stretch ratio (NSR).[1] For PET, the differences in NSR cannot be distinguished between 95 °C and 100 °C but the level of stress decreases with increasing temperature, which can be attributed to increased viscous flow. As shown in Figure 1, the

PEF stress-strain curves are different from those of PET. At 95 °C the PEF curves does not show a classical rubbery-type behavior, because they exhibit a yield point at ASR = 1.5 x 1.5. This is absent at 100 °C and at 105 °C as well as for PET in the full temperature range, although it is known to occur for PET at lower temperatures.[1] The occurrence for such a yield point for PEF at 95 °C while absent for PET at the same temperature can be explained by the α-relaxation of amorphous PEF occuring ~10 °C higher than PET. More notably, the viscous region of PEF extents much further in comparison to PET since strain hardening is beginning only for ASR > 4.5 x 4.5 (on 100 °C curves), indicating a larger possible extent of stretching for PEF than for PET. This difference can be explained by a lower entanglement density in PEF as observed in the previous chapter. A single chain with a higher distance between two entanglements would require more extension until fully oriented, and consequently a collective set of PEF chains and entanglements also requires more orientation than PET until the resistance to deformation due to entanglements becomes apparent.

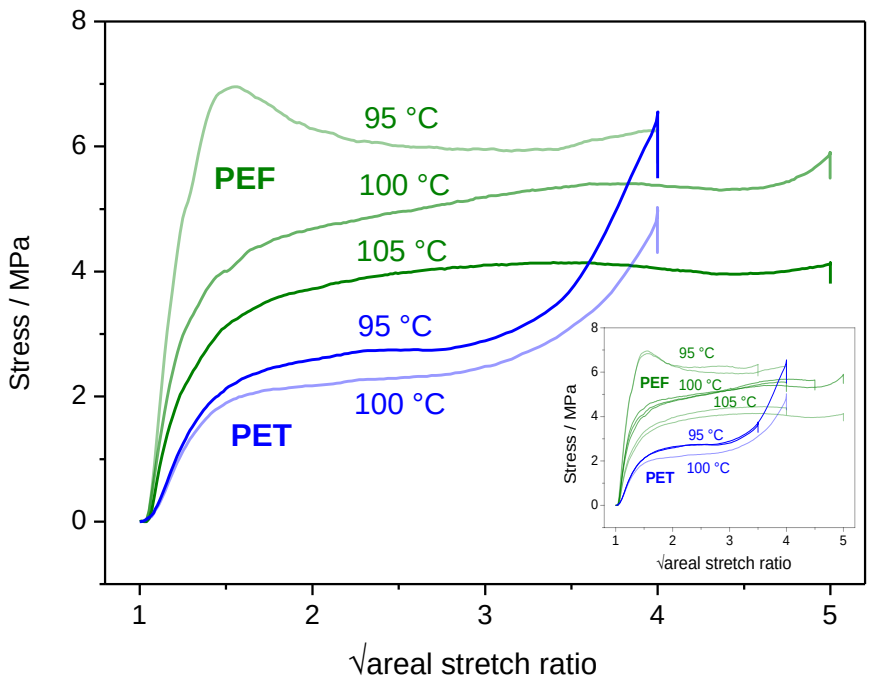

Figure 1 – Stress-strain curves during biaxial stretching of PEF (green line) and PET (blue line). The orientation temperature is indicated by each curve. Insert: overview of samples stretched at lower stretch ratios, indicating variation of the test.

3.2 PROPERTIES OF ORIENTED SAMPLES

CRYSTALLINITY AND SHRINKAGE

DSC measurements were performed on the oriented PEF and PET samples in order to investigate the development of strain induced crystals. Figure 2 shows the DSC curves obtained for different temperature and areal stretching ratios. For non-oriented samples the glass transition temperature occurs at 80 °C and 85 °C respectively for PET and PEF. The scan of the non-oriented PET sample shows an exothermic cold crystallization peak at 128 °C and an endothermic melting peak at 248 °C, in line with previous work.[1,13,15] At the same heating rate (e.g. 10 K/min), the non-oriented PEF curve does not exhibit these features because PEF cold crystallization is slower than PET.[15] After biaxial orientation, the PEF scans exhibit cold crystallization exotherms. This indicates that orientation of amorphous chains has introduced some local organization which resulted in the development of nuclei thus permitting crystallization on heating. With increasing areal stretch ratio, the PEF DSC curves show a progressive shift of the cold crystallization peak to lower temperature, as is shown for example in the PEF curves at 105 °C in Figure 2. The cold crystallization progressively approaches T_g and becomes wider and flatter at high ASR. This can be attributed to a higher degree of strain-induced nucleation which logically results in faster cold crystallization rate, combined with the build-up of actual Strain-Induced Crystallinity (SIC) which limits the formation of additional crystals in the DSC.

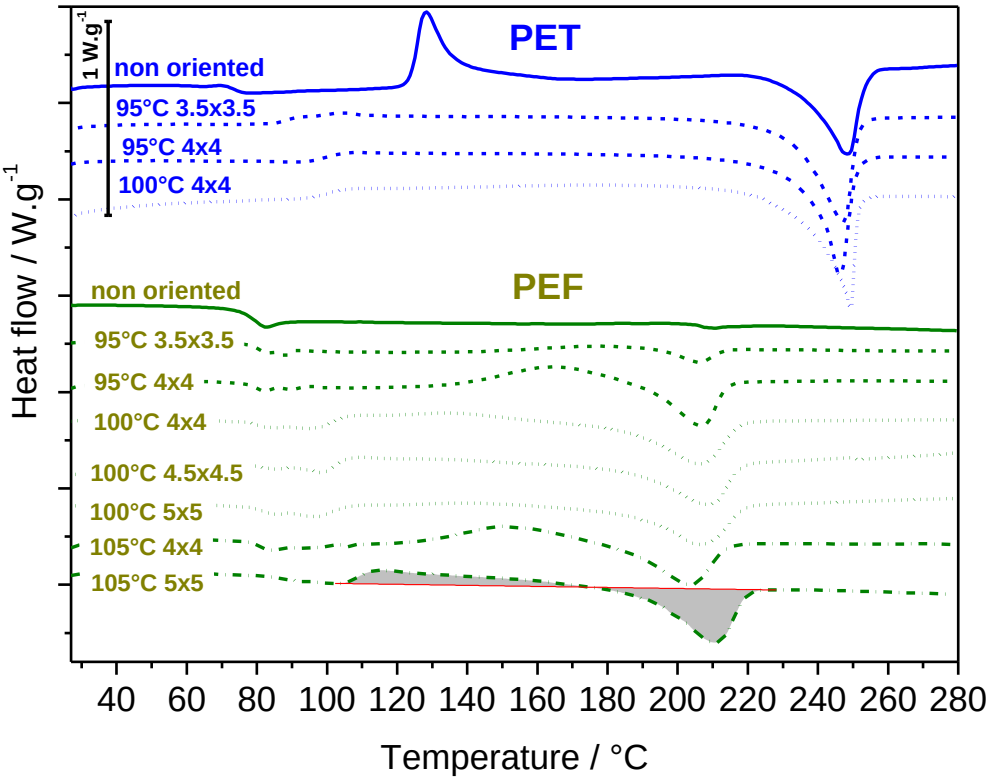

Figure 2 – DSC curves obtained at 10 K/min after biaxial orientation. The orientation temperature and the areal stretch ratio is indicated by each curve.

The correct quantitative evaluation of the cold crystallization and melt enthalpy is difficult. One aspect thereof is that shrinkage can occur in the sample immediately after the T_g. Indeed, the elastic energy stored in the sample during the orientation can be released upon heating, which in non-crystallizable polymers such as PS can lead to small heat capacity variations in the vicinity of the glass transition.[16] In the present case, this exothermal increase was not found to correlate to physical shrinkage and so the entire endotherm following the T_g was attributed to cold crystallization as highlighted in Figure 2. The evaluation of the DSC curves can thus allow determination of the melting enthalpy of the strain-induced crystals $\Delta H_{melt(SIC)}$ and subsequently the total percentage of SIC (%SIC) via the following equations:

$$\Delta H_{melt(SIC)} = \Delta H_{melt(total)} - |\Delta H_{cc}| \quad \text{and} \quad \%SIC = \frac{\Delta H_{melt(SIC)}}{\Delta H^{\circ}_{melt}}$$

Where $\Delta H_{melt(total)}$ is the total melting enthalpy, ΔH_{cc} is the cold crystallization enthalpy as described previously and $\Delta H°_{melt}$ the equilibrium melting enthalpy taken at 140 J/g for PEF and PET respectively.

Figure 4 shows the variations of ΔH_{cc} and $\Delta H_{melt(SIC)}$ and the corresponding percentage of crystallinity obtained for films stretched at different ASR's. PET oriented at 95 °C has developed SIC percentage values which agree well with those found from previous DSC studies conducted on biaxially-oriented PET.[17,18] For PEF, SIC is absent in the samples stretched at 95 °C but increases when PEF is oriented at 100°C with increasing ASR. Accordingly, the cold crystallization phenomenon slightly decreases with ASR. Although the trend is still increasing with ASR, the maximum percentage of SIC found for PEF was around 11% at ASR = 5 x 5, which is lower than the values found for PET (between 15 and 22 % for ASR = 4 x 4). This is in agreement with the samples of PET being drawn well into the region of strain hardening, whereas the present PEF samples could not be drawn to stretch ratios above ASR = 5 x 5.

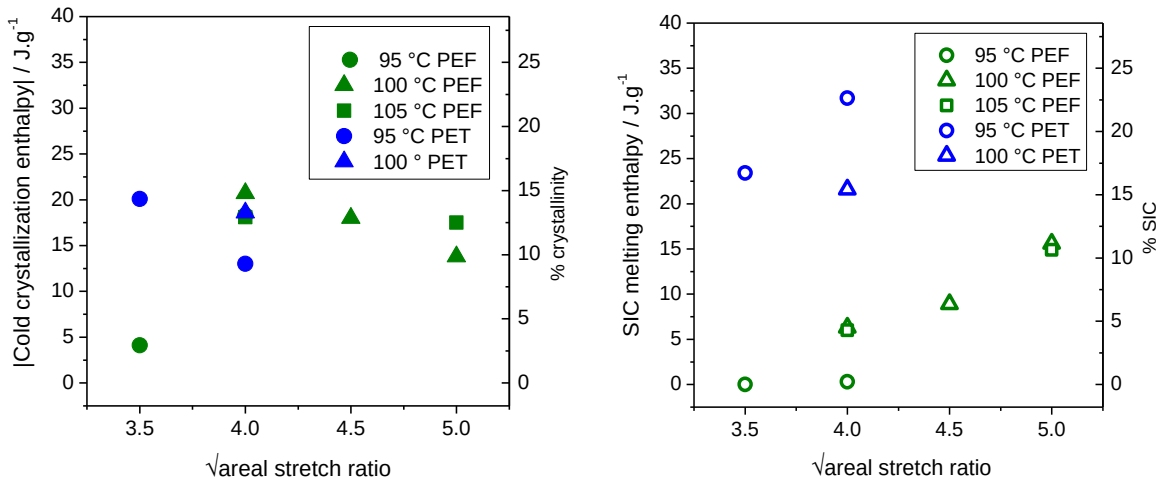

Figure 4 – Cold crystallization enthalpy and SIC melting enthalpy as function of the root square of the areal stretch ratio obtained for PEF (green) and PET (blue). The right hand axis shows the crystallinity percentage.

Shrinkage measurements were done and related to the levels of SIC in the samples. Figure 5 shows the evolution of shrinkage with percentage of SIC found by DSC. The thermally-induced shrinkage is strongly dependent on the temperature[19] and generally increases from 90 °C to 150 °C. In all cases, shrinkage of PEF film strongly decreases with increasing SIC.

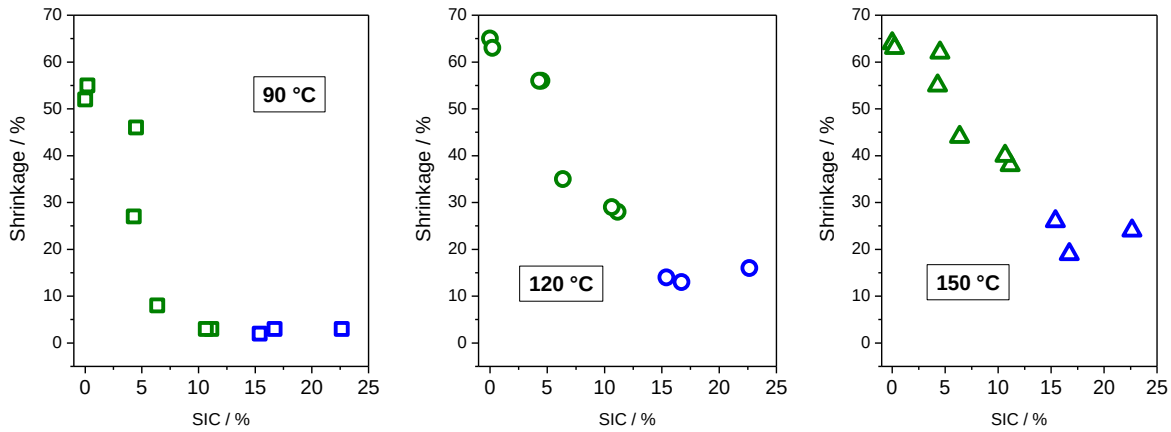

Figure 5 – Shrinkage as function of SIC percentage obtained for PEF (green) and PET (blue). The temperature for which shrinkage was measured is indicated on each graph.

For temperatures of 120 °C and 150 °C, it was found that the shrinkage of PEF and PET are in line with the degree of SIC present in the material. Indeed, the shrinkage of PEF decreases with increasing the percentage of SIC (from 0 to 12%) but is quasi-constant for PET (15-22%). At 90 °C however, PEF reaches the same shrinkage value as PET, which is not the case at 120 °C and 150 °C. At molecular level, the shrinkage results from the disorientation of oriented amorphous chains which releases internal stress and tends to retrieve their initial conformation. In absence of SIC, the thermally-induced shrinkage lead to a rubber-like contraction of the amorphous network. It is possible that at 90 °C the mobility of the chains is playing an additional role, since it is close to its α-transition.

DYNAMIC THERMAL BEHAVIOR

DMA was performed for biaxially stretched PEF and PET to better understand the interplay between the level of orientation and the relaxation processes occurring in both materials. The variation of elastic modulus with temperature is presented in Figure 6 and the corresponding tan δ curves are shown in Figure 6. In Figure 6, the α-relaxation of the amorphous phase of PEF samples is marked by a drop of the elastic modulus between 80 and 120 °C (~two decades), generally at higher temperatures for the oriented films (i.e. +12 °C) in comparison to the non-oriented specimens. For the PEF sample stretched until 4x4 the relaxation is followed by an increase of *E'* around 130 °C, which was attributed to cold crystallization in agreement with the DSC curves. At higher stretch ratio, the decrease of the *E'* during the α-transition becomes progressively lower and the tan δ peak is shifted from 101 °C to 107 °C and 108 °C (Figure 6) at ASR = 4.0 x 4.0, 4.5 x 4.5 and 5 x 5 respectively. This can be explained by an increase in molecular orientation, where oriented chains are progressively more constrained and have more difficulty to move cooperatively. It is worth noting that at higher stretch ratios (4.5 x 4.5 and 5 x 5), the increase of the *E*' modulus normally observed during heating above T_g, and attributed to cold crystallization during the DMA measurement, is absent. However, the small bump observed on these *E*' curves during the glass transition might be attributed to the cold crystallization which could merge with the relaxation process . This is consistent with the DSC data (Figure 2) where a cold crystallization peak was readily observed in the glass transition region.

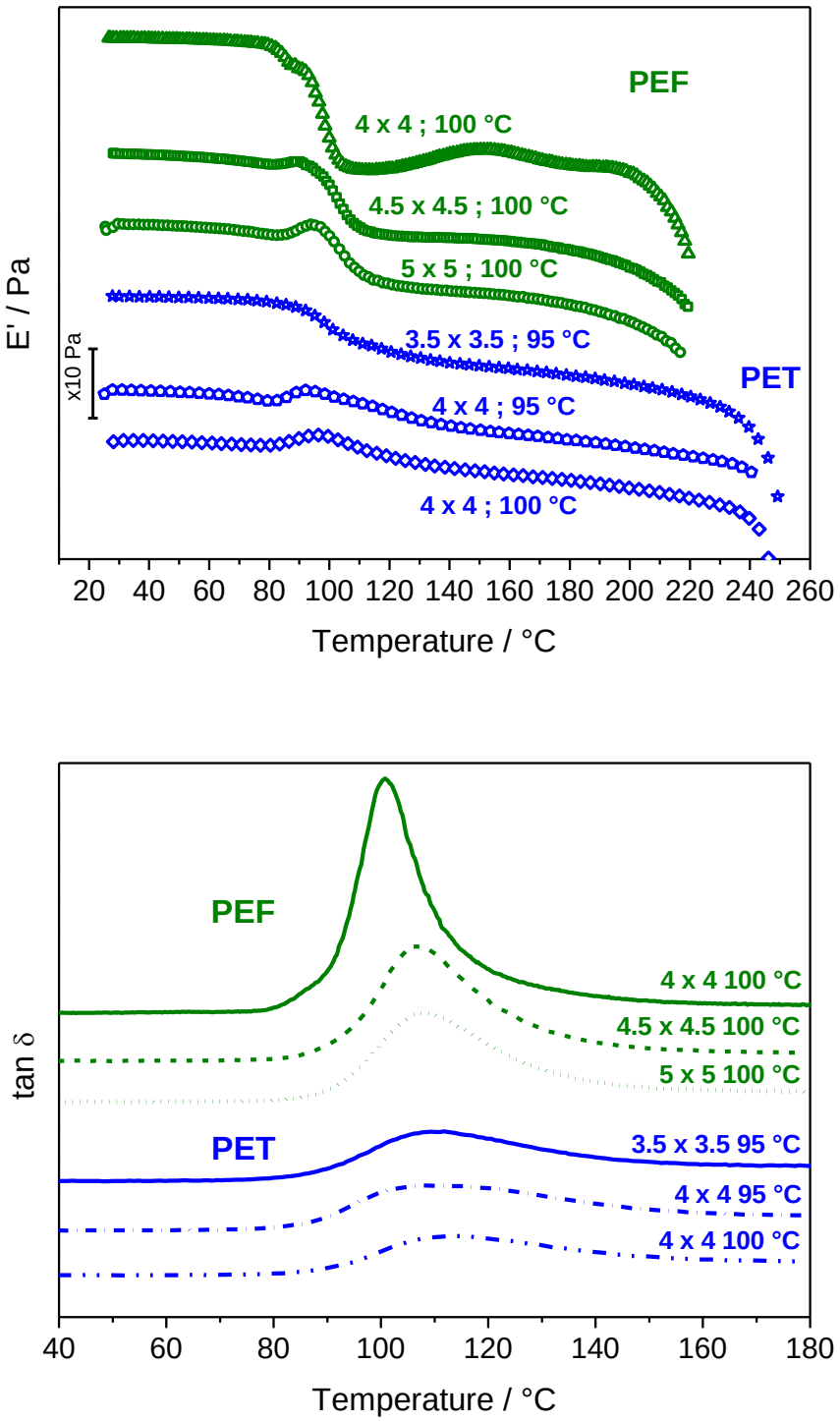

Figure 6 - DMA curves of the storage modulus *E'* (top) and phase angle tan δ (bottom) versus temperature for biaxially stretched PEF and PET. The areal-stretching ratio and temperature of orientation are indicated by each curve.

The same features found in PEF during the α-transition for the samples with ASR = 4.5 x 4.5 and ASR = 5.0 x 5.0 can be found for all the PET samples, although the drop in *E'* is lower

and the tan δ peak is broader. This can be explained by the higher values of SIC found in PET samples and a higher degree of molecular orientation based on the ASR relative to the onset of strain hardening. The *E'* and tan δ curves render it likely that shrinkage measured at 90°C corresponds to the early stages of the α-transition as opposed to the (semi-crystalline) rubbery plateau at 120 °C and 150 °C. Notably, the onset of the α-transition in the tan δ curves increase from 80 to 90 °C and the peak from 100 to 107 °C (peak) for PEF samples stretched at ASR 4.0 x 4.0 and 4.5 x 4.5 and 5.0 x 5.0 respectively. This can explain the particularly significant reduction in shrinkage measured at 90 °C (Figure 5). Furthermore, the T_g values are 15-22 °C higher than those reported previously for non-oriented PEF.

3.3 MECHANICAL PROPERTIES

Figure 7 shows the basic mechanical properties found by tensile testing of oriented PEF and PET samples versus the square root of the areal stretch ratio. In this figure it is clear that for PET both the modulus and strength at break decrease with increasing areal stretch ratio, as opposed to the general increasing trends expected from increasing orientation and observed in the literature for PET. This trend may not be generalized for the sample at 100 °C, but particularly at 95 °C it can be related to the relatively high ASR compared to the NSR for this sample. Previous work has shown a similar decrease in mechanical properties of PET at stretch ratios far beyond the NSR, at the relatively comparable conditions of 100 %/s stretch rate and 85 °C.[4] Although the authors do not provide an explanation of this phenomenon, it can be interpreted as a condition where additional disentanglement by chain slippage starts to occur, i.e. 'overstretching'. A closer examination of Figure 1 indeed shows that for PET at 95 °C, the slope of the strain hardening above ASR = 3.8 x 3.8 for PET exhibits a slight reduction. For PEF, the tensile modulus increases with stretch ratio in a similar way as described in PET literature. Particularly the samples at 5.0 x 5.0 which was stretched beyond the onset of strain hardening show an additional increase in modulus (Figure 7). In that case,

the modulus of PEF samples is higher than for the highest value of PET. The elongation at break shows a lot of variation but generally decreases with stretch ratio, likely since a higher degree of orientation is already achieved. The tensile strength at break of PEF also shows a wide variation. The value obtained for ASR = 5 x 5 are concistently in the range of the values obtained for PET while at lower stretch ratios the values are lower and/or show more variation.

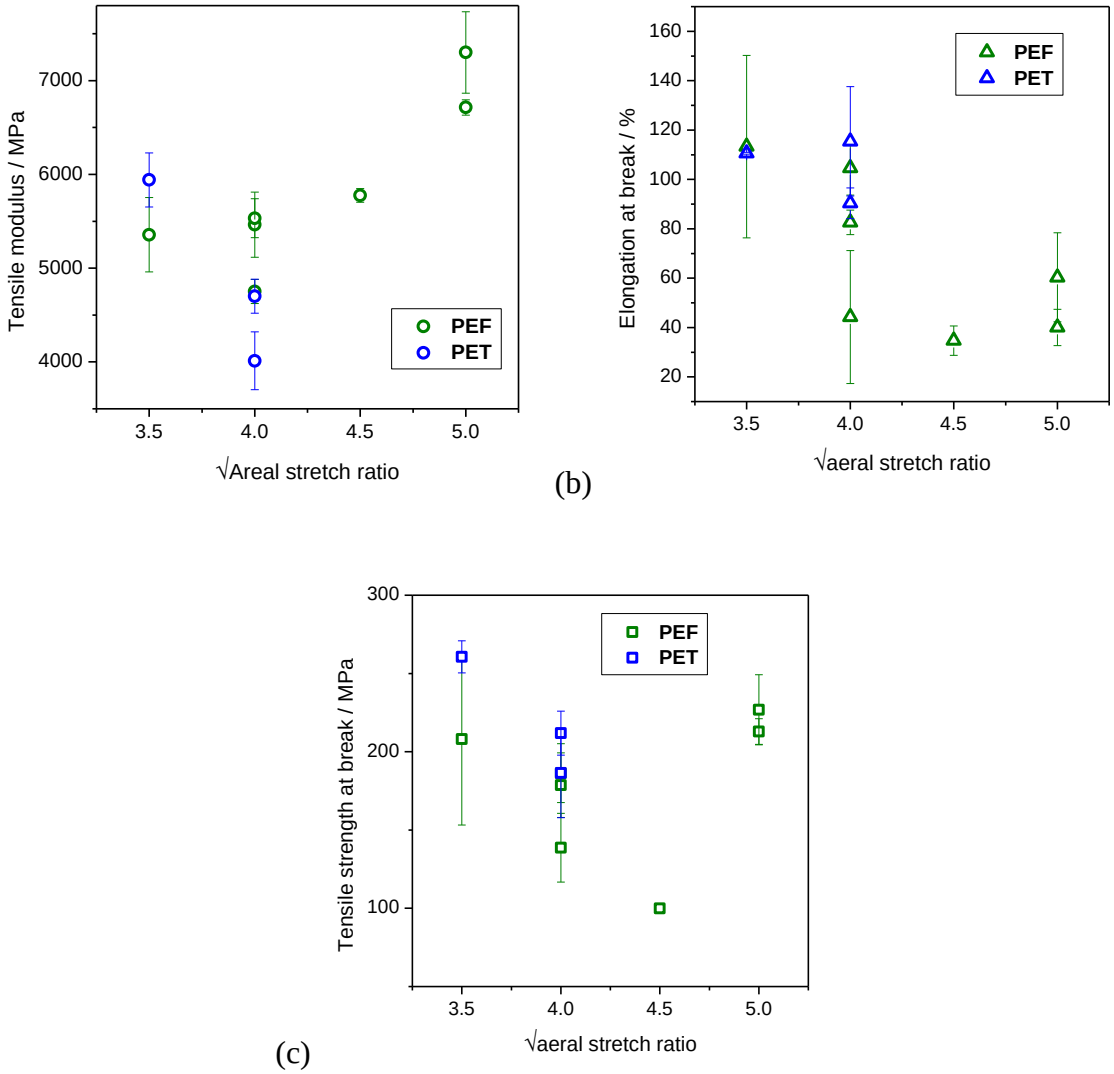

Figure 7 – Tensile modulus (a), elongation at break (b) and tensile strength at break (c) of oriented PEF and PET sample as a function of the square root of the areal stretch ratio.

Additional explanation of the observed behavior can be found in selected examples of stress-strain curves obtained from tensile testing as presented in Figure 8. For PET biaxially stretched at 95 °C, the comparison of 3.5 x 3.5 and 4 x 4 curves highlight the loss of tensile strength at break due to 'overstretching' of polymer chains while retaining the same curve shape, whereas the higher temperature sample (i.e. 100 °C) displays less strain hardening at room temperature. For the PEF samples stretched at 105 °C PEF it is however clear that increasing ASR from 4 x 4 to 5 x 5 led to higher strain hardening which simultaneously increases (average) break strength and decreases the break elongation. This behavior is more in line with literature on PET when stretched to ratios without or with lower degrees of strain hardening. Furthermore, the samples at ASR 4 x 4 at other temperatures further highlight the nature of the previously mentioned variation in the strength and elongation at break, since variation is already present in the stress measured after yield during the test. This can be explained by inhomogeneity across the samples when prepared by compression molding, i.e. by the continued presence of grain boundaries after melting of the resin particles or by fluctuations in the surface, which in turn can cause local differences in deformation during sample stretching. These effects can be diminished when drawing samples into the region of strain hardening, since strain hardening itself will first delocalize over the sample, straightening out any initial local inhomogeneous deformations. Indeed, the PET curves and the PEF sample at ASR = 5.0 x 5.0 show far less of this variation in the stress-strain curves.

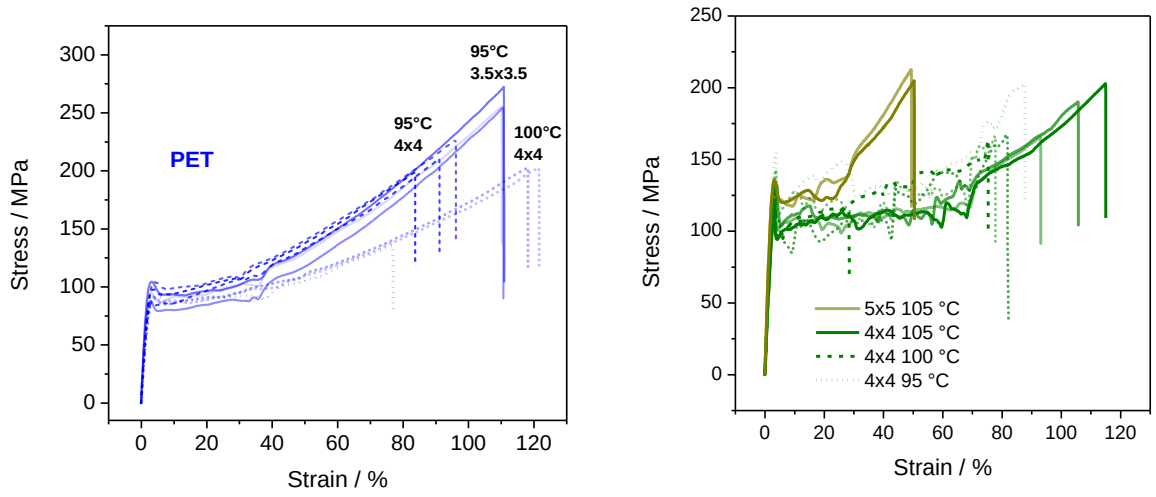

Figure 8 – Examples of stress-strain curves obtained during tensile testing of oriented PEF and PET samples at ambient temperature.

3.4 PERMEABILITY

The permeability of oxygen and carbon dioxide determined at equilibrium conditions for each sample is displayed versus the square root of the areal stretch ratio of PEF and PET in Figure 8. Although some variation can be observed, it shows that the permeability generally decreases with increasing stretch ratio and is significantly lower for PEF than PET.

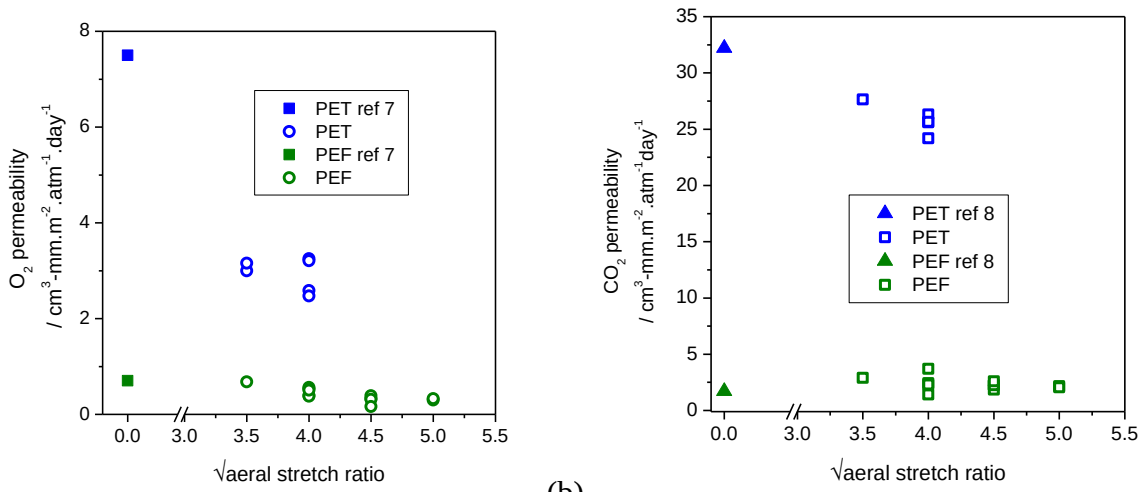

(a) (b)

Figure 8 – Permeability of Oxygen (a) and Carbon Dioxide (b) for biaxially oriented PEF and PET samples, determined at equilibrium permeation at 25 °C and 0% R.H, compared to literature values for amorphous PEF and PET.[20,21]

The oxygen permeability for oriented PET was found to be between 2.5 and 3.3 cm^3-mm/m^2.atm.day, while for PEF a relatively wider range from 0.7 down to 0.2 cm^3-mm/m^2.atm.day was found. For carbon dioxide, a similar observation can be done with permeability values of 24.2 to 27.6 vs 1.4 to 2.9 cm^3-mm/m^2.atm.day found for PET and PEF respectively. For both materials, lower permeability could be found for the oriented specimens compared to the literature values of the amorphous materials, although for certain PEF specimens values could be found that were closer to the amorphous isotropic ones. A wider range of oxygen permeability values was also reported by Orchard et al. for oriented PET, i.e. from 3.6 down to 1.4 cm^3-mm/m^2.atm.day, which they related to crystallinity.[22] For PEF, the permeability vs. previously reported crystallinity is shown in Figure 9.

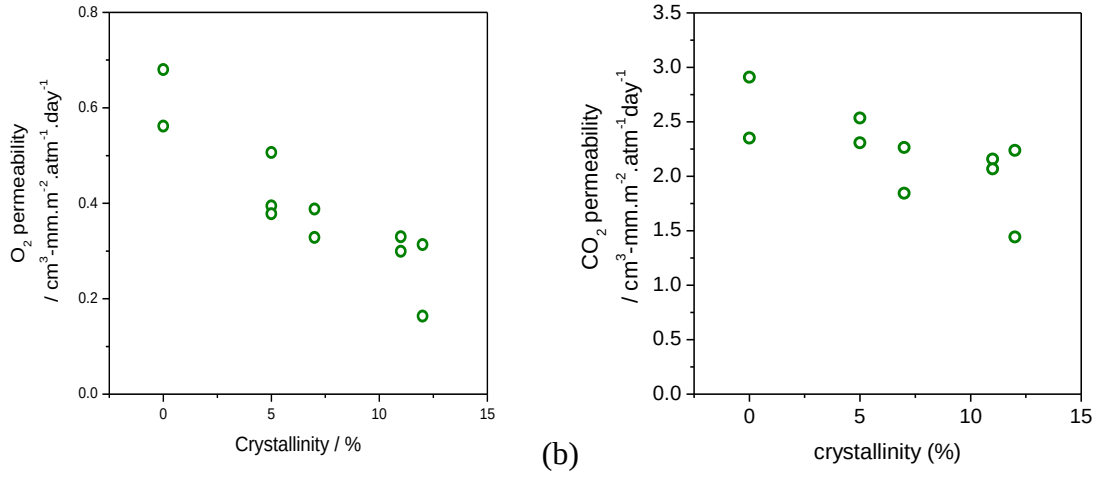

Figure 9 – Permeability of Oxygen (a) and Carbon Dioxide (b) for biaxially oriented PEF determined at equilibrium permeation at 25 °C and 0% R.H vs strain induced crystallinity.

Figure 9 shows that also for PEF there is a clear correlation between crystallinity and permeability, akin to what is known for PET. The values are furthermore in good agreement with previous findings by Burgess et al. of a factor 1.9 and 2.9 reduction in oxygen permeability and a factor 1.5 and 2.2 reduction in carbon dioxide permeability at 5% and 22% crystallinity (7% and 29% at ΔH_m^0 = 140 J/g) respectively compared to amorphous PEF.[23] At the highest degrees of orientation in this study, the oxygen permeability is also in line with the

values of 0.26 to 0.28 cm^3-mm/m^2.atm.day reported by Jun et al. on sequentially biaxially oriented PEF films.[24] Jun et al. also report values of 0.12 and 0.13 cm^3-mm/m^2.atm.day for PEF films following high temperature annealing, an effect which is in line with the permeability reduction from between 2.0 and 2.5 down to 1.4 cm^3-mm/m^2.atm.day for PET films annealed at higher temperatures.[22] For carbon dioxide permeability, a similar effect can be observed as for oxygen although the trend is present to a lesser extent.

3.5 GENERAL DISCUSSION

Strain hardening has a later onset for PEF compared to PET used in this study, which has a direct influence on most properties. For example, the crystallinity and dynamic mechanical behavior is more comparable for PEF at ASR 5 x 5 to PET at ASR 3.5 x 3.5 and the mechanical behavior is also more consistent. This finding is, however, specific to these samples which have roughly the same molecular weight. It is known for PET that molecular weight or Intrinsic Viscosity is inversely proportional to the stretch ratio at which strain hardening starts to occur, and it is likely that similar effects will exist in PEF. The stretching behavior of PET is also known to be affected by strain rate, although at least within an order of magnitude of the rates applied this is inversely related to temperature, which has been discussed in this work. Moreover, the lower entanglement density of PEF indicates that higher molecular weights will inherently be needed to achieve the same amount of entanglements per chain and consequently a comparable network of entanglements to sustain strain hardening. Such relations merit additional study and should be acknowledged with the conclusions.

4 CONCLUSIONS

1. During biaxial orientation, PEF generally exhibits strain hardening at higher stretch ratios compared to PET of the same molecular weight, and exhibits higher stresses when stretched at the same temperature as PET while approaching PET when stretched at higher temperatures.

2. Strain Induced Crystallization occurs in PEF, but for the samples used in this study it occurs at higher stretch ratios than PET and to a lesser degree. Thermal shrinkage shows a strong correlation to Strain Induced Crystallization across PEF and PET. At 90 °C, oriented PEF and PET samples can both exhibit low shrinkage, but at higher temperatures the shrinkage increases significantly and for PEF than PET.

3. The glass transition of PEF broadens when going to high stretch ratios, similarly to PET.

4. Oriented PEF samples with stretch ratios can exhibit a higher modulus than oriented PET samples, and more consistent mechanical behavior than PEF samples at low stretch ratios.

5. Oriented PEF samples exhibit significantly lower oxygen and carbon dioxide permeability than oriented PET samples.

It can therefore be expected in practical applications that both the mechanical properties and the barrier improvement factor of PEF compared to PET can be significantly affected by the orientation conditions and (locally) achieved stretch ratios.

5 REFERENCES

[1] C. Bonnebat, G. Roullet and A.J. de Vries, Polym. Eng. Sci. 21 (1981) 189-195.
[2] M. Cakmak, J.E. Spruiell, J.L. White, Polym. Eng. Sci. 24 (1984) 1390-1395.
[3] Y.Q. Rao, J. Greener, C.A. Avila-Orta, B.S. Hsiao, T.N. Blanton, Polymer 49 (2008) 2507-2514.
[4] S. K. Sharma, A. Misra, J. Appl. Polym. Sci. 34 (1987) 2231-2247.
[5] S. A. Jabarin, Polym. Eng. Sci. 32 (1992) 1341-1349.
[6] E. Gorlier, J. M. Haudin, N. Billon, Polymer (2001), 42, 9541-9549.
[7] Y. Marco, L. Chevalier, M. Chaouche, Polymer 43 (2002) 6569-6574.
[8] B. Wunderlich, Prog. Polym. Sci. 28 (2003), 383-450.
[9] F. Hamonic, V. Miri, A. Saiter Eric Dargent, Europ Polym. J. 58 (2014) 233-244
[10] C. Lixon, N. Delpouve, A. Saiter, E. Dargent, Y. Grohen, Europ. Polym. J. 44 (2008) 3377-3384.
[11] Y. Furushima, K. Ishikiriyama, T. Higashioji, Polymer 54 (2013) 4078-4084.
[12] N. Delpouve, G. Stoclet, A. Saiter, E. Dargent, S. Marais, J. Phys. Chem. B 116 (2012) 4615-4625.
[13] P. Chandran, S. Jabarin, Adv. Polym. Technol. 12 (1993) 119-132.
[14] A. Ajji, J. Guevremont, K. C. Cole, M. M. Dumoulin, Polymer 37 (1998) 3707-3714.
[15] A. Codou, N. Guigo, J. van Berkel, E. de Jong, N. Sbirrazzuoli. Macromol. Chem. Phys., 215 (2014), 2065−2074.
[16] M. G. Rogers, J. Mater. Sci. 26 (1991) 4285-4287.
[17] M. Hassan, M. Cakmak, Polymer 54 (2013) 6463-6470.
[18] M. Hassan, M. Cakmak, Macromolecules 48 (2015) 4657-4668.
[19] V.B Gupta, J. Radhakrishman, S.K. Sett, Polymer 34 (1993) 3814-3822.
[20] S.K. Burgess, O. Karvan, J.R. Johnson, R.M. Kriegel, W. J. Koros, Polymer, 55 (2014) 4748-4756.
[21] S. K. Burgess, D.S. Mikkilineni, D.B. Yu, D.J. Kim, C.R. Mubarak, R.M. Kriegel, W.J. Koros, Polymer 55 (2014) 6870-6882
[22] G.A.J. Orchard, P. Spiby, I.M. Ward, J. Pol. Sci. B. Pol. Phys. 28 (1990) 603-621.
[23] S.K. Burgess, G.B. Wenz, R.M. Kriegel, W.J. Koross, Polymer 98 (2016), 305-310.
[24] I. Jun, I. Katsuya, S. Toshiyuku, G. Shoichi, M. Chikao, J.G. Van Berkel, (2017) WO2017038092.

CHAPTER 9
GENERAL CONCLUSIONS AND OUTLOOK

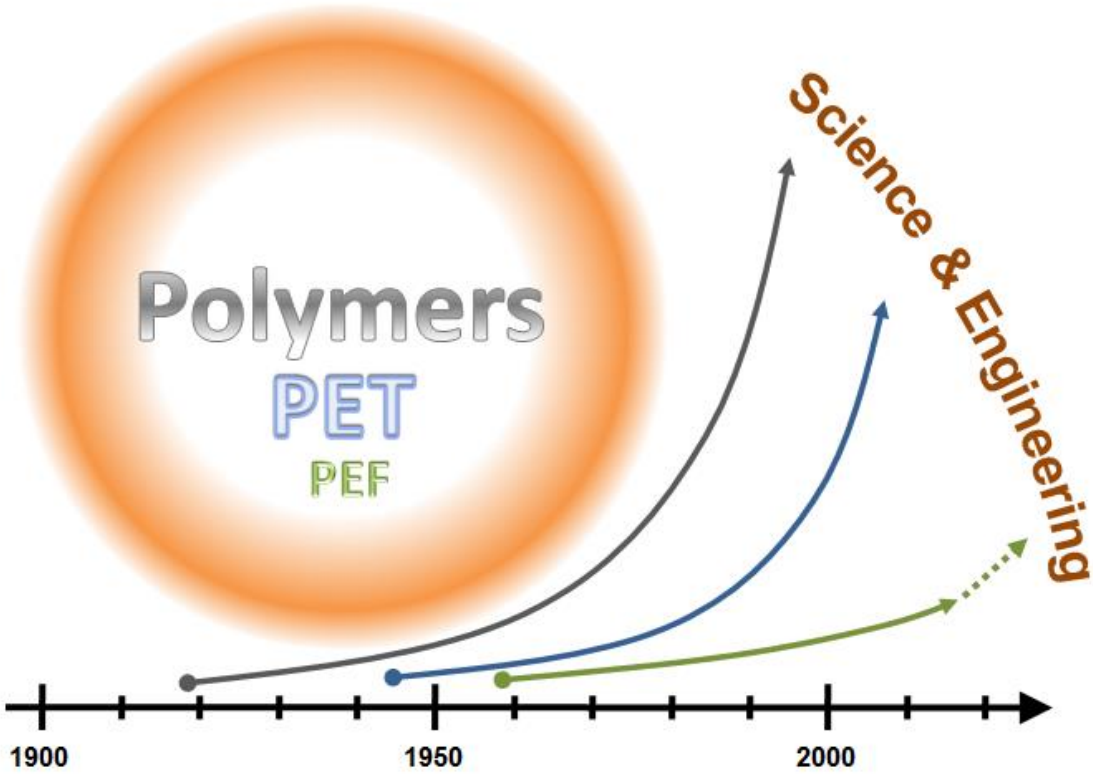

1 CONCLUSIONS

The first portion of this work focused on the melting and crystallization behavior of PEF.

Both Chapter 3 and 4 present mathematical relations that describe well the crystallization kinetics of PEF as function of molecular weight under ideal conditions such as isothermal and slow cooling from the melt, as well as more practical conditions such as faster cooling and heating from a glassy state. Chapter 5 shows that nucleation at temperatures closer to the glass increases the glass crystallization rate of samples that are cooled slowly or kept at lower temperatures. Likewise, certain catalyst residues can nucleate PEF.

Although Chapter 3 discusses the possibility that melting peak I and II originate from a primary and a secondary lamellar thickness distribution, Chapter 5 demonstrates that at 170°C only a single distribution exists which recrystallizes upon heating to higher temperatures at lower rates. The different crystallization behavior from the glassy state in Chapter 4 thus originates from a combination of nucleation during cooling and heating as well as recrystallization processes occuring when continuing to heat to higher temperatures.

Generally PEF crystallizes more slowly than PET, which kinetics show is caused by mobility related aspects such as a restricted segmental jump U^* or reduced reference growth rate G_0. The activation energy for secondary nucleation K_g is in line with PET although direct comparative studies as well as more information on ΔH_m^0 and T_m^0 is needed to conclude this. Although it is practical to accept the value of ΔH_m^0 = 140 J/g for PEF similar to PET, there is evidence in Chapter 6 as well as recent work by Burgess et al.[1] that points to a higher value as described in Chapter 3.

The second portion of this work focused on the physics and mechanics of PEF *vs* PET.

Chapter 6 shows that PEF crystals do not restrict the chain motion of the PEF in the same way as PET, but that the PEF chain motion is already restricted and is counteracted by a higher

free volume. This explains the higher T_g and modulus below the T_g than PET, while the volume for the cooperative rearranging region and activation energy of the glass transition are comparable.

Chapter 7 reveals that the unperturped chain dimensions of PEF are not significantly affected by conformational restrictions over PET, but simply reduced by the length of the FDCA monomer. This explains the higher free volume and a more loosely entangled network of chains, and furthermore indicates that reduced chain mobility in PEF is mainly caused by intermolecular forces such as dipole-dipole interactions of the furan rings. Mathematical relations for the melt viscosity of PEF were found that describe its dependence on molecular weight and shear rate, with higher activation energy and earlier onset of shear thinning for PEF compared to PET that are characteristic of a more loosely entangled network. Initial mechanical tests indicate a higher yield stress and increased tendency towards brittle behavior for PEF, although high elongations at break could be obtained with sufficient molecular weight. The mechanical behavior of PEF is comparable to PET around the β transition and could partially be explained by a lower entanglement density, but may also be affected by the reduced chain mobility, i.e. specific intermolecular interactions that do not occur in PET.

Initial biaxial stretching experiments in Chapter 8 indicate that PEF requires additional stretching force when not ofset by temperature, and reaches higher stretch ratios than PET before strain hardening and strain induced crystallization occur, again a result of a lower entanglement density. However, once higher stretch ratios are employed, similar features such as improved oriented properties and barrier were found as well as an increased T_g, indicating that the combination of crystallization and orientation can still yield chain confinement.

2 OUTLOOK

An approach to obtain more information on ΔH_m^0 and T_m^0 would be to study the lamellar thickening kinetics. Isothermal annealing experiments at various temperatures T_c supported by SAXS can pinpoint the T_m^0 more accurately, as the Hoffman Weeks Equation (1) shows that linear extrapolation to $T_m = T_c$ can only be done when β is constant, which is not a given for equal annealing times and may require non-linear extrapolations.[2]

$$T_m = T_m^0\left(1 - \frac{1}{\beta}\right) + \frac{T_c}{\beta} \qquad (1)$$

Furthermore, it is known that after primary crystallization is completed, PET crystallinity shows a linear increase with the logarithm of time, in which the slope increases with increasing temperature. If it is assumed that this occurs solely by increase of lamellar thickness β, T_m^0 can be fit by plotting T_m at various T_c and times t as per Equation (2).

$$\frac{T_c - T_m^0}{T_m - T_m^0} = \beta = k(T_c)\log t + C \qquad (2)$$

A more complete approach can be taken following Marand et al.[3], who fit lamellar thickening and primary crystallization kinetics simultaneously, as lamellar thickening will start to occur directly after crystals form. It shoud be noted that in such studies the DEG content should be taken into account, since this co-monomer readily forms from ethylene glycol during polycondensation of PET and is known to affect its melt point and crystal perfection.[4]

PEF in comparison to PET, PEI and PEN, as well as similar polyesters with longer diols, can serve as model systems to understand structure-property relations of polymers. Examples of studies that could contribute to such understanding are dynamic studies on the β-transition similar to Chapter 6 as well as spectroscopic techniques such as dielectric, Raman, infrared or solid state NMR at various temperatures or even combined with pVT measurements. Molecular simulations may furthermore help to support observed spectroscopic responses.

Dipole-dipole interactions of the furan ring may be highlighted by solid state NMR if excitation of the specific dipole of the furan ring can be shown to influence other motions such as the adjacent carboxylgroup rotation. Alternatively, synthesizing a polymer with 2,5-tiophenedicarboxylic acid may provide understanding of the effect of the dipole moment, which is lower for the tiophene ring than the furan ring and should thus yield properties in the direction of PEI.

Mechanical tests of amorphous materials may be expanded by compression, uniaxial and biaxial stretching at various temperatures and rates, which may be fit with the Robertson theory in the glassy state.[5] The effect of physical ageing on mechanical properties should also be considered[6], as well as plasticizers that may reduce the yield stress and promote toughness. As described in Chapter 2, initial work has been done on investigating strain-induced crystallization during stretching and upon relaxation at higher temperatures, by WAXD on quenched samples or *in situ*. Likewise, flow-induced crystallization can be investigated by high pressure injection into thin-walled cavities.

Finally, blending PEF and PET has been shown to yield copolyesters by trans-esterification[7], which is relevant for potential PEF contamination in the PET recycling stream as well as having some interesting applications. The kinetics thereof can be studied by blending the two materials and measuring the extent of trans-esterification by NMR.

---

[1] S.K. Burgess, G.B. Wenz, R.M. Kriegel, W.J. Koros, Polymer 98 (2016), 305
[2] H. Marand, J. Xu., S. Srinivas, Macromolecules 31 (1998), 8219
[3] H. Marand, Z. Huang, Macromolecules 37 (2004), 6492.
[4] M. Patkar, S.A. Jabarin, J. Appl. Polym. Sci., 47 (1993), 1748.
[5] R.A. Duckett, S. Rabinowitz, I.M. Ward, J. Mat. Sci. 5 (1970), 909.
[6] S.K. Burgess, C.R. Mubarak, R.M. Kriegel, W.J. Koros, J. Pol. Sci. B. Pol. Phys. 53 (2015), 389.
[7] Y. Brun, A.M. Castagna, K-H. Liao, F. Nederberg, E.F. McCord, J.C. Rasmussen, WO2015168563

LIST OF PUBLICATIONS AND PATENT APPLICATIONS

A. Codou, N. Guigo, J.G. Van Berkel, E. De Jong, N. Sbirrazzuoli, "Non-isothermal Crystallization Kinetics of Biobased Poly(ethylene 2,5-furandicarboxylate) Synthesized via the Direct Esterification Process", Macromol. Chem. Phys. 215 (2014), 2065.

J.G. Van Berkel, N. Guigo, J.J. Kolstad, L. Sipos, B. Wang, M.A. Dam, N. Sbirrazzuoli, "Isothermal Crystalization Kinetics of Poly(ethylene 2,5-furandicarboxylate) Synthesized via the Direct Esterification Process", Macromol. Mat. Eng. 300 (2015), 466.

J.J. Kolstad, B. Wang, R.J. Schavione, M.L. Andrews, E.E. Paschke, J.G. Van Berkel "Polyester and Method for Preparing Such a Polyester", WO2015137805 (2015).

J.J. Kolstad, G.J.M. Gruter, M.A. Dam, B. Wang, R.J. Schavione, M.L. Andrews, J.G. Van Berkel, E.E. Paschke "Process For Enhancing The Molecular Weight of a Polyester", WO2015137806 (2015).

J.J. Kolstad, G.J.M. Gruter, M.A. Dam, B. Wang, R.J. Schavione, M.L. Andrews, J.G. Van Berkel, E.E. Paschke "Polyester and Method for Preparing Such a Polyester", WO2015137807 (2015).

L. Martino, N. Guigo, J.G. van Berkel, J.J. Kolstad, N. Sbirrazzuoli, "Nucleation and Self-Nucleation of Bio-Based Poly(ethylene 2,5-furandicarboxylate) Probed by Fast Scanning Calorimetry", Macromol. Mat. Eng. 301 (2016), 466.

A. Codou, M. Moncel, J.G. Van Berkel, N. Guigo, N. Sbirrazzuoli, "Glass transition dynamics and cooperativity length of poly(ethylene 2,5-furandicarboxylate) compared to poly(ethylene terephthalate)", Phys. Chem. Chem. Phys 18 (2016), 16647.

L. Martino, N. Guigo, V. Niknam, J.G. van Berkel, N. Sbirrazzuoli, "Morphology and thermal properties of novel clay-based poly(ethylene 2,5-furandicarboxylate) (PEF) nanocomposites", RSC Advances 6 (2016), 59800.

J.J. Kolstad, J.G. Van Berkel, "Process for producing an oriented film comprising poly(ethylene 2,5-furandicarboxylate)", WO2016032330 (2016)

L. Martino, N. Guigo, J.G. van Berkel, N. Sbirrazzuoli, "Influence of organically modified montmorillonite and sepiolite clays on the physical properties of bio-based poly(ethylene 2,5-furandicarboxylate)", Composites Part B: Engineering 110 (2017), 96.

N. Guigo, J.G. van Berkel, E. De Jong, N. Sbirrazzuoli, "Modelling the non-isothermal crystallization of Polymers: Application to poly(ethylene 2,5-furandicarboxylate)", Thermochimica Acta 650 (2017), 66.

A. Codou, N. Guigo, J.G. Van Berkel, E. De Jong, N. Sbirrazzuoli, “Preparation and crystallization behavior of poly(ethylene 2,5-furandicarboxylate)/cellulose composites by twin screw extrusion”, Carbohydrate Polymers 174 (2017), 1026.

A. Codou, N. Guigo, J.G. Van Berkel, E. De Jong, N. Sbirrazzuoli, “Preparation and characterization of poly(ethylene 2,5-furandicarboxylate)/cellulose composites via solvent casting”, J. Pol. Eng. 37 (2017), 869.

J.G. Van Berkel, N. Guigo, J.J. Kolstad, N. Sbirrazzuoli, “Biaxial Orientation of Poly(ethylene 2,5-durandicarboxylate): An explorative study”, Macromol. Mat. Eng. 303 (2018), 1700507.

H. Nakajima, J.G. Van Berkel, “Masterbatch Polyester Composition”, WO2017023173 (2017)

H. Nakajima, J.G. Van Berkel, “Polyester Composition”, WO2017023174 (2017)

H. Nakajima, J.G. Van Berkel, “Poly(alkylene furandicarboxylate)-comprising polyester”, WO2017023175 (2017)

J. Inagaki, K. Ito, T. Shimizu, S. Gyobu, C. Morishige, J.G. Van Berkel “Polyester Film Containing Furandicarboxylate Unit” WO2017038092 (2017)

Y. Ikeda, K. Sugimoto, H. Nakajima, J.G. Van Berkel, “Manufacturing Method of PEF Raw Yarn, PEF Yarn and Tire”, WO2017043082 (2017)

J. Inagaki, Y. Numata, J.G. Van Berkel “Laminated Polyester Film” WO2017115736 (2017)

J. Inagaki, K. Sawada, Y. Numata, J.G. Van Berkel “Laminated Polyester Film” WO2017115737 (2017)

J. Inagaki, K. Ito, Y. Numata, S. Hayakawa, J.G. Van Berkel “Polyester Film” WO2017169553 (2017)

ACKNOWLEDGEMENTS

Firstly, my gratitude goes out to those who have enabled and guided me in doing the work in this thesis as well as pursuing a PhD. I gratefully acknowledge the funding provided by the EU as part of the "Marie Curie Industry Academia Partnerships and Pathways" (IAPP) framework (FP7-PEOPLE-2012-IAPP) which enabled the exchange under the BIOFUR project that led to this thesis. I would also like to thank Ed de Jong for initiating this project and facilitating the interactions with Université Côte d'Azur, as well as being a great colleague, and Gert-Jan Gruter for being fully supportive on letting me pursue this besides my employment activities. René Dam, my first line manager, has greatly supported me by giving me the individual freedom to conduct these studies, while pushing me to diligently consider the alternatives before drawing conclusions or as we say in Dutch "niet te kort door de bocht". My current line manager Alex Lachmund at Synvina also supported me to continue this work, and although not discussing many technical topics I sometimes still get the same feedback from him. Nathanaël Guigo, in our enjoyable collaborations in both Amsterdam and Nice, as well as Nicolas Sbirrazzuoli, have inspired me to make scientific contributions from my work as well as pursuing a PhD. Nicolas has offered me the opportunity to do this in his lab and has furthermore greatly contributed to my mathematical skills as well as teaching me the application of the Hoffman-Lauritzen theory to polymer crystallization in various ways. Furthermore both he and Nathanaël Guigo have greatly helped me by guiding me through the processes of scientific writing and publication.

Secondly, but definitely no less, I had the privilege to collaborate with many amazing people when doing this work. Besides those mentioned above, Jeff Kolstad has greatly contributed as a sparring partner on the majority of the content, and Roy Visser on the final two Chapters in particular. Lucrezia Martino and Amandine Codou have conducted the majority of the work in Chapter 5 and 6, challenging my views and deepening my understanding of these topics. Furthermore, Laszlo Sipos and Bing Wang have conducted all polyester synthesis, and Laszlo built the original GPC system that has been critical for much of this work. However, next to the direct contributions, the positive atmosphere of both the teams in Amsterdam and Nice is what gave me the energy to do this work; always open for respectable discussion or fun -

whichever was needed at a given time. This includes Danny, Sulivan, Benoit, Hajime, René Aberson, Ate, Robert-Jan, Nathan, Julia, Francesco and all my other colleagues at Avantium as well as Nicolas Bosq, Matthieu, Jean-Mathieu, Guillaume and Sébastien and many others at Université Côte D'Azur. Also my colleagues in Japan, especially at Toyobo, have brought me a lot of new experiences and I am definitely grateful to Nathan for sharing them and initiating these collaborations. I'm also happy to now see this trend continuing at Synvina, with Gerald, Erol, Thijs, Ingrid, Lucia, Ammad and many other new colleagues.

Finally, my immense gratitude goes out to my friends and family, who have both made me who I am today and kept supporting me through the amount of time I spent on studying PEF and trying to get it to the (super)market. To my parents, you have given me a great balance between self-learning and guidance with a listening ear. The stubbornness I inherited from you made it take me a while to value this guidance (and that of others), but I believe my independent critical thinking is also one of my biggest assets. Fabi, Kaja, Silje, Nina, Kevin, Gideon, Attila, Jasper, Mitchell, Dirk, Rianne, Tim, Mark, Arjan, Pepels, Jeroen, Tim, Thijs, Michiel, Macro, Chris, Beorn, and my cousins, aunts, uncles and grandparents, including those in Norway; you have brought fun, support and different perspectives to my life, and even managed to make me a somewhat social human being. Even though I don't see all of you or connect to you as much as I would like, knowing that you are there keeps me going and also made this work possible. Amandine, my love, we have met each other during this work and since then you have always given me love and support. We've had amazing times all over the world, and you kept my head straight and focused when I needed it. Without you I would not have completed this thesis, for that matter I do not know where I would have been. Therefore it is my honor to dedicate this work to you… albeit that you will share it with my grandfather Cor van der Ven, who has spent much of his working life technically supporting many PhD students at TU Delft and I hope to make proud by successfully defending mine.

ABSTRACT

Plastics have become an integral part of our lives, while the petrochemical feedstocks used to make them are not sustainable on the long term. In pursuit of production processes starting from renewable feedstocks, furanics were found to form quite readily from abundant plant-based carbohydrates and to bring new functionality as intermediates. Poly(ethylene 2,5-furandicarboxylate) or PEF is one of the plastics that can be made through 2,5-furandicaboxylic acid (FDCA) as an intermediate. It can be produced analogously to the ubiquitous material Poly(ethylene terephthalate) (PET) but has only recently been gaining more attention including the finding that it has greatly reduced gas permeability and a higher modulus and glass transition temperature, rendering it interesting as a packaging material. In the first part of this work we study the crystallization behavior of PEF, relevant for production and handling of pellets as well as transparency and thermal properties in end-use applications, as a function of molecular weight and the type of catalyst used. Mathematical models were found that describe both isothermal crystallization kinetics and non-isothermal kinetics for PEF, which is generally slower than PET. PEF crystallization from the glass found to be atypical and was modeled using unconventional models and the isoconversional approach. The origin of this behavior was found to be nucleation at low temperatures, which can be influenced to accelerate its crystallization. The second part of this work relates to the thermomechanical behavior of PEF, relevant for its processing and application in particular. The higher glass transition temperature was found to not increase as much by crystallinity as PET, and could be attributed to a reduced chain mobility compensated by increased free volume. The loose entanglement of PEF could be explained by reduced unperturbed chain dimensions following quite directly from the reduced bond length of FDCA. No significant conformational restictions were found, thus any mobility reduction should be intermolecular. A higher temperature and strain rate dependence of the melt viscosity was found for PEF across various molecular weights and catalyst types, which was described mathematically and can also be explained by a more loosely entangled network. The amorphous mechanical properties and higher strain rate dependence at room temperature also point to a low entanglement network although mobility reduction may also play a role. Biaxial orientation of PEF in the rubbery state, relevant for producing films and bottles, showed that higher draw ratios are needed than for PET until molecular orientation is maximized and strain hardening begins. However, it was found that upon using higher stretch ratios, oriented PEF can exhibit increased strength and T_g compared to oriented PET and further reduced gas permeability.